Experimental Investigation of Unsteady Loading and Fluid Dynamics of Tidal Stream Turbines



Daniel Rowe

St Edmund Hall

University of Oxford

A thesis submitted for the degree of

Doctor of Philosophy

Michaelmas Term, 2024

Acknowledgements

Firstly, I would like to acknowledge the support I received from the University of Oxford over the past four years, including the supervision of Prof. Richard Willden and Dr Christopher Vogel, as well as the advice of my college advisor, Prof. Eleanor Stride. I am also grateful to the numerous technicians—too many to name individually—who provided assistance across multiple departmental workshops, including electronics, geotechnical, maintenance, mechanical, and solid mechanics. Special thanks go to Dr Peter Walters and Simon Hills for their generosity in answering my design and manufacturing-related questions, as well as Alison May for her help over the past four years.

This research was funded through an EPSRC studentship, and I also wish to acknowledge the additional sources of funding that made my experimental work possible.

I have been fortunate to work alongside two outstanding engineers—Dr Sam Tucker Harvey and Dr James McNaughton—whose technical abilities and good nature were a source of invaluable support, particularly during the first year of my research.

I would also like to acknowledge members of the wind and tidal energy research group, both past and present, who contributed to the development of the turbine used in this research.

On a personal note, a huge thank you to my mum for her love and support throughout my years of study. I am forever grateful to my cat, Micky, whose companionship and emotional support have meant far more to me than he could ever realise.

Last, but certainly not least, I owe a heartfelt thank you to my wife, Julia, for her unwavering support and the sacrifices she has made over the past four years. I could not have done this without her.

Abstract

Tidal stream energy provides a largely untapped and predictable source of renewable energy with the potential to play a significant role in global decarbonisation efforts. However, the economic and technical challenges associated with tidal stream technologies, particularly the need to design systems capable of withstanding the harsh marine environment, present substantial barriers to its commercialisation. In the absence of a substantial body of available field data, and given the multitude of challenges associated with performing in-field test campaigns, carefully designed laboratory experiments—with appropriate levels of accuracy and quantified error—can provide valuable insights into the underlying flow physics and inform understanding of the performance and loading response of axial-flow tidal rotors.

Part I of this thesis begins with a description of an experimental methodology developed for the hydrodynamic characterisation of a recirculating water flume, in preparation for the model-scale testing of a horizontal axis tidal stream turbine. The methodology, which centres on the use of an acoustic Doppler velocimeter (ADV) for flow measurement, enabled a detailed investigation of the flow's spatial uniformity, temporal stability, and turbulence parameters, instilling confidence in establishing baseline flow conditions for model-scale experiments. Applying the methodology described, the Oxford flume was found to have high velocity uniformity, with deviations of less than 1% at the 95% confidence level, and controlled low turbulence levels ranging between 1–2%, providing a stable and reliable basis for evaluating model-scale turbine response.

Laboratory-based testing also provides flexibility for exploring parameter spaces of interest. For tidal developers, a key area of focus is understanding the unsteady loading effects of freestream turbulence. In this work, passive turbulence-generating grids were used to control the onset turbulence, primarily by influencing the turbulence intensity and integral length scales, with the resulting flow fields characterised in detail ahead of model-scale testing. At the intended rotor plane, the freestream turbulence was elevated relative to the clean flow case, with turbulence intensities ranging between 4–12%, while the integral length scales remained less than 20% of the 0.6 m rotor diameter. The transient nature of the generated turbulence was particularly evident in the turbulence intensity profiles, which showed that as the grid mesh size increased for a given bar width, turbulence production weakened, and the production region shifted further downstream.

To broaden the investigation, a second source of hydrodynamic unsteadiness was introduced through controlled vertical velocity shear. A practical methodology for generating and controlling the onset vertical shear was demonstrated, marking the first application of this approach in open-channel flow, with the resulting flow fields also characterised in detail ahead of model-scale testing. The profiles, characterised by the denominator of the power-law exponent with values of $n = 6$ and $n = 9$, effectively established an achievable range around the widely cited value of $n = 7$, partially capturing the considerable variation throughout the tidal cycle.

In Part II of this thesis, the focus shifts to model-scale testing under the characterised flow conditions. First, a detailed account of the development work required to prepare the turbine for testing in the flume is presented, with particular emphasis on ensuring that the instantaneous load response of each blade root was captured accurately and reliably. The requisite physical setup and experimental methodology are also described.

The turbine test campaign was the first of its kind in the Oxford flume, with an extended test period that allowed for a comprehensive analysis of the turbine's response across a range of Reynolds number-dependent flow regimes and operating points. The turbine operated most efficiently under clean flow conditions, achieving a maximum power coefficient of 0.57 and a maximum thrust coefficient of 1.43. Interpretation of the turbine's non-dimensional response was found to be highly sensitive to the choice of reference velocity used for normalisation, a sensitivity further exacerbated by higher non-uniformity in more unsteady approach flows. New insights into the effects of blade stall at low tip-speed ratios are also presented, revealing a phase shift exceeding 140° in the azimuthal position of the maximum blade load in clean flow relative to higher tip-speed ratios. Furthermore, the results indicate that sheared inflows generate more pronounced fluctuations in once-per-revolution blade forcing, equivalent to 16–21% of the time-averaged blade loads in the limiting case, compared to grid-generated turbulence, which has a maximum of 8.3%. This suggests that, as a first-order approximation of flow unsteadiness, vertical shear has a more significant effect on rotor loading.

Contents

1 Introduction **1**
- 1.1 Harnessing the Tidal Resource . . . 2
- 1.2 Industry Challenges . . . 4
  - 1.2.1 Economic Challenges . . . 4
  - 1.2.2 Technical Challenges . . . 5
- 1.3 Motivation for Model-Scale Testing . . . 7
- 1.4 Thesis Objectives . . . 8
- 1.5 Thesis Outline . . . 10

I Flow Characterisation **12**

2 Experimental Methodology for Flow Characterisation **13**
- 2.1 Experimental Set-up . . . 14
  - 2.1.1 University of Oxford Flume . . . 14
  - 2.1.2 Acoustic Doppler Velocimetry . . . 15
  - 2.1.3 Linear Traverse . . . 16
  - 2.1.4 Vibration . . . 17
  - 2.1.5 Wave Gauges . . . 18
- 2.2 Methodology . . . 18
  - 2.2.1 ADV Configuration . . . 19
  - 2.2.2 Flow Sampling Strategy . . . 19
  - 2.2.3 ADV Signal Quality . . . 21
  - 2.2.4 Post-processing . . . 22
  - 2.2.5 Flow Analysis . . . 28
  - 2.2.6 Vibration Analysis . . . 34
- 2.3 Limitations of the Methodology . . . 36
- 2.4 Summary . . . 37

3 Clean Flow Characterisation in a Hydraulic Flume **39**
- 3.1 Observed Hydrodynamics . . . 39
  - 3.1.1 Mean Velocities . . . 40
  - 3.1.2 Bottom Boundary Layer . . . 46

3.1.3 Free-Surface Response . . . 48
3.2 Observed Turbulence Characteristics . . . 49
3.2.1 Turbulence Intensities . . . 49
3.2.2 Reynolds Stresses . . . 55
3.2.3 Integral Scales . . . 57
3.3 Velocity Spectra . . . 59
3.4 Summary . . . 61

4 Generation, Control, and Characterisation of Onset Turbulence 64
4.1 Historical Approaches . . . 65
4.2 Turbulence Generation Methodology . . . 66
4.3 Centreline Measurements . . . 70
4.3.1 Mean Velocities . . . 70
4.3.2 Anisotropy . . . 72
4.3.3 Turbulence Intensities . . . 74
4.3.4 Kinetic Energy Decay . . . 76
4.3.5 Integral Scales . . . 79
4.3.6 Velocity Spectra . . . 81
4.4 Parameter Space Selection For Model-Scale Testing . . . 83
4.5 Characterisation of Turbulent Flow Fields . . . 86
4.5.1 Mean Velocities . . . 86
4.5.2 Turbulence Intensities . . . 89
4.5.3 Integral Scales . . . 91
4.5.4 Reliability of Centreline Statistics . . . 92
4.6 Limitations of the Investigation . . . 94
4.7 Summary . . . 95

5 Generation, Control, and Characterisation of Vertical Shear 98
5.1 Historical Approaches . . . 99
5.2 Shear Generation Methodology . . . 100
5.3 Characterisation of Sheared Flow Regimes . . . 103
5.3.1 Mean Velocities . . . 104
5.3.2 Turbulence Intensities . . . 107
5.3.3 Integral Scales . . . 109
5.3.4 Quadrant Analysis . . . 113
5.4 Limitations of the Investigation . . . 116
5.5 Summary . . . 117

II Model-Scale Testing 119

6 Literature Review on the Hydrodynamics of Tidal Rotors 120
6.1 Steady Loading . . . 120
6.2 Unsteady Hydrodynamics . . . 124

6.3 Sources of Unsteady Hydrodynamic Loading . . . 127
6.3.1 Deterministic Sources of Unsteadiness . . . 127
6.3.2 Stochastic Sources of Unsteadiness . . . 131
6.4 Research Gaps in Model-scale Testing . . . 137

7 Turbine Adaptation and Experimental Methodology 138
7.1 Turbine Design and Instrumentation . . . 138
7.1.1 Scope of Hardware Development . . . 140
7.1.2 Blade Sub-assembly . . . 141
7.1.3 Tower Assembly . . . 148
7.2 Calibration of Blade Root Bending Moments . . . 149
7.3 Methodology for Turbine Test Campaign . . . 154
7.3.1 Turbine Installation . . . 154
7.3.2 Data Acquisition and Control Strategy . . . 156
7.3.3 Data Processing of Turbine Signals . . . 158
7.3.4 Test Strategy . . . 160
7.3.5 Influence of ADV Position . . . 160
7.3.6 Selection of Effective Radii . . . 165
7.4 Summary . . . 168

8 Turbine Performance and Loading Response 170
8.1 Test Conditions . . . 170
8.2 Preliminary Flow and Performance Analysis . . . 171
8.2.1 Upstream Flow Characterisation . . . 172
8.2.2 Turbine Reference Velocity . . . 173
8.2.3 Reynolds Number Independence . . . 177
8.3 Steady-State Rotor Loads . . . 181
8.3.1 Integrated Quantities . . . 181
8.3.2 Blockage Correction . . . 183
8.3.3 Uncertainty Quantification . . . 184
8.4 Unsteady Blade Loads . . . 190
8.4.1 Loading Distributions . . . 190
8.4.2 Azimuthal Load Variations . . . 192
8.4.3 Angle of Attack and Reduced Frequency Variations . . . 199
8.4.4 Loading Spectra . . . 201
8.5 Limitations of the Investigation . . . 206
8.6 Summary . . . 208

9 Conclusions and Future Work 211
9.1 Conclusions . . . 211
9.1.1 Flow Characterisation and Unsteady Flow Generation . . . 212
9.1.2 Model-Scale Preparation and Testing . . . 214
9.2 Future Work . . . 216
9.2.1 Unsteady Flow Generation . . . 216

9.2.2 Turbine Optimisation and Load Relief 217
9.3 Contributions 217

A Flow Mapping Co-ordinates **220**

B Definition of Resistance Grading for Vertical Shear **223**

References **225**

Nomenclature

Acronyms

2D	Two-dimensional
3D	Three-dimensional
ADCP	Acoustic Doppler current profiler
ADV	Acoustic Doppler velocimeter
ALM	Actuator line model
BDC	Bottom dead centre
BEM	Blade element momentum
CFD	Computational fluid dynamics
CfD	Contract for Difference
DAQ	Data acquisition
DoES	Department of Engineering Science
EMEC	European Marine Energy Centre
EW	Edgewise
FSI	Fluid-structure interaction
FW	Flapwise
IMU	Inertial measurement unit
IQR	Interquartile range
ITTC	International Towing Tank Conference
LCoE	Levelised cost of electricity
LDV	Laser Doppler velocimetry
LES	Large-eddy simulation
NI	National Instruments
NVR	Nominal velocity range
PCB	Printed circuit board
PDF	Probability density function
PIV	Particle image velocimetry
PSD	Power spectral density
PWRA	Power-weighted rotor average
RANS	Reynolds-averaged Navier-Stokes
RBM	Root bending moment
RMSE	Root mean square error
SEE	Standard error of the estimate
SEM	Standard error of the mean

SNR	Signal-to-noise ratio
TDC	Top dead centre
TTD	Thrust and torque transducer
UK	United Kingdom
VIV	Vortex-induced vibration
VLM	Vortex lattice method

Greek Symbols

α	Yaw angle
β	Pitch angle
χ	Hole size
δ	Uncertainty or error
η	Free surface elevation
γ	Roll angle
κ	von Kármán constant
λ	Tip-speed ratio
Λ_i	Integral length scale of the i^{th} velocity fluctuation component
ν	Kinematic viscosity
Ω	Angular velocity
ϕ	Blade angular position
ψ	Rotation matrix
ρ	Fluid density
ρ_{ii}	Autocorrelation coefficient of the i^{th} velocity fluctuation component
σ_i	Standard deviation of the i^{th} random variable
σ_i^2	Variance of the i^{th} random variable
τ	Time lag
θ	Porosity

Roman Symbols

$1/n$	Power-law exponent for vertical velocity shear
A	Rotor swept area
Bi	Blade number, where $i \in \{1, 2, 3\}$
c	Blade chord length
C	Coefficient of turbulence decay
$\text{CI}_{0.95}$	95% confidence interval
C_P	Turbine power coefficient
C_{RBM}	Blade root bending moment coefficient
C_T	Turbine thrust coefficient
d	Characteristic dimension of the bar/rod element
f	Frequency
f_s	Sampling frequency
H	Flow depth
iP	Turbine excitation frequency, where i is a harmonic multiple of Ω

I_i	Turbulence intensity of the i^{th} velocity fluctuation component
k	Reduced frequency
K	Resistance coefficient
l	Centre-to-centre spacing of the bar/rod elements
m	Power-law exponent for turbulence decay
M	Mesh size
p	Static pressure
Q	Rotor torque
Qi	Quadrant number, where $i \in \{1, 2, 3, 4\}$
r	Local radius of the blade section with respect to the turbine axis
R	Turbine rotor radius
Re	Reynolds number
RS_i	Fractional contribution of each bursting event, where $i \in \{1, 2, 3, 4\}$
S_{ii}	Power spectral density of the i^{th} fluctuation component
t	Time
$T_{\text{int},i}$	Integral time scale of the i^{th} velocity fluctuation component
T	Rotor thrust
u, v, w	Flow velocity directions
u_τ	Friction velocity
$-u_i'u_j'$	Reynolds stress tensor (instantaneous)
U	Velocity modulus
U_0	Reference flow velocity (at the centre of the intended rotor plane)
U_∞	Freestream velocity
U_T	Turbine reference velocity
V_rel	Relative blade velocity
W	Width
x, y, z	Cartesian coordinates
x_0	Virtual origin of turbulence
z_0	Roughness dimension

Subscripts

0.7	70% of non-dimensionalised blade radius
30	30 minutes
3D	Three-dimensional
60	60 minutes
bar	Bar element
CL	Centreline
comb	Combined
eff	Effective
exp	Expanded
F	Outer frame
loc	Local
max	Maximum

meas	Measured
noise	Signal noise
NY	Nyquist frequency
opt	Optimum
period	Sampling period
random	Random
rot	Rotational
shed	Vortex shedding
stat	Stationarity
sys	Systematic
tot	Total
true	True

Other Symbols

$()'$	Fluctuating component
$\mathcal{O}()$	Order of magnitude
$\langle() \rangle$	Spatially averaged component
$(^{-})$	Time-averaged component

CHAPTER 1

Introduction

The increase in living standards over the past century has rapidly accelerated global energy demand. Coupled with growing concerns about the environment and energy security, it is widely acknowledged that a transition from fossil fuel-based energy production to a diverse range of renewable energy sources is required [1]. The single most important lever to bring about the reduction in carbon dioxide emissions needed by 2030 is to triple the global installed capacity of renewable power [2]. Leading the expansion of renewable energy technologies are wind and solar power; however, their intermittent nature necessitates additional infrastructure in electricity networks to ensure a stable power supply. Marine renewable energy, with its more predictable generation patterns, offers a complementary solution to energy diversification. Among these, tidal energy stands out as an abundant and largely unexploited resource, with the distinct advantage of a predictable, 24-hour energy supply.

Tides are deformations of the Earth caused by the periodic gravitational forces exerted by the Sun and Moon, combined with the Earth's rotation within their respective gravitational fields [3]. The relative distances and positions of these three celestial bodies affect the size and magnitude of the Earth's two tidal bulges, with local tidal amplitudes also influenced primarily by coastal topography, water depth, as well as the arrangement and relative positioning of continental land

masses [4]. While oceanic tidal amplitudes are typically $\mathcal{O}(1)$ m, values in faster-moving coastal waters can be significantly higher due to increased energy flux, making these areas prime targets for economic energy extraction. As an extreme case, the tidal amplitude in the Bay of Fundy, Canada, can reach up to 16 m [5].

1.1 Harnessing the Tidal Resource

Energy extraction from the tides can be broadly classified into two categories. The first—tidal range—involves the construction of an artificial barrier to enclose a body of water, such as an estuary or bay, to harvest power from the potential difference between flood and ebb tides. The second—tidal stream—converts kinetic energy from energy-dense tidal currents in much the same way as wind turbines extract energy from the wind. The second of these methods is the focus of this thesis.

Tidal stream energy uses hydrokinetic turbines to convert the momentum of tidal flows into rotational motion through a cambered foil, which generates lift by deflecting the approach flow and creating a pressure differential across the foil surfaces. Compared to tidal range technologies, this form of energy generation is perceived to have a significantly lower ecological impact and requires a lower capital investment [6].

While several categories of tidal stream energy converters exist [7], development has largely converged on horizontal axis turbines [8], similar to those used in the wind industry. Despite the outward similarities of wind and tidal turbines, the harsh marine environment presents unique challenges for the installation, maintenance, and operation of tidal stream technology. For instance, the density of seawater, over 800 times greater than that of air, results in a more energy-dense flow, necessitating the use of much lower aspect ratio blades for comparable levels of thrust, even though the mean flow speeds are typically lower than those encountered by wind turbines [9]. Additionally, the lower rotational inertia of tidal stream rotors leads

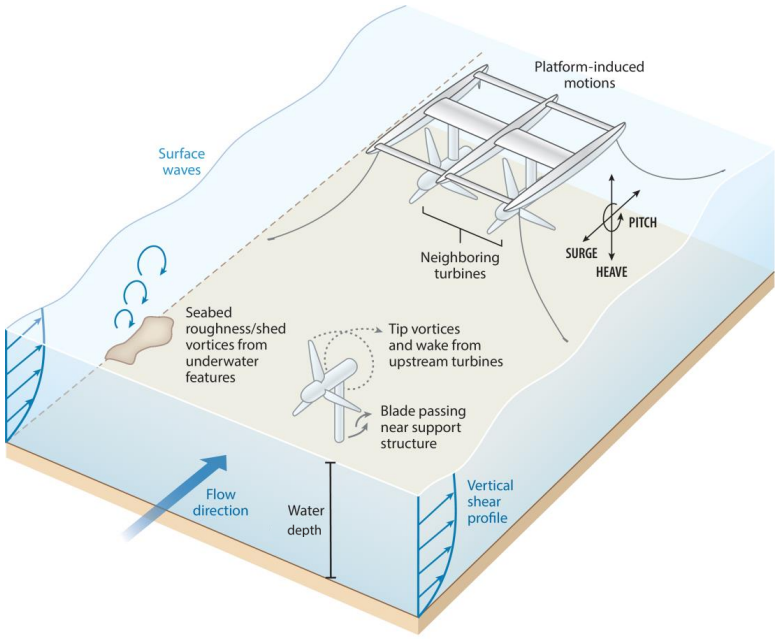


Figure 1.1: The flow environment and sources of important flow phenomena experienced by tidal stream turbines. Image from Adcock *et al.* [10].

to greater fluctuations in rotor speed, complicating control strategies aimed at maintaining optimal rotor performance. Beyond these mechanical differences, tidal stream technology must also contend with highly variable hydrodynamic environments, where the effects of vertically sheared flows, wave-induced velocities, and freestream turbulence must be mitigated [10]. For turbines supported by floating platforms, the rotors may experience additional flow unsteadiness. These flow phenomena are illustrated in Figure 1.1. Additionally, tidal stream devices typically occupy a larger portion of the available flow depth compared to wind turbines, resulting in increased power extraction [11], but also with a heightened risk of higher rotor loads and cavitation [12].

Estimates of the theoretical global tidal stream resource range between 100–500 TWh per year, with the bulk of this resource concentrated in the waters of the United States and China, estimated at 220 TWh per year [13] and 61.3 TWh per year [14], respectively. In Europe, the United Kingdom (UK) holds a significant share of the theoretical resource, with 34 TWh per year estimated to be

within its waters, which is equivalent to approximately 11% of the country's current annual electricity demand [15]. With approximately 12 500 km of coastline and a wealth of energetic tidal flows, the UK is fertile ground for tidal stream deployment and has been at the forefront of key developments in the industry. For instance, the world's first tidal stream turbine arrays were deployed in Scotland at the MeyGen site in the Pentland Firth [16] and at Bluemull Sound in Shetland [17]. Furthermore, in 2003, the European Marine Energy Centre (EMEC), the world's first marine energy test facility, was established in the Orkney Islands, Scotland. Several pre-commercial projects at EMEC have successfully demonstrated the technological feasibility of tidal stream energy and its integration into local utility networks, with notable examples including Orbital Marine Power's 2 MW O2 device [18] and Alstom's 1 MW turbine [19].

1.2 Industry Challenges

Tidal stream technologies, while projected to contribute a small percentage to the overall energy mix, have the potential to play an oversized role in helping to maintain balanced and resilient energy systems. However, the challenges facing the industry remain significant. These challenges can be broadly categorised into economic and technical hurdles, each requiring targeted solutions to support wider deployment and competitiveness in domestic energy markets.

1.2.1 Economic Challenges

As a less developed technology, the cost of installing and operating tidal stream technologies remains high, which has typically limited deployments to single turbine demonstration projects [20]. To compete with more established forms of renewable generation, such as solar and wind energy, reductions in the levelised cost of electricity (LCoE) are essential. ORE Catapult, a UK-based innovation centre, suggests that near-term cost reductions can be achieved through a combination of

increasing site and device capacity, economies of scale, technological innovation, and reduced capital costs [21]. While industry-led initiatives can drive a significant downward cost reduction trajectory, this must be complemented by robust domestic supply chains and effective policy mechanisms. Among the available policy levers, access to government subsidy schemes remains a critical component. In the UK, the Contract for Difference (CfD) scheme, which guarantees a fixed price for electricity production to a renewable power generator, recently ringfenced tidal stream energy projects to increase device deployment and promote wider investment in the industry. This is particularly crucial for emerging technologies, where initial costs are high, and market uncertainty can hinder investor confidence. In the latest round of CfD allocations (September 2024, at the time of writing), a strike price[1] of £172 per MWh was agreed for six projects to deliver 28 MW of tidal stream capacity by 2029 [22]. This contrasts with 3.29 GW of solar power at £50.07 per MWh and 3.36 GW of offshore wind at £58.87 per MWh. As the tidal stream industry matures and costs reduce, future projects will be perceived as lower risk by investors, which will, in turn, reduce financing costs.

1.2.2 Technical Challenges

One of the primary challenges facing tidal stream turbines is the ability of devices to endure the hostile nature of the operating environment [10]. A lack of design convergence, driven by limited understanding of these flow regimes and the resulting turbine loads, is a key reason the tidal industry has not yet bridged the gap between a high technology readiness level and commercial-scale deployment. Liu and Veitch [23] attributed this lack of understanding to the premature failures of prototype devices, such as the Atlantis AK1000 [24]. In response, developers have tended to over-engineer devices to meet lifetime targets of 20–25 years, driving up the LCoE. Against such a backdrop, there is a clear need for improved understanding, and hence detailed characterisation, of the unsteady flow regimes to which tidal stream

[1] All strike prices are in 2012 prices.

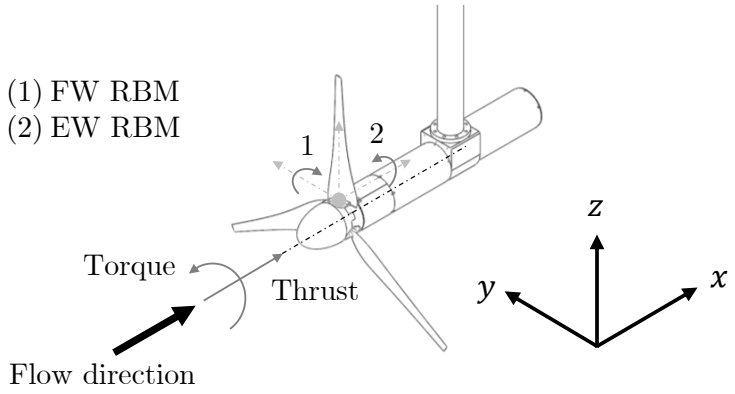


Figure 1.2: Turbine co-ordinate system and the principal loads of interest (dark grey) for the rotor. The rotor thrust and torque correspond to the force acting along, and the moment about, the x-axis, respectively. Each blade root has a rotating Cartesian co-ordinate system (shown only for the blade in the most upright position), with the flapwise (FW) and edgewise (EW) blade root bending moments (RBMs) acting about the y-axis and x-axis, respectively. Note that a positive edgewise moment aligns with the direction of rotation. Blade loading about the z-axis (twist) has been omitted for brevity. Turbine model from McNaughton *et al.* [25].

turbines are subjected, leading to a more informed design process.

The unsteady rotor loads that develop from such a complex flow environment consist primarily of loads averaged across the rotor, such as thrust and torque, as well as those acting on individual blades. These loads, a key focus of this thesis, are illustrated in Figure 1.2, noting that the flapwise (FW) root bending moments (RBMs) are driven predominantly by rotor thrust, while the edgewise (EW) root bending moments are imparted by rotor torque and gravitational forces, which are partially relieved by the buoyancy of the blades. Along with the effects of turbulence, vertical velocity shear, waves, and potentially platform-induced motions, each revolution of the low-speed shaft results in a complete gravity stress reversal, as well as additional cyclic loading caused by yaw error, shaft tilt, and tower shadow. Consequently, the design of many tidal (and wind) turbine components is often governed by fatigue rather than extreme loads [26].

Large experimental datasets are essential for the development and validation of engineering design tools; however, only a few well-documented datasets exist on the unsteady loading of tidal stream turbines. Moreover, the available data often

focuses on whole rotor loads, which is insufficient for refining higher fidelity models, particularly in the context of more complex onset flow conditions. This highlights the need for a broader experimental database that includes detailed measurements of unsteady blade loads at the required level of accuracy. Such data are crucial for understanding the underlying hydrodynamic phenomena and for developing more cost-effective rotor designs optimised for both performance and survivability.

1.3 Motivation for Model-Scale Testing

Considering the significant spatial and temporal variations within marine environments [27], along with the multitude of challenges associated with conducting in-field test campaigns, parameterising site conditions for tidal stream turbines presents a highly complex challenge [28]. Several studies have characterised the conditions at various existing and potential tidal energy sites, such as [29–31], providing valuable insights that enable researchers and developers to optimise device design for the target operating environment. The high cost associated with this approach, however, can often be prohibitive. Furthermore, the site-specific nature of the data collected may not be transferable to other locations, making it difficult for developers to maintain design and operational consistency across different turbine deployments. A potential solution to these constraints is to characterise parameter spaces of interest in a laboratory setting, offering a more cost-effective, controlled, and flexible alternative to costly in-field test campaigns. By manipulating the onset flow conditions, various forms of hydrodynamic unsteadiness can be rigorously characterised, thereby providing more accurate inputs for engineering models.

In addition, and provided the device is equipped with the appropriate level of instrumentation, laboratory testing provides the opportunity to evaluate the response of a model-scale device under well-defined flow conditions. This approach not only allows for systematic characterisation of the device's performance and loading response across a range of operating conditions, but also reduces uncertainty,

ensuring tests can be consistently reproduced to accurately quantify experimental errors. Achieving this level of precision is challenging in field tests, making laboratory results crucial for generating reliable datasets. The output from such campaigns can provide valuable insights into how turbines respond to complex flow environments, leading to better validation of engineering models and more informed design strategies for full-scale devices.

1.4 Thesis Objectives

The overall aim of this research is to investigate the unsteady loading and fluid dynamics of a model-scale tidal rotor under controlled onset flow conditions. The investigation is experimentally focused and will be conducted in a new recirculating water flume at the University of Oxford. This challenge is addressed through four primary objectives.

Objective 1: Development of Flow Characterisation Methodology and Clean Flow Analysis

The first objective is to develop a robust methodology for flow characterisation, encompassing the experimental setup, uncertainty quantification, and data processing techniques necessary to generate a meaningful description of the flow. A key component of this task is the development of laboratory apparatus capable of accurately and reliably measuring the flow. The methodology will then be applied to characterise the flume's clean flow regime, including the identification and quantification of biases within the experimental setup. Establishing baseline measurements is crucial, as they serve as a reference for comparative analysis with more complex flow conditions and inform interpretation of the turbine's interaction with the flow post-installation.

Objective 2: Generation, Control, and Characterisation of Unsteady Flow Regimes

Two notable sources of hydrodynamic unsteadiness in tidal flows are freestream turbulence and vertical velocity shear through the water column. While there is a wealth of literature on generating these phenomena in wind tunnel experiments, e.g. [32–35], practical implementations in tidal energy research remain limited. This gap is surprising, given the simplicity and effectiveness of many of these methods, which offer significant potential for investigating their effects on the performance and loading response of a model-scale rotor. This study leverages insights from wind tunnel experiments to develop methodologies for generating and controlling freestream turbulence and vertical velocity shear in the flume, with the resulting unsteady flows to be characterised in detail ahead of model-scale testing.

Objective 3: Turbine Adaptation in Readiness for Model-Scale Testing

One of two highly instrumented horizontal axis turbine models, which have been successfully tested in towing tanks at SSPA, Sweden [25], and QinetiQ, UK, is to be adapted for testing in the flume. A key aspect of the adaptation is accounting for the flume's smaller cross section and the reduced demand on the rotor's instrumentation compared to the much larger towing tanks, driving the development of new turbine components. This includes instrumentation at the root of each blade, which is essential for quantifying the instantaneous load response to the onset hydrodynamic forcing. Beyond the turbine adaptation, test preparation also involves the development of assembly aids, test rigs, an experimental methodology, and a carefully designed assembly procedure to ensure the turbine's safe installation into the flume.

Objective 4: Evaluate Turbine Performance and Loading Response Under Clean, Elevated Turbulence, and Sheared Flow Conditions

A comprehensive test campaign will be conducted to evaluate the turbine's performance and loading response across the various flow regimes characterised in the preceding objectives. In addition to measuring rotor thrust and torque, individual blade root bending moments will be captured for both the flapwise and edgewise loads at high angular resolution, enabling detailed characterisation of the azimuthal variations in blade loading as a function of the different hydrodynamic conditions. Furthermore, the effects of systematically adjusting the blades' chord-based Reynolds number will be investigated, providing further insights into the turbine's response across various operational scenarios.

1.5 Thesis Outline

The thesis is broadly divided into two main sections. The first focuses on the detailed characterisation of the various flow regimes intended for model-scale testing, while the second addresses the preparation and subsequent testing of the turbine under these flow conditions.

The first section begins with a description of the experimental methodology developed for flow characterisation (Chapter 2), which draws upon established methods from the literature and serves as a framework for other researchers looking to characterise similar facilities. In Chapter 3, the methodology is applied to characterise the flume's mean ambient flow and turbulence characteristics. Chapters 4 and 5 demonstrate the application of methodologies to generate and control freestream turbulence and vertical velocity shear, respectively, with the resulting flow fields characterised in detail ahead of model-scale testing.

The second section begins with an overview of the relevant literature on turbine-based investigations (Chapter 6), covering both computational and experimental studies on tidal stream turbines operating in various unsteady flow environments.

The review also highlights how the research objectives of this study address gaps in the existing literature. Chapter 7 focuses on the turbine adaptation process, detailing the modifications necessary to accommodate the laboratory environment, as well as the requisite test preparations, including sensor calibration, assembly aids, and the development of an experimental methodology. Chapter 8 presents results of the turbine test campaign, including a characterisation of the turbine's performance and loading response across the various flow regimes and a range of chord-based Reynolds numbers.

Chapter 9 presents the main conclusions of the thesis and suggestions for further work.

Part I

Flow Characterisation

CHAPTER 2

Experimental Methodology for Flow Characterisation

While laboratory-based flow characterisations frequently feature in published experimental investigations, they are rarely reported as standalone studies, e.g. [36]. Instead, these activities are typically performed to establish a set of baseline flow metrics, which are subsequently used to inform interpretation a model-scale device's response during the latter stages of an experimental campaign. Notable exceptions to this trend are the studies of Park *et al.* [37] and Sutherland *et al.* [38], who conducted in-depth facility characterisations and provided detailed accounts of the experimental methods employed. Furthermore, it is apparent that for the characterisation studies reported, the level of detail provided and the methodologies applied can vary widely, which, for a researcher conducting a flow characterisation of a new facility, can appear a formidable task.

The objective of this chapter is to outline a robust methodology for the hydrodynamic characterisation of a recirculating water flume, in preparation for the model-scale testing of a horizontal axis tidal stream turbine. The turbine to be tested has a rotor diameter of 0.6 m and is a modified version of one of two model-scale turbines previously tested in towing tanks at SSPA in Sweden [25] and at QinetiQ in the UK [39], with further details of the turbine provided in Chapter 7. Much of this work draws upon established methods from the literature,

e.g. [38, 40], and serves as a framework for other researchers seeking guidance when characterising similar facilities. The scope of the analysis includes the experimental setup, data processing techniques, and uncertainty quantification.

The chapter begins with a description of the experimental arrangement, followed by a detailed account of the techniques used for data acquisition, quality control, post-processing, and statistical analysis, including example measurements in clean flow conditions to illustrate their application. The limitations of the methodology are then discussed.

2.1 Experimental Set-up

2.1.1 University of Oxford Flume

The University of Oxford's recirculating water flume is a combined wave and current test tank capable of delivering bulk flow speeds up to $1.0\,\mathrm{m\,s^{-1}}$. A schematic of the flume is shown in Figure 2.1, with a corresponding summary of the key specifications shown in Table 2.1. The flow is driven by two impellers via twin return pipes, each of diameter 0.5 m. The flume has glass sides and bottom and uses a Cartesian co-ordinate system, with its origin at the centre of the flume's cross-section at the beginning of the working section ($x = 0$). Upstream of the working section are two laminarisers to straighten the flow and a horizontal and vertical contraction with arrays of guide vanes to return the flow into the working section smoothly. Downstream of the working section, there are three hinged dry-back wave paddles capable of generating opposing waves. Two FLEXIM WD1200 ultrasonic flow meters with an accuracy of $\pm 1.2\%$ [41] are clamped onto the flume's return pipes to measure the volumetric flow rate. While the flow depth can be varied, all experiments in this investigation were conducted at the maximum flow depth ($H = 1.0\,\mathrm{m}$) to minimise channel blockage in future turbine tests. The design speed of the flume at full depth is $0.6\,\mathrm{m\,s^{-1}}$.

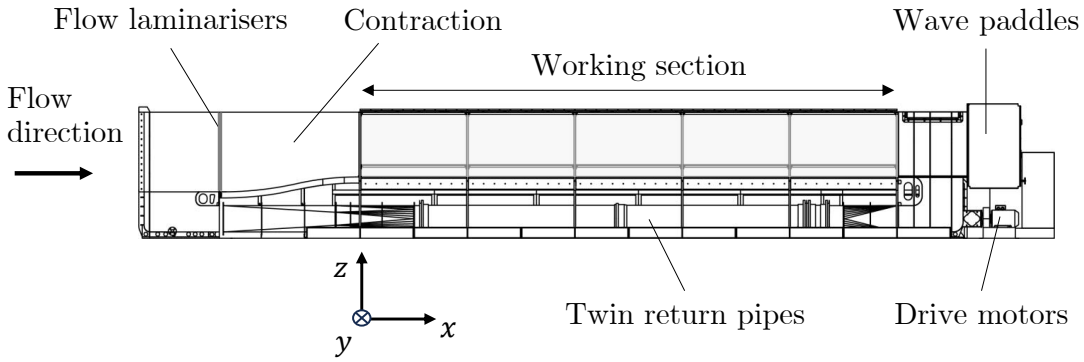


Figure 2.1: Schematic of the Oxford recirculating water flume.

Parameter	Value / description
Capacity	$27\,\mathrm{m}^3$
Bulk flow speed	Up to $1.0\,\mathrm{m\,s}^{-1}$
Water depth, H	1.0 m (maximum)
Flume width, W	1.1 m
Working length	10.0 m
Flow measurement	Ultrasonic flow meters
Wave generation	Dry-back wave paddles

Table 2.1: Key specifications of the Oxford recirculating water flume.

2.1.2 Acoustic Doppler Velocimetry

Although a variety of flow measurement techniques have been employed in both laboratory and field research into tidal energy, such as particle image velocimetry (PIV) [42], laser Doppler velocimetry (LDV) [43], and acoustic Doppler current profilers (ADCP) [31], acoustic Doppler velocimeters (ADV) have emerged as a popular choice owing to their relative affordability, robustness, and ease of use [44]. In this study, a 10 MHz Nortek Vectrino, equipped with a downwards-looking four-armed probe (see Figure 2.2), was used to characterise the flume's three-dimensional (3D) turbulent flow field.

The ADV transmits acoustic pulses at a known frequency into a sampling volume located 50 mm beneath the probe head. Suspended particulate matter,

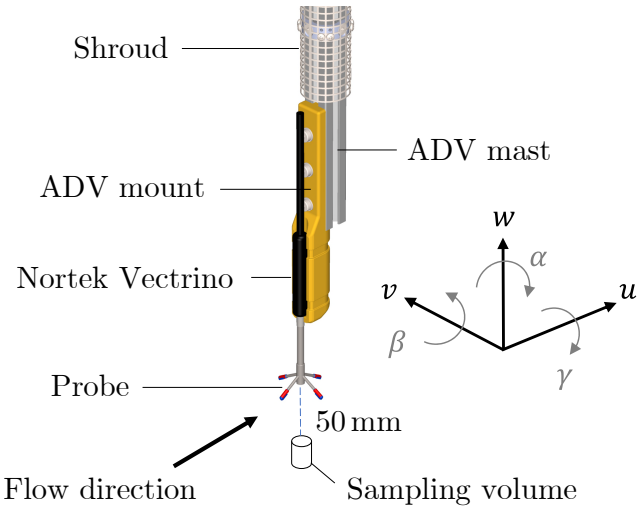


Figure 2.2: Illustration of the ADV mast assembly and its co-ordinate system. The geometric pitch, β, roll, γ, and yaw, α, of the probe are shown for clarity, noting that positive rotations follow the direction of the arrows around their respective axes.

referred to here as seeding material, reflects some of these pulses back to the transducer. The changes in frequency of the reflected signals correspond to a Doppler shift proportional to the flow velocity [44]. The ADV data were sampled using a Cartesian co-ordinate system aligned with both the flume's co-ordinate system and the principal flow direction. Nortek cites the instrument accuracy as $\pm 1\%$ of the measured flow velocity [45], defined here as a source of systematic error, δ_{sys}.

2.1.3 Linear Traverse

A bespoke two-dimensional (2D) linear traverse system was developed to support and automate accurate positioning of the ADV (see Figure 2.3). The system features a toothed belt drive for cross-stream travel and a lead screw mechanism for vertical travel, both supplied by igus UK. The ADV is secured to the vertical axis via an aluminium extrusion (30×30 mm cross section), hereafter referred to as the ADV mast. Both axes offer high positional accuracy (± 0.2 mm [46]) and are actuated by direct-drive stepper motors, controlled by two drive units housed in an

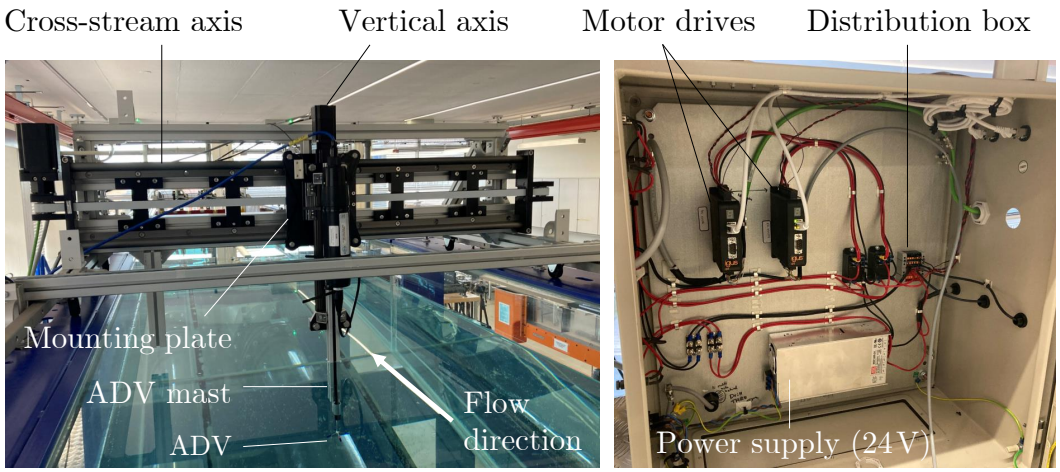


Figure 2.3: Photographs of the 2D linear traverse system (left panel) and the electrical drive cabinet (right panel).

electrical cabinet on the flume's gantry. Carriage positions are measured relative to limit switches located at the end of travel on each axis. The streamwise position of the traverse is manually adjustable via a set of castor wheels and clamps.

2.1.4 Vibration

A key design consideration during the development of the traverse was ensuring the stability of the ADV to minimise the risk of velocity signal contamination from system vibrations [45]. Furthermore, to suppress the influence of vortex-induced vibration (VIV), the wetted length of the ADV mast was enveloped in perforated sheets of stainless steel to form a porous shroud, as shown in Figure 2.2. To quantify the impact of vibration on the ADV mast, an LSM6DS3 inertial measurement unit (IMU) housed in a waterproof enclosure was installed on the mast's downstream face (see Figure 2.4). The IMU, embedded in a low-cost Arduino Nano 33 IoT board [47], measures triaxial acceleration and triaxial angular velocity at a sampling frequency of 104 Hz. The accelerometer range was set to $\pm 4\,g$ with a resolution of 0.122 mg, and the zero-point accuracy is $\pm 40\,\mathrm{m}g$ [48].

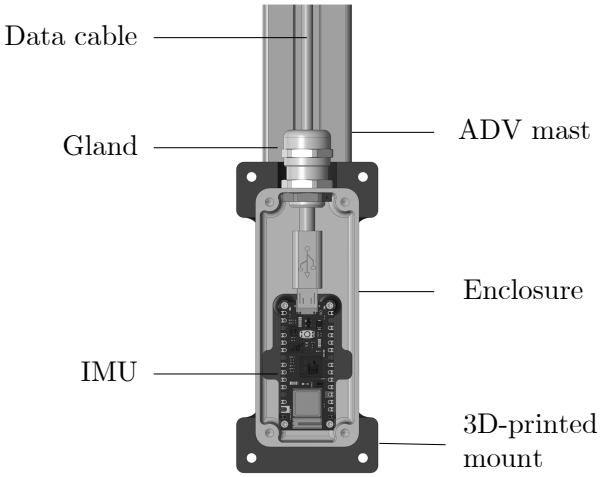


Figure 2.4: Illustration of the IMU enclosure mounted on the downstream face of the ADV mast. Enclosure lid not shown.

2.1.5 Wave Gauges

Wave gauges are a commonly used tool for quantifying free-surface elevation in laboratory settings. In this study, resistive wave gauges, which operate by measuring the water resistance between two parallel stainless steel rods, each with a diameter of 3 mm, were used, with the resulting current converted into an output voltage directly proportional to the immersion depth of the rods. The gauges used were 700 mm long, and the displacement data were sampled at 125 Hz. To mitigate temporal changes in water conductivity, the wave gauges were calibrated every two hours. The displacement accuracy is reported to be $< 0.1\%$ of a full-scale measurement [49].

2.2 Methodology

The following section details the experimental methodology, which is described in four stages: (i) setup, (ii) flow sampling, (iii) post-processing, and (iv) data analysis, as shown in Figure 2.5. Note that the methodology does not prescribe

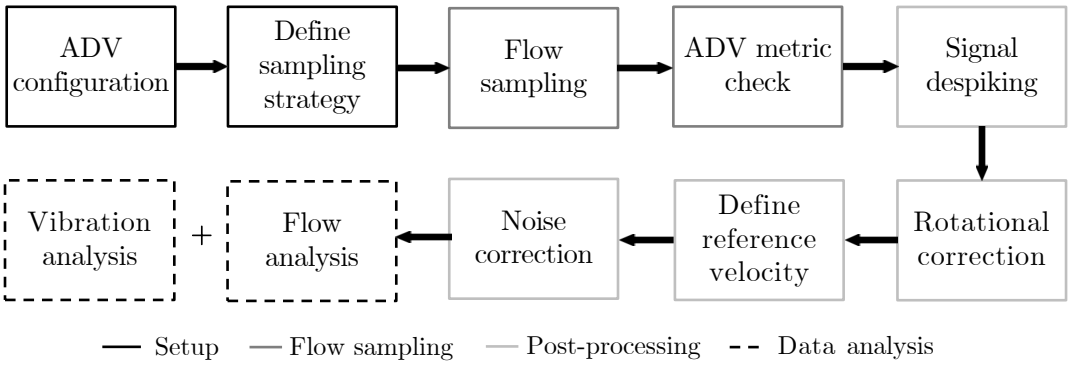


Figure 2.5: A flow-chart illustrating the workflow of the experimental methodology, which comprises a setup phase (black), flow sampling (dark grey), post-processing (light grey), and data analysis (black dashed).

a strict sequence in the workflow, as there is often feedback between stages. For instance, when defining a sampling strategy that aligns with the test campaign objectives, it may be necessary to conduct preliminary flow sampling and data analysis to determine the minimum period over which the flow can be considered statistically stationary (see Section 2.2.2).

2.2.1 ADV Configuration

Configuration of the ADV's settings within the data acquisition (DAQ) software is necessary to optimise data quality. The nominal velocity range (NVR) was set to $\pm 0.3\,\mathrm{m\,s^{-1}}$ to encompass the expected range of velocity fluctuations about the operating conditions. The sampling volume height and transmit pulse length were set to 7.0 mm and 1.8 mm, respectively, to minimise pulse interference when measuring close to the channel boundaries (≤ 150 mm).

2.2.2 Flow Sampling Strategy

A sampling frequency, f_s, of 200 Hz was selected to encompass the highest frequency of turbulence in the flume, $f_{\max}$, that could be accurately resolved by the ADV, thus satisfying the Nyquist criterion to avoid signal aliasing, i.e. $f_s \geq 2f_{\max}$.

The maximum resolvable frequency is governed by the 6.0 mm diameter of the ADV's sampling volume (see Figure 2.2), which, at the design speed of the flume, corresponds to $f_{\max} \approx 100\,\text{Hz}$.

Defining a sampling period for flow measurement involves a compromise between achieving statistical accuracy and minimising the time required for data collection. Thomson *et al.* [31] empirically determined a sampling period of 300 s based on the flow velocity exhibiting a stable mean and variance. The authors reported that periods shorter than 300 s were insufficient to capture the large-scale flow structures. In contrast, Blackmore *et al.* [50] prioritised the number of measurements in their campaign over the temporal stability of the integral scales, opting for a shorter sampling period of 200 s.

A variation of the method employed by Sutherland *et al.* [38] was adopted here to define a period of stationarity, t_{stat}, as a proxy for the flow's temporal stability. An hour-long steady-state time series taken at the centre of the flume's working section, $(x, y, z) = (5, 0, 0)$, was discretised into a range of sampling periods from 1–600 s in 1-second increments, at the design speed of the flume. For each sampling period of interest (denoted by the subscript *period*), the variance of the velocity modulus was calculated separately for six equal and consecutive periods. These six individual variances were then ensemble-averaged to obtain $\sigma^2(U_{\text{period}})$, where U represents the velocity modulus. The time taken for $\sigma^2(U_{\text{period}})$ to stabilise within $\pm 3\%$ of the variance over 60 minutes, $\sigma^2(U_{60})$, was used to define t_{stat}. The $\pm 3\%$ threshold for convergence, analogous to the settling time in control theory, was chosen to account for instability in the signal variance due to its sensitivity as a second-order statistic.

Figure 2.6 illustrates the convergence of $\sigma^2(U_{\text{period}})$ towards $\sigma^2(U_{60})$ as the sampling period increases, yielding $t_{\text{stat}} = 267\,\text{s}$, which represents the minimum theoretical sampling period for each flow measurement. As verification of the t_{stat} estimate, the augmented Dickey–Fuller unit root test [51] was performed on a truncated $\sigma^2(U_{\text{period}})$ array, considering only the values up to the time index

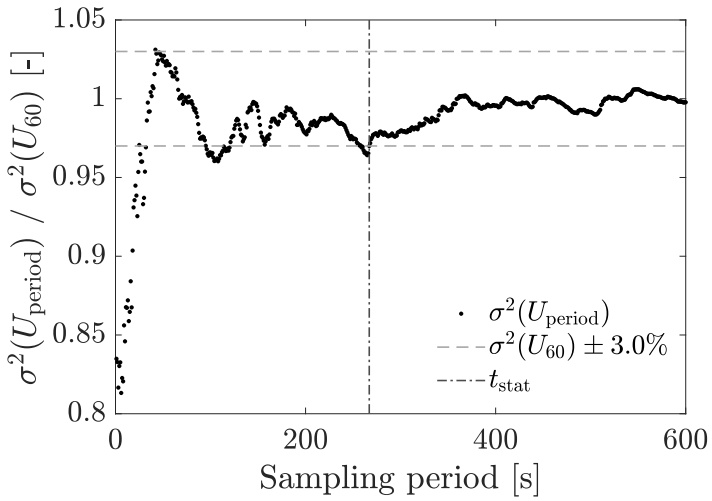


Figure 2.6: Variance of the velocity modulus for each sampling period of interest (black scatter), $\sigma^2(U_{\text{period}})$, normalised on the variance of the velocity modulus over 60 minutes, $\sigma^2(U_{60})$. Also shown are a $\pm 3\%$ threshold about unity (light dashed) and the period of stationarity (dash-dotted), t_{stat}. Test conditions: $\overline{U_0} = 0.57\,\text{m}\,\text{s}^{-1}$; $(x, y, z) = (5, 0, 0)$.

corresponding to t_{stat}. The p-value obtained was less than the 5% significance level; thus, the null hypothesis that the array was non-stationary was rejected. The ADV sampling period was conservatively set to 300 s.

2.2.3 ADV Signal Quality

The reliability of the flow measurements is underpinned by the flume's seeding material. Kaolin (also known as China clay) has previously been used as a suspended sediment to evaluate ADV response in turbulent flows [52], offering a cost-effective and environmentally friendly alternative to more conventional seeding materials, such as glass microspheres. Using Stokes' law, a kaolin particle's terminal velocity, $\mathcal{O}(10^{-4})\,\text{m}\,\text{s}^{-1}$, was found to reside well within the systematic error of the ADV; however, its particle size (25–35 μm [53]) results in a buoyancy force approximately twice that of more conventional seeding material (4–16 μm [54]). The subsequent degradation in the clay's ability to track fluid motion over an extended period was addressed by regularly seeding the flow, typically on a daily basis, until the ADV's signal correlation and signal-to-noise ratio (SNR) met Nortek's recommended

threshold criteria of 70% and 15 dB, respectively. Before testing commenced each day, both metrics improved following 15 minutes of high-speed running in both forwards and reverse directions, to redistribute the seeding material throughout the flow. If the threshold criteria were not met, samples were not discarded, as a signal correlation of $< 70\%$ and a SNR of < 15 dB can still provide useful data [55].

2.2.4 Post-processing

This section details several post-processing techniques that were applied to the flow data prior to statistical analysis. These include corrections to unwanted artefacts inherent in ADV datasets, such as instrument noise and signal spikes.

Spike Removal

ADV measurements are often contaminated by non-physical ambiguities, or spikes, caused by aliasing of the Doppler signal, which erode the statistical accuracy of the datasets. A number of researchers have proposed methods to detect and remove the spikes from ADV time series, such as [56–58]. In this study, the widely cited phase-space thresholding method of Goring and Nikora [58] was employed. The spikes are replaced through linear interpolation of a third-order polynomial fitted through 12 points on either side of each spike. The chosen method also incorporates the suggestion by Wahl [59] to adopt the median and the median absolute deviation as location and scale estimators, respectively, due to their higher robustness to outliers. Each velocity component was despiked individually, and the corresponding data points in the other velocity components were also despiked. Typically, $< 1\%$ of the data were removed and replaced by the despiking algorithm. Figure 2.7 illustrates the implementation of this algorithm as applied to an instantaneous streamwise velocity signal.

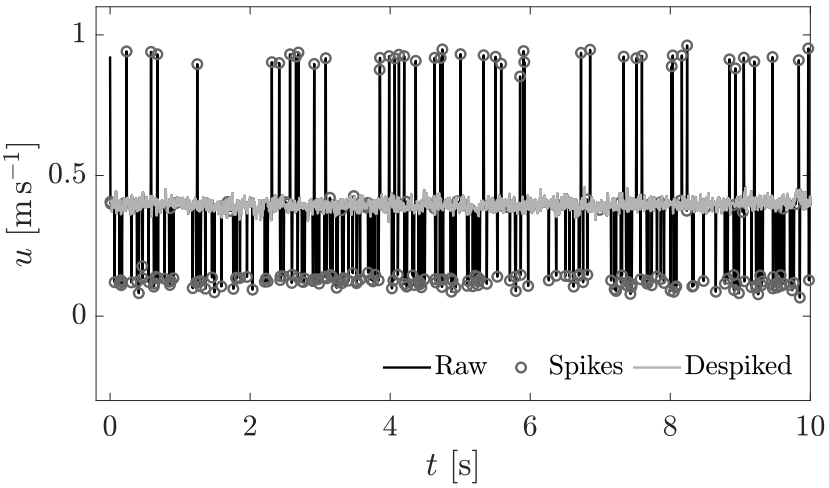


Figure 2.7: Application of the despiking algorithm to an instantaneous streamwise velocity signal (black), u, over a 10-second time series. 12.7% of the data were identified as spikes (circles). The despiked signal is also shown (light grey). Test conditions: $\overline{U_0} = 0.40\,\mathrm{m\,s^{-1}}$; $(x, y, z) = (5, 0, -0.4)$.

Calibration for ADV Probe Misalignment

Physical alignment of the ADV probe with the flume's co-ordinate system was achieved using a custom 3D-printed fixture mounted on the ADV mast. Material tolerances associated with part manufacture, however, imposed limitations on the precision of the alignment. Consequently, a correction was applied to each velocity component using a 2D rotation matrix, ψ, based on the probe's pitch (β) and yaw (α)—see Figure 2.2 for sign convention—at the centre of the flume's cross section, $(y, z) = (0, 0)$:

$$\psi(\alpha, \beta) = \begin{bmatrix} \cos\alpha\cos\beta & -\sin\alpha & \cos\alpha\sin\beta \\ \sin\alpha\cos\beta & \cos\alpha & \sin\alpha\sin\beta \\ -\sin\beta & 0 & \cos\beta \end{bmatrix}. \tag{2.1}$$

The yaw component was evaluated from the time-averaged streamwise ($\overline{u}$) and cross-stream ($\overline{v}$) velocities as follows:

$$\alpha = \tan^{-1}\left(\frac{\overline{v}}{\overline{u}}\right). \tag{2.2}$$

Similarly, the pitch offset between the ADV mast and the pulse transmission axis of the ADV was evaluated using:

$$\beta = \tan^{-1}\left(\frac{\overline{w}}{\sqrt{\overline{u}^2 + \overline{v}^2}}\right), \tag{2.3}$$

where $\overline{w}$ represents the time-averaged vertical velocity. The subsequent 2D rotational correction assumes the following:

- The mean flow direction aligns with the flume's xz-plane at $y = 0$.
- The time-averaged cross-stream and vertical velocities along the flume's centreline are zero[1].
- The pitch and yaw offsets of the probe remain constant across the yz-plane of interest[2].
- The probe experiences zero roll.

An example illustration of the 2D rotational correction applied to a 3D velocity vector is shown in Figure 2.8.

Reference Flow Velocity

The reference flow velocity, $\overline{U_0}$, is defined as the time-averaged centreline velocity modulus at the streamwise location where the turbine rotor will be deployed in future turbine tests[3]. To ensure consistency across streamwise locations, centreline velocities were referenced back to the intended rotor plane location. This process, detailed below, accounts for variations in the mean flow speed through the working section, corresponding to small changes in the flow depth:

[1]This assumption is valid only if the cross-stream and vertical velocity profiles are highly uniform and exhibit minimal variation about zero (within $\pm 0.02\,\mathrm{m\,s^{-1}}$).

[2]This assumption remains valid long as the probe is rigid and does not deflect under hydrodynamic load.

[3]The rotor plane was initially planned to be positioned at $x = 5\,\mathrm{m}$ for the clean flow case and subsequently adjusted for other flow conditions. However, due to time and logistical constraints, only one rotor location, $x = 3.9\,\mathrm{m}$, was tested, as discussed further in Section 7.3.1.

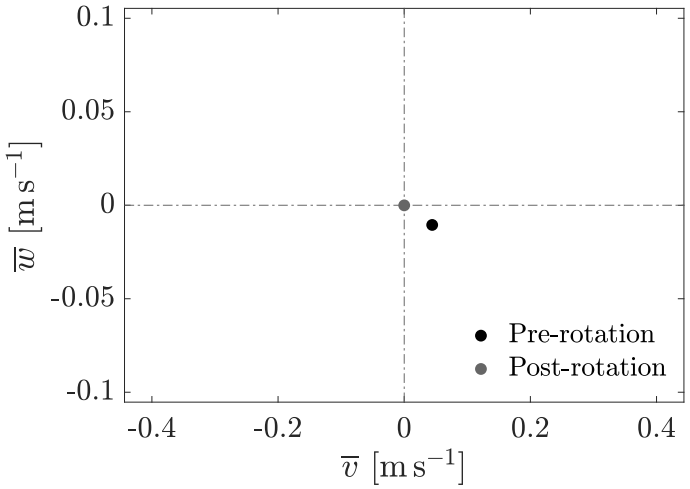


Figure 2.8: Example illustration of a 2D rotational correction in the vw-plane. The markers show the pre-rotated (black) and rotated (grey) heads of a 3D velocity vector. The dash-dotted lines indicate $\overline{v}, \overline{w} = 0$. Pitch correction $= 1.05°$; yaw correction $= -4.43°$. Test conditions: $\overline{U_0} = 0.57\,\mathrm{m\,s^{-1}}$; $(x, y, z) = (5, 0, 0)$.

i. Generate reference datasets of the flume's motor duty (in 100 rpm increments) and the time-averaged centreline velocity modulus at both the intended rotor plane and at least two other streamwise locations of interest.

ii. Use linear regression to relate the velocities measured at each location to the flume's motor duty. (The maximum fitting error was 0.7%.)

iii. For streamwise locations away from the intended rotor plane, estimate $\overline{U_0}$ as a function of motor duty using the regression coefficients obtained in Step 2.

The application of this method is illustrated in Figure 2.9 for three equidistant points along the flume's centreline ($x = 2.5\,\mathrm{m}$, $5.0\,\mathrm{m}$, and $7.5\,\mathrm{m}$) and indicates a modest acceleration of the centreline velocity through the working section. Note that the reference dataset for each streamwise location was generated separately because only one ADV was available.

Noise Floor

A further source of error in the velocity signals is the ADV's noise floor. Voulgaris and Trowbridge [60] attribute the noise to various sources, including the

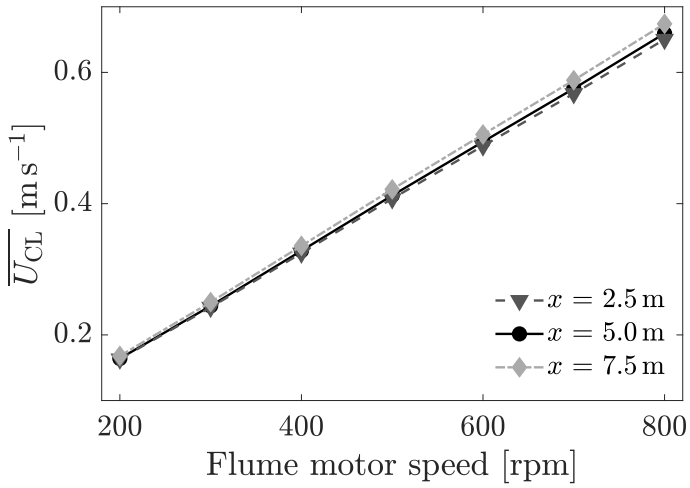


Figure 2.9: Variation of the time-averaged centreline velocity modulus, $\overline{U_{\mathrm{CL}}}$, with the speed of the flume's drive motors at three equidistant locations: $x = 2.5$ m (down-pointing triangles), 5.0 m (circles), and 7.5 m (diamonds). Linear regression lines are included. Test conditions: $(x, y, z) = (x, 0, 0)$.

instrument's electronics circuitry and a flow-related component that depends on the velocity shear across the sampling volume. The most significant contribution to signal noise, however, is Doppler noise, which introduces a bias in the variance of the measured signal for the i^{th} velocity component ($i = u, v, w$), given by:

$$\sigma^2_{\mathrm{meas},i} = \sigma^2_{\mathrm{true},i} + \sigma^2_{\mathrm{noise},i}. \tag{2.4}$$

Assuming the noise to be normally distributed across the frequency range, akin to white noise, the noise-induced bias, $\sigma^2_{\mathrm{noise},i}$, can be calculated in two stages using power spectral density (PSD) estimates[4] of the i^{th} component of the velocity fluctuations, S_{ii}. First, as the power spectrum becomes saturated by noise at higher frequencies, a noise-related PSD can be estimated by averaging the PSD over a narrow frequency band (95–100 Hz) in the tail of the spectrum [60]. Next, by integrating the noise-related PSD over the bandwidth of the spectrum, $\sigma^2_{\mathrm{noise},i}$ can be determined [61]. Figure 2.10 presents estimates of the velocity power spectra and the corresponding noise floors for an hour-long dataset at the centre of the working

[4]Further commentary on estimates of the PSD is provided in Section 2.2.5.

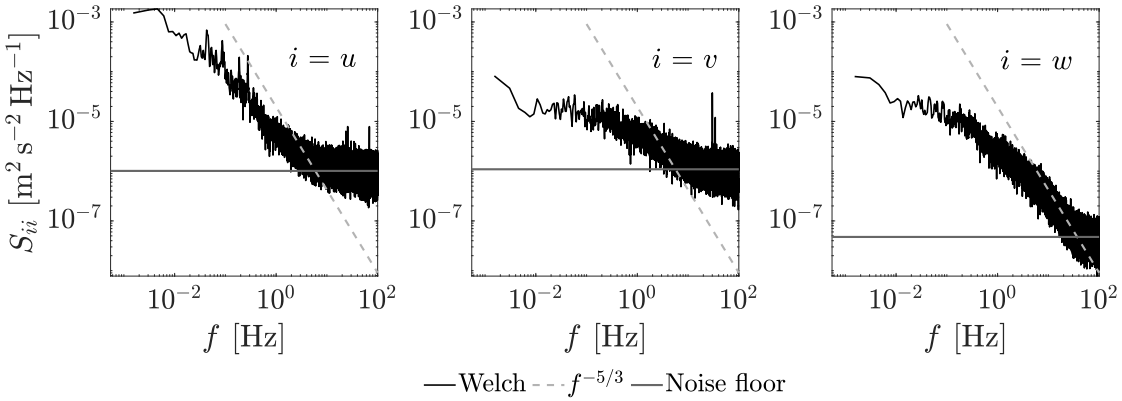


Figure 2.10: Noise floor of the ADV (grey solid) and Kolmogorov's $f^{-5/3}$ decay gradient (grey dashed) overlaid onto power spectral density (PSD) estimates of the i^{th} component of the velocity fluctuations (black solid), S_{ii}. The noise floor was estimated by averaging the PSD across the frequency range 95–100 Hz. Test conditions: $\overline{U_0} = 0.57\,\text{m}\,\text{s}^{-1}$; $(x, y, z) = (5, 0, 0)$.

z/H [-]	$\sigma^2_{\text{noise},i} \times 10^{-4}$ [m^2 s^{-2}]			Noise contribution to $\sigma^2_{\text{meas},i}$ [%]		
	u	v	w	u	v	w
0.400	0.89	1.16	0.05	54.0	79.9	18.3
0	0.82	1.12	0.04	56.4	76.3	20.0
-0.385	1.87	1.43	0.08	67.8	68.5	21.5

Table 2.2: Estimates of the noise-induced bias ($\sigma^2_{\text{noise},i}$) and the corresponding contribution to the measured velocity variance ($\sigma^2_{\text{meas},i}$) as a function of measurement depth. Test conditions: $\overline{U_0} = 0.58\,\text{m}\,\text{s}^{-1}$; $(x, y, z) = (5, 0, z)$.

section. There is at least one order-of-magnitude difference in the noise-related PSD between the horizontal and vertical components, consistent with other experimental studies [60, 62], and reflecting the lower sensitivity of the vertical velocity spectrum to noise contamination.

Table 2.2 provides estimates of $\sigma^2_{\text{noise},i}$ as a function of measurement depth, along with the corresponding contribution to the measured variance, $\sigma^2_{\text{meas},i}$. Estimates of $\sigma^2_{\text{noise},i}$ yield broadly consistent values through the water column, although the slight increase at z/H = -0.385 may indicate the probe's susceptibility to pulse interference when measuring closer to the channel boundaries. The high noise contribution to $\sigma^2_{\text{meas},i}$ is primarily attributed to the low SNR and the flume's low

turbulence levels (1–2%, see Section 3.2) in clean flow.

2.2.5 Flow Analysis

The following section outlines a series of methods for developing insights into the mean and turbulence characteristics of the flow.

Spatial Variation

The most effective way to evaluate spatial variation through the working section is by profiling the flow along the three axes of the flume at an appropriate spatial resolution. For the survey area ($750 \times 750\,\text{mm}$) shown in the left-hand panel of Figure 2.11, the measurement resolution is 125 mm in both directions. Given the five-minute sampling period for each measurement point and the time required for repeated measurements across multiple yz-planes and flow speeds, the 125 mm increment represents a reasonable compromise to develop insights into the qualitative behaviour of the flow at a given streamwise location.

The right-hand panel of Figure 2.11 presents 2D contours of the time-averaged velocity modulus, $\overline{U}$, at $x = 5\,\text{m}$, halfway along the working section of the flume. The contours, generated via piecewise cubic spline interpolation, reveal a slight negative vertical shear, characterised by higher local flow velocities at increased measurement depths. The narrow velocity range of $0.02\overline{U_0}$ between top dead centre (TDC) and bottom dead centre (BDC) of the rotor's swept area equates to a vertical velocity shear of $\partial\overline{U}/\partial z = 0.022\,\text{s}^{-1}$.

One of the key indicators of hydrodynamic performance is the spatial uniformity of the time-averaged velocities. Table 2.3 summarises the spatial variation of $\overline{U}$ across the yz-plane, measured halfway along the working section. The results reveal a velocity range of just $\pm 0.23\%$ at the 95% confidence level ($\text{CI}_{0.95}$) for a reference flow velocity of $\overline{U_0} = 0.58\,\text{m}\,\text{s}^{-1}$, demonstrating a high degree of velocity uniformity.

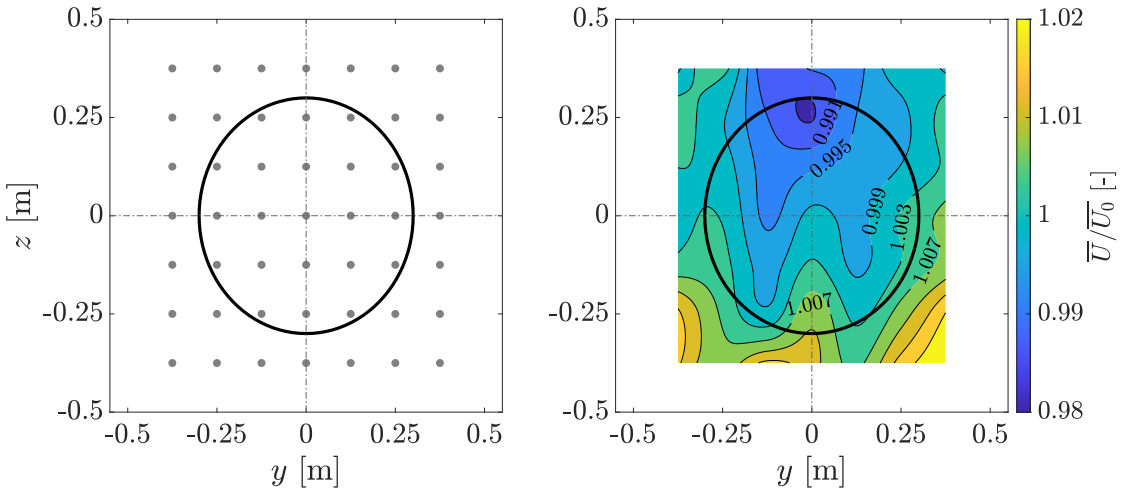


Figure 2.11: ADV measurement co-ordinates across the 750 × 750 mm survey area (left panel) and 2D contours of the time-averaged velocity modulus, $\overline{U}$, normalised on $\overline{U_0}$, at $x = 5\,\mathrm{m}$ (right panel). The box outline delineates the channel cross section[a], with dash-dotted lines indicating the centre planes, and the black circle represents the intended swept area of the turbine rotor. Test conditions: $\overline{U_0} = 0.58\,\mathrm{m\,s^{-1}}$.

[a]The axes are presented in dimensional form to avoid distortion of the geometric relationship between the intended swept area of the rotor and the channel cross section.

x [m]	$\overline{U_0}$ [m s^{-1}]	$\langle\overline{U}\rangle/\overline{U_0}$ [-]	$\sigma(\overline{U})/\overline{U_0}$ [-]	$\mathrm{CI}_{0.95}(\overline{U})$ [%]
5.0	0.579	1.003	0.008	0.229

Table 2.3: Summary statistics of velocity uniformity across the survey area at $x = 5\,\mathrm{m}$. $\langle()\rangle$ denotes spatial averaging, σ represents the standard deviation, and $\mathrm{CI}_{0.95}$ refers to the 95% confidence interval, expressed as a percentage of $\overline{U_0}$.

Uncertainty Quantification

Measurement error in the flow velocities was quantified as an expanded uncertainty, δ_{exp}, calculated by applying a coverage factor[5] to the combined uncertainty, δ_{comb}. The combined uncertainty was determined by taking the root sum of squares of the random (δ_{random}) and systematic errors (δ_{sys}) [63], expressed as:

$$\delta^2_{\mathrm{comb}} = \delta^2_{\mathrm{random}} + \sum_{i=1}^{j} \delta^2_{\mathrm{sys},\,i}, \tag{2.5}$$

[5]The coverage factor is based on the Student's t-distribution, with the degrees of freedom equal to the sample size minus one.

where i indexes each individual source of systematic error, and j is the total number of systematic errors, yielding an expanded uncertainty of $\delta_{\text{exp}} = \pm 0.03\,\text{m}\,\text{s}^{-1}$ ($\pm 0.04\overline{U_0}$) at the 95% confidence level. The random error, defined here as the standard error of the mean (SEM), is calculated from three repeated measurements and spatially averaged across all measurement co-ordinates within the survey area. Notably, the combined uncertainty is dominated by the ADV's systematic error, which is approximately an order of magnitude greater than the random error.

Power Spectra

The PSD of the velocity fluctuations provides insight into the distribution of turbulent kinetic energy across the frequency spectrum, which can be broadly divided into three distinct regions: (i) a low-frequency, energy-containing range, (ii) an inertial subrange where turbulence dissipation follows a universal power law [64], and (iii) a high-frequency dissipation range dominated by viscous effects. While various methods exist for estimating the PSD of stationary signals, this analysis considers three different approaches.

The first approach involves computing the discrete Fourier transform of the input signal using a fast Fourier transform (FFT) algorithm [65]. The signal power is then estimated by squaring and rescaling the magnitude of the transform. This method was used to determine the ADV's noise floor, as discussed in Section 2.2.4.

The Welch method [66] offers an alternative approach to estimating the PSD by dividing the input signal into equal overlapping segments and averaging the modified periodograms. In this analysis, a 50% overlap was specified for each of the ten segments. Each segment was multiplied by a symmetrical Hann window, with the first and last samples zero-weighted to reduce spectral leakage. While the Welch method is often preferred for its cleaner visual output and lower susceptibility to signal noise, it provides uncorrelated estimates of the true PSD [67].

The third method used in this study involves the von Kármán spectrum [68],

which is commonly used to model atmospheric turbulence [26]. Predictions of the von Kármán spectra require estimates of the i^{th} integral length scale, Λ_i, which can be computed by via non-linear curve-fitting in a least-squares sense [69]. Further discussion of this approach can be found in Section 3.3.

Spectral plots also help to identify unexpected sources of energy at specific frequencies, which, in the context of a physical experiment, are often attributed to vibrations or electrical signals, either inherent or external to the test setup. For instance, the estimated power spectra shown in Figures 2.10 and 3.17 reveal discrete energy peaks concentrated within a narrow frequency band of $f = 0.98$–$1.55\,\text{Hz}$ in the streamwise and cross-stream velocity components. Section 2.2.6 discusses the potential source of these peaks.

Turbulence Intensity

The most commonly used metric to quantify turbulence is the turbulence intensity, I_i, which, when accounting for noise-induced bias, is defined as:

$$I_i = \sqrt{\frac{\overline{u_i'^2} - \sigma^2_{\text{noise},i}}{\sum \overline{u_i}^2}}, \tag{2.6}$$

where the prime symbol represents a fluctuating quantity. Figure 2.12 illustrates the required corrections to I_i as a function of $\overline{U_0}$ when accounting for the ADV's noise floor. The corrections are defined as the percentage change between the uncorrected and corrected values, noting that they are only valid in a statistical sense. The substantial magnitude of the corrections, which is unique to clean flow conditions, reflects the dominance of noise in the velocity signals and reinforces earlier observations made in relation to Table 2.2. Although the noise-induced bias ($\sigma^2_{\text{noise},i}$) increases with flow speed (not shown), the proportion of the signal due to noise decreases, while the flow-related proportion increases, consistent with findings from other studies [60, 70]. The distinct relationships between $\overline{U_0}$ and the required correction for the i^{th} component reflect the unique sensitivity of each

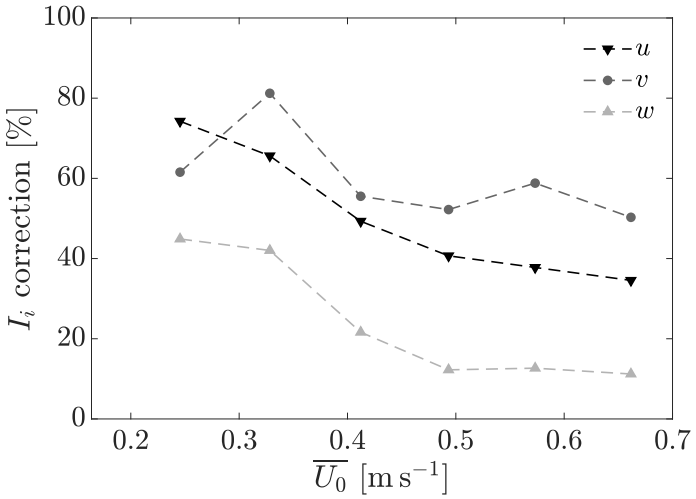


Figure 2.12: Corrections to I_u (down-pointing triangles), I_v (circles), and I_w (up-pointing triangles) as a function of $\overline{U_0}$. Linear piecewise fits have been added as a visual aid. Test conditions: $(x, y, z) = (5, 0, 0)$.

velocity component to noise, which is attributed to the geometry of the ADV probe [60].

Integral Scales

Various methods, including those proposed by [32, 65, 69, 71], can be used to estimate the integral scales of turbulence. In this analysis, the autocorrelation coefficient for velocity fluctuations at a single point in space [72] is applied:

$$\rho_{ii}(\tau) = \frac{\overline{u_i'(t)u_i'(t+\tau)}}{{\sigma_i}^2}, \tag{2.7}$$

where τ represents the time lag between a signal and a delayed copy of itself, and t denotes a point in time. Since $\rho_{ii}(\tau)$ is an even function, it follows that $\rho_{ii}(0) = 1$ and $|\rho_{ii}(\tau > 0)| \leq 1$ [65]. Applying the temporal autocorrelation coefficient is often preferred for analysing experimental data due to its comparative robustness over curve-fitting procedures and its effectiveness in handling non-monotonically decaying quantities [73].

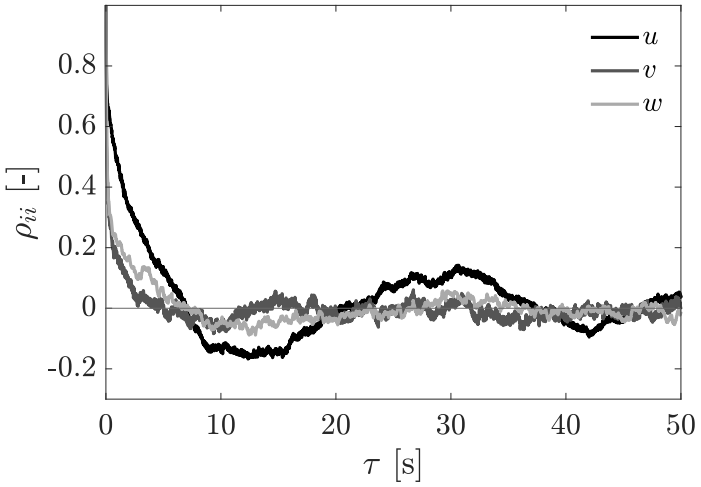


Figure 2.13: Example illustration of the autocorrelation coefficient, $\rho_{ii}(\tau)$, applied to the i^{th} velocity fluctuations (u = black, v = dark grey, and w = light grey). Integration of $\rho_{ii}(\tau)$ up to the first zero-crossing yields the integral time scales: $T_{\text{int},i} = 0.96\,\text{s}$ (u), $0.22\,\text{s}$ (v), and $0.78\,\text{s}$ (w). Test conditions: $\overline{U_0} = 0.49\,\text{m}\,\text{s}^{-1}$; $(x, y, z) = (5, -0.25, 0)$.

The first step in determining Λ_i is to calculate the integral time scale, given by:

$$T_{\text{int},i} = \int_0^\infty \rho_{ii}(\tau)\,\mathrm{d}\tau, \tag{2.8}$$

which characterises the duration for which the largest eddies remain correlated. Assuming $u_i' \ll \overline{u}$, Taylor's frozen turbulence hypothesis [65], which asserts that the advection of a field of frozen turbulence is entirely due to the mean flow, can be applied, and the integral scales of turbulence can be related by:

$$\Lambda_i = \overline{u} T_{\text{int},i}. \tag{2.9}$$

O'Neill and Nicolaides [72] perform the integration in Equation 2.8 using different upper limits, e.g. $\rho_{ii}(\tau) = 1/e$, and conclude that the limit defined by the first zero-crossing, i.e. where $\rho_{ii}(\tau) = 0$, proves to be the most robust, despite the small systematic error this incurs. Similar to several other studies in tidal research, e.g. [29, 31, 50], the analysis herein integrates the autocorrelation coefficient up to the first zero-crossing. The implementation of this method is illustrated in

Figure 2.13, highlighting the characteristic oscillatory tail (truncated in the figure) that persists for many multiples of $T_{\text{int},i}$ and the high-frequency noise component, attributed to the flume's low turbulence levels in clean flow.

To compensate for Doppler noise in estimates of the integral scales, the correction method proposed by Romagnoli *et al.* [74] can be applied to the autocorrelation coefficient. However, caution should be exercised when treating low-turbulence flow data with high noise content, as the corrections can be substantial. Applying the proposed correction to the data shown in Figure 2.13 results in an 86% increase in the streamwise integral length scale, from 0.47 m to 0.88 m. At higher flow speeds, the increase can be several times the pre-corrected values.

2.2.6 Vibration Analysis

Characterising the ADV mast's response through the water column helps to identify its natural frequencies and any associated resonance conditions in the flow velocity spectra. For the following analysis, PSD estimates of the ADV mast's accelerations, S_{jj} (where $j = x, y, z$), were used as a proxy for the structural response of the ADV probe, due to the impracticality of mounting the IMU directly onto the probe head. The depth difference between the IMU and the ADV's sampling volume was 261 mm, and the IMU sampling period was set to five minutes, consistent with the ADV.

The approach involved comparing the power spectra from a running flume with the corresponding spectra obtained after the flume's pumps were stopped and the flow was allowed to settle for 15 minutes[6], as shown in Figure 2.14. The peaks around 4 Hz likely correspond to vortex shedding, as these align closely with an analytical estimate of the shedding frequency, f_{shed}, based on the ADV mast's width and a Strouhal number of 0.2, which represents an upper limit for rectangular bodies [75]. Additionally, a vertical indicator at 24 Hz is shown, corresponding to a peak

[6]The settling period was introduced to minimise the likelihood of residual turbulence contaminating the IMU measurements.

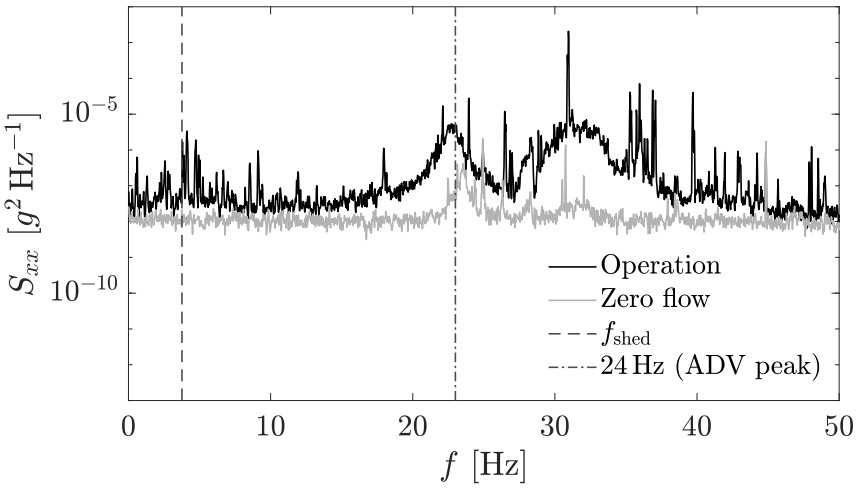


Figure 2.14: PSD estimates of streamwise accelerations, S_{xx}, obtained from the ADV mast in a running flume (black) and after the flume's pumps were stopped and the flow was allowed to settle for 15 minutes (grey). Vertical indicators denote the estimated vortex shedding frequency, f_{shed} (dashed), and a frequency of interest from Figure 2.10 (dash-dotted), corresponding to a peak in the velocity power spectra. Test conditions: $\overline{U_0} = 0.61\,\text{m}\,\text{s}^{-1}$; $(x, y, z) = (5, 0, 0)$.

observed in the power spectra of the streamwise and cross-stream flow velocities in Figure 2.10. The indicator aligns closely with a peak detected at zero flow speed and lies within 1 Hz of the nearest spectral peak during flume operation, suggesting an additional source of interference in the measurement system, potentially originating from the traverse motors or other laboratory equipment.

Elevated spectral energy within a narrow frequency range, common to both the PSD estimates of the flow velocities and the ADV mast's accelerations, indicates the influence of extraneous energy sources on the measurement system, distinct from the turbulent energy cascade. Figure 2.15 presents non-dimensional PSD estimates of the acceleration response from both the flume's supporting frame and the ADV mast, overlaid with the streamwise velocity power spectra. Two modest, narrow-banded energy peaks in the flow velocities at 24 Hz and 26 Hz (cf. Figure 2.10) closely align with increases in the acceleration power spectra, indicating the presence of two small resonances in the measurement system. Analogous to $\sigma^2_{\text{noise},i}$, the incremental signal variance associated with these resonances can be accounted for

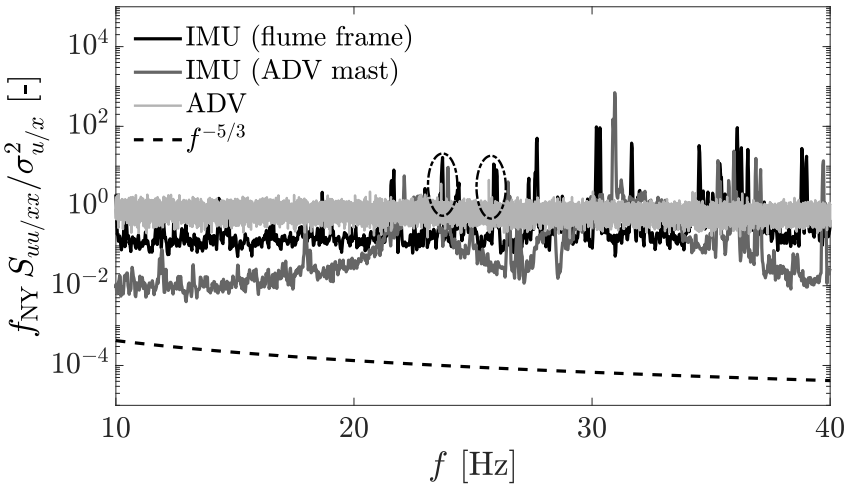


Figure 2.15: Non-dimensional PSD estimates of streamwise accelerations obtained from the flume's supporting frame (black) and the ADV mast (dark grey) are overlaid with PSD estimates of the flow's streamwise velocity fluctuations (light grey). The subscript NY denotes the Nyquist frequency. Also shown are the $f^{-5/3}$ decay gradient (black dashed) and two dash-dotted ellipses highlighting regions where increases in spectral energy coincide. Test conditions: $\overline{U_0} = 0.57\,\mathrm{m\,s^{-1}}$; $(x, y, z) = (5, 0, 0)$.

when calculating the turbulence statistics. For the data shown, the magnitude of the incremental variance, $\mathcal{O}(10^{-8})\,\mathrm{m^2\,s^{-2}}$, is four orders of magnitude smaller than $\sigma^2_{\mathrm{noise},i}$. Consequently, any potential influence on the turbulence statistics was deemed negligible, and no additional correction was applied.

2.3 Limitations of the Methodology

The mechanical design of the traverse restricted the vertical travel of the ADV mast to 300 mm. As a result, four discrete mast lengths were used to support flow measurements through the water column. Any disturbance to the probe's orientation when exchanging the masts could unintentionally introduce bias into the time-averaged velocities, making careful handling essential. If an investigator chooses not to correct for probe misalignment according to the procedure outlined in Section 2.2.4, it is recommended to physically align the probe with the mean flow direction as accurately as possible. For the results presented, the rotational corrections ranged between 0–1.5° (pitch) and 0–5° (yaw), corresponding to a

velocity bias $\mathcal{O}(\pm 0.01)\,\mathrm{m\,s^{-1}}$, similar in magnitude to the expanded uncertainty.

Another challenge when using the ADV was avoiding acoustic reflections when measuring the flow with a downwards-looking probe close to the channel bed. To avoid weak spots and minimise the number of data points replaced as spikes, the deepest measurement co-ordinate was set to 115 mm above the channel bed. As a guideline, investigators should aim to replace no more than 1% of a sampling record through the despiking algorithm.

Due to the flume's low ambient turbulence, the correspondingly high noise content in the measured velocities posed a challenge when calculating the integral scales. At lower flow speeds in particular, e.g. $\overline{U_0} \leq 0.4\,\mathrm{m\,s^{-1}}$, applying a correction to the autocorrelation coefficient often yielded non-physical scales. This issue likely stems from the method's limitations when applied to low turbulence conditions, as the required corrections often exceeded 50% of the signal variance (see Table 2.2). Given the uncertainty associated with applying corrections of this magnitude, the integral scales reported for clean flow measurements (see Section 3.2.3) were not corrected for noise. In contrast, investigations into more turbulent flows reveal much smaller corrections ($\leq 10\%$), which are discussed further in Chapter 4.

2.4 Summary

A robust methodology has been developed for the hydrodynamic characterisation of a recirculating water flume, in preparation for the model-scale testing of a horizontal axis tidal stream turbine. An ADV was used to measure the flow, enabling the investigation of the flow's spatial uniformity, temporal stability, and turbulence parameters. Several examples of data treatment for both flow and vibration measurements in clean flow conditions have been provided to illustrate the application of the methods described. Measurement uncertainty and biases within the test setup, such as instrument noise and vibration, have also been considered and accounted for in the analysis.

To generate an accurate statistical description of the flow, it is recommended to follow a prescribed sequence of data processing steps. One of the first steps involves defining a sampling strategy, which includes establishing a period of stationarity for flow measurements. In this study, a stationarity period of 300 s was determined based on the stability of the velocity variance over a one-hour period. Other steps include, but are not limited to, eliminating ADV data spikes, calibrating the measured velocities for probe misalignment, and removing the ADV's noise floor. For flow measurements dominated by noise, such as those reported herein for the clean flow case, corrections to account for noise in the turbulence statistics can be substantial, often exceeding 50% in the streamwise and cross-stream directions. For higher-order quantities, such as the integral length scales, corrections of this magnitude can lead to non-physical results, introducing significant uncertainty and casting doubt on the suitability of this approach for low-turbulence conditions.

Low-cost IMU arrangements can provide insights into unexpected sources of signal interference, whether internal or external to the test setup. By identifying and accounting for these sources of interference through analysis of the power spectra, researchers can enhance the accuracy and reliability of their results. In the analysis presented, the incremental variance in the velocity signals caused by system vibration was four orders of magnitude lower than the variance due to signal noise. Consequently, any potential influence on the turbulence statistics was deemed negligible.

The methodology described will be of interest to researchers planning to characterise similar facilities using an ADV and instils confidence in establishing baseline flow conditions for model-scale experiments.

CHAPTER 3

Clean Flow Characterisation in a Hydraulic Flume

This chapter describes the mean flow and turbulence characteristics of a recirculating water flume at the University of Oxford, in preparation for the model-scale testing of a horizontal axis tidal stream turbine. The analysis quantifies the spatial and temporal variations of the clean flow regime, including an analysis of the bottom boundary layer and free-surface response. Additionally, the spectral characteristics of the measured velocities are examined to provide insight into the energy distribution across different flow scales.

This work serves as a valuable reference for researchers within the university seeking to understand the flume's flow characteristics, validate numerical models, or inform predictions of model-scale rotor performance.

3.1 Observed Hydrodynamics

The following analysis is based on flow measurements collected at three equidistant yz-planes in the flume ($x = 2.5\,\text{m}$, $5.0\,\text{m}$, and $7.5\,\text{m}$) and assumes that the turbine rotor plane will be aligned with the centre of the working section under clean flow conditions.

3.1.1 Mean Velocities

In addition to 2D contour maps of the flow field, the following analysis includes measurements along the flume's vertical and horizontal centre planes using the cruciform measurement profile shown in Appendix A, Figure A.1. The cruciform measurement profile, which combines both horizontal and vertical traverses of the flume, provides increased spatial resolution and covers a broader measurement span along the target measurement axis compared to the transect co-ordinate map shown in Figure 2.11. A further advantage of the cruciform measurement profile is that it reveals local flow effects more clearly, as individual measurements along the target axis are more distinctly represented in graphical form. While 2D contours offer a broader view of the flow field, interpolation between points can obscure true values and mask smaller-scale variations in the flow.

Depthwise Profiling

Figure 3.1 shows the streamwise evolution of $\overline{u_i}(z)$ in the flume's vertical centre plane, along with the random error calculated from three repeated measurements. Slightly higher streamwise velocities are observed in the bottom half of the water column, which is likely to be an artefact of how the flow is returned to the working section via the turning vanes and contraction section. While this behaviour is atypical of open-channel flows [76], the narrow 95% confidence intervals for velocity uniformity ($< 0.01\overline{U_{\mathrm{CL}}}$), as shown in Table 3.1, indicate a high degree of depthwise uniformity for each velocity component. As the flow develops downstream, increasing uniformity in the streamwise component is observed, as evidenced by progressively narrower 95% confidence intervals in the depth-averaged velocities about the corresponding centreline values. Additionally, there is a 2% increase in the depth-averaged streamwise velocity between $x = 2.5\,\mathrm{m}$ and $x = 7.5\,\mathrm{m}$.

The time-averaged cross-stream and vertical velocities are at least two orders of magnitude smaller than the dominant streamwise component and exhibit anti-

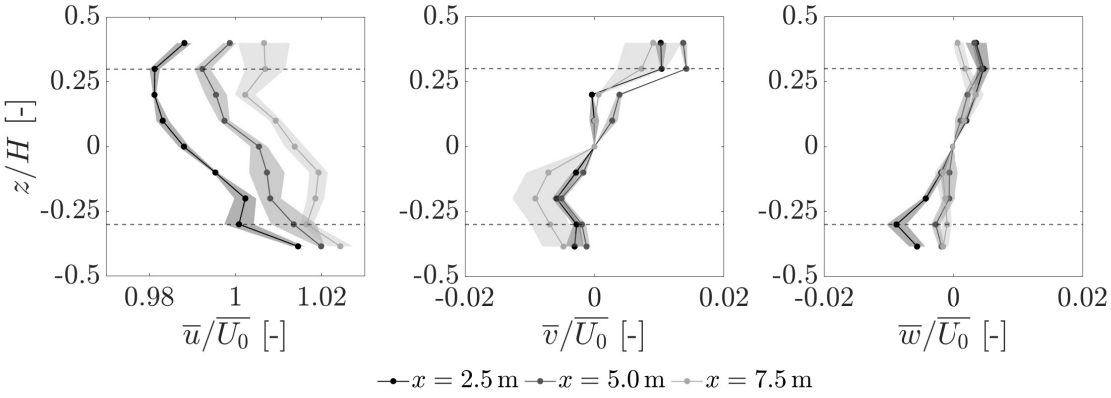


Figure 3.1: Depthwise profiles of $\overline{u_i}$, normalised on $\overline{U_0}$, at three streamwise locations: $x = 2.5$ m (black), 5.0 m (dark grey), and $x = 7.5$ m (light grey). The profiles comprise measurements along the flume's vertical centre plane, as illustrated in Appendix A, Figure A.1. The random error is represented by ± 1 SEM (shaded areas). Linear piecewise fits have been added as a visual aid. The intended swept area of the rotor is also shown (dashed). Test conditions: $\overline{U_0} = 0.58\,\mathrm{m\,s^{-1}}$.

x [m]	$\overline{U_{\mathrm{CL}}}$ [m s^{-1}]	$\langle\overline{u}\rangle/\overline{U_{\mathrm{CL}}}$ [-]	$\mathrm{CI}_{0.95}(\overline{u})$ [%]	$\langle\overline{v}\rangle/\overline{U_{\mathrm{CL}}}$ [-]	$\mathrm{CI}_{0.95}(\overline{v})$ [%]	$\langle\overline{w}\rangle/\overline{U_{\mathrm{CL}}}$ [-]	$\mathrm{CI}_{0.95}(\overline{w})$ [%]
2.5	0.570	1.004	0.886	0.001	0.450	-0.001	0.368
5.0	0.580	0.999	0.690	0.003	0.523	0.001	0.185
7.5	0.585	0.999	0.548	-0.001	0.484	2×10^{-4}	0.140

Table 3.1: Summary statistics of depthwise velocity uniformity along the vertical centre plane of the flume. The 95% confidence intervals are expressed as a percentage of the centreline velocity modulus at each streamwise location, $\overline{U_{\mathrm{CL}}}$.

symmetric profiles about the flume's centreline. Although minor, this asymmetry reflects the three-dimensional nature of the flow, which becomes more pronounced further from the horizontal centre plane of the flume. As downstream distance increases, the magnitude of the vertical velocities decreases, suggesting a weakening of any flow effects likely originating at the junction of the contraction and the inlet to the working section, resulting in reduced vertical momentum transport. Furthermore, the effect of the 2D rotational correction about the flume's centreline (see Section 2.2.4) is evident from the zero values of both the cross-stream and vertical velocities at $(y, z) = (0, 0)$. The pitch corrections range between 0.9–1.2°, while the yaw corrections range between 4.3–4.9°, consistent with the analysis

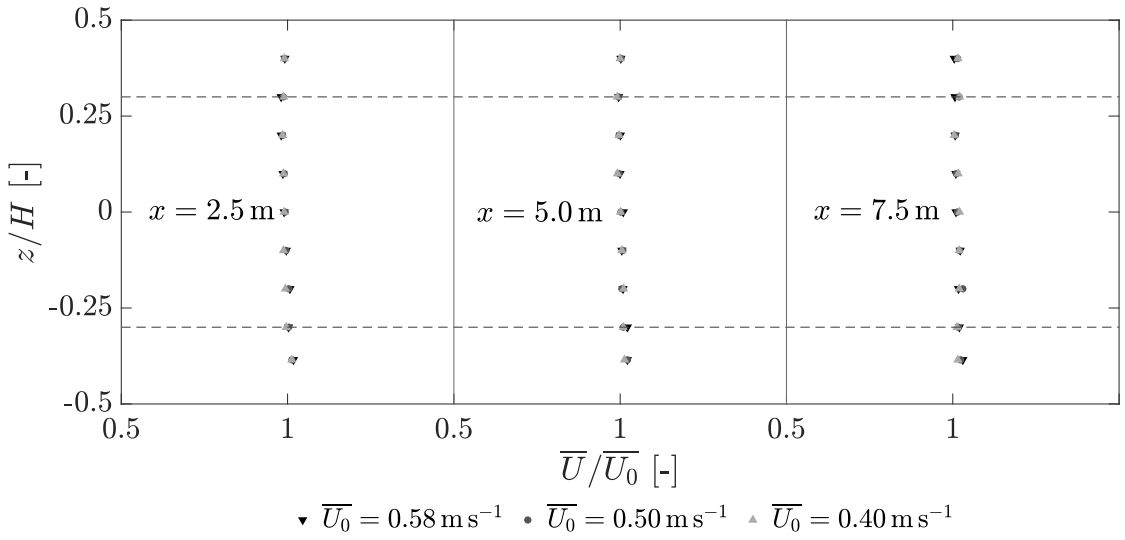


Figure 3.2: Depthwise profiles of $\overline{U}$, normalised on three reference flow velocities: $\overline{U_0} = 0.58\,\mathrm{m\,s^{-1}}$ (down-pointing triangles), $0.50\,\mathrm{m\,s^{-1}}$ (circles), and $0.40\,\mathrm{m\,s^{-1}}$ (up-pointing triangles), at three streamwise locations. The profiles comprise measurements along the flume's vertical centre plane, as illustrated in Appendix A, Figure A.1. The intended swept area of the rotor is also shown (dashed).

	$\overline{U_0} = 0.50\,\mathrm{m\,s^{-1}}$			$\overline{U_0} = 0.40\,\mathrm{m\,s^{-1}}$		
x [m]	$\overline{U_{\mathrm{CL}}}$ [$\mathrm{m\,s^{-1}}$]	$\langle\overline{U}\rangle/\overline{U_{\mathrm{CL}}}$ [-]	$\mathrm{CI}_{0.95}(\overline{U})$ [%]	$\overline{U_{\mathrm{CL}}}$ [$\mathrm{m\,s^{-1}}$]	$\langle\overline{U}\rangle/\overline{U_{\mathrm{CL}}}$ [-]	$\mathrm{CI}_{0.95}(\overline{U})$ [%]
2.5	0.492	1.003	0.712	0.394	1.003	0.644
5.0	0.497	1.002	0.641	0.399	1.001	0.612
7.5	0.503	1.003	0.519	0.406	0.996	0.390

Table 3.2: Summary statistics of depthwise velocity uniformity along the vertical centre plane of the flume as a function of $\overline{U_0}$. The 95% confidence intervals are expressed as a percentage of $\overline{U_{\mathrm{CL}}}$ at each streamwise location. The statistics corresponding to $\overline{U_0} = 0.58\,\mathrm{m\,s^{-1}}$ are omitted to avoid duplication with Table 3.1.

presented in Chapter 2.

Having characterised the flow at the flume's design speed, the next step was to evaluate its response across different flow speeds. The motivation for this analysis was to determine whether the spatial uniformity of the non-dimensional flow characteristics likely to be experienced by the turbine rotor (e.g. mean velocities, turbulence intensity, etc.) varies with flow speed. Such variations could affect the turbine's non-dimensional performance and loading response, depending on

the operating strategy (i.e. whether tip-speed ratio is controlled by flow speed or rotor speed; see Equation 6.3). Figure 3.2 shows the streamwise evolution of $\overline{U}(z)$ for three reference flow velocities along the flume's vertical centre plane. The non-dimensional depthwise profiles not only collapse at each streamwise location but also maintain a broadly consistent shape with downstream distance. The spatial uniformity of the two lower-speed profiles, detailed in Table 3.2, aligns with previous observations. Specifically, the depth-averaged velocities remain within 0.4% of $\overline{U_{\mathrm{CL}}}$ at each streamwise location, while the 95% confidence intervals progressively narrow with downstream distance, indicating improved flow uniformity.

Cross-stream Profiling

The streamwise evolution of $\overline{u_i}(y)$ at mid-water depth is shown in Figure 3.3, along with the random error calculated from three repeated measurements. A notable feature of the profiles is their slight asymmetry about the flume's vertical centre plane, the underlying causes of which are not addressed in this work. Additionally, peak streamwise velocities for each profile are observed within 175 mm of the flume's sidewalls, which may attributed to small secondary flows drawing high momentum fluid away from the core of the channel. At $x = 7.5\,\mathrm{m}$, a shear layer emerges just beyond the rotor's swept area, along the vertical edges of the survey area. This is likely attributed to boundary layer growth and disturbances at the interfaces between the non-co-planar glass panes, which run along the length of the flume in 1.7 m sections. The development of the shear layers lead to a loss of uniformity across the profile, as indicated by the increase in $\mathrm{CI}_{0.95}(\overline{u})$ from $\pm 0.45\%$ at $x = 2.5\,\mathrm{m}$ to $\pm 0.70\%$ at $x = 7.5\,\mathrm{m}$ (see Table 3.3). A 2% increase in the streamwise velocity, when spatially averaged across each profile, is observed once again between $x = 2.5\,\mathrm{m}$ and $x = 7.5\,\mathrm{m}$.

Similar to the depthwise profiles, the magnitudes of the time-averaged cross-stream and vertical velocities are negligible relative to the bulk flow ($< 0.01\overline{U_0}$), yet the profiles reveal some interesting characteristics. The antisymmetric nature of the

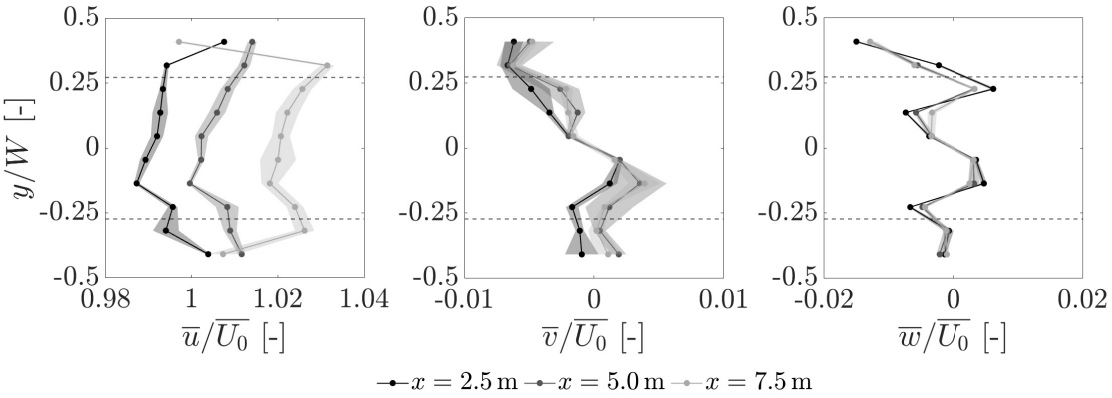


Figure 3.3: Cross-stream profiles of $\overline{u_i}$, normalised on $\overline{U_0}$, at three streamwise locations: $x = 2.5$ m (black), 5.0 m (dark grey), and $x = 7.5$ m (light grey). The profiles comprise measurements at mid-water depth, as illustrated in Appendix A, Figure A.1. The random error is represented by ± 1 SEM (shaded areas). Linear piecewise fits have been added as a visual aid. The intended swept area of the rotor is also shown (dashed). Test conditions: $\overline{U_0} = 0.58\,\mathrm{m\,s^{-1}}$.

x [m]	$\overline{U_{\mathrm{CL}}}$ [$\mathrm{m\,s^{-1}}$]	$\langle\overline{u}\rangle/\overline{U_{\mathrm{CL}}}$ [-]	$\mathrm{CI}_{0.95}(\overline{u})$ [%]	$\langle\overline{v}\rangle/\overline{U_{\mathrm{CL}}}$ [-]	$\mathrm{CI}_{0.95}(\overline{v})$ [%]	$\langle\overline{w}\rangle/\overline{U_{\mathrm{CL}}}$ [-]	$\mathrm{CI}_{0.95}(\overline{w})$ [%]
2.5	0.571	1.004	0.448	-0.002	0.210	-0.002	0.463
5.0	0.577	1.005	0.341	-0.001	0.230	-0.003	0.366
7.5	0.588	0.999	0.704	-0.001	0.214	-0.002	0.348

Table 3.3: Summary statistics of cross-stream velocity uniformity at mid-water depth. The 95% confidence intervals are expressed as a percentage of $\overline{U_{\mathrm{CL}}}$ at each streamwise location.

$\overline{v}/\overline{U_0}$ profiles is attributed to the geometrical relationship between the ADV probe and the positive wall-normal velocities, while the $\overline{w}/\overline{U_0}$ profiles exhibit greater complexity.

When the analysis was expanded to include different reference flow velocities, the non-dimensional velocity profiles again exhibited self-similar behaviour, as shown in Figure 3.4. Although not shown for brevity, spatially averaged velocities across each profile were within 0.7% of $\overline{U_{\mathrm{CL}}}$ at each streamwise location, with a slight deterioration in uniformity compared to the depthwise profiles, due to the growth of the shear layers along the vertical edges of the survey area. The 95% confidence intervals for uniformity, measured relative to centreline values,

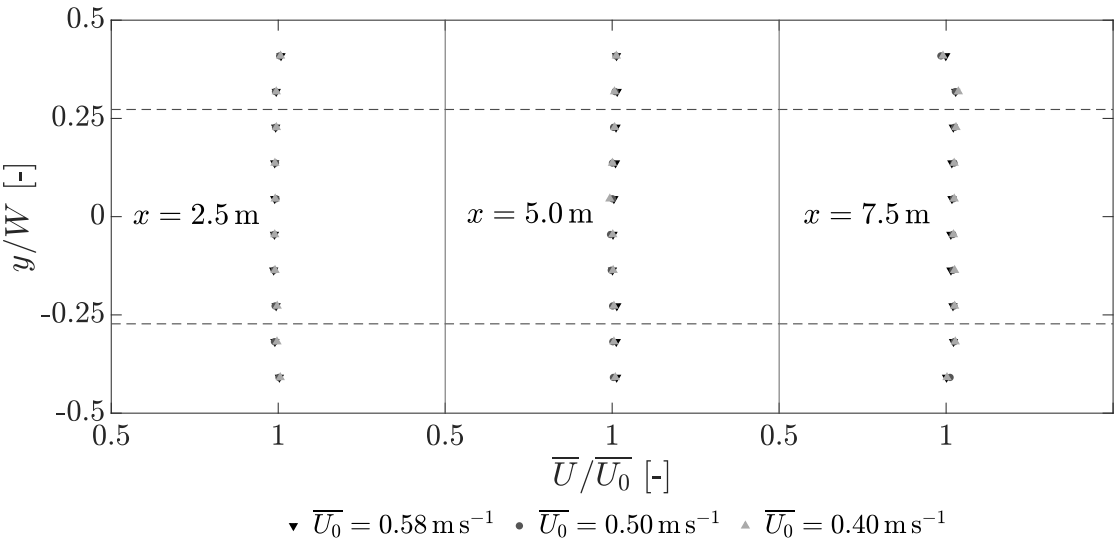


Figure 3.4: Cross-stream profiles of $\overline{U}$, normalised on three reference flow velocities: $\overline{U_0} = 0.58\,\mathrm{m\,s^{-1}}$ (down-pointing triangles), $0.50\,\mathrm{m\,s^{-1}}$ (circles), and $0.40\,\mathrm{m\,s^{-1}}$ (up-pointing triangles), at three streamwise locations. The profiles comprise measurements at mid-water depth, as illustrated in Appendix A, Figure A.1. The intended swept area of the rotor is also shown (dashed).

equate to $0.01\overline{U_0}$, which is well within the expanded uncertainty of the velocity measurements.

Transect Profiling

To complement the cruciform profiles presented above, Figure 3.5 shows the streamwise development of $\overline{U}$[1] in contour form across the survey area. The figure supports three key observations previously noted: (i) a modest negative vertical velocity shear envelops the intended swept area of the rotor at each measurement plane, (ii) the flow accelerates modestly (by 2%) through the measurement domain, and (iii) the flow speed is marginally higher away from the vertical centre plane of the flume. The location of the intended rotor plane, $x = 5.0\,\mathrm{m}$, offers the highest velocity uniformity across the three streamwise locations, with ±0.23% at the 95% confidence level, as detailed in Table 3.4.

[1]The velocity modulus is considered representative of the bulk flow because the v and w velocities are negligible compared to the u component.

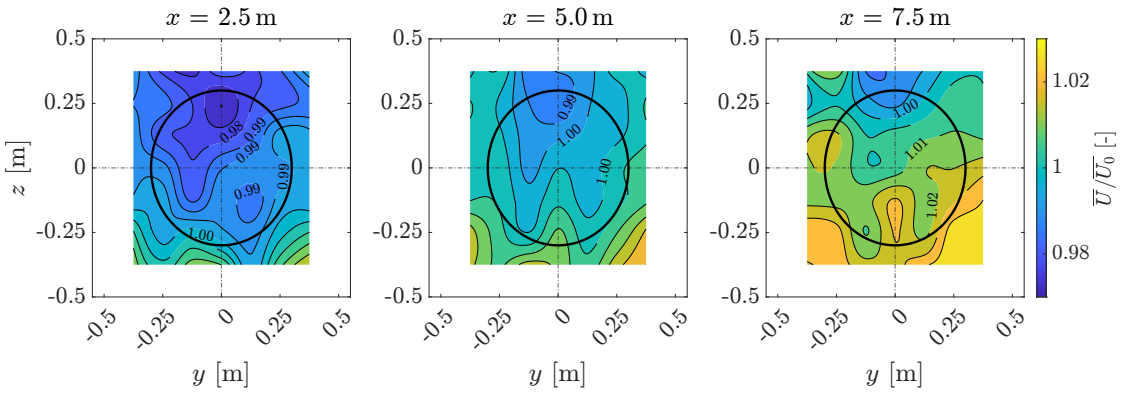


Figure 3.5: 2D contours of $\overline{U}$, normalised on $\overline{U_0}$, across three individual transects of the flume. The profiles correspond to the measurement co-ordinates illustrated in Figure 2.11. The box outline delineates the flume's cross section, and the black circle represents the intended swept area of the turbine rotor. Test conditions: $\overline{U_0} = 0.58\,\mathrm{m\,s^{-1}}$.

x [m]	$\overline{U_{\mathrm{CL}}}$ [$\mathrm{m\,s^{-1}}$]	$\langle\overline{U}\rangle/\overline{U_{\mathrm{CL}}}$ [-]	$\sigma(\overline{U})/\overline{U_{\mathrm{CL}}}$ [-]	$\mathrm{CI}_{0.95}(\overline{U})$ [%]
2.5	0.572	1.003	0.010	0.290
5.0	0.579	1.003	0.008	0.229
7.5	0.583	1.005	0.010	0.292

Table 3.4: Summary statistics of velocity uniformity across individual transects of the flume. The 95% confidence intervals are expressed as a percentage of $\overline{U_{\mathrm{CL}}}$ at each streamwise location.

3.1.2 Bottom Boundary Layer

The highly variable environments in which full-scale tidal stream turbines operate pose a significant challenge for hydrodynamic characterisation. The flow dynamics of such environments are in part driven by the bottom boundary layer, the thickness of which, relative to the channel height, can far exceed the equivalent dimension in a laboratory setting [77]. For fixed-bottom turbines, the bottom boundary layer can fully envelop the device, which is typically sited in an intermediate region between the channel bed and the free surface, i.e. $0.15 < z/H \leq 0.6$ [76], where $z/H \in \{0, 1\}$. This positioning can lead to higher levels of fatigue loading on the turbine rotor and drivetrain due to increased velocity fluctuations and azimuthal variations in blade forces.

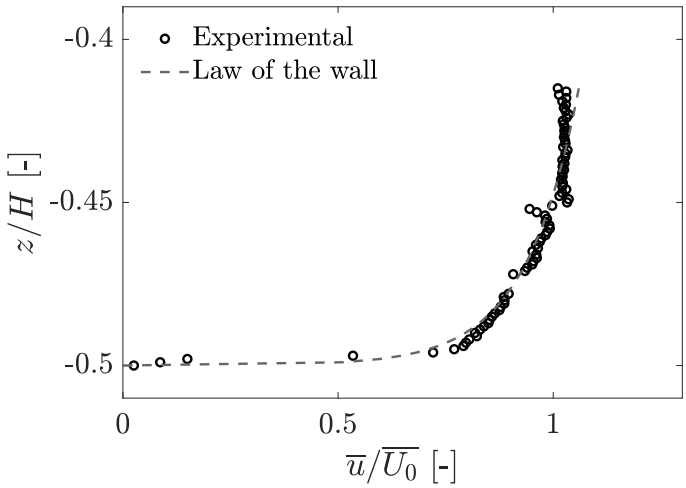


Figure 3.6: Time-averaged streamwise velocities, normalised on $\overline{U_0}$, as a function of distance from the channel bed. Experimental results (circles) are compared with von Kármán's logarithmic law of the wall (dashed). Measurements were recorded at 1 mm intervals along the vertical centre plane of the flume. Test conditions: $\overline{U_0} = 0.57\,\mathrm{m\,s^{-1}}$; $(x, y, z) = (5, 0, z)$.

In view of the depthwise velocity profiles presented in Section 3.1.1, the deepest measurement co-ordinates appear to lie outside the bottom boundary layer. This analysis aims to validate this observation by characterising the velocity profile of the bottom boundary layer halfway along the working section and comparing it with von Kármán's logarithmic law of the wall [78], which describes the relationship between flow velocity and elevation from the channel bed. The distribution, which typically applies to $< 20\%$ of the total flow depth, is given by:

$$u(z) = \frac{u_\tau}{\kappa} \ln\left(\frac{z}{z_0}\right), \tag{3.1}$$

where u_τ denotes the friction velocity, κ is the von Kármán constant (≈ 0.41), and z_0 is a constant of integration, analogous to a roughness length.

The resulting velocity profile, shown in Figure 3.6, aligns closely with the theoretical distribution, indicating the bottom boundary layer extends approximately 50 mm above the channel bed, corresponding to an elevation where $\overline{u} = 0.99\overline{U_0}$. As a result, it is unlikely for the bottom boundary layer to penetrate the intended

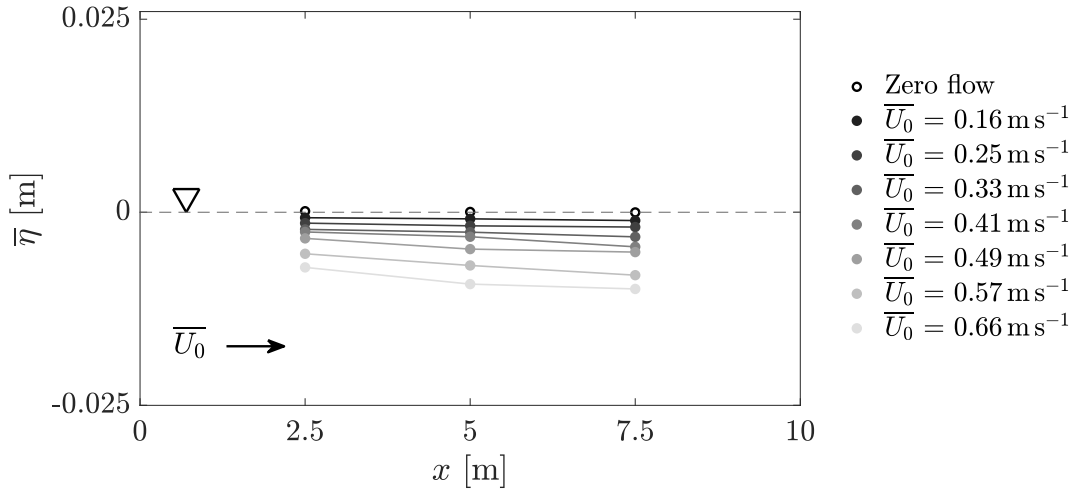


Figure 3.7: Time-averaged free-surface elevation, $\overline{\eta}$, as a function of $\overline{U_0}$ (greyscale) along the flume's vertical centre plane at three streamwise locations. Linear piecewise fits have been added as a visual aid. The dashed line indicates the still water level. Test conditions: $(x, y, z) = (x, 0, 0.4)$.

swept area of the model-scale rotor, which has a diameter of 0.6 m.

3.1.3 Free-Surface Response

Resistive wave gauges can provide insight into the mean free-surface behaviour of controlled open-channel flows. Each gauge measures the local surface elevation, η, relative to the still water level, which can be time averaged across the sampling record. Three wave gauges were positioned along the flume's vertical centre plane at $x = 2.5\,\mathrm{m}$, 5.0 m, and 7.5 m, spaced equidistantly. Measurements were sampled for five minutes, consistent with the ADV and IMU setups.

Figure 3.7 shows the time-averaged free-surface elevation, $\overline{\eta}$, as a function of $\overline{U_0}$, revealing an increasing head drop between $x = 2.5\,\mathrm{m}$ and $x = 7.5\,\mathrm{m}$ as the flow velocity increases. In order to conserve the mass flow rate, an increase in flow velocity reduces the flow area—limited in this case to the height—yielding $\Delta\overline{\eta} = 2.8\,\mathrm{mm}$ at the design speed of the flume. This result does not account for the 2% increase in flow velocity observed in Section 3.1.1, which implies a head drop of $\Delta\overline{\eta} \approx 20\,\mathrm{mm}$. This discrepancy can likely be attributed to several factors

within the experimental setup that may have biased the measurements.

One such source of measurement bias was a seiche, which originated at the downstream end of the flume, introducing unintended oscillations in the free surface. Additional sources of bias included the gauges' susceptibility to signal drift, and the substantial VIV of the partly-submerged steel rods. Due to the impracticality of mounting the IMU directly onto the gauges, quantifying the influence of VIV on the measured displacements was not feasible.

Although the results appear qualitatively reasonable, several sources of measurement error have not been accounted for, leading to significant uncertainty in the free-surface response. Consequently, any calculations involving the local water depth, such as bulk flow velocity, are highly uncertain and should be avoided.

3.2 Observed Turbulence Characteristics

3.2.1 Turbulence Intensities

This section presents spatial distributions of the noise-corrected turbulence intensity, I_{3D}, calculated as the modulus of the individual directional components. Similar to the mean velocities, the flow analysis is organised into depthwise, cross-stream, and transect profiles.

Depthwise Profiling

Figure 3.8 shows the streamwise evolution of $I_{3D}(z)$ along the flume's vertical centre plane, together with the expanded uncertainty at the 95% confidence level. Similar to the time-averaged velocities, a high degree of uniformity is apparent, as evidenced by the limited range of values across the measurement domain, 0.98–1.55%, and the narrow 95% confidence intervals (expressed as absolute values) for each depthwise profile about its respective centreline value ($\pm 0.12\%$ at $x = 2.5\,\mathrm{m}$, $\pm 0.11\%$ at $x = 5.0\,\mathrm{m}$, and $\pm 0.09\%$ at $x = 7.5\,\mathrm{m}$).

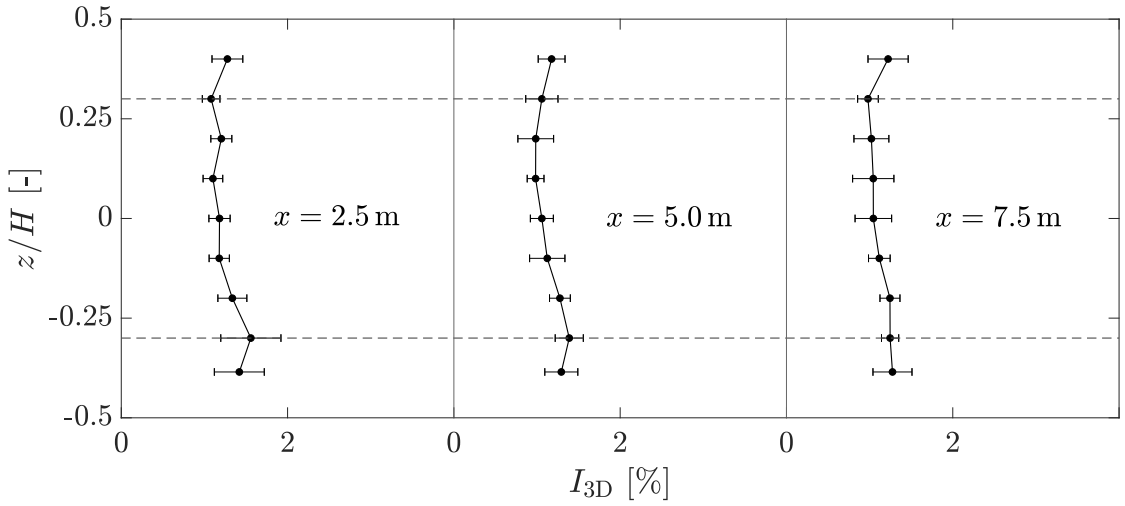


Figure 3.8: Depthwise profiles of I_{3D} at three streamwise locations. The error bars indicate the expanded uncertainty at the 95% confidence level. The profiles comprise measurements along the flume's vertical centre plane, as illustrated in Appendix A, Figure A.1. Linear piecewise fits have been added as a visual aid. The intended swept area of the rotor is also shown (dashed). Test conditions: $\overline{U_0} = 0.58\,\mathrm{m\,s^{-1}}$.

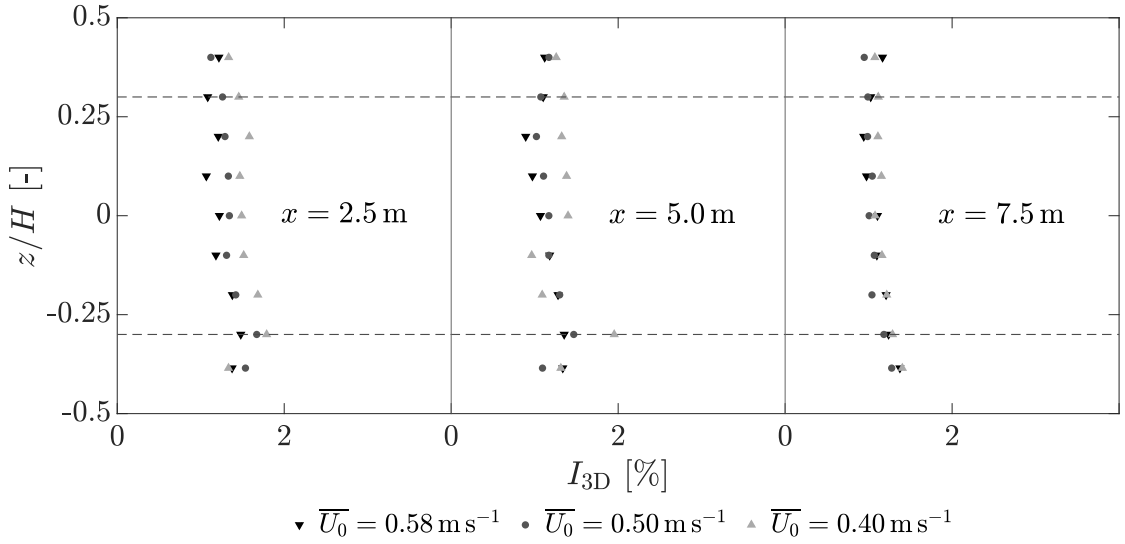


Figure 3.9: Depthwise profiles of I_{3D} as a function of three reference flow velocities: $\overline{U_0} = 0.58\,\mathrm{m\,s^{-1}}$ (down-pointing triangles), $0.50\,\mathrm{m\,s^{-1}}$ (circles), and $0.40\,\mathrm{m\,s^{-1}}$ (up-pointing triangles), at three streamwise locations. The profiles comprise measurements along the flume's vertical centre plane, as illustrated in Appendix A, Figure A.1. The intended swept area of the rotor is also shown (dashed).

The systematic error was approximated by propagating the velocity error through Equation 2.6, yielding a relative error of $0.01\sqrt{3} \approx 1.73\%$ of I_{3D}, while the

random error was estimated from three repeated measurements. When spatially averaged across the measurement domain, the expanded uncertainty was estimated as $1.18 \pm 0.18\%$ (expressed as an absolute value) at the 95% confidence level, noting the random error was approximately $\sqrt{3}$ times greater than the systematic error.

When comparing the profiles across different reference flow velocities, self-similarity across the measurement domain is evident once again, with the magnitude of the turbulent fluctuations scaling proportionally with $\overline{U_0}$, as shown in Figure 3.9. The absolute variation in turbulence intensity at each streamwise location is, on average, 0.26% across the different flow speeds. This provides valuable insight for future turbine tests, suggesting that the rotor will experience similar turbulence intensities, regardless of the approach flow velocity.

Cross-stream Profiling

The streamwise evolution of $I_{3D}(y)$ at mid-water depth is shown in Figure 3.10, together with the expanded uncertainty at the 95% confidence level. Across the intended swept area of the rotor, I_{3D} ranges between 1.08–1.46% through the measurement domain. However, for measurements closest to the sidewalls, values progressively increase to over 3% at $x = 7.5\,\mathrm{m}$, driven primarily by local increases in I_u, which are attributed to the development of the shear layers. Notably, the measurement uncertainty scales with the turbulence, peaking at $3.15 \pm 0.50\%$ (expressed as an absolute value) at the 95% confidence level at $y/W = \pm 0.41$, reflecting the greater variability in the sampling records.

Cross-stream profiles of I_{3D} as a function of $\overline{U_0}$, shown in Figure 3.11, exhibit a similar collapse to the depthwise profiles, although slightly higher values are observed once again at the lowest reference velocity, $\overline{U_0} = 0.40\,\mathrm{m\,s^{-1}}$. Notably, the absolute variation of I_{3D} across the different flow speeds is, on average, 0.26%, consistent with the variation in the depthwise profiles. However, within the shear layers at $x = 7.5\,\mathrm{m}$, where I_{3D} can exceed 3%, the variation increases to as much as 0.78%.

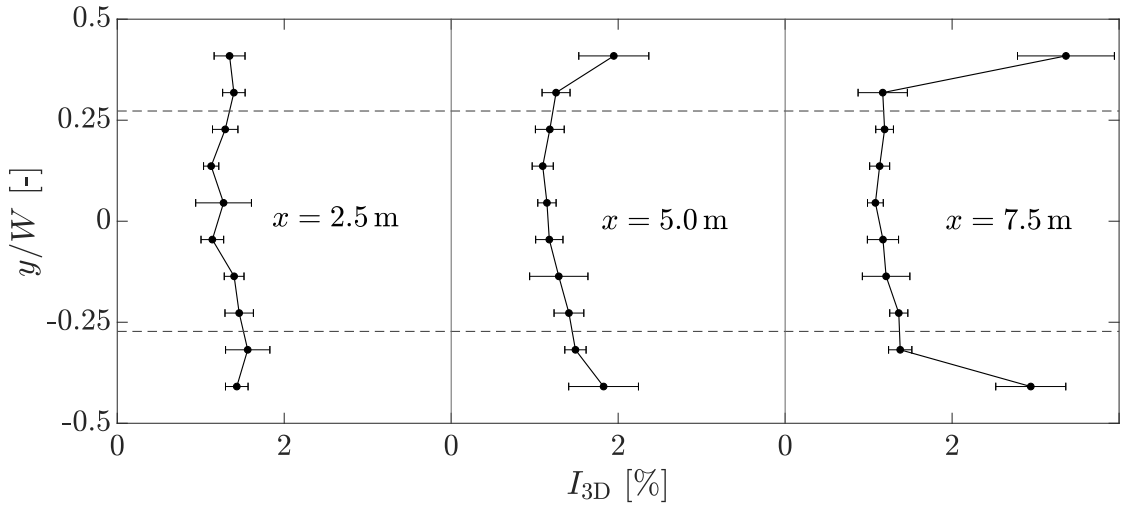


Figure 3.10: Cross-stream profiles of I_{3D} at three streamwise locations. The error bars indicate the expanded uncertainty at the 95% confidence level. The profiles comprise measurements at mid-water depth, as illustrated in Appendix A, Figure A.1. Linear piecewise fits have been added as a visual aid. The intended swept area of the rotor is also shown (dashed). Test conditions: $\overline{U_0} = 0.58\,\mathrm{m\,s^{-1}}$.

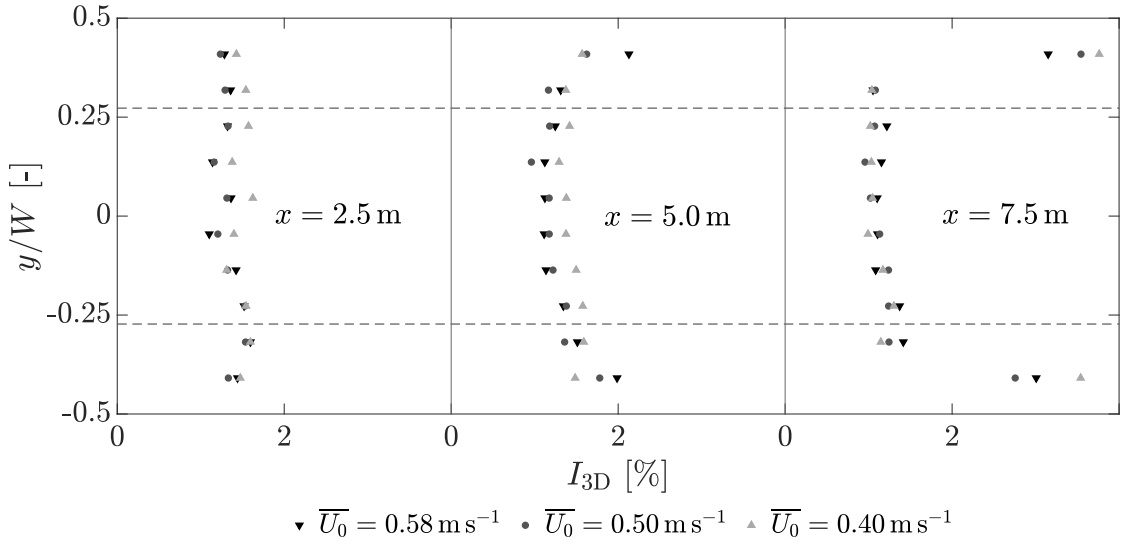


Figure 3.11: Cross-stream profiles of I_{3D} as a function of three reference flow velocities: $\overline{U_0} = 0.58\,\mathrm{m\,s^{-1}}$ (down-pointing triangles), $0.50\,\mathrm{m\,s^{-1}}$ (circles), and $0.40\,\mathrm{m\,s^{-1}}$ (up-pointing triangles), at three streamwise locations. The profiles comprise measurements at mid-water depth, as illustrated in Appendix A, Figure A.1. The intended swept area of the rotor is also shown (dashed).

Transect Profiling

For completeness, Figure 3.12 presents 2D contours of I_{3D} across the survey area at three streamwise locations, confirming two key observations. First, the turbulence in-

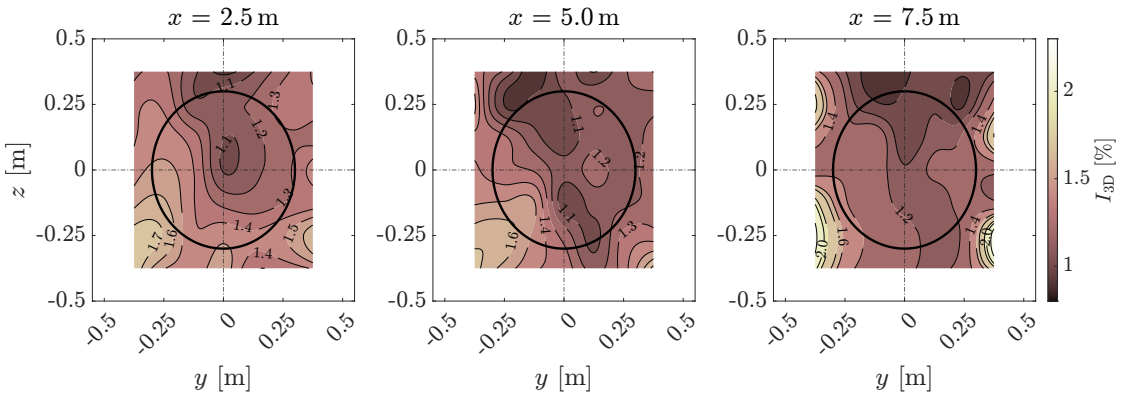


Figure 3.12: 2D contours of I_{3D} across three individual transects of the flume. The profiles correspond to the measurement co-ordinates illustrated in Figure 2.11. The box outline delineates the flume's cross section, and the black circle represents the intended swept area of the turbine rotor. Test conditions: $\overline{U_0} = 0.58\,\mathrm{m\,s^{-1}}$.

tensities remain broadly uniform across the rotor area, ranging between 0.97–1.64%. Second, regions of slightly higher turbulence intensity, between 2.0–2.5%, associated with increased velocity shear, emerge along both vertical edges of the survey area at $x = 7.5\,\mathrm{m}$, although they are unlikely to extend into the intended swept area of the rotor in future turbine tests.

Comparing the cross-stream and vertical turbulence intensities to the streamwise component provides insight into the flow anisotropy. The ratios at the centre of the working section, $I_u : I_v : I_w = 1.00 : 0.69 : 0.51$, are comparable to the widely cited values of $1 : 0.71 : 0.55$ from Nezu and Nakagawa [76] for 2D open-channel flows.

Probability Distributions

Establishing the best-fitting probability distributions for turbulence intensity helps to interpret experimental data by providing insights into the flow behaviour and its statistical properties. Eighteen probability distribution functions were evaluated for binned I_i data at the centre of the working section, with the best-fitting model identified by the highest log-likelihood value using maximum likelihood estimation[2] [80]. For the dataset shown in Figure 3.13, the log-logistic distribution

[2]The calculation was performed using a code developed by de Castro [79].

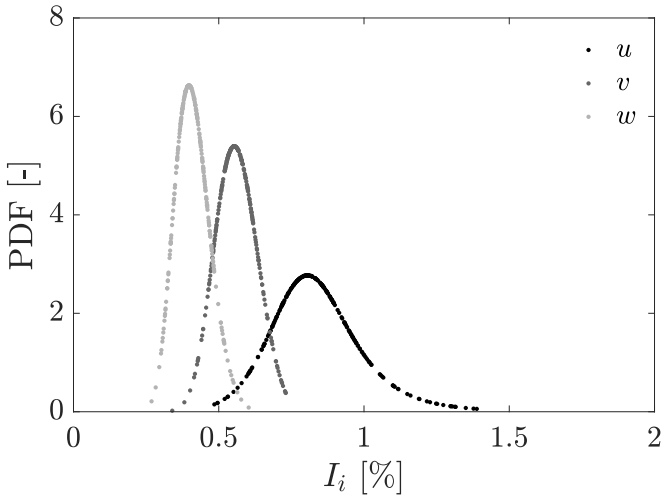


Figure 3.13: Probability density function (PDF) of I_u (black), I_v (dark grey), and I_w (light grey). The distributions were generated by subdividing an hour-long time series into 15-second data bins, before applying Equation 2.6 to evaluate I_i for each bin. PDF values were computed based on the highest log-likelihood value obtained through maximum likelihood estimation. Specifically, the log-logistic distribution provided the best fit for I_u, while the log-normal distribution was the best fit for both I_v and I_w. Test conditions: $\overline{U_0} = 0.57\,\mathrm{m\,s^{-1}}$; $(x, y, z) = (5, 0, 0)$.

best represents I_u, while the log-normal distribution provides the best fit for both I_v and I_w. However, the log-likelihood values of several distributions are comparable in each case, suggesting that the highest-ranking distribution may not represent a statistically significant result. Applying the Akaike information criterion yields a similar outcome.

While the log-normal distribution is frequently used in the analysis of turbulent flows, e.g. [81–83], the heavier tails of the log-logistic distribution better capture the occurrence of extreme events. This represents an unexpected result for controlled, highly uniform open-channel flows and suggests that infrequent but high-energy turbulent bursts can disproportionately influence the distribution. The source of these perturbations is unclear but may arise from irregularities in the flume's drivetrain, such as oscillations or vibrations, or subtle imperfections in the channel geometry, including uneven surfaces or asymmetries. These findings challenge the assumption that controlled flows are free from significant perturbations and highlight the need for closer examination of experimental setups to account for

sources of intermittent turbulence.

3.2.2 Reynolds Stresses

Reynolds' derivation of the mean-momentum equations [84] yields a symmetric second-order tensor that describes the apparent stresses arising from the additional momentum flux caused by velocity fluctuations in a turbulent flow [65]. For an incompressible fluid, the Reynolds stress tensor, denoted by $-\overline{u_i' u_j'}$, where i and j represent the directional velocity components, consists of three normal stresses (diagonal terms) and three shear stresses (off-diagonal terms). In the principal axes of the tensor, the normal stresses correspond to the eigenvalues, and the covariance terms disappear [65], indicating that shear stresses have no effect on the mean flow.

Klipp [85] emphasises the importance of precise alignment between the measurement co-ordinate system and the principal flow directions to prevent bias in the tensor, thereby ensuring accurate estimates of the Reynolds stresses. However, due to physical limitations in the experimental setup—primarily related to fixture alignment and equipment tolerances—the alignment in this study represented the best that could be achieved manually. Note that any uncertainty in estimates of the Reynolds stresses due to this potential misalignment has not been quantified. Furthermore, the results reported have not been corrected for noise, as the tensor is calculated directly from time-averaged velocities, effectively nullifying any potential signal contamination [60].

Depthwise Profiles

Figure 3.14 shows the streamwise evolution of $-\overline{u_i' u_j'}(z)$ along the vertical centre plane of the flume, together with the random error calculated from three repeated measurements. The profiles remain close to zero through the water column and exhibit minimal variation with downstream distance, reflecting the stable, highly uniform flow conditions through the working section.

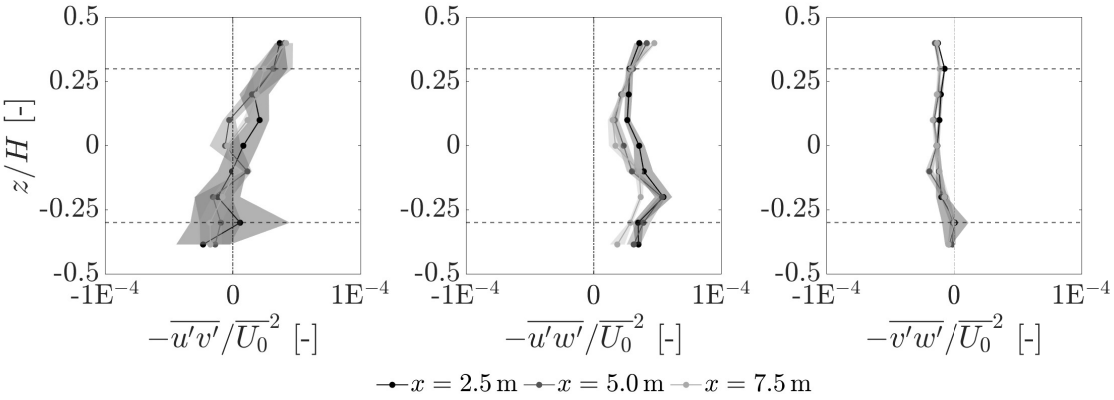


Figure 3.14: Depthwise profiles of the Reynolds shear stresses, normalised on $\overline{U_0}^2$, at three streamwise locations: $x = 2.5\,\mathrm{m}$ (black), 5.0 m (dark grey), and 7.5 m (light grey). The profiles comprise measurements along the flume's vertical centre plane, as illustrated in Appendix A, Figure A.1. The random error is represented by ± 1 SEM (shaded areas). Linear piecewise fits have been added as a visual aid. The intended swept area of the rotor is also shown (dashed) along with a dash-dotted line indicating zero shear stress. A linear scale is applied to the x-axis. Test conditions: $\overline{U_0} = 0.58\,\mathrm{m\,s^{-1}}$.

Classical depthwise profiles of the Reynolds shear stresses in a 2D open-channel flow typically depart from zero at the boundary, increase to a peak value within the viscous wall region, before decreasing linearly with wall-normal distance as the mean velocity shear asymptotes to zero [65]. The profiles presented do not exhibit this behaviour for several reasons. First, the $\overline{U}(z)$ profiles deviate from those of fully developed channel flow, maintaining a modest negative shear through the measurement domain. Second, the deepest measurement co-ordinate, z/H = -0.385, is located 115 mm above the channel bed, beyond the region of amplified turbulence in the viscous wall region. Third, a potential misalignment between the ADV's co-ordinate system and the principal flow axes may explain the small deviations from zero stress, particularly towards the top of the water column.

The highest shear stress magnitudes are observed in the $-\overline{u'w'}$ component, indicating shearing in the xz-plane. This aligns with the primary flow direction and the modest vertical velocity gradient noted previously in Section 3.1.1. In contrast, the $-\overline{v'w'}$ component consistently remains an order of magnitude lower than both the $-\overline{u'v'}$ and $-\overline{u'w'}$ components, reflecting the limited momentum

exchange between lateral and vertical motions.

The largest source of measurement uncertainty relates to the random error, which can be several times the magnitude of $-\overline{u_i' u_j'}/\overline{U_0}^2$, resulting in significant overall uncertainty. Although Figure 3.14 does not visually convey substantial random error relative to the mean values, the small magnitude of the non-dimensional shear stresses, $\mathcal{O}(10^{-5})$, causes the random error to contribute disproportionately to the combined uncertainty. In contrast, the systematic error, also determined by propagating the velocity error, equates to just 2.8% of the non-dimensional shear stresses. Given the inherent sensitivity of second-order statistics to fluctuations in the sampling records, increasing the number of repeated measurements is a prudent strategy for reducing random error in Reynolds stress estimates.

3.2.3 Integral Scales

The integral scales of turbulence characterise the spatial and temporal extent of the largest coherent structures in a turbulent flow, corresponding to the most energetic structures in the lower-frequency range of the turbulence spectrum.

Depthwise Profiles

Figure 3.15 shows the streamwise evolution of $\Lambda_i(z)$ along the vertical centre plane of the flume, together with the random error calculated from three repeated measurements. Also shown is an empirical relationship for $\Lambda_u(z)$, derived by Nezu and Nakagawa [76] for 2D open-channel flows, given by:

$$\frac{\Lambda_u}{H} = \begin{cases} \sqrt{z/H}, & \text{for } z/H \leq 0.6 \\ 0.77, & \text{for } z/H > 0.6, \end{cases} \tag{3.2}$$

where $z/H \in \{0, 1\}$. Compared to canonical open-channel flow experiments, the measured distributions deviate from the expected empirical relationship. For instance, the largest length scales are observed in the lower half of the water column,

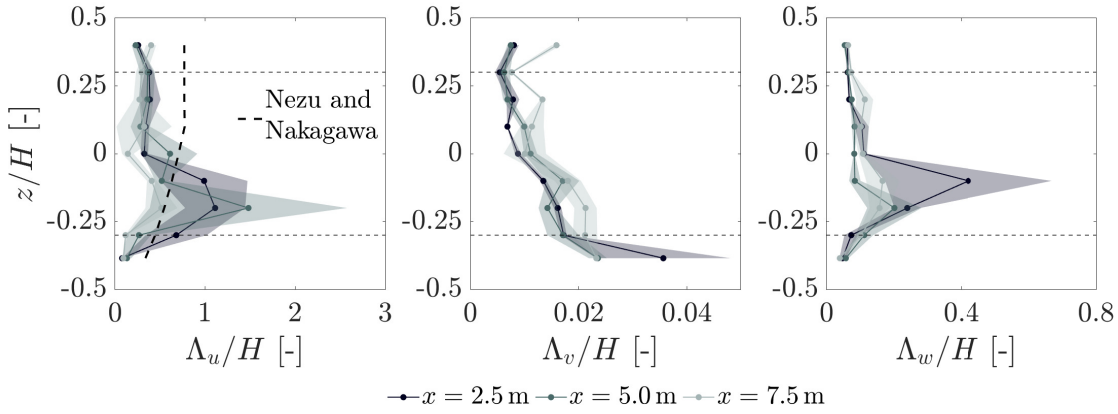


Figure 3.15: Depthwise profiles of Λ_i, normalised on the flow depth, at three streamwise locations: $x = 2.5\,\mathrm{m}$ (black), $5.0\,\mathrm{m}$ (dark grey), and $7.5\,\mathrm{m}$ (light grey). The profiles comprise measurements along the flume's vertical centre plane, as illustrated in Appendix A, Figure A.1. The random error is represented by $\pm 1\,\mathrm{SEM}$ (shaded areas). Linear piecewise fits have been added as a visual aid. The intended swept area of the rotor is also shown (grey dashed), along with the empirically derived relationship by Nezu and Nakagawa (thick dashed). Test conditions: $\overline{U_0} = 0.58\,\mathrm{m\,s^{-1}}$.

where the mean flow speeds are slightly higher. Additional factors contributing to this discrepancy, such as test conditions, will not be discussed further.

The results reveal greater variation through the water column in the non-dimensional streamwise (0.08–1.48) and vertical (0.04–0.42) components, compared to the cross-stream component (0.01–0.04). Several factors likely contribute to these complex spatial distributions and the pronounced inter-profile variation, with high signal noise being a major contributor. Noise-dominated signals increase the likelihood of signal decorrelation, biasing the integral scales towards lower values. Additionally, although less critical, the systematic error associated with integrating the autocorrelation coefficient up to the first zero-crossing adds further error in calculations of the integral scales.

While the reported length scales appear compatible with the channel geometry [72], they also indicate that certain regions of the flow are more correlated than others, suggesting that the flow is not statistically stationary, contrary to initial findings (see Section 2.2.2). This non-stationarity implies that, in future turbine tests, the rotor is likely to encounter substantial variation in the turbine's approach

flow, with differences in length scales potentially exceeding 1 m, equivalent to more than three times the rotor radius. Such variation could cause portions of the rotor to sample large, coherent eddies over multiple rotations, leading to pronounced fluctuations in rotor loading [86].

For the uncertainty analysis, the systematic error in the velocity measurements introduces a proportional error of $0.03\Lambda_i$, after accounting for the contributions from both $\rho_{ii}(\tau)$ and $\overline{u}$ (see Equations 2.7–2.9). The broad variability observed across repeated measurements, as illustrated in Figure 3.15, results in random errors that exceed the corresponding systematic errors by factors of nine for Λ_u, four for Λ_v, and five for Λ_w, based on median values across the measurement domain. When quantifying the expanded uncertainty, the width of the 95% confidence intervals for both the streamwise and vertical components often extends several times beyond the corresponding length scale, suggesting unrealistically large or non-physical values. This indicates that an alternative approach may be needed to quantify the integral scales more accurately, particularly for measurements dominated by noise.

Figure 3.16 shows the streamwise evolution of $\Lambda_u(z)$ as a function of $\overline{U_0}$ along the flume's vertical centre plane. While the length scales increase proportionally with $\overline{U_0}$, this results in reduced spatial uniformity through the water column. The increased uniformity at lower flow speeds is reflected in narrower 95% confidence intervals for Λ_u, when normalised on depth-averaged values (not shown). For instance, at $\overline{U_0} = 0.57\,\mathrm{m\,s^{-1}}$, the 95% confidence interval, when averaged across the measurement domain, is ±59.06%, whereas at $\overline{U_0} = 0.40\,\mathrm{m\,s^{-1}}$, it narrows to ±43.48%, although this still represents significant variation through the water column.

3.3 Velocity Spectra

The exact frequencies that delineate each region of the power spectra, as described in Section 2.2.5, are not always identifiable. For instance, the dissipation range may

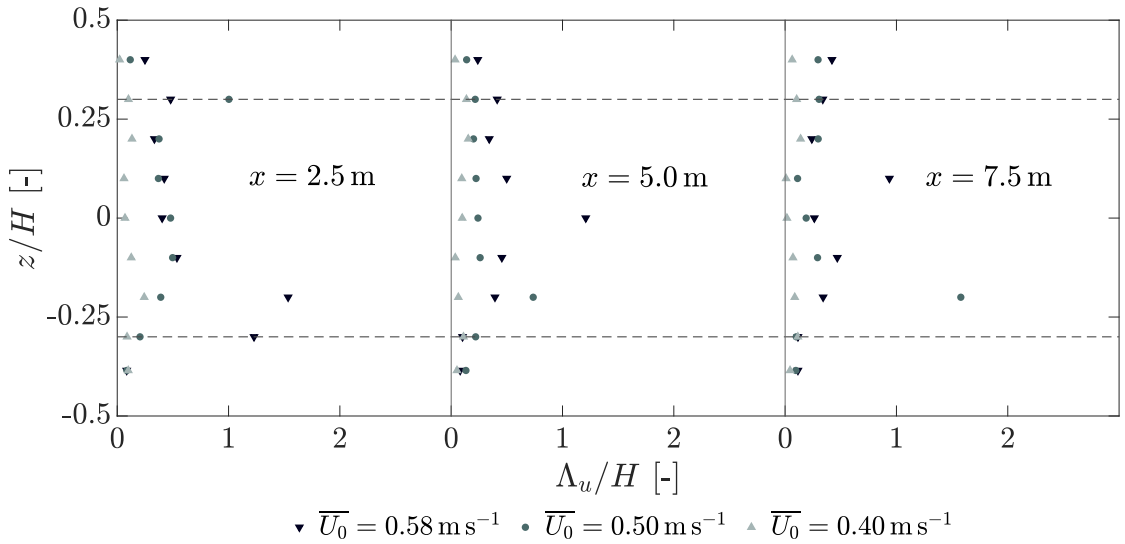


Figure 3.16: Depthwise profiles of Λ_u, normalised on the flow depth, as a function of three reference flow velocities: $\overline{U_0} = 0.58\,\mathrm{m\,s^{-1}}$ (down-pointing triangles), $0.50\,\mathrm{m\,s^{-1}}$ (circles), and $0.40\,\mathrm{m\,s^{-1}}$ (up-pointing triangles), at three streamwise locations. The profiles comprise measurements along the flume's vertical centre plane, as illustrated in Appendix A, Figure A.1. The intended swept area of the rotor is also shown (dashed).

be obscured by signal noise, leading to spectral flattening at higher frequencies. This effect is particularly pronounced in the streamwise and cross-stream velocity spectra shown in Figure 2.10. At the lower end of the frequency range, the spectral energy of the streamwise velocities exceeds that of the orthogonal components by at least one order of magnitude. This is an expected result for controlled open-channel flow conditions and reflects the flow's tendency towards one-dimensionality. The deviation of the cross-stream velocity spectrum from the $f^{-5/3}$ decay gradient suggests that the signal may be disproportionately contaminated by noise in low turbulence conditions. This is in contrast to the vertical velocity spectrum, which is much less sensitive to noise due to the ADV beam geometry [60].

Figure 3.17 compares non-dimensional PSD estimates of the i^{th} velocity fluctuations, calculated using the Welch method, with predictions from the semi-empirical von Kármán model. While the spectral estimates exhibit broad qualitative agreement, deviations increase significantly beyond a threshold non-dimensional frequency, likely due to instrument noise, particularly in the streamwise and cross-

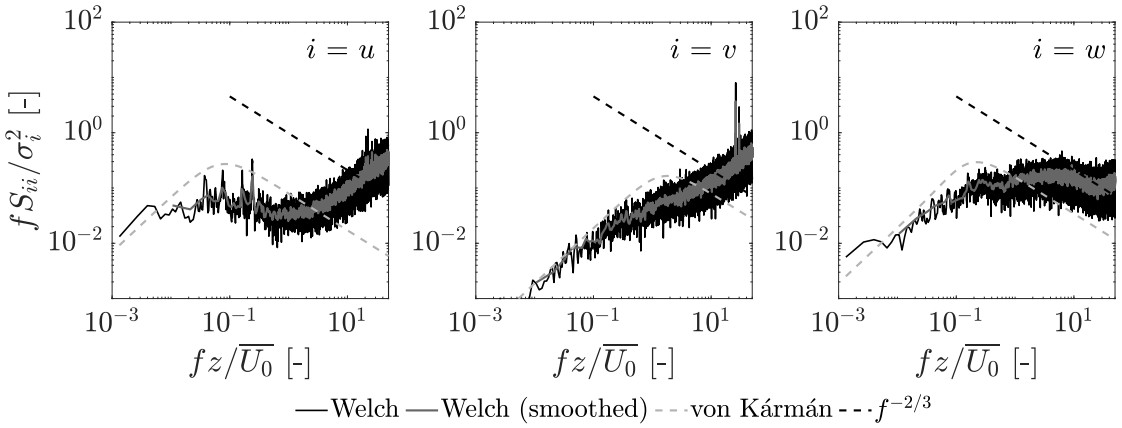


Figure 3.17: Non-dimensional PSD estimates of the i^{th} velocity fluctuations, calculated using the Welch method (black solid), are compared with empirical predictions from the von Kármán model (grey dashed) as a function of non-dimensional frequency. Also shown are a bin-averaged representation of the Welch power spectra (grey solid) and Kolmogorov's constant of proportionality, $f^{-2/3}$ (black dashed). Test conditions: $\overline{U_0} = 0.57\,\mathrm{m\,s^{-1}}$; $(x, y, z) = (5, 0, 0)$.

stream velocities. For the data shown, estimates of the integral length scales, calculated using non-linear regression, yield relative differences of -34.2% for Λ_u, 23.5% for Λ_v, and 16.8% for Λ_w, compared to those obtained using the autocorrelation method described in Section 2.2.5. These discrepancies, illustrated in the figure by the misalignment of the spectra within the energy-containing range, can be attributed to the assumption of homogeneous, isotropic turbulence in the von Kármán model, which is unsuitable for the flow under consideration (see Section 3.2.1). This conclusion aligns with the findings of Naberezhnykh *et al.* [87], who applied the model to field data collected at two tidal test sites.

3.4 Summary

The mean flow and turbulence characteristics of a recirculating water flume have been characterised, in preparation for the model-scale testing of a horizontal axis tidal stream turbine. The investigation adhered to the methodology detailed in Chapter 2, which accounts for biases in the test setup and measurement uncertainty.

The time-averaged velocity profiles demonstrated high spatial uniformity across

different reference flow velocities, with deviations of $< 1\%$ at the 95% confidence level. Notable features of the velocity fields included a modest negative vertical velocity shear gradient that persisted through the measurement domain and a slight flow acceleration of approximately $0.02\overline{U_0}$. Peak streamwise velocities were observed within 175 mm of the flume's sidewalls, likely related to how the flow was returned to the working section. Although the flume's low aspect ratio ($W/H = 1.1$) may be more susceptible to sidewall effects under certain conditions, no significant distortions to the core flow were observed. Furthermore, the free surface appeared stable across a range of flow speeds, with no significant deformations observed.

A high degree of uniformity was also apparent in the turbulence intensities, which ranged from 1–2% across the intended swept area of the turbine rotor. At the furthest downstream location, and along the vertical edges of the survey area, slightly higher values of around 3% were observed, indicating the presence of shear layers, most likely due to boundary layer trips at the interfaces between the non-co-planar glass panes along the flume's sidewalls. The shear layers are unlikely to penetrate the swept area of the rotor in future turbine tests. At the centre of the working section, the flow anisotropy ($I_u : I_v : I_w = 1.00 : 0.69 : 0.51$) was consistent with observations from canonical open-channel flow experiments, while the best-fit probability distributions for the turbulence intensities were the log-logistic distribution for I_u and the log-normal distribution for I_v and I_w. This suggests that high-energy turbulent bursts disproportionately influence the streamwise component. The source of these perturbations is unclear but likely results from periodic shedding events related to the flume's geometric features.

Depthwise profiles of the Reynolds shear stresses showed minimal variation through the water column, suggesting that the measurement co-ordinates were likely beyond the influence of boundary-induced shear stresses. Measurement uncertainty was predominantly affected by the random error, which could be several times the magnitude of $-\overline{u_i' u_j'}/\overline{U_0}^2$, leading to significant overall uncertainty. To reduce the random error associated with Reynolds stresses estimates, increasing the number of

repeated measurements is recommended, although this would necessitate additional testing time.

The streamwise integral length scales were found to be on the order of the channel height and width, with significant variability observed across repeated measurements, particularly in the streamwise and vertical components. This was likely an artefact of high signal noise in low turbulence conditions, leading to decorrelation in the sampling records. The wide 95% confidence intervals for the expanded uncertainty often extended to several times the corresponding length scale, indicating unrealistically large or non-physical values. This suggests that an alternative method may be required to achieve more accurate quantification of the integral scales and to reduce the significant random error, particularly for flow measurements disproportionately affected by noise.

In the energy-containing region of the power spectra, the spectral energy of the streamwise velocity fluctuations exceeded that of the orthogonal components by at least one order of magnitude. This is consistent with controlled open-channel flow conditions and reflects the flow's tendency towards one-dimensionality. However, the combination of flow anisotropy and high signal noise rendered the von Kármán model unsuitable for generating more accurate PSD estimates in clean flow conditions.

While the flume's high velocity uniformity and controlled low turbulence levels provide a stable and reliable basis for evaluating model-scale turbine response, they do not reflect the more unsteady flows often observed in the marine environment. Therefore, to isolate the effects of specific in-field flow phenomena on a model-scale device, additional mechanisms, such as a wave-maker or turbulence-generating grid may be required depending on the parameter space of interest.

CHAPTER 4

Generation, Control, and Characterisation of Onset Turbulence

Careful characterisation of freestream turbulence in a laboratory setting provides an opportunity to elucidate key aspects of the unsteady hydrodynamics experienced by tidal stream rotors. This chapter focuses on the generation and control of freestream turbulence, laying the foundation for future experiments to evaluate the impact of selected turbulence parameters on a model-scale rotor.

This chapter comprises two key components: (i) a description of a methodology used to generate and control freestream turbulence in a hydraulic flume, and (ii) a detailed characterisation of selected turbulent flows, intended for the model-scale testing of a horizontal axis tidal stream turbine.

The chapter begins with an overview of previously tested methods for generating freestream turbulence in laboratory-based experiments, followed by a detailed description of the experimental methodology applied in this study. Preliminary flow measurements along the flume's centreline are then presented, followed by an examination of the parameter space relevant to future turbine tests, additional flow characterisation results, and finally, a discussion of the investigation's limitations.

4.1 Historical Approaches

Grid-generated turbulence has long played a pivotal role in the advancement of various aerodynamic applications, including bluff body mechanics [88], aircraft design [89], and wind energy [90], among others. The literature commonly categorises turbulence grids into three main families: (i) active [91], (ii) fractal [92], and (iii) passive [32], the focus of the present study.

Since the pioneering works of Simmons and Salter [93] in the 1930s, passive turbulence grids have offered a simple and cost-effective means of approximating homogeneous, isotropic turbulence. In the near-field region, turbulence is generated as a result of shearing between accelerated flow through porous regions of the grid and wakes shed from the grid members. Beyond the production region, the flow transitions towards a homogeneous, isotropic state at approximately 20 mesh sizes[1] downstream [94]. Additionally, the dominant vortical structures shed from the grid grow in size [32], driven by the redistribution of turbulent kinetic energy towards the integral scales. The literature suggests that the turbulence intensity and integral length scales are not only the most common metrics for characterising freestream turbulence but also the most practical parameters to modify.

While there is a wealth of literature dedicated to grid-generated turbulence in wind tunnels, relatively few experimental studies have focused on turbulence grids in open-channel flows. Notable examples include the work of Murzyn and Bélorgey [95] and Yao *et al.* [96], both of whom sought to improve the understanding of sediment transport phenomena, while other studies have focused on the development of numerical models, such as Panda *et al.* [97].

In tidal energy research, relatively few researchers have employed turbulence grids in laboratory-based studies. Experimental investigations involving elevated turbulence can be broadly categorised into two main areas: (i) the effect on model-

[1]The mesh size is defined as the centre-to-centre spacing between grid members, as shown in Figure 4.2c.

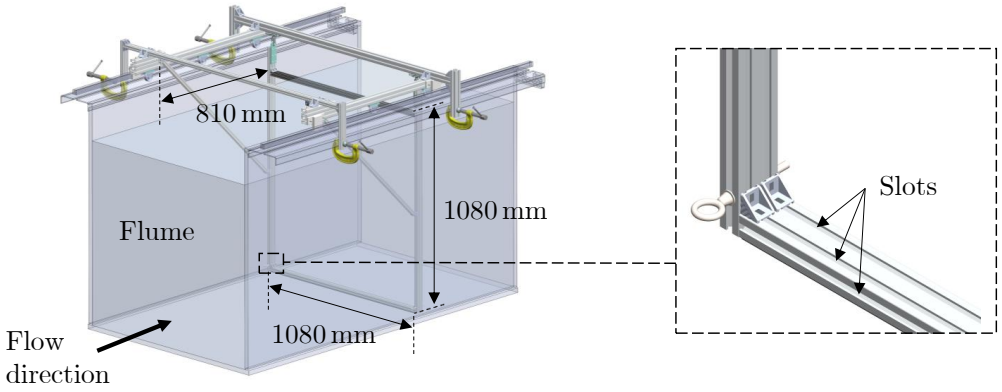


Figure 4.1: Illustration of the outer frame in its lowered (submerged) position along with its supporting structure on top of the flume. The yz-plane of the frame is located 1.5 m from the inlet to the working section. The inset image shows the potential attachment points along the outer frame.

scale rotor loading [50], and (ii) its influence on downstream wake characteristics [98]. For further discussion, the reader is referred to Section 6.3.2.

4.2 Turbulence Generation Methodology

Experimental Setup

To enable a flexible approach for testing parameter spaces of interest, an outer frame capable of supporting a variety of flow-resisting geometries was developed (see Figure 4.1). The frame was constructed from standardised aluminium extrusions, providing rigidity, corrosion resistance, and compatibility with various fixing elements. In this investigation, all flow-resisting geometries were constructed using standardised aluminum extrusions (20×20 mm cross section), enabling efficient adjustments to the grid geometry as required. Since square bars were used, the likelihood of flow separation was higher than with circular rods [99]; however, this effect was not quantified in the present study. A 10 mm clearance was maintained between the frame and the glass panes, with a soft elastomer profile added along the outer faces to dampen any potential contact. Other design considerations

for the outer frame included resistance to torsion under hydrodynamic loading, streamwise positional adjustment, geometric alignment with the flume, and ease of deployment and retrieval.

The basic geometry of a square turbulence grid, defined by its bar width, W_{bar}, and mesh size, M, as shown in Figure 4.2c, is related to the grid's porosity, θ, by:

$$\theta = \left(1 - \frac{W_{\text{bar}}}{M}\right)^2. \tag{4.1}$$

In the near-field region, defined as 5–10M downstream of the grid plane, much of the turbulent kinetic energy is concentrated at a wavelength $\mathcal{O}(M)$ [94], with the dominant length scales depending primarily on the bar width [32]. It follows, therefore, that by controlling the bar width the integral scales can also be controlled. Furthermore, since downstream turbulence production is governed by the velocity shear, which is itself a function of the mesh size, adjusting the mesh size provides a means to control the downstream turbulence, provided that the bar width remains constant. To test this approach, four different turbulence grids with square mesh sizes[2] were examined, with schematics shown in Figure 4.2 and the corresponding geometric parameters listed in Table 4.1. Also included in the table are three examples of square turbulence grids commonly cited in the literature, noting that the mesh sizes and bar widths of the grids used in this study were significantly larger than those cited.

The direction of the experimental campaign was guided by three key objectives:

i. To evaluate the influence of grid geometry on the mean downstream flow and turbulence characteristics.

ii. To define a parameter space that will reasonably demonstrate the effects of turbulence intensity and the streamwise integral length scales on the unsteady loading response of a model-scale rotor in future turbine tests.

[2] An artefact of this approach was that the outer frame, also square, protruded beyond the free surface. This deviates from setups in wind tunnels, where the perimeter of the flow obstruction typically occupies the full extent of the tunnel cross section [100].

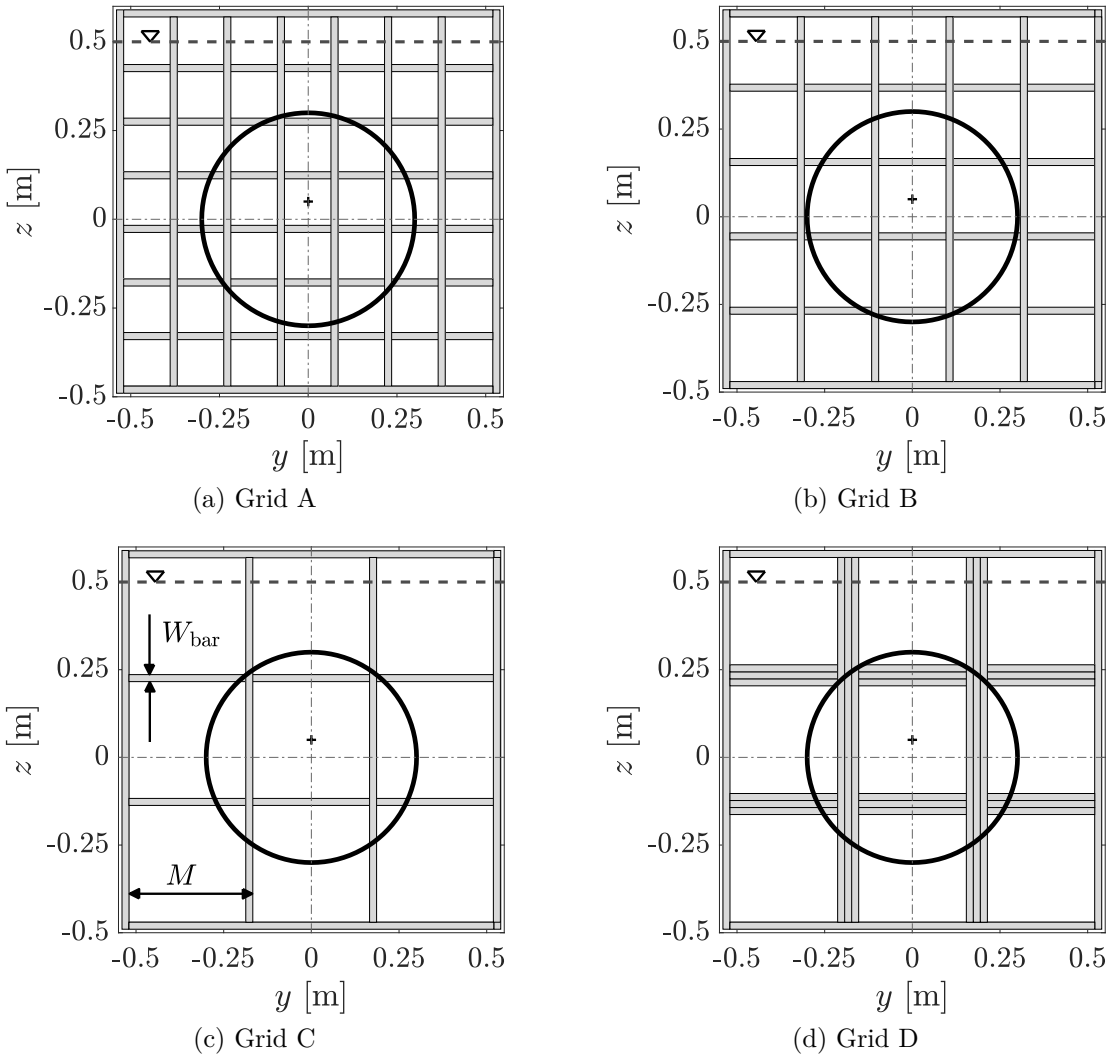


Figure 4.2: Schematics of grids A–D. Also shown are the intended swept area of the rotor (black circle), the still water level (dashed), the geometrical centre of each grid (black cross), and both centre planes of the channel cross section (dash-dotted). The grid mesh size, M, and bar width, W_{bar} are indicated in c). Each grid comprises a bi-planar arrangement of square bars, evenly distributed in both directions to ensure the flume's centreline, and hence the ADV's sampling volume, were not directly aligned with any of the bars.

iii. To characterise the flow field in detail at three streamwise locations of interest, one of which aligns with the intended rotor plane.

To address Objective i, preliminary measurements were conducted along the flume's centreline, in line with the turbine's intended hub height. While this

Grid	M [m]	W_{bar} [m]	θ [%]	M/H [-]
A	0.151	0.020	73.9	0.151
B	0.212	0.020	80.5	0.212
C	0.353	0.020	87.3	0.353
D	0.367	0.060	73.9	0.367
Krogstad and Davidson [101]	0.040	0.010	56.0	0.022
Yao *et al.* [96]	0.034	0.006[a]	66.0	0.007
Murzyn and Bélorgey [95]	0.033	0.006	67.0	0.047

Table 4.1: Summary of grid geometries for grids A–D. The bar width of grid D was achieved by combining three square bars side by side, as illustrated in Figure 4.2d. Also listed are the geometries of three turbulence grids widely cited in the literature.

[a]This value refers to the diameter of the circular rods used in this grid.

approach does not capture the flow dynamics across the entire survey area, centreline measurements are commonly used in wind tunnel experiments as a time-efficient and pragmatic solution for developing insights into the core region of the flow [100], where boundary effects are minimal, and for facilitating comparisons with theoretical models. The results of this analysis, presented in Section 4.3, inform the approach for Objectives ii and iii.

Refinements to Flow Characterisation Methodology

To accommodate the increased turbulence levels in the flume, several adjustments were made to the experimental methodology detailed in Chapter 2.

- The correction method proposed by Romagnoli *et al.* [74] was applied to calculations of the integral scales, given the significantly lower noise contribution to $\sigma^2_{\text{meas},i}$ ($< 10\%$; cf. Table 2.2), which was due to the higher flow-related proportion of the velocity measurements.
- 2D rotational corrections were not applied to the measured velocities (see Section 2.2.4) due to significant flow deflection and non-uniformity in the near-field region of each grid, potentially negating some of the assumptions required for the correction.

- Close to the grid plane, the ADV settings were reconfigured to accommodate the increased range of the velocity fluctuations. The NVR, transmit pulse length, and sampling volume height were all adjusted according to the downstream distance from the grid under test. Specifically, larger NVRs of $\pm 1.0\,\mathrm{m\,s^{-1}}$ and $\pm 2.5\,\mathrm{m\,s^{-1}}$ were used[3], while the transmit pulse length and sampling volume height were set to 2.4 mm and 9.1 mm, respectively, consistent with the approach of Kazemi *et al.* [102], who reported more accurate flow metrics in elevated turbulence using a larger sampling volume.

4.3 Centreline Measurements

The initial phase of the characterisation involved preliminary flow mapping along the centreline of the flume's working section. Centreline measurements are a fundamental component of studies on grid-generated turbulence and are used here not only to characterise the downstream turbulence but also to define a suitable parameter space for future turbine tests.

4.3.1 Mean Velocities

Figure 4.3 presents the streamwise evolution of $\overline{u_i}$ as a function of grid geometry. For grids B–D, the largest magnitudes of the time-averaged streamwise and cross-stream velocities are observed close to the grids, at $x - x_\mathrm{F} < 0.5\,\mathrm{m}$ (x_F indicates the streamwise location of the outer frame), due to the constraining effect of the grids' solidities on the flow. In contrast, the streamwise flow profile of grid A exhibits a steady acceleration of approximately 6% along the centreline, nearly double that observed in clean flow. The difference in flow behaviours between grid A and grids B–D is likely due to the 30 mm vertical offset between the centre

[3]The incremental signal noise introduced by a larger NVR was accounted for in calculations of the turbulence statistics. A comparison of measurements taken $10M$ downstream of each grid revealed negligible differences between statistics derived using modified ADV settings and those derived using the settings described in Section 2.2.1.

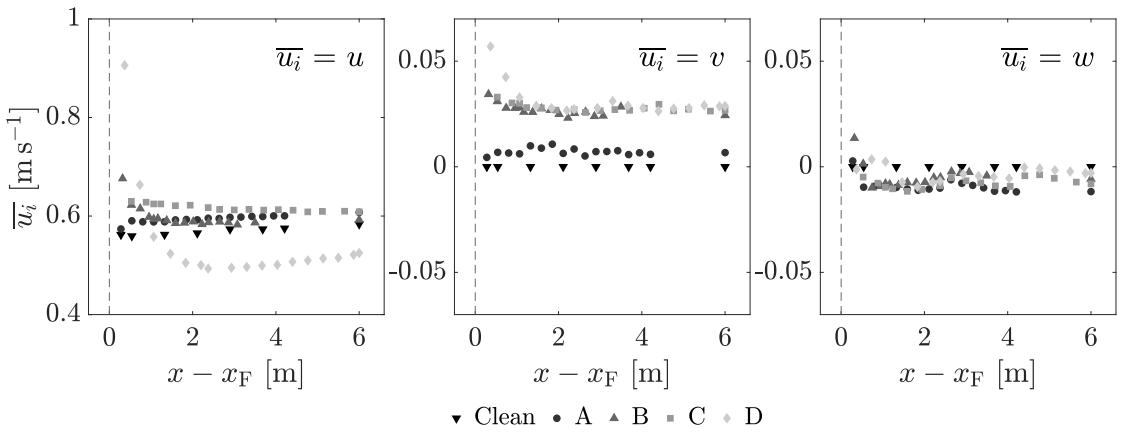


Figure 4.3: Streamwise evolution of $\overline{u_i}$ along the flume's centreline. Clean flow measurements (down-pointing triangles) are compared with measurements taken downstream of four turbulence grids defined in Table 4.1: A (circles), B (up-pointing triangles), C (squares), and D (diamonds). The x-axis indicates the streamwise location relative to the outer frame (dashed). Test conditions: $\overline{U_\infty} = 0.57\,\mathrm{m\,s^{-1}}$.

of each grid and the centre of the channel (see Figure 4.2), which biases the position of the ADV's sampling volume towards the nearest horizontal bar. This effect is particularly pronounced for grid A due to the smaller mesh size, which increases the likelihood that the sampled flow in the near-field region is more affected by the wake of this bar, resulting in relatively lower streamwise velocities.

Grids B and C yield similar velocity profiles, although the smaller mesh size of grid B results in a slightly sharper acceleration and deceleration in the near-field region. In contrast, grid D induces the most pronounced effect on both the streamwise and cross-stream velocities compared to the other grids, most notably grid A, which shares the same porosity. The significant variation in $\overline{u}(x)$ for grid D—reaching $0.72\overline{U_\infty}$, compared to $0.04\overline{U_\infty}$ for grid A, both within 2.4 m of the grid plane—further highlights the influence of the wider bars and the difference in local flow dynamics between grids A and D. Note that $\overline{U_\infty}$ represents the time-averaged freestream velocity, equivalent to $\overline{U_0}$ in the clean flow case[4].

Consistent with the clean flow characterisation, both the time-averaged cross-stream and vertical velocities are at least one order of magnitude smaller than the

[4]The clean flow case represents the baseline against which all other flows are compared, with the same flume duty applied across all test cases.

dominant streamwise component. However, unlike the vertical velocities, which broadly converge to within a narrow range of $0.04\overline{U_\infty}$, the cross-stream velocities exhibit greater variation, ranging up to $0.09\overline{U_\infty}$, likely due to higher lateral deflection of the flow. While the disparity between the $\overline{v}(x)$ profile of grid A and those of the other grids may be attributed to differences in local flow dynamics, it may also stem from unintended variation in the probe orientation between test cases, although this remains uncertain.

In the absence of a 2D rotational correction for the flow downstream of the turbulence grids, non-zero cross-stream and vertical velocities may also reflect unintended misalignment of the ADV probe. Assuming these velocities to be entirely due to probe misalignment, the maximum velocity magnitudes correspond to angular offsets of 2.0° and 3.7° for pitch and yaw, respectively, consistent with the clean flow analysis.

The expanded uncertainty for $\overline{U_{\mathrm{CL}}}$ yields a 95% confidence interval identical to that observed in clean flow, $\mathrm{CI}_{0.95}(\overline{U}) = \pm 0.03\,\mathrm{m\,s^{-1}}$, highlighting the insensitivity of the random error to turbulence generation. This insensitivity to the flow conditions is further supported by the invariance of the non-dimensional velocity profiles across different reference flow velocities, the results of which are omitted here for brevity.

4.3.2 Anisotropy

While turbulence grids are often used to approximate homogeneous, isotropic turbulence, experimental studies have consistently shown that grid-generated turbulence deviates from both homogeneity and isotropy [100, 103]. Figure 4.4 presents centreline distributions of flow anisotropy, defined here as the ratios of the noise-corrected standard deviation of the cross-stream and vertical velocity fluctuations, respectively, to that of the streamwise component.

The centreline distributions of σ_v/σ_u generally trend towards unity for grids A, B, and D, suggesting that flow anisotropy decreases with downstream distance. For $x - x_{\mathrm{F}} > 2.2\,\mathrm{m}$, σ_v/σ_u values across all turbulence grids fluctuate

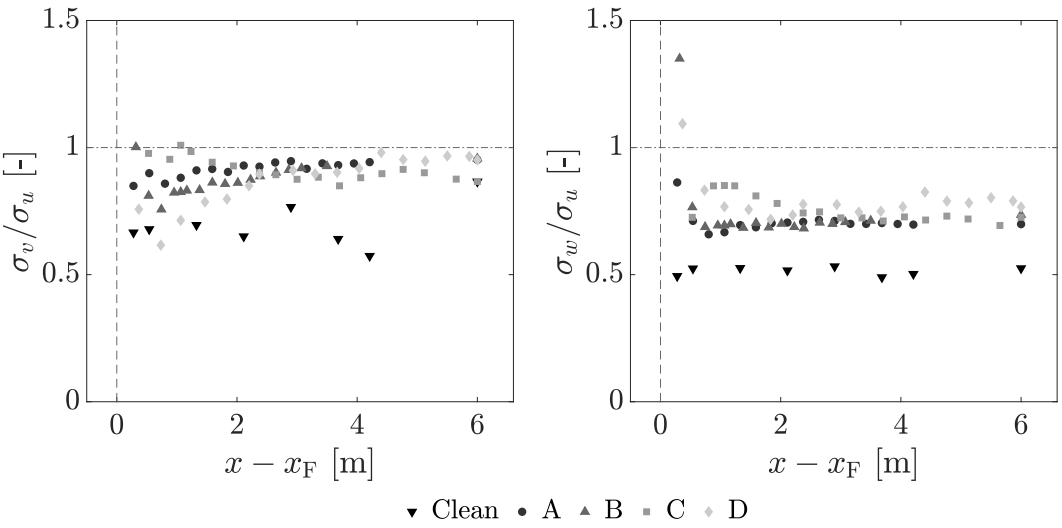


Figure 4.4: Streamwise evolution of flow anisotropy, σ_i/σ_u, along the flume's centreline. Clean flow measurements (down-pointing triangles) are compared with measurements taken downstream of four turbulence grids defined in Table 4.1: A (circles), B (up-pointing triangles), C (squares), and D (diamonds). Note that σ_i has been corrected for noise as described in Section 2.2.5. The dash-dotted line indicates the isotropic relation and the x-axis indicates the streamwise location relative to the outer frame (dashed). Test conditions: $\overline{U_\infty} = 0.57\,\mathrm{m\,s^{-1}}$.

between 0.85–0.98. Closer to the grid plane, however, deviations from this trend are observed for grids B and C, where σ_v/σ_u values reach unity, suggesting that the horizontal and streamwise velocity fluctuations become equal in magnitude within the production region. In contrast to grids A, B, and D, σ_v/σ_u values for grid C trend downwards away from unity with downstream distance, providing an unexpected result.

When examining the corresponding distributions for the vertical velocities, the fluctuations are typically smaller in magnitude compared to the horizontal components, with σ_w/σ_u values across all grid geometries converging to a range of 0.68–0.82 at $x - x_F > 1.5\,\mathrm{m}$. The sharp spike in σ_w/σ_u values within 0.5 m of the grid plane suggests a temporary energy flux in the vertical direction, likely driven by more distorted turbulence in the near-field region [104].

Although flow anisotropy is reduced across all turbulence grids compared to the clean flow case, the observed ratios still deviate significantly from ideal isotropic

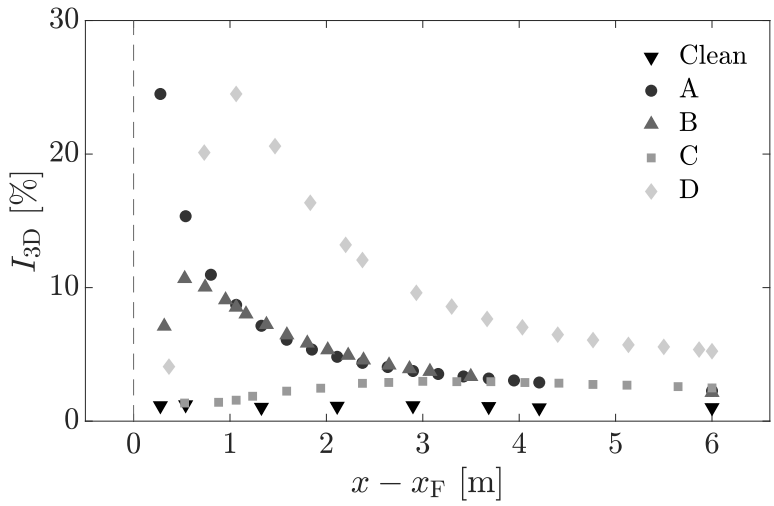


Figure 4.5: Streamwise evolution of I_{3D} along the flume's centreline. Clean flow measurements (down-pointing triangles) are compared with measurements taken downstream of four turbulence grids defined in Table 4.1: A (circles), B (up-pointing triangles), C (squares), and D (diamonds). The x-axis indicates the streamwise location relative to the outer frame (dashed). Test conditions: $\overline{U_\infty} = 0.57\,\mathrm{m\,s^{-1}}$.

conditions. One potential explanation is that the grid geometries, as summarised in Table 4.1, do not satisfy the empirically derived criterion of $M/W < 0.1$, which Roach [32] suggests is required for achieving flow homogeneity and isotropy.

4.3.3 Turbulence Intensities

Quantifying I_{3D} along the flume's centreline provides insight into the locations of turbulence production and decay relative to the grid plane. As demonstrated by Ting [94] in wind tunnel experiments, the magnitude of the turbulent velocity fluctuations peaks just downstream of the maximum time-averaged streamwise velocities, which occur very close to the grid plane, at $x - x_F \leq 1M$. A similar result is observed for grids B–D in Figures 4.3 and 4.5, where the streamwise velocities peak within $1.5M$ of the grid plane, while the corresponding values of I_{3D} peak further downstream, between 2–$8M$. The absence of a near-field velocity spike immediately downstream of grid A supports the hypothesis that the sampled flow was more affected by the wake of a nearby horizontal bar.

Figure 4.5 illustrates the transient nature of the turbulence as it decays beyond

the production region, the end of which is identified by the maxima of I_{3D} [94]. Both the magnitudes of the velocity fluctuations and the location where the production region ends reveal a dependency on grid geometry. The results suggest that as the mesh size increases for a given bar width, turbulence production weakens, and the production region shifts further downstream, reflecting the increased distance required for the wakes of the bars to converge. Interestingly, the downstream decay profiles of grids A and B are remarkably similar at $x - x_F > 1M$, indicating that beyond the production region, grid porosity has little impact on the turbulence when the bar width remains constant. When grid porosity is held constant, as with grids A and D, the larger bar width of grid D injects more kinetic energy into the flow, offsetting the effect of the increased mesh size and resulting in a similar maximum turbulence intensity of $I_{3D} \approx 24\%$. As the turbulence decays downstream, the turbulence intensities converge to levels commensurate with the bar width: $I_{3D} \approx 2.2\%$ for grids A–C and $I_{3D} \approx 5.3\%$ for grid D.

Due to the elevated turbulence in the flume compared to the clean flow case, the corresponding noise corrections to I_i are significantly lower than the values shown in Figure 2.12. Although not shown here for brevity, the corrections ranged from 6–8% for I_u and I_v, and approximately 1% for I_w, reflecting the much higher proportion of turbulence in $\sigma^2_{\text{meas},i}$ relative to signal noise.

Consistent with the clean flow analysis, the expanded uncertainty scales with the level of turbulence generated, peaking at $\delta_{\text{exp}} = 24.53 \pm 1.87\%$ (expressed as an absolute value) at the 95% confidence level, 0.3 m downstream of grid A. Within $6M$ of the grid plane, the 95% confidence interval narrows to $< 1\%$ across all grid geometries. Additionally, the turbulence intensities were found to be invariant across different reference flow velocities, although the results are omitted here for brevity.

4.3.4 Kinetic Energy Decay

The decay of freely evolving, isotropic turbulence downstream of a turbulence grid can be approximated by a power-law function [105], given by:

$$\frac{\overline{u_i'^2} - \sigma^2_{\text{noise},i}}{\overline{U_\infty}^2} = C\left(\frac{x - x_0}{M}\right)^m, \tag{4.2}$$

which relates relates three unknown parameters: the coefficient of decay, C, the virtual origin of the turbulence, x_0, and the decay exponent, m. While the power-law decay region has been widely studied in turbulence research, there is significant variation in the values reported, often attributed to inconsistencies in calculation methods and the types of turbulence grids tested [33, 100]. No universal solution to the rate of turbulence decay has been identified, although classical predictions, $m = -6/5$ [101] and $m = -10/7$ [64], which both assume self-similarity of the integral scales, are frequently used as benchmarks in related studies [106].

For open-channel flows, relatively few estimates of the decay exponent have been made compared to wind tunnel experiments. A notable example is the study by Yao *et al.* [96], who predicted a range of values, $m = -1.3$ to $m = -0.5$, through the water column for a single turbulence grid ($M = 0.034\,\text{m}$; $\theta = 0.34$) in a recirculating water flume ($H = 0.3\,\text{m}$; $W = 0.5\,\text{m}$; $\overline{U_\infty} = 0.36\,\text{m}\,\text{s}^{-1}$).

This analysis contributes to the existing literature by providing estimates of the decay parameters for four turbulence grids in an open-channel flow.

Methodology

Centreline measurements are well-suited for estimating the decay parameters because the flow along the centreline is less affected by boundary effects and asymmetries that could otherwise distort the results, allowing for more accurate comparisons with theoretical models. One approach to estimating the parameters involves applying non-linear regression to the measured data using Equation 4.2.

However, as noted by Kurian and Fransson [100], estimates of each parameter can vary significantly depending on where the curve fit begins [106]. To identify the lower bound of the power-law decay region, the method of Krogstad and Davidson [101] was adopted. In this approach, data from the most upstream position were sequentially removed from the curve fit until the variance of the fit reached its minimum, indicating the optimal starting point for the regression. Given the short length of the measurement domain relative to the mesh sizes, the upper bound of the curve fit was defined by the most downstream measurement at $x - x_{\mathrm{F}} = 6.0\,\mathrm{m}$. This contrasts with other researchers who have extended measurements to $(x - x_{\mathrm{F}})/M \gg 10^2$, allowing them to refine the upper bound specifically to avoid noise contamination [100, 101].

Results

Figure 4.6 presents a non-dimensional log-log plot of the noise-corrected streamwise velocity variance as a function of downstream distance. Note that the left-hand side of Equation 4.2 is essentially a variation of Equation 2.6 for turbulence intensity; however, the freestream velocity was used here to ensure consistency across the grids. The figure clearly shows that, beyond the production region, the downstream flows follow similar decay gradients, consistent with a power-law relationship. For flows downstream of grids A, B, and D, the positional indices marking the start of the decay region occur within $10M$ of the grid plane. In contrast, for grid C, the regression analysis was limited to the four furthest downstream data points due to the limited extent of the measurement domain relative to the mesh size, introducing significant uncertainty in estimates of the decay parameters, as shown in Table 4.2.

Downstream of grids A and D, estimates of the decay exponent align closely with Saffman's exponent of $-6/5$, while the exponents for grids B and C are closer to Kolmogorov's exponent of $-10/7$. The physical implication of this is that the turbulence decays at different rates and the one-dimensional energy spectrum scales

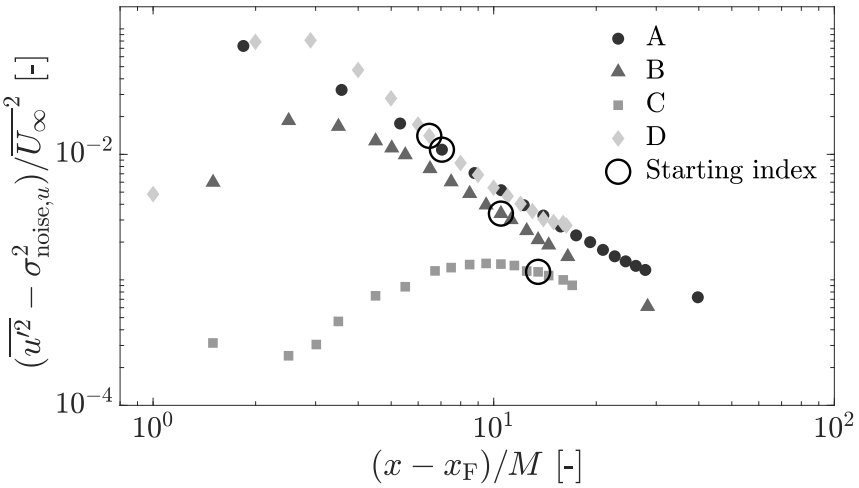


Figure 4.6: Non-dimensional distributions of noise-corrected streamwise velocity variance along the flume's centreline. The flow is compared downstream of four turbulence grids defined in Table 4.1: A (filled circles), B (up-pointing triangles), C (squares), and D (diamonds). Positional indices marking the start of the decay region (unfilled circles) are also shown. The x-axis indicates the streamwise location relative to the outer frame. Test conditions: $\overline{U_\infty} = 0.57\,\mathrm{m\,s^{-1}}$.

Grid	Mean			$\mathrm{CI}_{0.95}$ (±)		
	C [-]	x_0 [m]	m [-]	C [-]	x_0 [m]	m [-]
A	0.07	0.38	-1.29	0.01	0.05	0.06
B	0.07	0.51	-1.44	0.13	0.77	0.48
C	0.24	-5.63	-1.53	386.74	3777.31	469.36
D	0.07	1.15	-1.26	0.08	0.54	0.09

Table 4.2: Estimates of the decay parameters in Equation 4.2 based on the mean of three repeated measurements, with 95% confidence intervals to quantify the uncertainty due to model variability.

differently as wavenumbers approach zero, leading to disparities in the distribution and transfer of energy across different scales. The discrepancies between estimates of the decay exponents are most likely due to differences in the initial conditions and the sample sizes used for the regression analysis—an artefact of the relatively large mesh sizes used in the investigation (see Table 4.1)—and the limited spatial resolution of the measurements compared to other studies. Comte-Bellot and Corrsin [107] recommended restricting measurements to 25–30M downstream of the grid plane

to avoid flow inhomogeneity and prevent the inadvertent inclusion of data from the production region in the analysis, which can bias estimates of the decay exponent higher [106]. Applying this criterion to grids C and D, however, would have placed flow sampling beyond the working section.

Accurately quantifying the virtual origin has also proved challenging for researchers [108], as its location does not necessarily coincide with the grid plane [109]. Estimates for grids A, B, and D range between $x_0 = 1$–$3M$, consistent with values reported in the literature [108]. However, the negative estimate for grid C suggests that the measurement domain was too short to capture the relevant flow dynamics, introducing considerable uncertainty into the regression analysis. This limitation likely accounts for the slightly larger estimate of the dimensionless decay coefficient for grid C. In contrast, the corresponding value for grids A, B, and D is $C = 0.07$, aligning closely with other reported values [100, 109].

4.3.5 Integral Scales

As the turbulence decays downstream, turbulent kinetic energy is redistributed across the energy spectrum, leading to the growth of the integral length scales. This behaviour is well-documented in the literature [32, 94, 100] and is reproduced here in Figure 4.7. Due to the larger mesh sizes of grids C and D, the onset of turbulence production and the subsequent formation of smaller turbulent eddies appears delayed compared to the flow downstream of grids A and B, where the smallest length scales are observed within $2M$ of the grid plane.

Downstream of the production region, the distributions exhibit similar growth gradients and a clear dependency on the downstream flow speed. For instance, the growth profiles for grids A and B remain closely aligned along the centreline, corresponding with similar mean flow recovery and turbulence decay profiles shown in Figures 4.3 and 4.5, respectively. The vertical offsets to the profiles for grids C and D are attributed to differences in the mean streamwise velocity profiles downstream of these grids, noting that the gradients of length scale growth appear

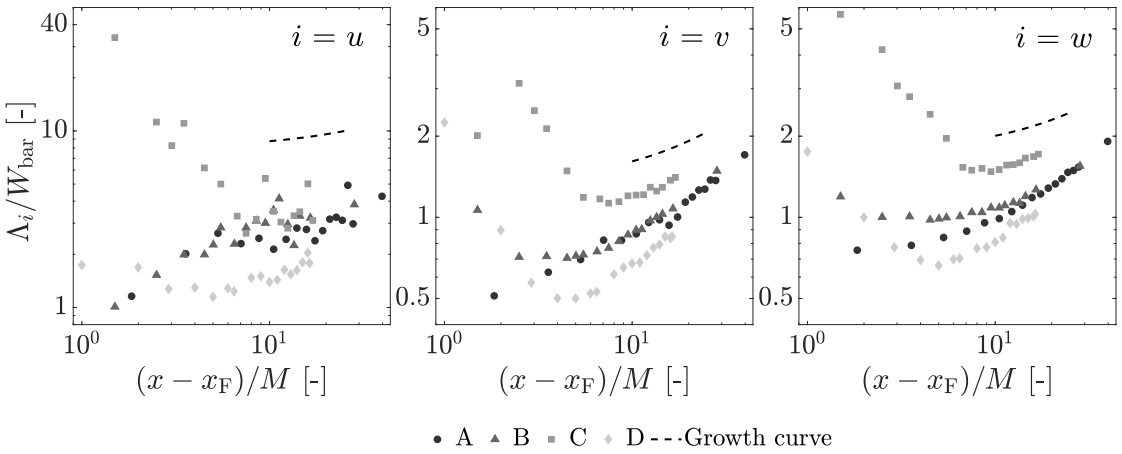


Figure 4.7: Non-dimensional distributions of the i^{th} integral length scale along the flume's centreline. Estimates of the length scales are based on the mean of three repeated measurements. The flow is compared downstream of four turbulence grids defined in Table 4.1: A (circles), B (up-pointing triangles), C (squares), and D (diamonds). Also shown are the mean non-dimensional growth gradients across the grids (thick dashed). Test conditions: $\overline{U_\infty} = 0.57\,\mathrm{m\,s^{-1}}$.

to scale with the bar width, with the gradients for grid D slightly larger than those for grids A–C.

The non-dimensional growth gradients for the i^{th} integral length scale shown in Figure 4.7 are calculated as the mean of the slopes of regression lines fitted to the regions of length scale growth for each grid. Each region begins at the point where the length scale reaches its minimum value along its respective profile, typically occurring between $1M \leq x - x_{\mathrm{F}} \leq 8M$. Expressed in non-dimensional terms as $\Lambda_i/W_{\mathrm{bar}}$ divided by $(x - x_{\mathrm{F}})/M$ along the streamwise axis, the gradients equate to 0.083, 0.031, and 0.029 dimensionless units per mesh size for Λ_u, Λ_v, and Λ_w, respectively, with the standard errors of the mean approximately 10% of these values. This suggests that the streamwise integral length scales recover at nearly three times the rate of the corresponding cross-stream and vertical length scales.

By comparing the relative magnitudes of Λ_i across the grids, the influence of grid geometry, particularly the bar width, becomes apparent. Grid D yields length scales that are, on average, twice as large as those observed downstream of grids A–C. This difference would likely be even more pronounced if the mean

streamwise velocity profiles across all grids exhibited similar recoveries downstream of the production region.

In the uncertainty analysis, the broad scatter in the streamwise component leads the random error to outweigh the systematic error by a factor of two to six. Conversely, for Λ_v and Λ_w, the systematic error contributes slightly more to the combined uncertainty than the random error. The 95% confidence intervals for the expanded uncertainty are significantly narrower than those reported for the clean flow case, with values of $\pm 0.52\Lambda_u$, $\pm 0.18\Lambda_v$, and $\pm 0.17\Lambda_w$, when spatially averaged across the measurement domain. Note that these values are averaged across all grids for brevity. The reduction in uncertainty is attributed to the significantly lower noise contribution to $\sigma^2_{\text{meas},i}$ ($< 10\%$), which reduces variation in calculations of the autocorrelation coefficient.

4.3.6 Velocity Spectra

Figure 4.8 presents the one-dimensional energy spectra of the turbulent velocity fluctuations as a function of (i) streamwise location downstream of grid A and (ii) grid geometry. The figure provides an expected result, in that the PSD, which serves as a proxy for turbulent kinetic energy, decays with downstream distance. Furthermore, the stronger adherence to Kolmogorov's $f^{-5/3}$ decay gradient compared to the clean flow case (see Figure 2.10) provides compelling evidence for the existence of an inertial subrange. In light of this result, the applicability of the von Kármán model to capture the flow's spectral response is revisited, as shown in Figure 4.9. Compared to the clean flow case (see Figure 3.17), there is closer qualitative agreement between the von Kármán model and the power spectra, both in overall shape and magnitude, demonstrating its suitability for flows approaching isotropy.

The comparison of spectral energy across different turbulence grids in the right-hand panel of Figure 4.8 complements several key findings from the turbulence intensity profiles in Figure 4.5. Grids A and B yield similar spectral profiles,

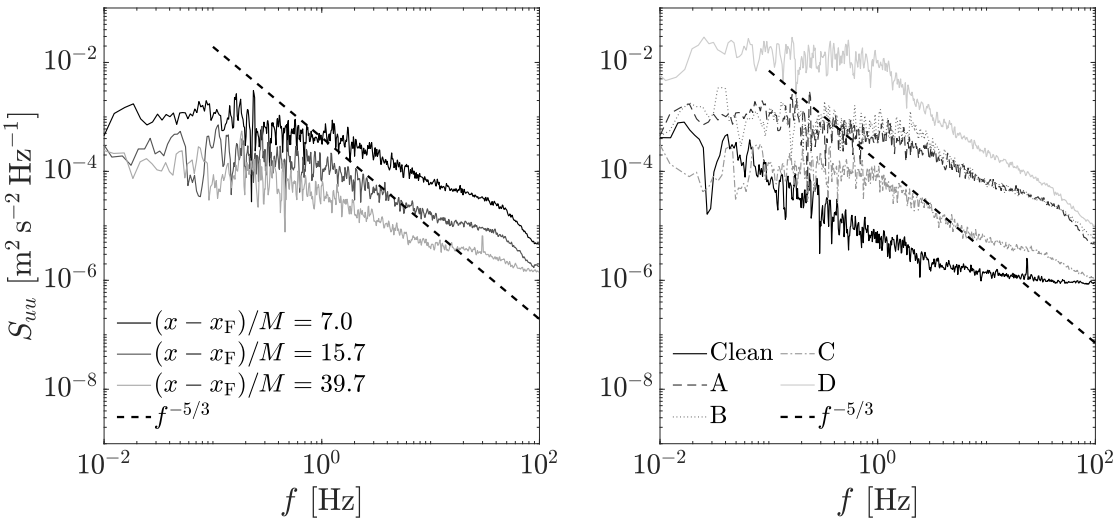


Figure 4.8: PSD estimates of the streamwise velocity fluctuations, S_{uu}, as a function of streamwise location (greyscale) downstream of grid A (left panel) and grid geometry (right panel). In the right-hand panel, clean flow measurements at $x = 5\,\mathrm{m}$ (black solid) are compared with measurements taken at $x - x_F = 2.4\,\mathrm{m}$ downstream of four turbulence grids defined in Table 4.1: A (dark grey dashed), B (dotted), C (dash-dotted), and D (grey solid). Also shown is Kolmogorov's $f^{-5/3}$ decay gradient (black dashed). Test conditions: $\overline{U_\infty} = 0.57\,\mathrm{m\,s^{-1}}$.

whereas grid C exhibits the lowest PSD in the energy-containing range but shows noticeably higher energy content in the inertial subrange compared to the clean flow case. Grid D, which generates the highest overall turbulence, displays the highest PSD across the frequency range. Additionally, the figure provides insight into the relative contributions of the flow-related content and noise to the velocity signals. Unlike the clean flow case, the power spectra for grids A, B, and D do not become saturated by noise at higher frequencies, suggesting that a Nyquist frequency of $f_{NY} = 100\,\mathrm{Hz}$ may be inadequate for accurately quantifying the noise floor under elevated turbulence conditions. For the results presented, it is possible that the parametric evaluations of $\sigma^2_{\mathrm{noise},i}$ are biased high; however, the impact on the turbulence statistics is likely to be $< 10\%$ given the estimated proportion of noise in the velocity signal.

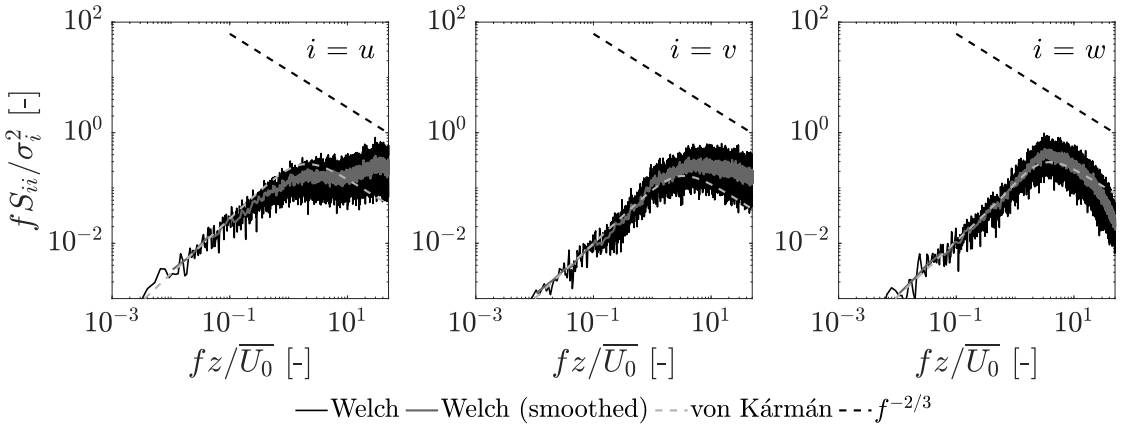


Figure 4.9: Non-dimensional PSD estimates of the i^{th} velocity fluctuations downstream of grid A. The PSD estimates were obtained using the Welch method (black solid), and compared with empirical predictions from the von Kármán model (grey dashed) as a function of non-dimensional frequency. Also shown are a bin-averaged representation of the Welch power spectra (grey solid) and Kolmogorov's constant of proportionality, $f^{-2/3}$ (black dashed). Test conditions: $\overline{U_{\text{CL}}} = 0.58\,\text{m}\,\text{s}^{-1}$; $(x, y, z) = (2.6, 0, 0)$.

4.4 Parameter Space Selection For Model-Scale Testing

To investigate the unsteady response of a model-scale rotor to freestream turbulence, two turbulence parameters—the turbulence intensity and streamwise integral length scales—serve as key variables in defining the parameter space for future turbine tests. As demonstrated by various researchers, both parameters are critical to the unsteady response of tidal stream rotors (see Section 6.3.2). However, a significant challenge when using passive turbulence grids is maintaining independent control of both parameters while modifying the grid geometry. One approach to investigating the influence of each parameter, albeit with the risk of unintended variations in the other, is to vary the distance between the grid plane and the measurement location, ensuring that the change in one parameter is more significant than the change in the other. Although this is a subjective evaluation, this differential can help isolate the influence of the more significantly varying parameter, allowing for a clearer understanding of its impact on the rotor's unsteady response.

$x - x_\mathrm{F}$ [m]	I_3D [%]				Λ_u [mm]			
	A	B	C	D	A	B	C	D
1.1	8.6	8.6	1.6	24.4	46.0	45.3	165.3	76.4
2.4	4.4	4.6	2.8	12.1	55.4	82.7	65.9	74.1
3.3	-	-	-	8.6	-	-	-	90.3
6.0	2.3	2.2	2.5	5.3	85.3	76.6	62.2	107.0

Table 4.3: Estimates of I_3D and Λ_u, based on the mean of three repeated measurements, at multiple streamwise locations along the flume's centreline for grids A–D. Only grid D was tested at $x - x_\mathrm{F} = 3.3\,\mathrm{m}$.

To test this approach, combinations of I_3D and Λ_u along the flume's centreline were evaluated to determine whether the variation in one parameter was more significant than the other. Table 4.3 summarises the results at selected streamwise locations and reveals the following:

- An approximately 50% reduction in I_3D is observed at each of the three locations downstream of grid A, resulting in an absolute reduction of 6.3%, while Λ_u shows a cumulative increase of 39.3 mm.
- The differences in both I_3D and Λ_u profiles between grids A and B are negligible.
- The larger value of Λ_u at $x - x_\mathrm{F} = 1.1\,\mathrm{m}$ downstream of grid C reflects the delayed onset of turbulence production compared to the other grids.
- Grid C induces minimal change in I_3D, with a change of $< 1\%$ across the measurement domain.
- The flow downstream of grid D yields the sharpest absolute reduction in I_3D (19.1%) across the measurement domain, accompanied by an increase in Λ_u comparable to that of grids A and B. Notably, this includes an absolute reduction of 12.3% between $x - x_\mathrm{F} = 1.1\,\mathrm{m}$ and 2.4 m, corresponding to a 2.3 mm reduction in Λ_u.
- The turbulence intensity at $x - x_\mathrm{F} = 3.3\,\mathrm{m}$ downstream of grid D matches that observed downstream of grid A at $x - x_\mathrm{F} = 1.1\,\mathrm{m}$, with a corresponding difference in Λ_u of 44.3 mm.

The results of this analysis suggest that there is sufficient scope to investigate the effects of each turbulence parameter, provided the rotor location can be readily adjusted in the streamwise direction during future turbine tests. However, it is important to note that the parameter space presented is more conducive to examining the unsteady effects of I_{3D} rather than Λ_u. When normalised on the rotor diameter, the relative magnitudes of Λ_u between streamwise locations are much less significant than changes in I_{3D}. Additionally, I_{3D} values align more closely with reported in-field values than the non-dimensional length scales. Offshore estimates of I_{3D} generally range upwards from 5% [110], with median values varying widely depending on site conditions, as well as the time and location of the measurements. In contrast, Λ_u tends to scale with the channel height, often making them comparable to a full-scale rotor diameter [30]. However, the values of Λ_u observed here are relatively small, at $< 20\%$[5] of the 0.6 m rotor diameter, making their impact on the model-scale rotor less likely to be significant. To reliably generate integral length scales with a more substantial influence on turbulence-rotor interactions, a larger flow obstruction with a characteristic dimension $\mathcal{O}(R)$, where R is the rotor radius, would likely be required. Low-order modelling of a wind turbine's structural response has demonstrated that as the wavelength of the inflow signal increases (analogous to the size of eddies), the aerodynamic rotor torque also increases, resulting in an integrated load response several times greater than that for wavelengths comparable to blade chord lengths [111].

Based on the above analysis, and to narrow the scope of the next phase of the investigation, grids A and D were selected for further flow characterisation in support of Objective iii. An important consideration in this selection was that both grids share the same porosity, ensuring the same mass flux through the grid plane, which is crucial for isolating the effects of turbulence in future turbine tests.

[5]This excludes the 165.3 mm value observed downstream of grid C at $x - x_F = 1.1$ m, noting the significant uncertainty associated with calculating the integral scales in very low turbulence (see Section 3.2.3).

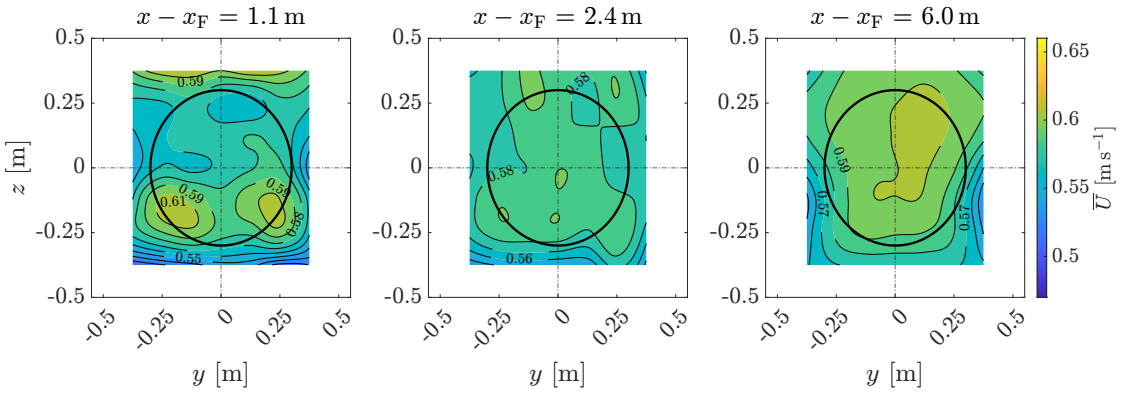
4.5 Characterisation of Turbulent Flow Fields

This section presents results of the flow characterisation at three streamwise locations downstream of grids A and D. The objective of this analysis was to develop further insights into the downstream turbulence fields and to evaluate how representative centreline measurements are of a broader cross-section of the flow field. All tests were run at a single flume duty, corresponding to a freestream velocity of $\overline{U_\infty} = 0.57\,\mathrm{m\,s^{-1}}$.

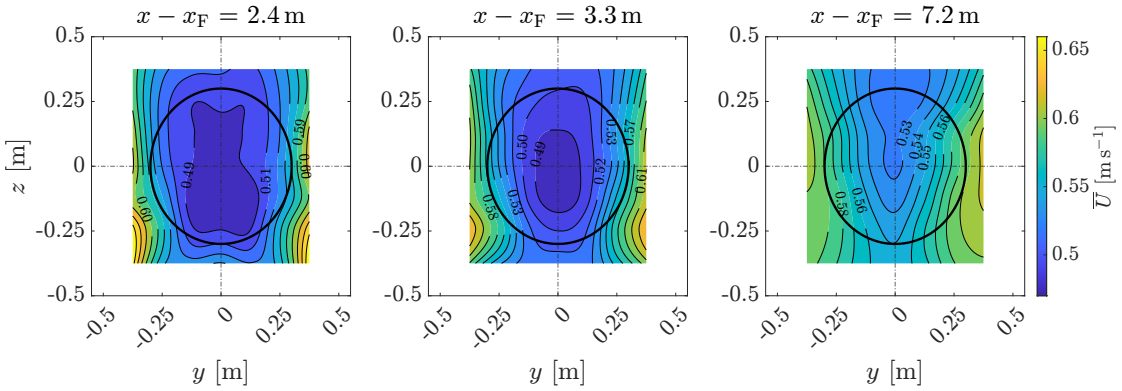
The chosen streamwise locations for both grids were based on the analysis presented in Section 4.4 and therefore did not align with the equidistant yz-planes characterised for the clean flow case. As a result, the location of $\overline{U_0}$ was adjusted for tests involving grid A or D. It follows, therefore, that this new reference point, which forms the basis for $\overline{U_0}$ in the following analysis, was positioned to coincide with a common streamwise location, should the turbine test campaign be limited to a single rotor location. Based on an approximately 8% difference in turbulence intensities between grids A and D, for a difference of $< 20\,\mathrm{mm}$ $(0.07R)$ in the streamwise integral length scales (see Table 4.3), this location was chosen to be $x - x_\mathrm{F} = 2.4\,\mathrm{m}$, i.e. four rotor diameters downstream of the grid plane. To ensure consistency with the process outlined in Section 2.2.4, centreline velocities at two other streamwise locations unique to each grid were referenced back to this location. The furthest downstream location for grid D was set at $x - x_\mathrm{F} = 7.2\,\mathrm{m}$, allowing the flow to be characterised where the turbulence is approximately homogeneous, i.e. at $20M$ from the grid plane [94].

4.5.1 Mean Velocities

The first stage in the flow characterisation was to evaluate the spatial variation of the velocity field, as shown in the 2D contour plots of $\overline{U}$ at three streamwise locations downstream of grids A and D in Figure 4.10. At $x - x_\mathrm{F} = 1.1\,\mathrm{m}$ downstream of grid A, the effects of turbulence production are most apparent,



(a) Grid A



(b) Grid D

Figure 4.10: 2D contours of $\overline{U}$ at three streamwise locations downstream of grid (a) A and (b) D. The profiles correspond to the measurement co-ordinates illustrated in Appendix A, Figure A.2. The box outline delineates the flume's cross section, and the black circle represents the intended swept area of the turbine rotor. Test conditions: $\overline{U_0} = 0.59\,\mathrm{m\,s^{-1}}$ (grid A), $0.49\,\mathrm{m\,s^{-1}}$ (grid D).

with increased velocity variation across the survey area compared to the clean flow case (see Figure 3.5). The elevated turbulence levels result in a complex, non-uniform velocity distribution, characterised by sharp gradients between regions of accelerated and decelerated flow. This is particularly evident near the bottom edge of the survey area, where two distinct islands emerge within the isovels. These islands, symmetrically positioned about the vertical centre plane of the flume, correspond to the peak flow speeds across the survey area. By the time the flow reaches the intended rotor plane at $x - x_F = 2.4\,m$, velocity uniformity improves, as indicated by the narrower 95% confidence interval and reduced velocity range,

$x - x_F$ [m]	$\overline{U_{CL}}$ [m s^{-1}]	$\langle\overline{U}\rangle/\overline{U_{CL}}$ [-]	$CI_{0.95}(\overline{U})$ [%]	Range$(\overline{U})/\overline{U_{CL}}$ [-]	$\langle$Skew$(u)\rangle$ [-]	$\langle$Kurt$(u)\rangle$ [-]
			Grid A			
1.1	0.588	0.979	1.286	0.178	0.018	3.289
2.4	0.594	0.974	0.691	0.097	0.023	3.174
6.0	0.591	0.993	0.913	0.121	-0.030	3.164
			Grid D			
2.4	0.492	1.117	3.267	0.406	0.059	3.020
3.3	0.487	1.124	2.696	0.317	0.084	3.024
7.2	0.489	1.168	1.717	0.196	0.065	3.061

Table 4.4: Summary of velocity statistics across individual transects of the flume downstream of grids A and D. The 95% confidence intervals quantify flow uniformity across the survey area and are expressed as a percentage of the centreline velocity modulus at each streamwise location, $\overline{U_{CL}}$.

as shown in Table 4.4. However, at $x - x_F = 6.0\,\text{m}$, a higher-velocity core develops, flanked by shear layers along both sides and the bottom edge of the survey area, leading to a reduction in velocity uniformity.

The greater injection of turbulent kinetic energy into the flow downstream of grid D results in increased velocity non-uniformity and pronounced cross-stream velocity shear that extends through the depth of the survey area. A key feature of the profiles is the presence of a lower-velocity core region, in which the centreline velocities are between 15–20% lower than those observed downstream of grid A (see Figure 4.3), which persists through the measurement domain. Away from the vertical centre of the channel, the flow velocities increase, likely due to a bypass flow effect around the vertical bars. This observation is somewhat unexpected, as the velocity distribution does not correspond with the uniform spacing of the grid's mesh. At the intended rotor plane, the velocity shear along the horizontal centre of the channel to the flume's centreline is $\partial\overline{U}/\partial y = 0.373\,\text{s}^{-1}$, in contrast to $\partial\overline{U}/\partial y = 0.041\,\text{s}^{-1}$ at the corresponding location downstream of grid A. Further downstream, the effects of flow mixing become apparent, with a reduction in localised shear gradients and an increase in velocity uniformity, as shown by the

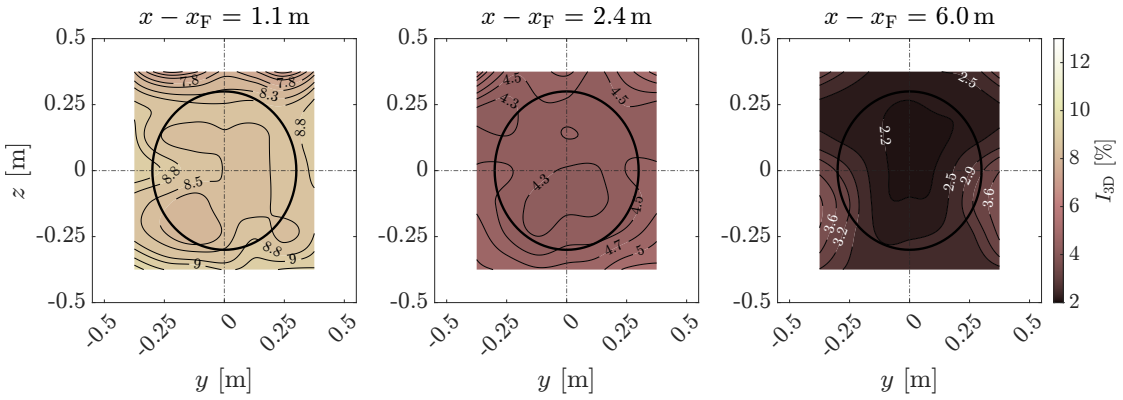
progressively narrower 95% confidence intervals in Table 4.4.

For isotropic turbulence, the skewness and kurtosis are expected to be zero and three, respectively, for all three velocity components [94]. The spatially averaged skewness and kurtosis for the streamwise velocity fluctuations across the survey area reveal values close to zero and slightly above three, respectively, as shown in Table 4.4. While the velocity fields do not exhibit characteristics of a fully developed turbulent flow, the results indicate that the single-point velocity statistics are almost Gaussian, although not perfectly so, aligning closely with the findings of Krogstad and Davidson [101].

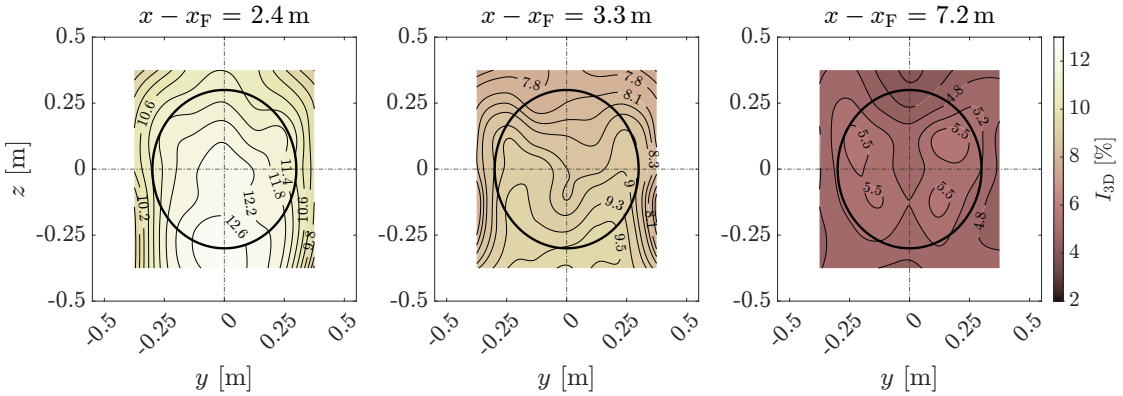
4.5.2 Turbulence Intensities

Figure 4.11 presents 2D contour maps of I_{3D} at three streamwise locations downstream of grids A and D. Similar to the time-averaged velocities, the effects of turbulence production are most pronounced at $x - x_F = 1.1\,\mathrm{m}$ downstream of grid A, where the turbulence field exhibits significant inhomogeneity. Slightly elevated values of turbulence intensity, approaching 10% and comparable to in-field measurements reported at Puget Sound [31], are observed along the bottom edge of the survey area, corresponding to decelerated flow in the wake of the bottom horizontal bar of the outer frame. The highest spatial uniformity is observed at the intended rotor plane (see Table 4.5), but decreases further downstream due to the emergence of vertical and cross-stream velocity gradients along all sides of the survey area. The lowest turbulence intensity values ($I_{3D} \approx 2\%$) are observed at the furthest downstream location, $x - x_F = 6.0\,\mathrm{m}$, concentrated in the higher-velocity core of the channel, where the flow is well mixed compared to upstream locations.

2D contours of I_{3D} at the intended rotor plane downstream of grid D complement the corresponding velocity field, revealing sharp cross-stream gradients and elevated values of turbulence intensity, in excess of 12%, in the channel core, where the flow velocities are lower. As turbulence decays downstream, flow uniformity increases, as indicated by the narrowing 95% confidence intervals and the reduced range



(a) Grid A



(b) Grid D

Figure 4.11: 2D contours of I_{3D} at three streamwise locations downstream of grid (a) A and (b) D. The profiles correspond to the measurement co-ordinates illustrated in Appendix A, Figure A.2. The box outline delineates the flume's cross section, and the black circle represents the intended swept area of the turbine rotor. Test conditions: $\overline{U_0} = 0.59\,\mathrm{m\,s^{-1}}$ (grid A), $0.49\,\mathrm{m\,s^{-1}}$ (grid D).

of turbulence intensities, shown in Table 4.5. Notably, at $x - x_F = 7.2\,m$, two cellular structures corresponding to regions of slightly higher turbulence intensity ($I_{3D} \approx 5.5\%$) emerge symmetrically about the vertical centre plane at approximately $(y, z) = (\pm 0.2, 0.1)$. These regions align closely with the geometric intersections of the horizontal and vertical bars of grid D, suggesting these as the likely sources of elevated turbulence. Although this streamwise location corresponds to $20M$ downstream of the grid plane, the flow field does not approximate homogeneity, as persistent local gradients and lower turbulence levels around the periphery of the survey area remain.

$x - x_F$ [-]	$I_{3D(CL)}$ [%]	$\langle I_{3D} \rangle / I_{3D(CL)}$ [-]	$CI_{0.95}(I_{3D})$ [%]	Range(I_{3D}) [%]
		Grid A		
1.1	8.49	1.01	0.16	2.79
2.4	4.28	1.08	0.10	1.62
6.0	2.17	1.26	0.15	1.93
		Grid D		
2.4	12.40	0.89	0.33	4.36
3.3	8.80	0.97	0.20	2.35
7.2	5.03	0.99	0.11	1.56

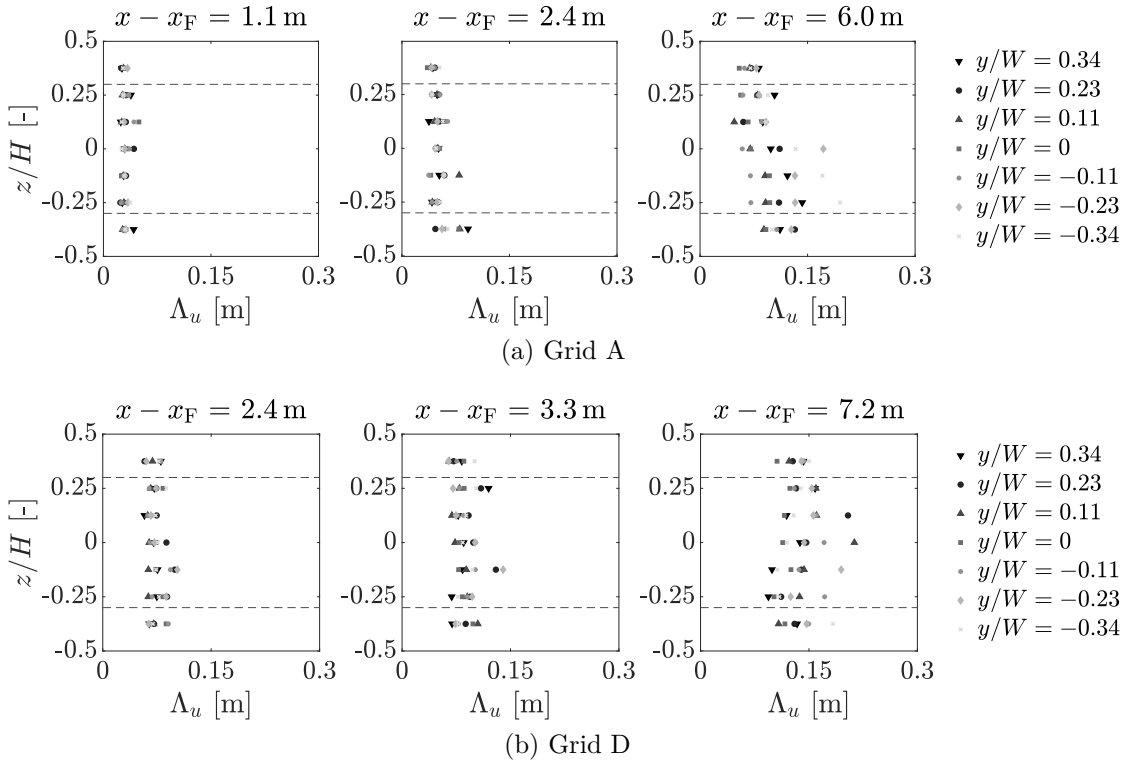
Table 4.5: Summary statistics of I_{3D} across individual transects of the flume downstream of grids A and D. The 95% confidence intervals (for flow uniformity) and the range are expressed as absolute values of I_{3D} at each streamwise location.

4.5.3 Integral Scales

Figure 4.12 presents depthwise profiles of Λ_u as a function of cross-stream position at three streamwise locations downstream of grids A and D. Depthwise profiles are preferred in this instance to avoid obscuring the finer-scale flow dynamics, which can often be masked in contour plots when the range of values is narrow, as is the case for the integral scales downstream grids A and D.

In contrast to both $\overline{U}$ and I_{3D}, Λ_u exhibits the highest uniformity at the streamwise location closest to the grid plane, as evidenced by the widening 95% confidence intervals and increasing length scale ranges with downstream distance (see Table 4.6). As turbulent kinetic energy cascades towards the larger eddies, the length scales grow non-linearly with downstream distance, leading to greater variation in Λ_u across the flow field. For both grids, values of $\langle \Lambda_u \rangle$ increase by approximately 70 mm across the measurement domain, spanning almost 5 m. When non-dimensionalised by the model-scale rotor diameter, $\langle \Lambda_u \rangle$ spans from 5–23% across both grids, with the largest value for each grid occurring furthest downstream, coinciding with the lowest turbulence intensity.

Notably, the local recovery of Λ_u is more pronounced at measurement locations



(a) Grid A

(b) Grid D

Figure 4.12: Depthwise profiles of Λ_u as a function of cross-stream position at three streamwise locations downstream of grid (a) A and (b) D. The profiles correspond to the measurement co-ordinates illustrated in Appendix A, Figure A.2. The intended swept area of the rotor is also shown (dashed). Test conditions: $\overline{U_0} = 0.59\,\mathrm{m\,s^{-1}}$ (grid A), $0.49\,\mathrm{m\,s^{-1}}$ (grid D).

less aligned with the grid structure (see Appendix A, Figure A.2), corresponding to regions of the flow with slightly higher local velocities. This is particularly evident at $x - x_F = 7.2\,\mathrm{m}$ downstream of grid D, where some values exceed 180 mm ($3W_{bar}$). By comparison, the largest length scales downstream of grid A also reach this value ($9W_{bar}$), although, interestingly, these occur at measurement locations more aligned with the grid structure, where a slower local recovery of the length scales would typically be expected.

4.5.4 Reliability of Centreline Statistics

To evaluate the suitability of centreline measurements for the reference flow velocity, the following analysis quantifies the comparability of centreline and spatially

$x - x_F$ [-]	$\Lambda_{u(CL)}$ [mm]	$\langle\Lambda_u\rangle/\Lambda_{u(CL)}$ [-]	$CI_{0.95}(\Lambda_u)$ [%]	$\langle\Lambda_u\rangle/2R$ [-]	$Range(\Lambda_u)/\Lambda_{u(CL)}$ [-]
			Grid A		
1.1	27.4	1.107	5.732	0.051	0.940
2.4	52.5	0.987	6.423	0.086	1.083
6.0	70.5	1.412	17.800	0.166	3.636
			Grid D		
2.4	73.7	1.009	4.170	0.124	0.619
3.3	78.9	1.110	5.761	0.146	0.960
7.2	113.7	1.217	6.636	0.231	1.046

Table 4.6: Summary statistics of Λ_u across individual transects of the flume downstream of grids A and D. The 95% confidence intervals quantify flow uniformity across the survey area and are expressed as a percentage of the centreline value at each streamwise location, $\Lambda_{u(CL)}$.

averaged flow metrics across the survey area[6]. In the context of turbine testing, discrepancies between centreline and spatially averaged values could lead to an under- or overestimation of the available kinetic energy in the turbine's approach flow, thereby biasing assessments of a turbine's non-dimensional performance and loading response.

In contrast to the clean flow case, where values of $\langle\overline{U}\rangle$ are within 0.5% of $\overline{U_{CL}}$ at each streamwise location (see Table 3.4), the relative differences downstream of the turbulence grids range from -0.7% to -2.6% for grid A (where $\overline{U_{CL}} > \langle\overline{U}\rangle$) and from 11.7% to 16.7% for grid D (where $\overline{U_{CL}} < \langle\overline{U}\rangle$). The results suggest that centreline values are more representative of the broader flow field when the flow is more uniform, highlighting the need for caution when drawing conclusions about mean flow behaviour based solely on centreline statistics. To illustrate this, Figure 4.3 shows the flow along the centreline downstream of grid D is significantly decelerated compared to the other grid geometries. At the intended rotor plane,

[6]It is important to note the limitations of the measurement strategy adopted in this study, as insights into the flow field are constrained by the extent and resolution of the survey area. The spatially averaged metrics discussed here are based on 49 single-point measurements, as illustrated in Figures 2.11 and A.2 in Appendix A, which are unlikely to capture the full complexity of the flow field.

$x - x_F = 2.4\,\text{m}$, there is a 17.1% difference in $\overline{U_{CL}}$ between grid A and grid D; however, when the velocities are spatially averaged across the survey area, the difference is much smaller, although still significant, at 5.0%.

The sensitivity of centreline measurements to local flow dynamics is also evident in the turbulence intensity metrics. When expressed as an absolute difference, the largest discrepancies between centreline and spatially averaged values for both grid geometries exceed those observed under clean flow conditions, which yield a discrepancy of just 0.24%. Specifically, the discrepancies are 0.56% for grid A and 1.34% for grid D, further supporting the idea that centreline values serve as a more reliable indicator of the broader flow field in more uniform flow conditions.

A similar analysis of the streamwise integral length scales reveals much smaller absolute differences between centreline and spatially averaged values under elevated turbulence conditions compared to clean flow, where the variation in length scales is significantly greater (see Figure 3.15). To illustrate this, the largest discrepancy across both grids is just 29.1 mm, whereas in clean flow, the discrepancies range between 43.2–94.7 mm through the working section.

4.6 Limitations of the Investigation

A key distinction between the experiments described herein and those in other studies is the order-of-magnitude difference between the mesh sizes—and, consequently, the mesh-to-channel height ratios—used in this work and those in other experimental studies (see Table 4.1). The aluminium extrusions used for each grid were chosen to ensure compatibility with the outer frame; however, the 20 mm bar width inadvertently constrained the inter-bar spacing, such that the minimum recommended grid porosity target of 60% [94] could be met. This constraint not only limited the number of square mesh grid geometries that could be tested without obstructing the flume's centreline—and, consequently, the ADV's sampling volume—but also necessitated a longer distance to achieve fully developed

turbulence. Given the restricted length of the measurement domain relative to the mesh sizes, the flow measurements were largely limited to capturing mean flow non-uniformities rather than fully developed, homogeneous turbulence preferred for future turbine tests.

It is important to acknowledge that some flow features in the 2D contour maps resulted from the partial or complete alignment of the ADV's sampling volume with the grid structure at certain measurement locations for specific grids (see Appendix A, Figure A.2). This highlights the inherent limitations of combining a coarse measurement spacing with a single-point measurement device. As a result, some flow dynamics may not have been fully captured, while others may have been over-emphasised. A higher measurement density across the survey area would ensure more accurate resolution of the flow field, although this would necessitate additional testing time.

Another artefact of the experimental setup was the interaction between the flume's background turbulence and the turbulence generated by each grid. This interaction complicates the analysis of the turbulence statistics by conflating two turbulence fields, as noted by Roach [32]. Decoupling this interaction, however, was beyond the scope of the present study.

4.7 Summary

This chapter has outlined a methodology for generating and controlling the freestream turbulence in a hydraulic flume, and has provided a detailed characterisation of the resulting turbulent flows, in preparation for the model-scale testing of a horizontal axis tidal stream turbine.

The first phase of the investigation focused on the mean flow and turbulence characteristics along the centreline of the flume, downstream of four turbulence grids. The transient nature of the turbulence generated was most evident in the turbulence intensity profiles, which showed that as the grid mesh size increased for a given bar

width, turbulence production weakened, and the production region shifted further downstream. At the centre of the intended rotor plane downstream of the four turbulence grids, the flow anisotropy was approximately $I_u : I_v : I_w = 1.0 : 0.9 : 0.7$, representing a significant reduction in anisotropy compared to the clean flow case. Estimates of the decay parameters for each grid geometry were also provided, with the decay exponents for grids A and D aligning closely with Saffman's classical prediction of $m = -6/5$, while those for grids B and C were closer to Kolmogorov's prediction of $m = -10/7$. The integral length scales were observed to scale primarily with the bar width and increase non-linearly with downstream distance. Additionally, the one-dimensional energy spectra supported the idea that as a turbulence field approaches isotropy, PSD estimates of the velocity fluctuations align more closely with the von Kármán model.

The second phase of the investigation focused on defining a parameter space for future turbine tests, expressed in terms of the turbulence intensity and streamwise integral length scales. Given the relative magnitudes of both parameters along the flume's centreline, the parameter space is better suited to examining the unsteady effects of turbulence intensity on a model-scale rotor rather than the streamwise integral length scales, which were $\mathcal{O}(W_{\text{bar}})$ and $< 20\%$ of the rotor diameter.

The final stage of the investigation involved flow characterisation at three streamwise locations downstream of two turbulence grids selected for model-scale testing: grid A and grid D. Despite having the same porosity, marked differences were observed in flow uniformity across the survey area and in the local flow effects induced by each grid. This was particularly noticeable in the development of the core flow region, where centreline velocities downstream of grid D were 15–20% lower than those of grid A. At the intended rotor plane, freestream turbulence was elevated compared to the clean flow case, with grid A yielding turbulence intensities of $I_{3\text{D}} \approx 4\%$ and grid D generating significantly higher levels of $I_{3\text{D}} \approx 12\%$, comparable to in-field conditions. It is worth noting that the coarse spacing between flow measurements may have overstated the prominence of certain features

in the 2D contour maps, while others may have gone undetected. This highlights the need for a higher measurement density across the survey area to achieve finer resolution of the flow field.

An analysis was also conducted to evaluate the comparability of centreline and spatially averaged flow metrics across the survey area. The sensitivity of centreline measurements to local flow dynamics led to discrepancies from the spatially averaged metrics, with these discrepancies increasing as flow non-uniformity grew. This effect was most pronounced for the mean velocities downstream of grid D, where a 17% relative difference was observed. In the context of future turbine tests, relying on an unrepresentative reference flow velocity could introduce bias into assessments of model-scale rotor performance and loading.

CHAPTER 5

Generation, Control, and Characterisation of Vertical Shear

Turbulent sheared flows arise naturally in open water due to bathymetric features and bed friction, which together drive the formation of channel boundary layers. The generation and control of vertical velocity shear in a controlled open-channel flow provides an opportunity to characterise key aspects of the hydrodynamics of sheared flows, laying the foundation for an investigation into the influence of vertical shear on model-scale turbine performance and loading.

This chapter encompasses two main components: (i) a detailed methodology for generating and controlling vertical velocity shear in a hydraulic flume, and (ii) a comprehensive characterisation of the resulting shear profiles, intended for the model-scale testing of a horizontal axis tidal stream turbine.

The chapter begins with an overview of previously tested methods for generating vertical velocity shear in laboratory-based experiments. This is followed by a description of the experimental methodology and the resulting flow characterisations. Finally, the limitations of the investigation are discussed.

5.1 Historical Approaches

Similar to grid-generated turbulence, vertical shear profiles have been generated in wind tunnels for several decades, often to simulate the effects of the atmospheric boundary layer in applications ranging from civic architecture [112] to wind turbines [113] and solar power [114], among others. One of the simplest methods to generate vertical shear involves placing surface roughness elements along the floor of the working section to promote the laminar-turbulent transition [115]. Active turbulence-generating grids can also be used, providing better control over the shear gradients and onset turbulence [113], albeit at the expense of increased system complexity and cost [116]. Another common approach involves introducing resistance to the flow through a graded obstruction placed normal to the onset flow. Previous examples include non-uniformly spaced grids of parallel rods [117] or gauze screens [118] across the width of the working section. However, as noted by Karnik and Tavoularis [35], simplified flow theories used to arrange such flow-resisting geometries often neglect three-dimensional flow effects, so an empirical approach to tuning the geometry may be required.

In controlled open-channel flows, vertical shear profiles are often generated to approximate the bottom boundary layer of a channel using methods similar to those described above. For example, surface roughness elements, designed to simulate sedimentary features in alluvial channels, have been used to study changes in downstream velocity profiles through the water column [119]. Additionally, multiple layers of mesh panels with varying porosities have been used to create target shear profiles resembling those observed in oceanic flows [120, 121].

Similar to experimental studies involving grid-generated turbulence, investigations into the effects of vertical shear in tidal energy research can be broadly divided into two main categories: (i) its impact on model-scale rotor loading [122], and (ii) its influence on downstream wake characteristics [43, 123]. For further discussion, the reader is referred to Section 6.3.1.

5.2 Shear Generation Methodology

The shape of a tidal channel's vertical shear profile is influenced by several factors, including bed roughness, the point in the tidal cycle, and the prevailing met-ocean conditions. As a result, inter- and intra-site variations in vertical shear can be significant, leading to a complex onset flow profile that varies continuously throughout the tidal cycle. Despite this variability, depthwise velocity profiles measured in large open-channel flows are often approximated by a power-law model [27], given by:

$$\frac{u(z)}{U_{\mathrm{CL}}} = \left(\frac{z}{H}\right)^{1/n}, \tag{5.1}$$

where $1/n$ is the power-law exponent that characterises the degree of vertical shear in the profile. An exponent of $1/7$ is often used as a reasonable approximation for depthwise velocity profiles, as demonstrated by Lewis *et al.* [27] for potential tidal stream energy sites in the Irish Sea. The present study uses this finding to inform the design of a vertical shear profile generation mechanism.

Experimental Setup

To create vertical shear profiles approximated by the power-law model, an empirical approach was combined with the method of Cowdrey [124] to define various geometrical arrangements of an upstream flow obstruction comprising the outer frame (first discussed in Section 4.2) and aluminium extrusions reused from the turbulence grids. Building on earlier work by Cockrell and Lee [34], Cowdrey proposed a simple analytical model for arranging non-uniformly spaced parallel rods across the width of the working section, placed normal to the onset flow[1]. By grading the flow resistance through the height of the test section, the downstream velocity profiles could be adjusted, characterised by changes in the denominator of the power-law exponent, n. This contrasts with the approach of Tedds [43],

[1] A complete derivation of Cowdrey's solution can be found in Appendix B.

where the position of the rods in the water column was fixed, preventing any fine adjustments to the resistance grading, which partially explains the discrepancy between the author's target velocity profile ($n = 7$) and the measured profile ($n = 5$).

To demonstrate the application of this approach, two vertical shear profiles with exponent denominators, $n = 6$ and $n = 9$, were generated. This choice effectively establishes an achievable range around the widely cited value of $n = 7$, capturing in part the considerable variation throughout the tidal cycle. For both exponent denominators, the initial positioning of the bars[2] was based on Cowdrey's theory. However, careful adjustments to the relative spacing between the bars were necessary to minimise the root mean square error (RMSE) between the measured streamwise velocities through the water column and the theoretical distribution corresponding to the target (integer) exponent denominator in Equation 5.1. The RMSE was evaluated at the design speed of the flume, corresponding to a freestream velocity of $\overline{U_\infty} = 0.57\,\mathrm{m\,s^{-1}}$, at the intended rotor plane located four rotor diameters downstream of the obstruction, at $x - x_\mathrm{F} = 2.4\,\mathrm{m}$. Consistent with the turbulence grid tests, $\overline{U_0}$ was also defined at this location (see Section 4.5). The error criterion was set to $\leq 0.03\,\mathrm{m\,s^{-1}}$ ($\leq 0.05\overline{U_0}$).

Figure 5.1 shows close agreement in the bottom two-thirds of the water column between the final bar positions and those predicted by Cowdrey's model, noting that no bars were placed at $z/H > 0.15$. As the elevation from the channel bed approaches zero, the centre-to-centre spacing of the bars, l, also tends towards zero, such that at $z/H = -0.5$, $l/W_\mathrm{bar} = 1$. The geometry of each obstruction (shown in Appendix A, Figure A.3) is hereafter referred to as SP1, corresponding to a vertical shear profile characterised by $n = 6$, and SP2, characterised by $n = 9$. The corresponding porosities were 75.6% and 81.3%, respectively. The experimental arrangement is shown in Figure 5.2, with the bars arranged horizontally on the

[2]The use of square bars contrasts with the use of circular rods in Cowdrey's study. As a result, the characteristic dimension of the rods (see Appendix B, Equation B.5), d, is equated to the bar width, W_bar.

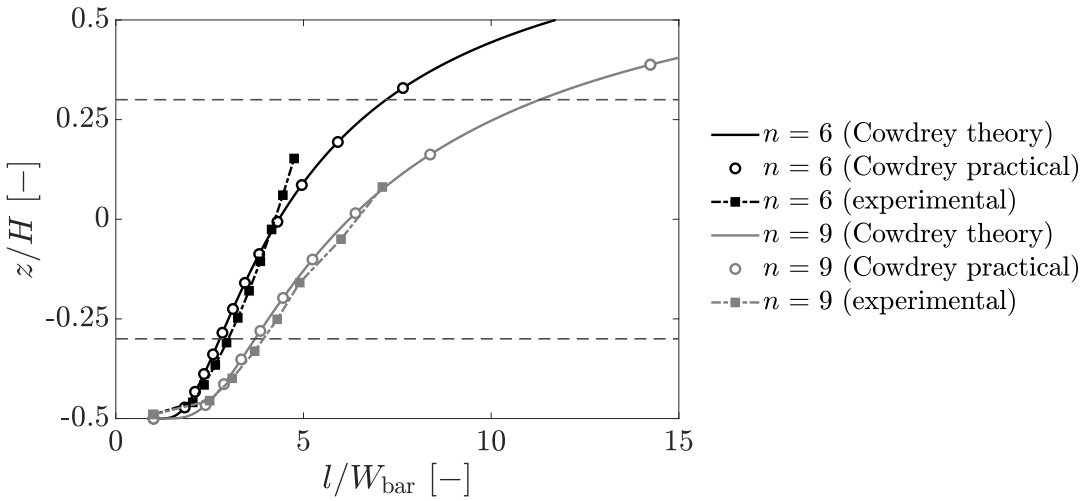


Figure 5.1: Bar spacing configuration curves for two velocity distributions, characterised by the denominator of the power-law exponent (see Equation 5.1), n, where l represents the centre-to-centre bar spacing. Applying Cowdrey's method yields two families of curves: one for $n = 6$ (black) and the other for $n = 9$ (grey). A finely discretised theoretical curve (solid) is overlaid with a practical implementation of the theory (unfilled circles) based on physical limits imposed by the bar width, $W_{\text{bar}} = 20\,\text{mm}$, and the final bar positions from the experiments (dash-dotted with filled square markers). Linear piecewise fits have been added to the experimental results as a visual aid, along with the intended swept area of the rotor (dashed).

upstream face of the outer frame, while a welded mesh panel ($M = 0.075\,\text{m}$, gauge $= 0.003\,\text{m}$) was attached to the downstream face, intended to enhance flow mixing.

Refinements to Flow Characterisation Methodology

To accommodate the increased turbulence levels in vertically sheared flow, several adjustments were made to the experimental methodology detailed in Chapter 2.

- The correction method proposed by Romagnoli *et al.* [74] was applied to calculations of the integral scales, given the significantly lower noise contribution to $\sigma^2_{\text{meas},i}$ ($< 10\%$; cf. Table 2.2), which was due to the higher flow-related proportion of the velocity measurements.
- Due to increased vertical velocity shear and enhanced vertical momentum transport compared to the clean flow case (see Section 5.3.4), no pitch

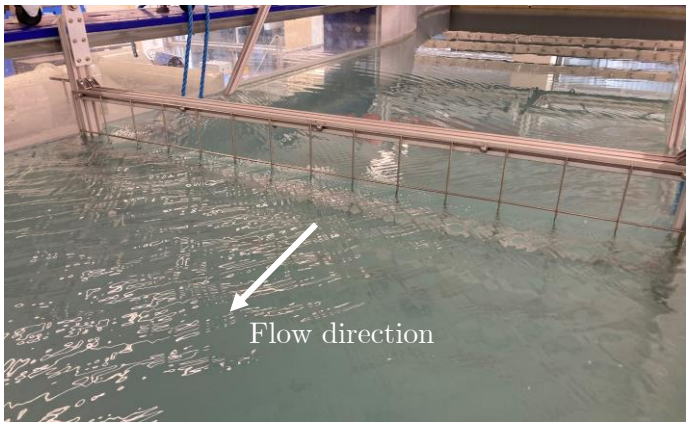


Figure 5.2: Experimental arrangement of shear profile mechanism in the flume. The shallowest submerged horizontal bars (20×20 mm cross section) are visible just beneath the free surface, with the welded mesh panel affixed to the downstream face of the outer frame.

correction (see Section 2.2.4) was applied, resulting in non-zero vertical velocities at $(y, z) = (0, 0)$.

5.3 Characterisation of Sheared Flow Regimes

Flow measurements downstream of SP1 and SP2 were conducted at three equidistant yz-planes in the flume: $x - x_{\mathrm{F}} = 2.4\,\mathrm{m}$, $4.2\,\mathrm{m}$, and $6.0\,\mathrm{m}$, the first of which corresponds to the likely rotor location in future turbine tests. The uniform spacing of the streamwise locations was selected to ensure a like-for-like comparison of the downstream flow evolution between SP1 and SP2. As with the turbulence grid tests, the streamwise locations did not align with the equidistant yz-planes characterised for the clean flow case.

Given the comparable levels of turbulence to the turbulence grid tests, the uncertainty metrics are similarly consistent, making it unnecessary to repeat them here. For uncertainty quantification of each flow metric, the reader is referred to Section 4.3.

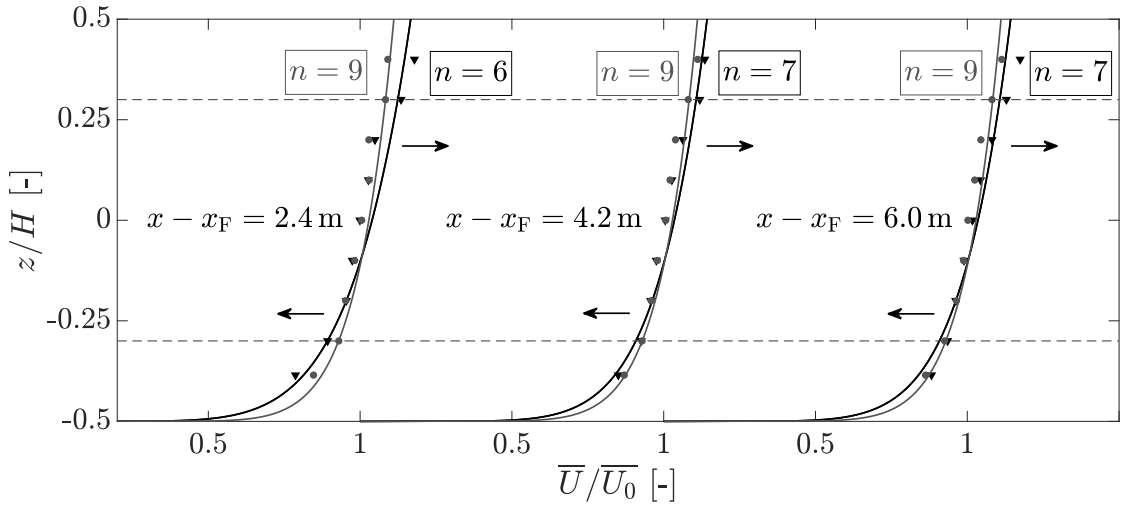


Figure 5.3: Depthwise profiles of $\overline{U}/\overline{U_0}$ in vertically sheared flow at three streamwise locations. The profiles comprise measurements along the flume's vertical centre plane, as illustrated in Appendix A, Figure A.3. Measured velocities (symbols) are overlaid onto best-fit power-law velocity profiles (solid lines), with the power-law exponent denominator, n, labelled on either side. Symbol colours correspond to the theoretical profiles and their labels. Also shown are the intended swept area of the rotor (dashed) and pairs of opposing arrows indicating the effect of increased vertical shear on the velocity gradient. Test conditions: $\overline{U_0} = 0.61\,\mathrm{m\,s^{-1}}$ (SP1); $0.61\,\mathrm{m\,s^{-1}}$ (SP2).

5.3.1 Mean Velocities

Figure 5.3 presents depthwise profiles of $\overline{U}$ normalised on $\overline{U_0}$ along the vertical centre plane of the flume at three streamwise locations. Theoretical velocity distributions, represented by the power-law model, are included as reference. In contrast to the vertical shear profile characterised by $n = 9$ at the intended rotor plane, the corresponding profile for $n = 6$ is not sustained through the measurement domain. This is indicated by an increase in the denominator of the power-law exponent, from $n = 6$ to $n = 7$, as the profile develops between $x - x_F = 2.4\,\mathrm{m}$ and $4.2\,\mathrm{m}$. No change in the exponent denominators was observed across three repeated measurements.

An artefact of the experimental method is the slight S-shaped distortion observed in each of the measured profiles, attributed to small velocity deficits relative to the theoretical distributions across the rotor's swept area. While the exact cause is difficult to pinpoint, potential explanations include local instabilities arising from

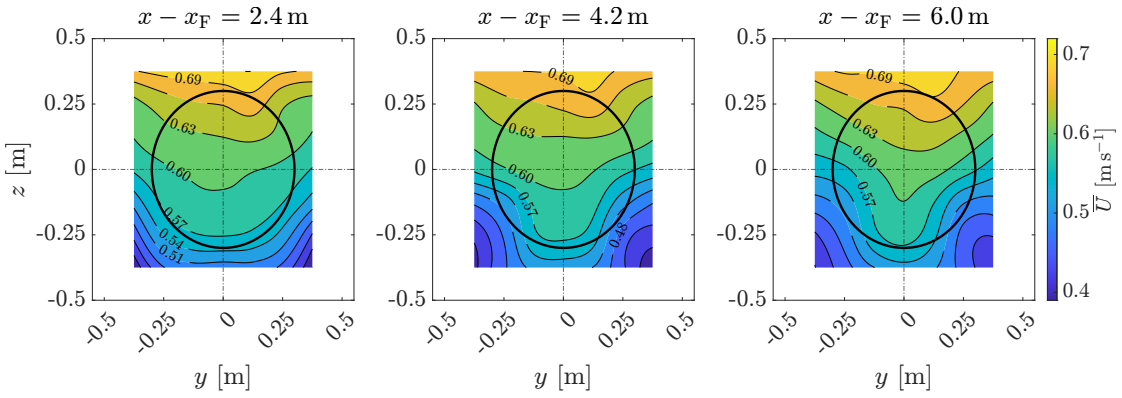
	$\overline{U_0} = 0.6$ m s^{-1}		$\overline{U_0} = 0.5$ m s^{-1}		$\overline{U_0} = 0.4$ m s^{-1}	
$x - x_F$ [m]	n(SP1) [-]	n(SP2) [-]	n(SP1) [-]	n(SP2) [-]	n(SP1) [-]	n(SP2) [-]
2.4	6	9	6	9	5	7
4.2	7	9	6	8	5	7
6.0	7	9	7	8	5	6

Table 5.1: Best-fit power-law exponent denominators at three streamwise locations along the vertical centre plane of the flume, as a function of $\overline{U_0}$, for two upstream obstructions designed to generate vertically sheared flow profiles: SP1 and SP2. The values for $\overline{U_0} = 0.6\,\mathrm{m\,s^{-1}}$ correspond to the profiles shown in Figure 5.3.

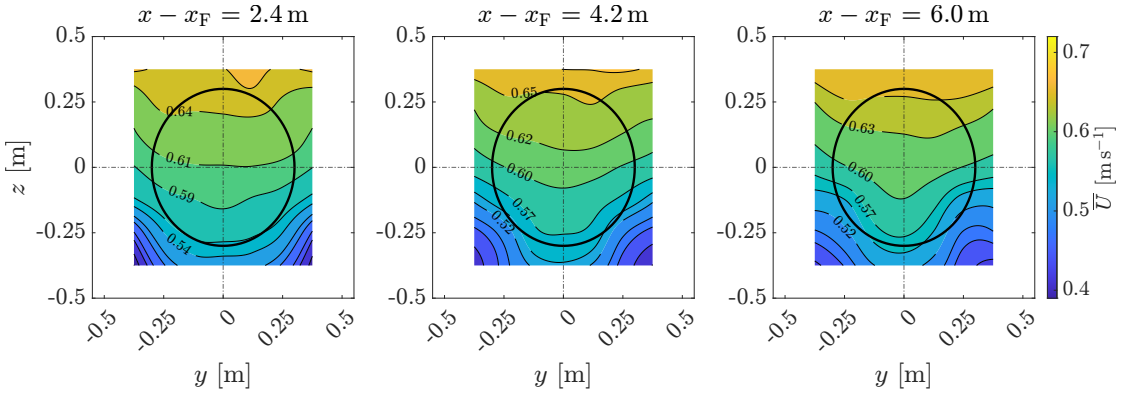
secondary circulations or, more likely, the partial or complete alignment of the ADV's sampling volume with the horizontal bars of the corresponding upstream obstruction (see Appendix A, Figure A.3).

When the analysis was expanded to include different reference flow velocities, the best-fit exponent denominators did not exhibit self-similar behaviour, as shown in Table 5.1. As the reference flow velocity decreased, the values of n for both SP1 and SP2 also decreased, indicating that the flow profiles became more sheared. While the non-dimensional velocities above mid-water depth broadly collapsed onto one other, this behaviour was not observed lower in the water column (not shown), where the velocities progressively decreased. This effect may result from the flow's increased sensitivity to viscous effects at lower reference flow velocities, which promote a thickening of the bottom boundary layer as inertial forces weaken.

For a more complete view of the velocity field in sheared flow, Figure 5.4 presents 2D contours of the velocity modulus, $\overline{U}$, downstream of SP1 and SP2 at three streamwise locations, revealing a non-uniform distribution of vertical shear across the width of the survey area. This non-uniformity is attributed to the differential shear between the cross-stream and target vertical shear profiles, resulting in turbulence anisotropy and the development of substantial corner flows through the measurement domain, likely influenced by the presence of the outer frame. Away from the vertical centre of the channel, the vertical shear increases



(a) SP1



(b) SP2

Figure 5.4: 2D contours of $\overline{U}$ at three streamwise locations downstream of (a) SP1 and (b) SP2. The profiles correspond to the measurement co-ordinates illustrated in Appendix A, Figure A.3. The box outline delineates the flume's cross section, and the black circle represents the intended swept area of the turbine rotor. Test conditions: $\overline{U_0} = 0.61\,\mathrm{m\,s^{-1}}$ (SP1); $0.61\,\mathrm{m\,s^{-1}}$ (SP2).

for both SP1 and SP2, with the depthwise profiles at $y = \pm 0.375\,\mathrm{m}$ characterised by $n = 4$ at $x - x_F = 2.4\,\mathrm{m}$, before reducing slightly to $n = 5$ at $x - x_F = 6.0\,\mathrm{m}$.

As the flow convects downstream, the profiles remain broadly symmetrical about $y = 0$; however, the intended swept area of the rotor becomes increasingly penetrated by the two corner flows as the isovels in the lower half of the water column progressively bulge towards the core of the channel along the corner bisectors. This leads to a lateral transfer of momentum towards the higher-velocity core region, which narrows with downstream distance, as illustrated by the evolution of the $\overline{u}(y)$ profile at mid-water depth downstream of SP1 in Figure 5.5. In narrow

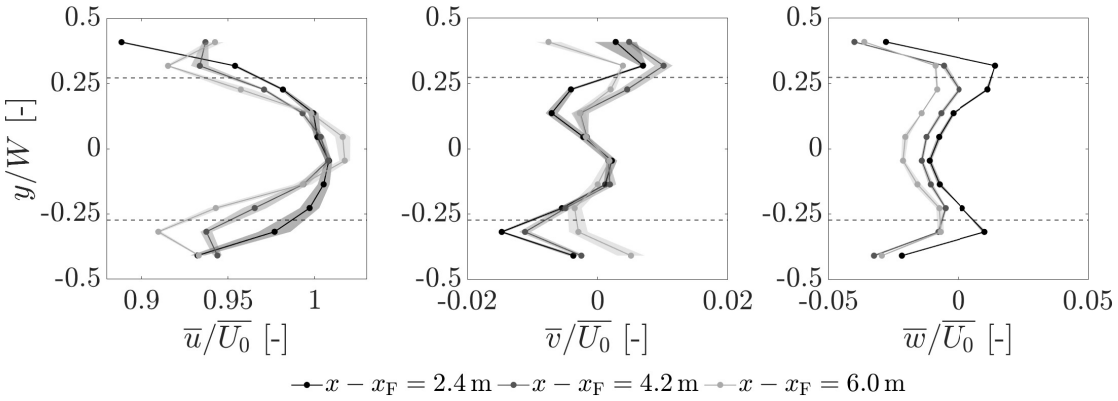


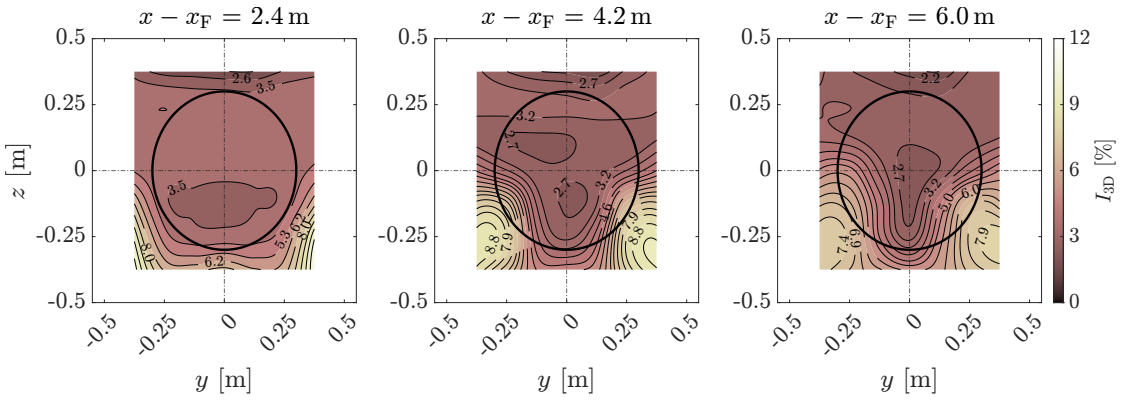
Figure 5.5: Cross-stream profiles of $\overline{u_i}$, normalised on $\overline{U_0}$, at three streamwise locations downstream of SP1: $x-x_F = 2.4\,m$ (black), $x-x_F = 4.2\,m$ (dark grey), and $x-x_F = 6.0\,m$ (light grey). The profiles comprise measurements at mid-water depth, as illustrated in Appendix A, Figure A.3. The random error is represented by ± 1 SEM (shaded areas). Linear piecewise fits have been added as a visual aid. The intended swept area of the rotor is also shown (dashed). Test conditions: $\overline{U_0} = 0.61\,m\,s^{-1}$.

open-channel flows, where the aspect ratio $W/H \leq 5$, the core flow is particularly susceptible to the lateral transfer of near-wall momentum, driven by secondary flows induced by anisotropy of the Reynolds shear stresses [76].

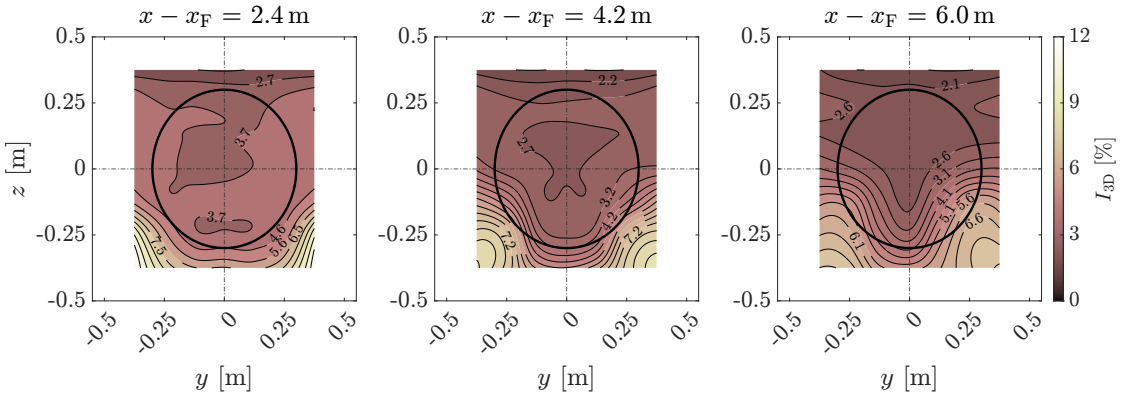
Consistent with the turbulence grid tests, both the time-averaged cross-stream and vertical velocities are at least one order of magnitude smaller than the dominant streamwise component. However, as expected, the vertical velocities exhibit greater variation, most evident in transects across the width of the flume (see Figure 5.5), where significant lateral shear is observed. Notably, the range of $\overline{w}(y)$ reaches up to $0.05\overline{U_0}$, compared to $0.02\overline{U_0}$ for $\overline{v}(y)$, while, for depthwise profiles along the vertical centre plane, the corresponding non-dimensional velocity magnitudes are broadly similar at approximately $0.01\overline{U_0}$ (not shown).

5.3.2 Turbulence Intensities

Figure 5.6 presents 2D contours of I_{3D} downstream of SP1 and SP2 at three streamwise locations. Similar to the velocity modulus, the figure reveals significant vertical and lateral variation, with the highest turbulence intensities confined to the bottom corners of the channel. As the corner flows extend further into the



(a) SP1



(b) SP2

Figure 5.6: 2D contours of I_{3D} at three streamwise locations downstream of (a) SP1 and (b) SP2. The profiles correspond to the measurement co-ordinates illustrated in Appendix A, Figure A.3. The box outline delineates the flume's cross section, and the black circle represents the intended swept area of the turbine rotor. Test conditions: $\overline{U_0} = 0.61\,\mathrm{m\,s^{-1}}$ (SP1); $0.61\,\mathrm{m\,s^{-1}}$ (SP2).

survey area, a region of lower turbulence intensity in the core of the channel gradually narrows (see also Figure 5.7b), complementing the previously observed local increases in flow speed. In general, the turbulence intensity scales inversely with the centre-to-centre spacing of the bars, with values along the top edge of the survey area only slightly elevated (2.0–2.7%) compared to the clean flow case, which is attributed to the absence of horizontal bars at $z/H > 0.15$.

Similar to the downstream flow of grids A and D, the turbulence intensity decays progressively through the measurement domain, coinciding with the modest reduction in vertical velocity shear, highlighted previously in Table 5.1. Despite the

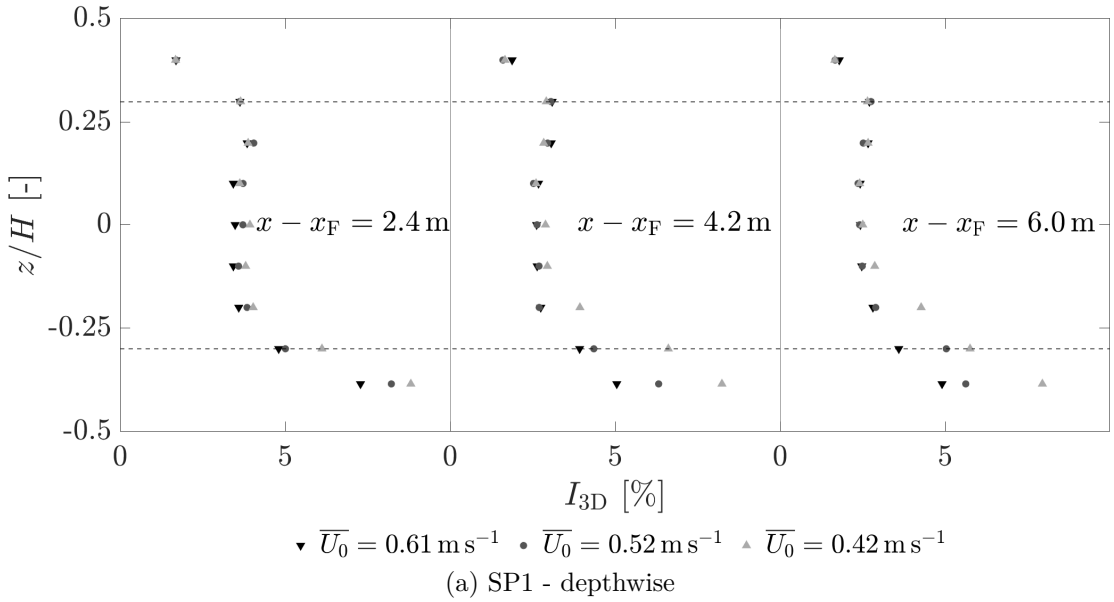
differing geometries of SP1 and SP2, the turbulence fields are remarkably similar, with spatially averaged turbulence intensities across the survey area ranging from $I_{3D} = 4.6$–4.7% at $x - x_F = 2.4\,\text{m}$ to 3.8–4.4% at $x - x_F = 6.0\,\text{m}$. The range of turbulence intensities also narrows from approximately 10% to 6% for both SP1 and SP2 at these locations, suggesting that the turbulence field is largely unaffected by the small difference in flow resistance between the obstructions.

When comparing turbulence intensities across different reference flow velocities, the depthwise profiles deviate from previously observed behaviour in both the clean flow and turbulence grid test cases, where minimal variation was observed across different flume duties. Figure 5.7a shows a marked increase in variation, most notably at the deepest measurement co-ordinate, which can reach up to 3.2% (in absolute terms). The reasons for this remain unclear, particularly given the self-similarity observed in the corresponding cross-stream profiles (see Figure 5.7b). For future turbine tests, this suggests that the rotor may encounter slightly different turbulence intensities depending on the approach flow velocity, although these discrepancies are limited to the lower portion of the rotor's swept area (the bottom 100 mm).

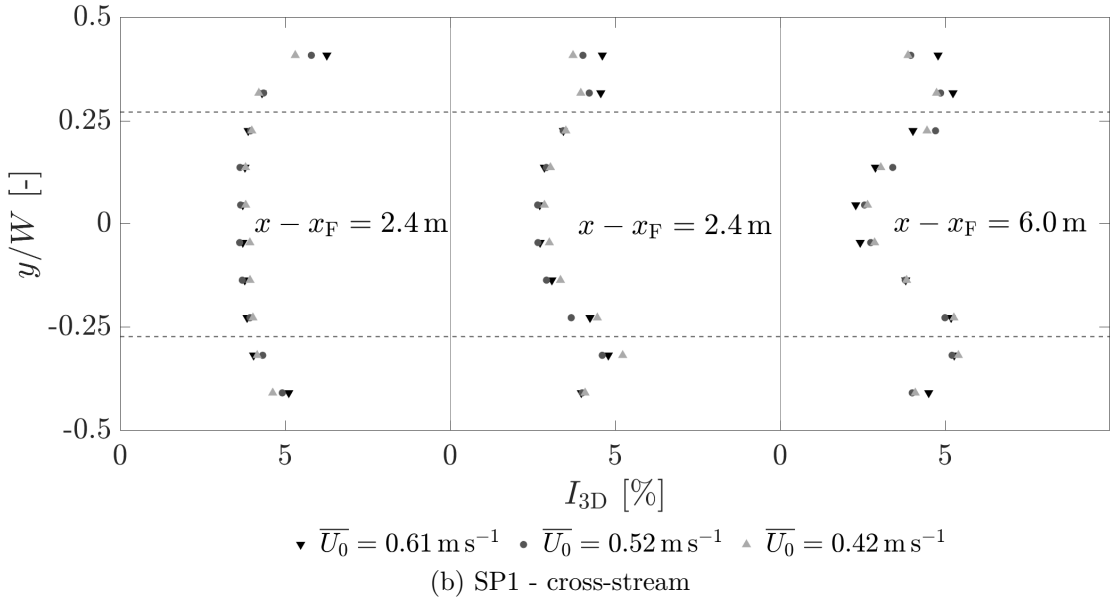
5.3.3 Integral Scales

Figure 5.8 shows the streamwise evolution of $\Lambda_u(z)$ along the flume's vertical centre plane downstream of SP1, along with the random error calculated from three repeated measurements. As the turbulence decays downstream, there is a corresponding growth in the length scales, starting from a characteristic dimension $\mathcal{O}(W_{bar})$—a trend also observed downstream of the turbulence grids (see Section 4.3.5).

The results suggest that, in future turbine tests, the rotor may encounter similar length scales across the lower two-thirds of its swept area, while the top third could experience greater variation, with differences in the length scales at the intended rotor plane equating to $0.4R$. Such spatial non-uniformity is likely to cause the



(a) SP1 - depthwise



(b) SP1 - cross-stream

Figure 5.7: (a) Depthwise and (b) cross-stream profiles of I_{3D} as a function of three reference flow velocities: $\overline{U_0} = 0.61\,\mathrm{m\,s^{-1}}$ (down-pointing triangles), $0.52\,\mathrm{m\,s^{-1}}$ (circles), and $0.42\,\mathrm{m\,s^{-1}}$ (up-pointing triangles), at three streamwise locations downstream of SP1. The profiles comprise measurements along the flume's vertical and horizontal centre planes, as illustrated in Appendix A, Figure A.3. The intended swept area of the rotor is also shown (dashed).

rotor to interact with regions of the flow that are more correlated than others, leading to rotational sampling [86] and azimuthal variations in blade loading.

For measurement depths of $z/H > 0.2$, a comparable level of variability is

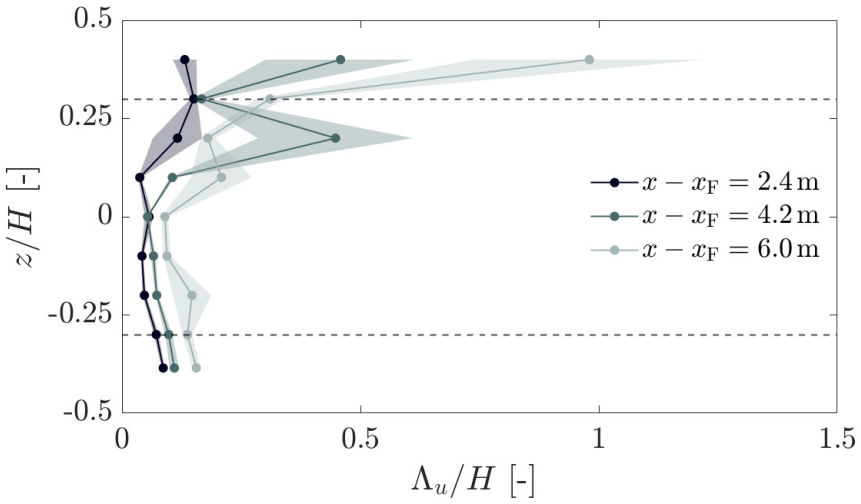


Figure 5.8: Depthwise profiles of Λ_u, normalised on the flow depth, at three streamwise locations downstream of SP1: $x - x_F = 2.4\,m$ (black), $x - x_F = 4.2\,m$ (dark grey), and $x - x_F = 6.0\,m$ (light grey). The profiles comprise measurements along the flume's vertical centre plane, as shown in Appendix A, Figure A.3. The random error is represented by ± 1 SEM (shaded areas). Linear piecewise fits have been added as a visual aid. The intended swept area of the rotor is also shown (grey dashed). Test conditions: $\overline{U_0} = 0.61\,m\,s^{-1}$.

observed as the clean flow case (see Figure 3.15), noting that the largest length scales, $\mathcal{O}(H, W)$, are confined to a region where the turbulence intensity is relatively low ($\leq 2\%$). In contrast, measurements obtained directly downstream of the bars, at $z/H < 0.15$, yield considerably lower random error, consistent with the analysis presented in Section 4.3.5. This variation in random error through the water column highlights the sensitivity of the autocorrelation function to both signal noise and the local flow turbulence, which is influenced by the positioning of the bars in the water column. In the top third of the water column, where no bars were present, signal noise constitutes a relatively large proportion ($> 50\%$) of $\sigma^2_{\text{meas},i}$, resulting in disproportionately wide 95% confidence intervals for both the random error and, hence, the expanded uncertainty. Conversely, in the bottom two-thirds of the water column, where the local turbulence is higher, the flow-related content of the signal dominates over Doppler noise ($\sigma^2_{\text{noise},u}/\sigma^2_{\text{meas},u} < 0.01$), yielding much narrower confidence intervals. The random error exceeds the systematic error by a factor

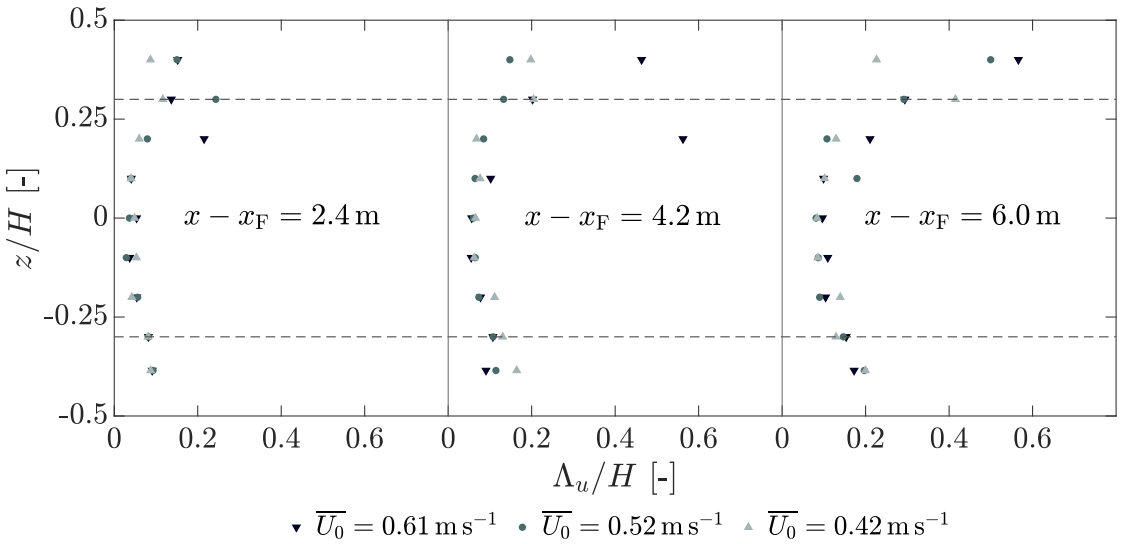


Figure 5.9: Depthwise profiles of Λ_u, normalised on the flow depth, as a function of three reference flow velocities: $\overline{U_0} = 0.61\,\mathrm{m\,s^{-1}}$ (down-pointing triangles), $0.52\,\mathrm{m\,s^{-1}}$ (circles), and $0.42\,\mathrm{m\,s^{-1}}$ (up-pointing triangles), at three streamwise locations downstream of SP1. The profiles comprise measurements along the flume's vertical centre plane, as illustrated in Appendix A, Figure A.3. The intended swept area of the rotor is also shown (dashed).

proportional to elevation from the channel bed, starting from 1–3 at $z/H = -0.5$ before rising to 11–15 in the top third of the water column.

The contrast in flow structures through the water column is further highlighted by comparing the streamwise integral length scales across different reference flow velocities. Figure 5.9 shows the streamwise evolution of $\Lambda_u(z)$ as a function of $\overline{U_0}$ along the flume's vertical centre plane downstream of SP1. Consistent with the previous analysis, the largest length scales and greatest variation are observed at $z/H > 0.2$, where the flow encounters the least resistance and most closely resembles clean flow conditions. Below this threshold, the non-dimensional depthwise profiles broadly collapse, with the most pronounced length scale recovery occurring unexpectedly in the bottom 20% of the water column, despite the relatively lower flow speeds in this region.

5.3.4 Quadrant Analysis

Quadrant analysis is a widely used data-processing technique to describe the trajectory and strength of turbulent coherent structures in sheared flow. The concept was introduced by Wallace *et al.* [125], who recognised the utility of using the signs of the products of the velocity fluctuations u' and w' to classify their contributions to the Reynolds shear stress $-\overline{u'w'}$, the dominant component of turbulence production in vertically sheared flow. A velocity time series can be classified into four bursting events, each corresponding to a separate quadrant on the uw-plane: Q1 ($u' > 0$, $w' > 0$), Q2 ($u' < 0$, $w' > 0$), Q3 ($u' < 0$, $w' < 0$), and Q4 ($u' > 0$, $w' < 0$). The largest contributions to the $-\overline{u'w'}$ shear stress typically arise from ejection (Q2) and sweep (Q4) events, which drive gradient-type momentum transport up and down the local mean velocity gradient. In the context of a turbulent boundary layer, ejections are often associated with the upward transport of low-momentum fluid from the near-wall region into the outer flow, leading to local reductions in the streamwise velocity. In contrast, sweep events draw higher-momentum fluid towards the wall, contributing to increased shear stresses in the near-wall region [126]. Q1 and Q3 events, referred to as outward and inward interactions, respectively, are countergradient-type motions that contribute negatively to $-\overline{u'w'}$ by redistributing momentum in directions that oppose the primary turbulent transport mechanisms. At a fixed distance from the wall, the sum of the fractional contributions of all four quadrants is unity.

The contributions of each bursting event to the instantaneous shear stress $-u'w'$ were examined in both clean and sheared flows to better understand the turbulent structures responsible for momentum transport in these two flow regimes. The first step was to compare differences in the mean flow field via depthwise profiles of $-\overline{u'w'}$ through the vertical centre of the flume at the intended rotor plane, as shown in the left-hand panel of Figure 5.10. The effect of vertical shear on the flow is apparent, with the profile shape resembling that of canonical open-channel flow

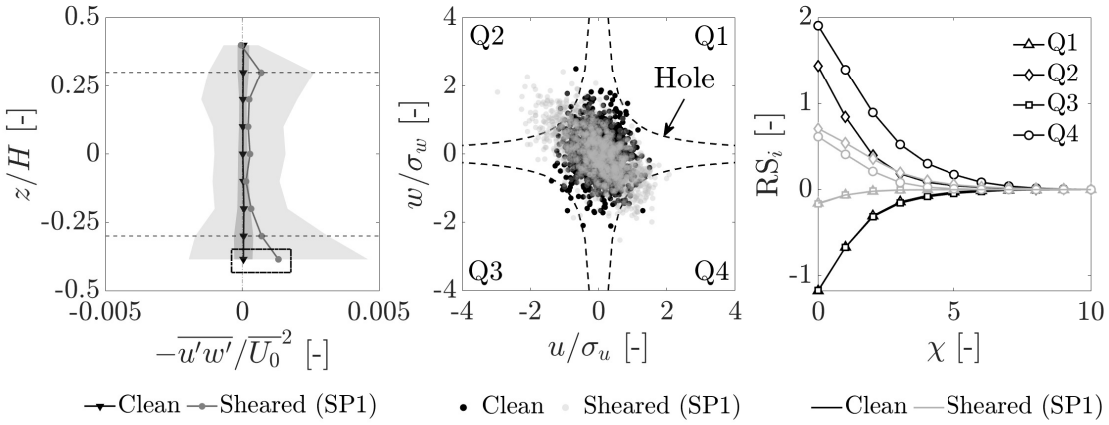


Figure 5.10: Analysis of the Reynolds shear stress $-\overline{u'w'}$ in both clean (black) and vertically sheared flows (grey). Measurements were taken at $x = 5\,\mathrm{m}$ for clean flow and $x - x_\mathrm{F} = 2.4\,\mathrm{m}$ downstream of SP1 for sheared flow. The left-hand panel shows depthwise profiles of $-\overline{u'w'}$, normalised by $\overline{U_0}^2$, based on measurements through the vertical centre of the flume, as shown in Appendix A, Figures A.1 and A.3. Depthwise variability is depicted by shaded regions representing $\pm 1\sigma(-\overline{u'w'})$, with linear piecewise fits added as a visual aid. The intended swept area of the rotor is also shown (dashed), along with a dash-dotted line indicating zero shear stress. A linear scale is applied to the x-axis. The middle panel presents a quadrant diagram of the velocities u and w, normalised on their corresponding standard deviations. The measurements were taken at $z/H = -0.385$, indicated by the thick dash-dotted box in the left-hand panel. The data were decimated by a factor of 40 for clarity, and the dashed lines represent a hole size of 0.25. The right-hand panel shows the corresponding fractional contributions of each bursting event, RS_i, to the shear stress as a function of hole size, χ. Test conditions: $\overline{U_0}$ (clean) $= \overline{U_\infty} = 0.58\,\mathrm{m\,s^{-1}}$; $\overline{U_0}$ (SP1) $= 0.61\,\mathrm{m\,s^{-1}}$.

experiments [76], exhibiting higher shear stress magnitudes and greater variation about the mean values compared to the clean flow case, where values remain much closer to zero, reflecting the increased flow uniformity. In sheared flow, the steeper velocity gradient near the channel bed enhances vertical momentum transfer, which drives local turbulence and results in elevated shear stresses.

The next stage was to map the instantaneous streamwise and vertical velocities in a quadrant diagram, as shown in the middle panel of Figure 5.10. The clean flow case yields a more balanced distribution across the four bursting events, suggesting that the flow is well-mixed, uniform, and lacks any significant directional bias in the transfer of momentum. In contrast, the sheared flow case produces an elliptically shaped distribution, with the major axis aligned along the Q2 and Q4 quadrants,

Case	Q1 [%]	Q2 [%]	Q3 [%]	Q4 [%]	Skew(j) [-]	Kurt(j) [-]
Clean	20.6	25.3	20.6	33.5	0.8	11.5
Sheared (SP1)	9.6	43.1	10.1	37.3	1.7	9.9

Table 5.2: Percentage contributions from each bursting event to the Reynolds shear stress $-\overline{u'w'}$ for a hole size of zero, along with higher-order statistics of the normalised instantaneous shear stress $u'w'/\overline{u'w'}$, denoted by j. Two flow regimes are considered: clean flow and vertically sheared flow downstream of SP1.

indicating the dominance of ejection and sweep events in shear stress production, consistent with findings from both laboratory [76] and field [127] studies.

Also shown on the quadrant diagram is a set of hyperbolas in each quadrant, referred to as the hole, an arbitrarily sized parameter used to filter the instantaneous flux data for more intense bursting events [128], given by $|u'w'| \geq \chi\,\sigma_u\sigma_w$, where χ represents the hole size. Instantaneous shear stresses that do not meet this threshold correspond to more quiescent bursting events. The fractional contributions of each bursting event, RS_i, to the shear stress can be computed as a function of hole size by:

$$\left.\begin{aligned} \mathrm{RS}_i(\chi) &= \int_{\chi}^{\infty} j\,\mathrm{PDF}_i(j)\,\mathrm{d}j \geq 0,\ (i=2,4) \\ \mathrm{RS}_i(\chi) &= \int_{-\infty}^{-\chi} j\,\mathrm{PDF}_i(j)\,\mathrm{d}j \leq 0,\ (i=1,3) \end{aligned}\right\}, \tag{5.2}$$

where j denotes the normalised instantaneous shear stress $u'w'/\overline{u'w'}$, and $\mathrm{PDF}_i(j)$ is the corresponding probability density function for the i^{th} quadrant.

Applying the algorithm of Milne *et al.* [127], the resulting fractional contributions, shown in the right-hand panel of Figure 5.10, illustrate the dominance of ejection and sweep events in both flow regimes. The more extreme contributions in clean flow are likely due to the more evenly distributed nature of the turbulence, characterised by higher intermittency and less directional coherence compared to sheared flow. This assumption is supported by the smaller skewness and larger kurtosis of the $u'w'/\overline{u'w'}$ distribution in clean flow, as shown in Table 5.2. For a hole size of zero, the relative contribution of ejection events in sheared flow

increases compared to clean flow, reflecting greater upward momentum transport, while interaction events offer comparatively less resistance to the primary turbulent transport mechanisms. As the hole size increases and fluctuations are progressively filtered out, the fractional contributions to the shear stress diminish, with only ejections responsible for shear stress production for $\chi \geq 4$ in sheared flow, consistent with the threshold identified by Lu and Willmarth [128].

5.4 Limitations of the Investigation

The geometrical arrangement, and hence the number of bars in each graded obstruction, was based on a practical implementation of Cowdrey's model, detailed in Appendix B. Despite differences in porosity and the resulting mass flux through SP1 and SP2, the impact on the respective velocity fields appears negligible. Comparisons of the centreline velocities from SP1 with those from SP2, as well as comparisons of spatially averaged velocities (across the survey area) between the two, show relative differences $\mathcal{O}(10^{-3})\,\mathrm{m\,s^{-1}}$ at each streamwise location. For future turbine tests, this is important to note as it corresponds to a difference in the approach flow's estimated kinetic flux of just 1% at the design speed of the flume, which equates to $< 0.5\,\mathrm{W}$ in the power generated. In contrast, the sensitivity of centreline measurements to the local flow dynamics results in discrepancies between the centreline and spatially averaged values that are an order of magnitude greater, leading to differences in the estimated kinetic flux of 10–12% (2.9–3.5 W). As discussed in Section 4.5.4, such discrepancies can lead to an under- or overestimation of the available kinetic energy in the turbine's approach flow, thereby biasing assessments of model-scale rotor performance and loading.

To address the S-shaped distortions observed in the depthwise velocity profiles, an alternative method for generating vertical shear may be necessary. Both Islam *et al.* [120] and Magnier *et al.* [122] demonstrated that graded mesh arrangements can also generate vertical shear in open-channel flow, producing finely mixed

turbulence mists and smoother downstream flow profiles. While this approach may reduce the RMSE between the target and measured profiles, it offers less flexibility than the bar arrangements used in this study and incurs higher material costs.

5.5 Summary

This chapter has outlined a methodology for generating and controlling vertical velocity shear in a hydraulic flume, and provided a detailed characterisation of the resulting flow fields, in preparation for the model-scale testing of a horizontal axis tidal stream turbine.

An empirical approach was applied to Cowdrey's method of defining a graded resistance across the width of the working section to generate two target vertical shear profiles. The profiles, characterised by the denominator of the power-law exponent with values of $n = 6$ and $n = 9$, established an achievable range around the widely cited value of $n = 7$, partially capturing the considerable variation throughout the tidal cycle. A practical criterion of an RMSE $\leq 0.03\,\mathrm{m\,s^{-1}}$ between the theoretical and measured velocity distributions was applied to finalise the geometry of the graded resistance for each target profile. The resulting bar arrangements closely matched theoretical predictions from Cowdrey's model, marking the first application of this method in open-channel flow.

The flow characterisations revealed non-uniform vertical shear across the survey area and substantial corner flows, attributed to the differential shear between the target vertical and cross-stream shear profiles. Away from the vertical centre of the channel, the vertical shear increased for both SP1 and SP2, with the depthwise profiles at $y = \pm 0.375\,\mathrm{m}$ characterised by $n = 4$ at the intended rotor plane. As the reference flow velocity decreased, the denominator of the power-law exponent for both SP1 and SP2 also decreased, indicating an increase in vertical shear, driven primarily by reductions in the non-dimensional streamwise velocities in the lower half of the water column.

2D contours revealed that the highest turbulence intensities were confined to the bottom corners of the survey area. The results also suggest that the turbulence field was largely unaffected by the small difference in flow resistance between SP1 and SP2, yielding similar spatially averaged values across the survey area, ranging between 4.6–4.7% at the intended rotor plane.

The evolution of the streamwise integral length scales along the vertical centre plane of the flume revealed contrasting levels of random error through the water column, indicating a quasi-stratification of the flow. This behaviour reflects the sensitivity of the autocorrelation function to both signal noise and the local flow turbulence, which is influenced by the positioning of the bars in the water column. The largest length scales, $\mathcal{O}(H)$, were calculated near the top of the water column, where the lack of flow resistance resulted in low local turbulence, with signal noise constituting more than half of the measured velocity variance.

A quadrant analysis of the Reynolds shear stress $-\overline{u'w'}$ showed good agreement with previous experimental observations, indicating that the dominant contributions to momentum flux arise primarily from ejection and sweep events. This was particularly evident in the quadrant diagram for sheared flow, which exhibited an elliptically shaped distribution. In contrast, the clean flow case yields a more balanced distribution across the four bursting events, indicating higher intermittency and less directional coherence compared to sheared flow.

Part II

Model-Scale Testing

CHAPTER 6

Literature Review on the Hydrodynamics of Tidal Rotors

6.1 Steady Loading

Tidal stream energy has benefitted from significant knowledge transfer from the wind industry [9]. This influence is evident in tidal rotor blade geometry, typically defined by selecting a suitable aerofoil family and then adapting it for use as hydrofoils by optimising the radial distributions of the chord, thickness, and blade twist angle [26]. For structural reasons, hydrofoil sections tend to be thicker than the hydrodynamic optimum towards the root, where bending stresses are greatest.

Figure 6.1 illustrates a 2D representation of the relationship between the blade forces and the flow relative to a hydrofoil section, which comprises both an axial- and a tangential-flow component. The axial component is reduced from the freestream velocity due to the induction effect, whereas the tangential velocity is enhanced by a whirl component to conserve the angular momentum of the flow. The lift force acts normal to the relative flow velocity, while the drag force acts parallel to it.

A combination of 2D blade element theory and momentum theory is often used to describe the quasi-steady forces and velocities acting on the rotor[1], with rotor

[1]Detailed coverage of blade element momentum (BEM) theory as applied to tidal stream turbines can be found in Vogel *et al.* [129].

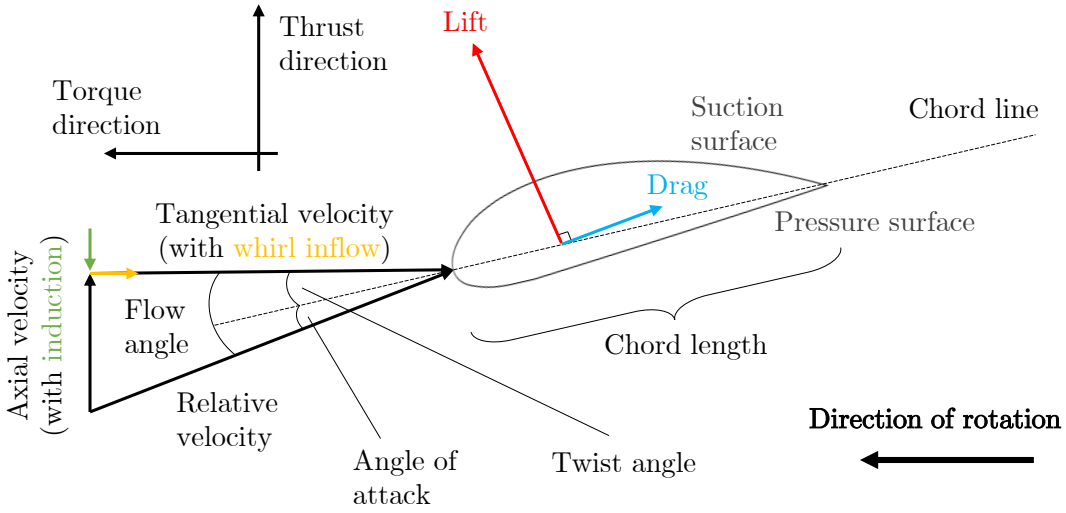


Figure 6.1: 2D illustration of the flow relative to a rotating hydrofoil section (grey), showing the resulting lift (blue) and drag (red) forces, along with the axial (green) and tangential (orange) induction factors. The blade rotates towards the left.

torque, Q, generated in the plane of rotation, and rotor thrust, T, exerted normal to it. While 2D models provide a useful framework to predict the performance of axial-flow rotors, 3D effects resulting from spanwise flows, shed vorticity, and wake development often necessitate a higher-fidelity approach, such as blade-resolved simulations [130].

The steady-state performance and loading of an axial-flow rotor are typically characterised by the non-dimensional power and thrust coefficients, given by:

$$C_P = \frac{Q\Omega}{\frac{1}{2}\rho U_{\mathrm{T}}^3 A}, \tag{6.1}$$

$$C_T = \frac{T}{\frac{1}{2}\rho U_{\mathrm{T}}^2 A}, \tag{6.2}$$

respectively, where Ω is the rotor speed, ρ is the fluid density, U_{T} is the turbine reference velocity, and A is the swept area of the rotor. Typically, U_{T} is defined as the freestream velocity at the turbine's hub height but may also be defined as an area-weighted average of flow speed over the swept area of the rotor in more non-uniform flows [10]. Both the turbine thrust and power coefficients are

characteristics of the rotor design and are often presented as functions of the turbine's tip-speed ratio, λ, defined as:

$$\lambda = \frac{\Omega R}{U_{\mathrm{T}}}. \tag{6.3}$$

Tidal stream turbines generally operate at lower tip-speed ratios than wind turbines to mitigate the risks of cavitation and excessive drag forces at high rotational speeds, which can damage blade surfaces and compromise hydrodynamic performance. Cavitation can occur when the local static pressure drops below the vapour pressure of the fluid, causing vapour bubbles to form and collapse, leading to surface erosion. This risk is especially pronounced on the suction surface when the blades pass close to the free surface, i.e. at top dead centre (TDC), where the static pressure is lowest. However, analysis by Wimshurst *et al.* [131] suggests that, due to spanwise flow and tip-loss effects, the lowest static pressure occurs slightly inboard of the blade tip, at 95% span.

Bahaj *et al.* [12] were among the first to measure steady loads on a three-bladed, model-scale tidal stream turbine, providing insights into the performance and loading responses of a 0.8 m diameter rotor across various operational scenarios in both a towing tank and a cavitation tunnel. Their study highlighted the operating conditions likely to promote cavitation and demonstrated the sensitivity of both power and thrust to the turbine's yaw angle. Such experimental data are invaluable for validating numerical models, as demonstrated in a subsequent study [132], which highlighted appreciable differences between the experimental results and BEM-based predictions. A notable source of error when comparing numerical and experimental datasets more generally is the reliance on analytical corrections to account for blockage effects. In the case of tidal rotors, flow confinement from channel boundaries, as encountered in experiments, restricts the turbine's bypass flow, resulting in increased thrust loading and power extraction for a given upstream velocity compared to a turbine operating in unbounded flow [11]. Corrections are

often necessary because a blocked flow domain can significantly alter a turbine's operating points. Additionally, they are used to convert laboratory-scale results to full-scale conditions or vice versa [133]. The study by Bahaj *et al.* [12] revealed reductions of 18% and 11% for the power and thrust coefficients, respectively, after applying the correction of Barnsley and Wellicome [134] to measurements obtained from a cavitation tunnel with a blockage[2] of 17.4%. Application of this method was later recommended by Ross and Polagye [135]. Further analysis by Schluntz and Willden [136] suggests that, in order to achieve maximum efficiency in highly blocked flows, rotors require greater solidity and lower blade twist than those designed for unbounded flows, ensuring that the design angle of attack can be maintained along the blade span.

Current tidal stream turbine blades are typically constructed from composite materials originally developed for the aerospace and wind industries [137]. The high-cycle fatigue loading experienced by the blades results in complex deformations, which can be described as a combination of flapwise, edgewise, and twist deformations (see Figure 1.2 for blade co-ordinate system). Blade-resolved Computational Fluid Dynamics (CFD) simulations of a three-bladed 20 m diameter rotor, based on a single RISØ A1-24 aerofoil, conducted by Zilic de Arcos *et al.* [138], demonstrated that flapwise deformation significantly affects both integrated power (with reductions of up to 20%) and the spanwise distribution of thrust due to 3D flow effects. The authors also reported a considerable influence of twist deformation on blade loading and rotor performance, as well as a feedback mechanism between the deformations and the hydrodynamic loads driving them. Provided the rotor is approximately normal to the principal flow direction, edgewise deformations are typically much smaller than those driven by thrust.

[2]Blockage is defined as the ratio of the swept area of the rotor to the cross-sectional area of the channel.

6.2 Unsteady Hydrodynamics

Tidal stream turbines operate in highly variable and unsteady hydrodynamic environments, with flow unsteadiness often described in terms of a gust in the axial-flow component. The degree to which a hydrofoil exhibits an unsteady load response to a forcing gust can be characterised by the reduced frequency, k, defined as:

$$k = \frac{2\pi f c}{V_{\text{rel}}}, \tag{6.4}$$

where c is the local blade chord length, f is a characteristic frequency of the gust, and V_{rel} is the local relative velocity, which accounts for both the axial-flow (u) and rotational velocity components (Ωr, where r is the local radius of the blade section with respect to the rotor axis). Moving inboard towards the blade root, reduced frequency values typically increase due to lower relative velocities and larger chord lengths. In their study applying classical 2D aerofoil theory to tidal stream turbines, Sequeira and Miller [139] described the parameter space for unsteady loads at the mid-span of a blade in terms of the reduced frequency and a non-dimensional velocity fluctuation amplitude. The authors reported that for a fixed-bottom turbine with an 18 m diameter rotor, wave-induced unsteadiness is predominantly low frequency ($k < 0.2$) and can be approximated as a quasi-steady problem. However, the perturbation amplitude of a 50-year extreme wave could push the blades' angle of attack beyond the static stall angle. While this is much less likely with freestream turbulence, the temporal and spatial variations elicit a range of unsteady responses, with reduced frequencies reaching up to $k = 0.65$. Rotation through nominally steady features, such as the shear layer or the potential field of the turbine tower, can generate reduced frequencies between 0.2–0.6, depending on the rotor speed.

While the experimental work presented in this thesis does not directly measure unsteady hydrodynamics at the blade section level, an overview of the fundamental

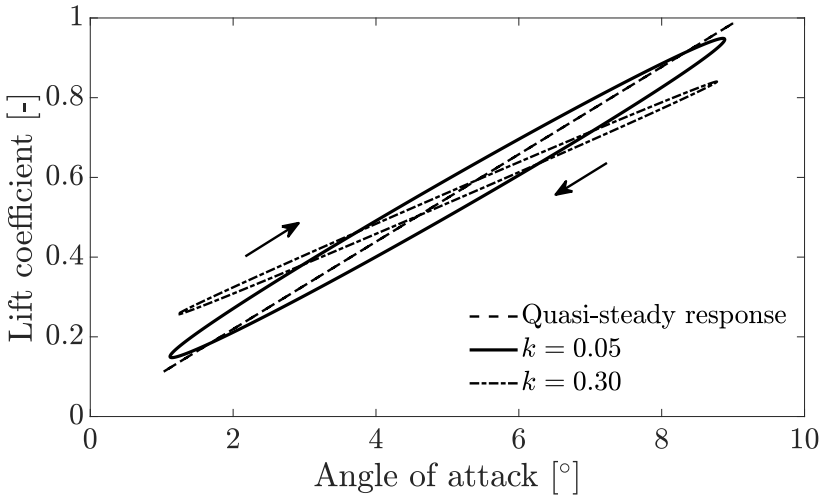


Figure 6.2: Quasi-steady lift coefficient response of a 2D hydrofoil (dashed) compared to the unsteady response at reduced frequencies of $k = 0.05$ (solid) and $k = 0.30$ (dash-dotted). The arrows indicate the progression through time. The flow is assumed to be fully attached to the hydrofoil surface. The unsteady lift response was calculated using Theodorsen's function [141].

concepts provides useful context for the broader literature review and for interpreting the loading response of the model-scale rotor in unsteady flow environments.

Attached Flow

From a 2D perspective, fluctuations in the axial velocity alter the relative velocity approaching the hydrofoil and, consequently, the flow angle. With the twist angle fixed, these changes lead to excursions in the angle of attack and, therefore, the hydrofoil's lift and drag coefficients. In fully attached flow, the hydrofoil's quasi-steady response—largely driven by changes in lift [26]—is directly proportional to the gust magnitude. In contrast, unsteady effects manifest primarily as an amplitude reduction and phase lag in the time-varying lift response, giving rise to a hysteresis effect that scales with the reduced frequency. An illustration of this behaviour is shown in Figure 6.2, noting that the flow may be considered quasi-steady only when $k < \mathcal{O}(0.01)$ [140].

The hysteresis effect shown in Figure 6.2 stems from circulatory and non-circulatory contributions to the unsteady rotor loads in attached flow [140]. The

circulatory component, driven by vorticity shed into the wake in response to changes in hydrofoil circulation, causes unsteady damping of the hydrofoil's lift. In contrast, the non-circulatory, or added mass, effect results from the acceleration of the potential flow field around the hydrofoil, producing a force proportional to the rate of change in circulation. Common approaches to modelling the 2D unsteady response of axial-flow turbines are described in detail by Leishman [140].

Separated Flow

Dynamic stall occurs when a lifting surface is subjected to a time-dependent forcing that pushes the angle of attack beyond the static stall angle [140]. Unlike quasi-steady loads, dynamic stall involves the reversal, separation, and subsequent reattachment of the flow, resulting in an abrupt decrease in lift and a significant increase in drag. A defining feature of dynamic stall is the formation and shedding of a leading-edge vortex, which moves across the chord, generating a pressure wave along the hydrofoil's upper surface and causing significant overshoots in sectional forces relative to quasi-steady values. Figure 6.3 illustrates the load overshoot, hysteresis, and phase variation observed in the unsteady lift coefficient during dynamic stall. McCroskey [142] provides a comprehensive overview of the dynamic stall phenomenon, with distinctions between light and deep stall regimes, while Leishman [140] discusses common modelling approaches to capture dynamic stall behaviour. In some cases, stall may initiate from the trailing edge, depending on the foil type and load amplitude.

In practical terms, a typical pitch-regulated tidal stream turbine is designed to operate at incidences well below the onset of stall, significantly reducing the likelihood of dynamic stall. In contrast, a stall-regulated turbine is engineered to promote flow separation along the blade once it reaches or exceeds rated power, leading to more pronounced unsteady loads and variability in power output. In laboratory-based experiments, dynamic stall is much less likely to occur, primarily due to the limited range of testable reduced frequencies and lower chord-based

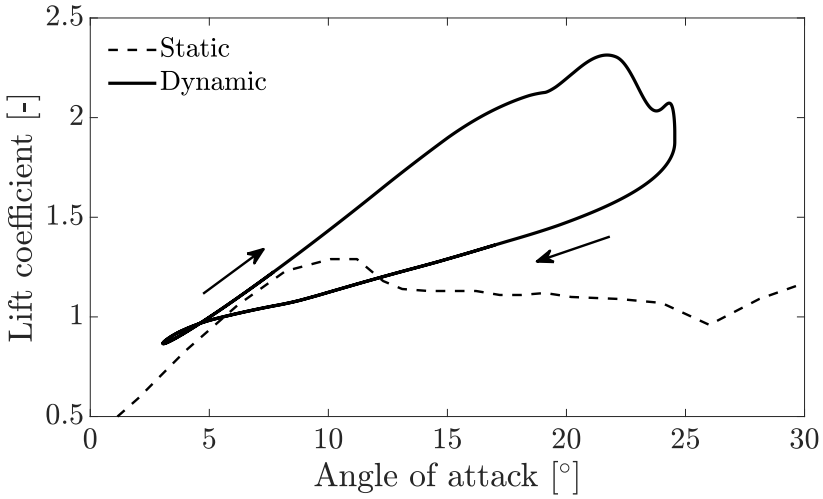


Figure 6.3: Comparison of hydrofoil lift characteristics during static stall (dashed) and dynamic stall (solid). The arrows indicate the progression through time. Data source: Viola and Scarlett [143].

Reynolds numbers—typically $\mathcal{O}(10^5)$ at mid-span compared to $\mathcal{O}(10^6)$ at full scale—which limit the likelihood of inducing flow separation.

6.3 Sources of Unsteady Hydrodynamic Loading

Adcock *et al.* [10] categorise hydrodynamic sources of unsteadiness as either deterministic or stochastic. Deterministic sources include periodic loading events arising from the assumed steady spatial variation of the onset flow across the swept area of the rotor, whereas stochastic sources, characterised by their inherent randomness, are best described probabilistically [26].

6.3.1 Deterministic Sources of Unsteadiness

Vertical Shear

As turbine blades rotate through the vertical shear layer, they experience a once-per-revolution (1P) load fluctuation due to depth-dependent changes in the axial-flow component and, hence, the flow angle along the blade. The resulting azimuthal variations in the blades' sectional forces lead to a 3P variation in rotor thrust and

torque. Velocity profiles from ADCP transects in the Severn Estuary reveal that much of this depth-related variation is concentrated in the lower third of the water column [144], with local bathymetry significantly influencing the extent of this variation.

Over the past two decades, numerous studies have examined the effects of vertically sheared flows on tidal rotors. Both quasi-steady and unsteady CFD models have revealed performance degradations as well as cyclic variations in blade loading when turbines are subjected to realistic inflow profiles [144, 145]. Similar findings have been reported using lower-order BEM models, although their predictive accuracy can be limited if the effects of dynamic stall are not accounted for [146].

There have also been notable experimental contributions. For instance, Tedds [43], using the methodology established by Cockrell and Lee [34], generated a sheared inflow with an exponent denominator of $n = 5$ to evaluate its influence on the wake of a 0.5 m diameter rotor in a low-turbulence ($I_{3D} \approx 2\%$) recirculating water flume. Building on Tedds' work, Vinod *et al.* [123] employed an active turbulence grid to simulate vertically sheared inflow profiles representative of flood and ebb tides. Subsequent turbine experiments investigated how these profiles influenced the performance and near-wake dynamics of a 0.28 m diameter rotor in a recirculating water flume. The authors reported a 5–15% drop in the peak power coefficient and an approximately 50% increase in thrust fluctuations compared to clean flow conditions, noting that the turbulence intensity reached as high as $16 \pm 11\%$ for more sheared inflows ($n = 2.3$).

A key differentiator in experimental studies examining turbulence-rotor interactions is the level of rotor instrumentation—specifically, the ability to measure loads directly on individual blades rather than relying solely on rotor-averaged data, as in the studies referenced above. This distinction is crucial, as individual blade load measurements enable detailed mapping of azimuthal load variations, providing insights into the rotor's unsteady response that would otherwise be obscured by

averaging. Gaurier *et al.* [147] demonstrated the value of this approach, showing the non-uniform distribution of phase-averaged blade root bending moments and their standard deviations in response to bathymetry-driven sheared flow in a recirculating water flume, with the authors reporting a 20% variation in flapwise loads across a single blade rotation. Their analysis also revealed that the azimuthal positions of the maximum and minimum blade loads did not align with TDC and BDC, respectively—a finding also noted by other investigators [145, 148]. Using the same 1:20 scale turbine model and facility, but with three graded-porosity mesh arrangements to generate vertical shear, Magnier *et al.* [122] were the first to demonstrate the scaling of both the phase-averaged blade loads and their fluctuations with the level of vertical shear in the onset flow.

Tower Shadow

To achieve a compact nacelle design, there is often limited clearance between the rotor blades and the supporting tower. As a result, the blades rotate through a region of disturbed flow as they pass the azimuthal position of the tower [149], eliciting a 1P load fluctuation similar to that caused by vertical shear. Compared to the period of rotation, the tower shadow effect is relatively brief, acting as an impulse-like disturbance on the blade [150].

To further explore these interactions, several studies have been conducted. Two of these studies used a fully blade-resolved CFD model with a Reynolds-averaged Navier-Stokes (RANS) formulation to examine the effects of different downstream support structures on rotor loading [144, 151]. Results from Muchala and Willden [151] indicated that the integrated rotor force coefficients for a full-scale turbine rotor of 18 m diameter were higher with a cylindrical support than with an elliptical one, due to the increased opposing thrust generated by the cylinder. Additionally, large-eddy simulations (LES) of a full-scale 1 MW tidal stream turbine at the Fall of Warness site, performed by Ahmed *et al.* [145], revealed power excursions of approximately $\pm 10\%$, resulting from the combined

cyclical effects of tower passing and vertical shear. A lower-order approach has also been applied, coupling potential flow theory with BEM models for wind turbine applications. An analysis by Ghandour *et al.* [150] demonstrated close agreement with experimental results from a 5 MW reference offshore wind turbine, indicating that variations in output power and blade root bending moments were largely independent of rotor diameter.

An experimental investigation into the effects of varying the distance between the rotor plane and the tower axis revealed an inverse relationship between this separation and fluctuations in both C_P and C_T, as well as the maximum flapwise root bending moments, for a 0.73 m diameter rotor in a recirculating water flume [152]. The analysis also showed that swirl in the rotor wake causes the azimuthal position of the tower shadowing effect to shift as the separation increases, highlighting the need for careful consideration of nacelle geometry during the design stage.

Similar to the tower passing effect, periodic load fluctuations may also occur when blades pass close to flow boundaries or neighbouring turbines [10]. This effect was demonstrated by McNaughton *et al.* [25], who revealed a high sensitivity of blade loading to interior array interactions in an experimental investigation of constructive interference between two twin 1.2 m diameter rotors in a towing tank.

Yaw Misalignment

Yawed flow occurs when the principal flow direction is not perpendicular to the rotor plane, which can result from changes in the local flow direction or limitations in the turbine's yawing capabilities. This causes an asymmetric induction effect, with the blade pointing upstream experiencing a higher relative velocity than the blade pointing downstream, leading to a 1P load fluctuation on each blade.

To investigate the effects of yaw, various numerical approaches have been applied, such as actuator line models (ALMs) [153], which have shown close agreement with blade-resolved simulations [154] and experimental results [155], revealing degraded rotor performance that scales with the degree of yaw misalignment. This aligns

with the assertion by Burton *et al.* [26] that power tends to decrease with the cosine of the yaw angle squared, while thrust decreases with the cosine of the yaw angle [12]. Lower-order BEM models have shown that a fixed yaw misalignment can elicit extreme local lift coefficients, leading to peaks in blade root bending moments that are twice the median load [156], potentially signalling the onset of dynamic stall. As angular misalignment increases, the mean loads also decrease—a trend observed by Galloway *et al.* [157], whose BEM implementation showed that yaw had a more significant effect on rotor-averaged loads, and thus turbine power, than on individual blade loads. Notably, the authors' experimental results, obtained using a 0.8 m diameter rotor in a towing tank, showed mixed agreement with model predictions, with closer alignment in cases without yaw misalignment.

6.3.2 Stochastic Sources of Unsteadiness

Freestream Turbulence

Turbulence is a complex, chaotic 3D phenomenon that manifests as irregularities in the onset flow, spanning a wide range of frequencies and spatial scales. Its influence on the flow dynamics and, consequently, the loads and performance of tidal rotors necessitates careful consideration in the design phase.

To adequately resolve onset flow turbulence and simulate its effects on tidal rotors, high-fidelity numerical models are typically employed. Using LES, Ahmed *et al.* [145] demonstrated how freestream turbulence distributes the spectral energy content of the blade loads between low frequency, periodic load phenomena and high frequency, blade-generated turbulence. Further LES by Ouro *et al.* [158] highlighted the substantial impact of bathymetry-driven turbulence on the loading of 1:30 scale turbine model, estimating an almost 30% increase in the peaks of both the flapwise and edgewise root bending moments when turbulence intensity is raised from zero to 10%. Other common observations of turbulence-rotor interactions include performance degradation [145], enhanced wake recovery [98], and

an increased range of load fluctuations, the latter of which raises the likelihood of fatigue-induced failure [159]—a finding supported by BEM-based analyses of a full-scale rotor's damage equivalent loads [160] and unsteady hydrodynamic response [156, 161]. Another computationally inexpensive alternative to CFD analysis is the vortex lattice method (VLM), which McNae [162] applied to model the unsteady response of a tidal rotor following a step change in flow velocity. The author reported significant overshoots in rotor thrust, attributing this to the dynamic inflow effect[3].

Several experimental studies have also explored the unsteady loading effects of freestream turbulence. For example, Maganga *et al.* [164] reported an approximately 15% reduction in power output and an increase in fluctuating thrust loads for a 1:30 scale turbine model, driven by an 18% increase in turbulence intensity in a recirculating water flume. Similarly, a benchmarking study by Tucker Harvey *et al.* [165] observed comparable effects for a 1.6 m diameter rotor towed downstream of a turbulence-generating grid. Chamorro *et al.* [166], comparing the power spectra of upstream turbulence with that of the output power of a 0.5 m diameter rotor, demonstrated that at sufficiently low frequencies, the instantaneous power is modulated by the onset turbulence. Beyond a critical frequency, which scales linearly with rotor speed, the turbine response decouples from the turbulence. In a subsequent study using the same turbine model in the same recirculating water flume, Chamorro *et al.* [167] further highlighted the strong scale-to-scale interaction between larger flow structures and turbine power.

Blackmore *et al.* [50] extended their analysis beyond turbine performance, using grid-generated turbulence to examine the effects of turbulence intensity and the integral length scales on the unsteady loads of a 1:20 scale tidal rotor in a recirculating water flume. They found that larger length scales $\mathcal{O}(R)$ had a more significant impact than increased turbulence intensity, resulting in higher blade root

[3]Further details on the coupling of dynamic inflow with BEM theory for unsteady aerodynamic analysis of wind turbine rotors are provided in Suzuki and Hansen [163].

bending moments as well as a 10% improvement in rotor performance, while higher turbulence intensities had the opposite effect. Using LES to model the response of a 15 MW reference wind turbine to an increase in the integral length scales from $0.6R$ to $3.4R$, Stanislawski *et al.* [168] also observed corresponding increases in rotor thrust and flapwise root bending moments. While the results suggested that the impact of turbulence on rotor loads is up to ten times greater than that of the mean shear profile, the authors also found that turbulence intensity had a substantially greater influence on rotor loads than the integral length scales alone. These findings contrast with other tidal-based studies, such as Milne *et al.* [169], whose simulations in Tidal Bladed indicated that blade root bending was insensitive to the integral scales, and Ebdon *et al.* [98], who reported minimal impact on both turbine performance and downstream wake evolution in a recirculating water flume.

In addition to current-only experiments, several studies have been designed to elicit an unsteady response from model-scale tidal rotors through oscillatory or ramped movements of the turbine, and to understand the relative significance of added mass and dynamic inflow contributions. Whelan [170] was the first to investigate the dynamic thrust response of a twin-bladed, 0.3 m diameter rotor subjected to harmonic axial motion in a small recirculating water flume. Due to limitations within the experimental setup, the maximum reduced frequency was restricted to just $k = 0.02$ at $r/R = 0.75$, effectively resulting in quasi-steady conditions. Building on Whelan's work at the same facility, McNae [162] found that as the oscillation frequency increased, the load response exhibited a phase lag relative to the forcing function. This contrasts with Whelan's findings and was attributed to the variable speed of the rotor during the experiments.

The investigations by Milne *et al.* [171, 172] sought to eliminate the influence of background turbulence, inherent in flume-based studies, by subjecting a 0.78 m diameter rotor to an unsteady surging motion superimposed on a steady forward speed in a towing tank. The experimental setup enabled the authors to quantify the flapwise root bending response to single- and multi-frequency oscillations under

both attached and separated flow conditions. For single-frequency oscillations, where the boundary layer remained attached, unsteady loads exceeded steady loads by up to 15%, with a small phase lead relative to the oscillatory forcing. In contrast, dynamic stall elicited loads that exceeded quasi-steady values by over 25%.

Surface Waves

Surface waves cause disturbances in the static pressure experienced by tidal rotors [139], leading to velocity perturbations that vary as a function of wave height, wave period, and depth. Data from EMEC indicate that for a water depth of approximately 55 m, wave-induced velocities can penetrate to a depth of 15 m [173], which can significantly impact device loading and power production. As a blade rotates through the velocity field, wave orbitals introduce additional temporal and spatial variations in the blade's relative velocity, resulting in a complex onset flow [139].

A range of numerical approaches have been used to model the interaction between waves and tidal rotors. An example of a fully resolved approach is the study of Tatum *et al.* [174], who simulated the response of a three-bladed, 10 m diameter rotor to regular waves using both uncoupled CFD and a fully coupled fluid-structure interaction (FSI) model. The authors reported increased amplitudes in both rotor-averaged and individual blade loads in the presence of waves, with no significant differences observed between the two modelling approaches. Similar qualitative findings were reported by Guy *et al.* [175], who applied a mid-fidelity ALM to simulate the response of a 1.5 MW full-scale tidal rotor under combined wave–current conditions, based on measurements from the MeyGen site in the Pentland Firth, Scotland. The simulations also demonstrated the sensitivity of rotor loads to wave effects at different turbine locations in the water column. A lower-order parametric study by Scarlett and Viola *et al.* [156] suggested that large, long-period waves (> 5 s) are the leading source of flow unsteadiness on turbine blades. The authors also found that flow separation is most prevalent under wave

conditions and can lead to light dynamic stall over a significant portion of the blade.

Barltrop *et al.* [176] conducted one of the earliest experimental investigations into the effects of combined wave–current conditions on the loading response of a model-scale tidal rotor in a towing tank. The authors demonstrated that both flapwise and edgewise root bending moments fluctuate significantly in the presence of waves, particularly for longer-period waves. Results from these experiments, along with those presented by Galloway *et al.* [157] were used to validate BEM codes that accounted for wave effects. The significance of the unsteady loads was further confirmed by Galloway *et al.* [157], who reported a maximum loading range of 175% of the median flapwise root bending moment and 100% of the median edgewise root bending moment for a 1:20 scale turbine model subjected to linear waves in a towing tank. A general consensus in the literature suggests that, although mean power and thrust remain largely unaffected by waves, wave-induced unsteadiness can be substantial [177, 178].

While experimental studies have primarily focused on the effects of monochromatic (regular) waves, real ocean waves are rarely classified as such [179]. To demonstrate the significant variation in wave-current interactions that tidal rotors experience over a tidal cycle, Draycott *et al.* [179] subjected a fully instrumented 1:15 scale turbine model to realistic irregular waves with both following and opposing currents to assess the resulting rotor loads. The authors reported wave heights nearly four times larger under opposing currents, with the standard deviations of the measured rotor loads more than doubling in the opposing current case.

Platform-induced Motions

Tidal rotors mounted on floating platforms offer several advantages over fixed-bottom devices, including easier site access, installation, and maintenance, as well as access to higher flow speeds near the top of the water column. Despite these benefits, platform-induced motions introduce additional complexity to rotor

analysis due to the system's rigid-body motions in response to environmental forces. A floating platform's rigid-body motions are typically described by six degrees of freedom: three of these—heave, pitch, and roll—are generally self-restoring and constrained by the platform's hydrostatic design, while the other three—surge, sway, and yaw—are typically restrained by mooring lines or other station-keeping solutions [180].

Compared to fixed-bottom devices, the literature on floating tidal rotors is limited and primarily focused on numerical investigations. To simplify the analysis, platform motions are often prescribed as simple harmonic motions, as demonstrated by Osman *et al.* [181] and Osman and Willden [182], who applied surge and pendulum motions, respectively, to a 20 m diameter rotor under steady flow conditions using blade-resolved CFD RANS simulations. Similar to other stochastic forms of hydrodynamic unsteadiness, time- and position-dependent variations in the relative blade velocity elicit transient load responses, which increase with the amplitude and frequency of the prescribed oscillations. The authors showed that, for sufficiently large surge amplitudes, flow separation over much of the blade surface leads to a deterioration in the mean power and thrust. To account for wave effects, Zilic de Arcos *et al.* [180] coupled a time-domain seakeeping model of a catamaran-style floating platform and a dynamic model of a 20 m diameter rotor based on BEM theory. The analysis revealed that power and thrust fluctuations are substantial in the presence of waves, both with and without platform motions; however, due to phase interactions between the waves and the platform response, platform-induced motions within certain ranges of wave periods do not necessarily have an adverse impact on the operation of floating tidal rotors.

Brown *et al.* [183] conducted a full system test of a 1:12 scale floating tidal platform model, using a catamaran-style platform equipped with a porous disc to simulate the rotor. The authors explored a range of environmental conditions, demonstrating the sensitivity of the turbine's unsteady loads to platform-induced motions. Particularly large load amplitudes were observed near the harmonics of

the pitch natural frequency, with further increases due to combined wave-current interactions, posing challenges for power quality and rotor fatigue.

6.4 Research Gaps in Model-scale Testing

While the effects of unsteady flow regimes on tidal rotor performance and loading response have been extensively studied over the past two decades, most model-scale experiments have focused on a single source of flow unsteadiness. This is often due to constraints in project scope or limited data collection time in external test facilities. An in-house flume, however, offers the advantage of extended testing periods, enabling a more comprehensive analysis of turbine response across a range of flow conditions and operating points. To the best of the author's knowledge, no study has yet investigated turbine performance and loading response under controlled onset turbulence and vertical shear independently. For the flow conditions already characterised, this approach provides an opportunity to relate the underlying flow characteristics to model-scale turbine response, offering insights into which unsteady hydrodynamic regime poses greater challenges for tidal rotors.

Owing to the geometric and cost constraints associated with developing model-scale turbines, most turbine experiments primarily focus on measuring rotor thrust and torque. Detailed measurements of blade root bending moments, both flapwise and edgewise, are much less common, despite their potential to reveal nuanced effects of hydrodynamic unsteadiness on the individual blade response. By directly extracting these measurements, this study allows for careful characterisation of the unsteady loads at the blade level. Furthermore, while most studies examine turbine response at a single operating point—typically peak performance—this investigation systematically varies the blades' chord-based Reynolds number, offering insights into the rotor's response across a range of operating conditions.

CHAPTER 7

Turbine Adaptation and Experimental Methodology

In advance of model-scale testing, extensive preparation was undertaken to ensure the turbine's test readiness. This involved the design, development, and procurement of new turbine components, calibration of sensors, development of assembly aids and test rigs, and the overall experimental setup. Particular emphasis was placed on accurately capturing the instantaneous load response of each rotor blade during turbine operation. Additionally, a carefully designed assembly procedure was necessary to overcome the logistical challenges of the laboratory environment and ensure the turbine's safe installation into the flume.

This chapter begins with a discussion of the turbine design and its adaptation for testing in the flume, followed by a detailed account of the calibration of the blade root flexures. The experimental methodology for the turbine test campaign is then described.

7.1 Turbine Design and Instrumentation

The turbine is a modified version of one of two model-scale, three-bladed horizontal axis turbines previously tested in towing tanks at SSPA, Sweden [25], and QinetiQ, UK [39]. Photographs of the assembled drivetrain, without the sealing covers and

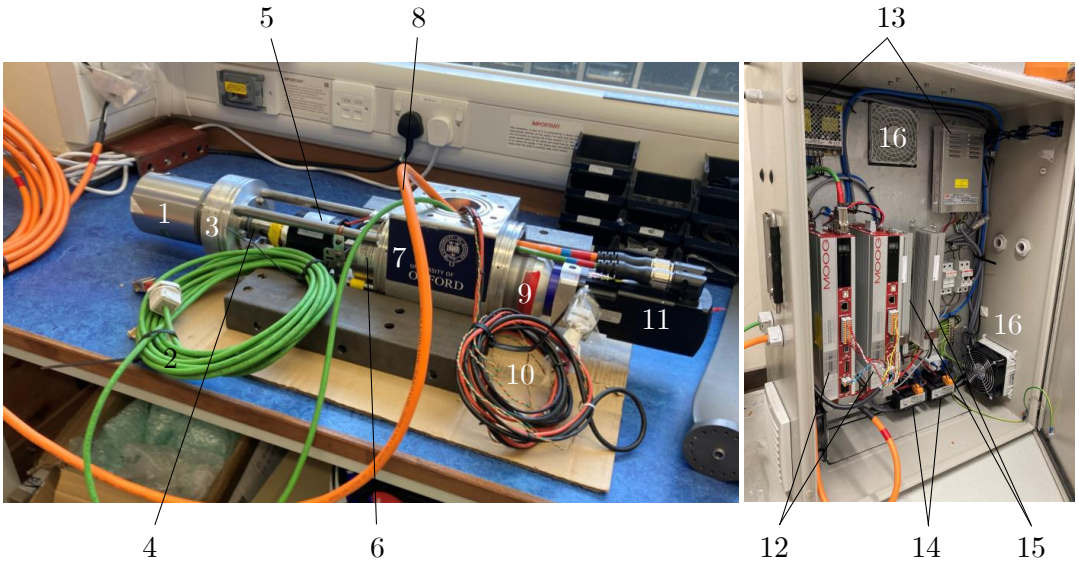


Figure 7.1: Photographs of the turbine's drivetrain (left panel), without the sealing covers and shrouds, and the electrical drive cabinet (right panel), with the key components labelled. Table 7.1 lists the corresponding component names for reference. Note that two of each component in the electrical cabinet were required, as the system was originally designed to support twin turbine models; however, only one turbine and one servo drive were used in this study.

Item	Component	Item	Component
1	Thrust and torque transducer (TTD)	9	Gearbox (20:1)
2	Servo motor signal cable	10	Rotor signal cable
3	Front bearing housing	11	Servo motor
4	Low-speed shaft	12	Motor drives
5	Slip ring	13	Power supplies (24 V)
6	Rotary incremental shaft encoder	14	Line chokes
7	Rear bearing housing and central section	15	Brake resistors
8	Servo motor power cable	16	Cooling fans

Table 7.1: List of key components used for the turbine and the electrical cabinet. The numbered items correspond to the components highlighted in Figure 7.1. For further details, refer to McNaughton *et al.* [25].

shrouds, and the drive cabinet are shown in Figure 7.1, with a corresponding key in Table 7.1.

Based on the approach of Payne *et al.* [184], the turbine was originally designed with a rotor diameter of 1.2 m and instrumentation sized for the higher loads

Item	Supplier	Material
Blades	Parallel Precision	Al 6082-T651
Blade shrouds	DoES (3D printing laboratory)	Polylactic acid polymer
Blade root flexures	Acrona Engineering	Al 2014A-T6511
Pitch plates	Acrona Engineering	Al 6082-T651
Tower assembly	Precision Sheet Engineering	Type 304 stainless steel
PCB assembly	DoES (electronics workshop)	Various
Flexure strain gauges	Applied Measurements	Various

Table 7.2: List of hardware changes for turbine adaptation, excluding standard components such as fasteners and O-rings. DoES refers to the Department of Engineering Science.

expected in larger hydrodynamic test facilities. The nacelle, constructed from two off-centre cylindrical sections of aluminium 6082-T6 and coated with a bespoke wet- and rust-tolerant finish supplied by ChemCo International, has a diameter of 150 mm and an overall length of 1106 mm.

7.1.1 Scope of Hardware Development

To accommodate the smaller cross-section and lower load demands of the Oxford flume, careful adaptation of the rotor upstream of the thrust and torque transducer (TTD) was necessary. Additionally, a supporting tower assembly was required to ensure precise positioning and secure mounting of the turbine within the flume. Figure 7.2 provides illustrations of the rotor and the proposed setup in the flume.

The scope of the hardware changes required to adapt the turbine for flume testing is outlined in Table 7.2. As stated in the table, the manufacture of several components was outsourced to third-party suppliers due to limited in-house capabilities within the Department of Engineering Science (DoES) at Oxford. The need to outsource component manufacturing, along with the requisite surface treatments—such as hard anodising for the aluminium components—and delays in finalising the blade's hydrodynamic design, resulted in the project slipping beyond its scheduled timeframe by approximately three months.

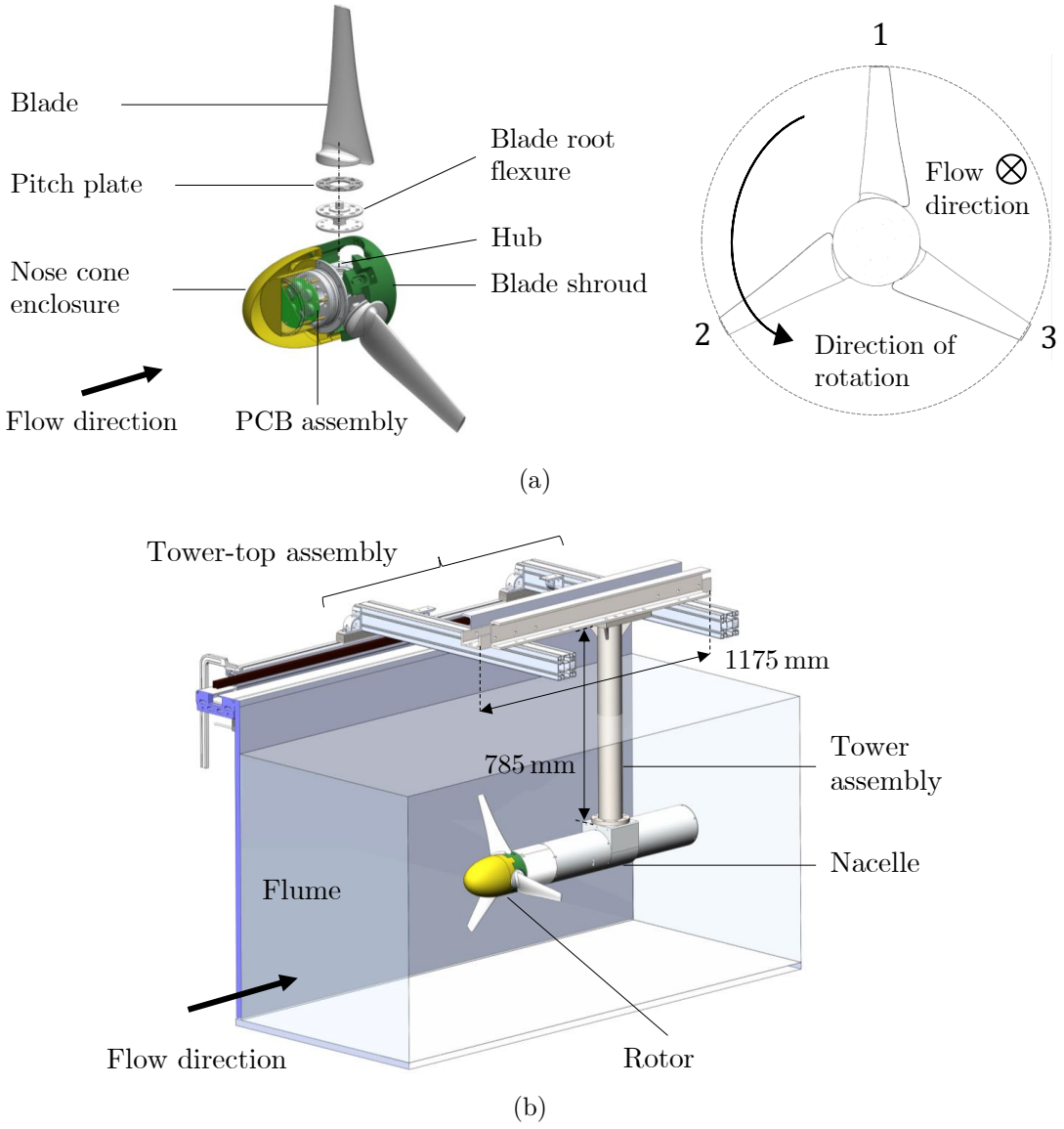


Figure 7.2: Illustration of (a) the rotor assembly and (b) the turbine assembly in the flume. The nose cone in (a), along with the flume and tower-top assembly in (b), are shown in section view for clarity. The relationships between the blade sub-assembly components—the blade, pitch plate, and blade root flexure—are depicted in an exploded view in (a), along with the blade numbering.

7.1.2 Blade Sub-assembly

This section describes the development work involved in adapting the turbine for testing in the flume.

Predictions of Rotor Loads

Before finalising the blade geometry, the hydrodynamic aspect of which was designed by a fellow student, an initial estimation of the rotor loads was necessary to guide the design and flexural response of the blade root flexures, positioned between the hub and the base of the blade (see Figure 7.2a). To achieve this, a blade element momentum (BEM) model, developed by Scarlett and Viola [143], was used to predict individual blade loads across a range of tip-speed ratios ($\lambda = 1$–10) for a steady, uniform approach flow. The implementation, described in [185], is based on the solution method of Ning [186], which uses a residual equation to iterate the flow angle, allowing the induction factors and angle of attack (see Figure 6.1) to be solved. To account for losses at the blade root and tip, the corrections detailed in [187] were applied. A detailed account of BEM theory is provided by Burton *et al.* [26].

As inputs into the BEM model, the blade sectional geometry was based on variations of the NACA 63-418 profile, as detailed by Gaurier *et al.* [188], while the lift and drag coefficients were extracted from XFOIL[1] [189] for chord-based Reynolds numbers between 50 000–150 000. Additionally, since standard BEM theory assumes an unbounded flow domain, the effects of channel blockage were considered. In a blocked flow scenario, a greater difference in static pressure across the rotor plane results in a higher flow speed through the rotor plane for a given level of thrust compared to unblocked flow, leading to increased blade root bending moments (RBMs), torque, and, therefore, power [129]. To account for this in the model, a freestream velocity of $U_\infty = 0.70\,\mathrm{m\,s^{-1}}$ was applied for all tip-speed ratios, equating to a 20% uplift relative to clean flow conditions (cf. Table 3.4). This adjustment follows from the analytical study of Houlsby *et al.* [190] and accounts for the increased axial induction effect of the rotor at its peak power extraction point in a constrained flow passage, assuming a blockage of 25.7% based on a rotor

[1] Although the relatively low Reynolds numbers led to some instability in the XFOIL predictions, the data were still used as first-order approximations.

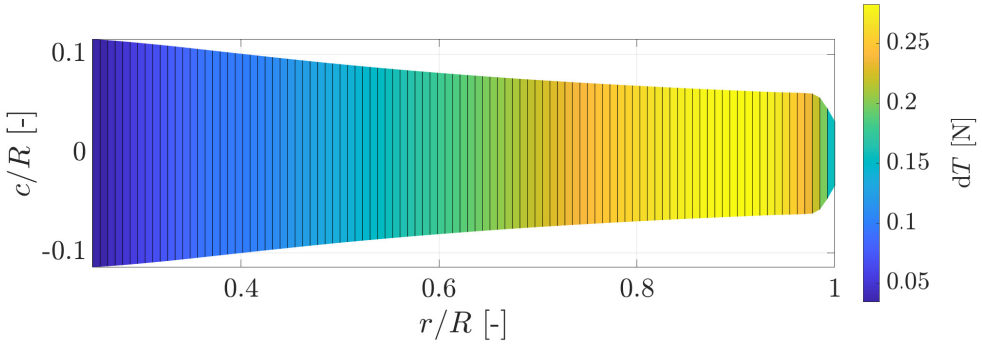


Figure 7.3: BEM prediction of blade sectional thrust, dT, at a local radius r from the rotor axis, normalised on the rotor radius, R. The simulation corresponds to the maximum thrust condition at a tip-speed ratio of $\lambda = 6.50$, with the blade sectional geometry based on variations of the NACA 63-418 profile, as detailed in [188].

radius of $R = 0.3\,\mathrm{m}$.

Figure 7.3 illustrates the BEM prediction of sectional blade thrust, dT, across 100 discretised radial sections at $\lambda = 6.50$, which represents the maximum thrust condition. The integrated steady-state load was calculated as 15.92 N, corresponding to a flapwise (FW) root bending moment of 3.36 N m and a rotor thrust of $T = 53.23\,\mathrm{N}$. Qualitatively, the prediction yields an expected result, with the thrust distribution increasing steadily from the blade root, peaking close to $0.9R$, before tapering off towards the tip. In the direction of rotation (see Figure 7.2a), the maximum steady-state load, integrated along the blade, was 3.01 N at $\lambda = 3.25$, corresponding to an edgewise (EW) root bending moment of 0.54 N m and a rotor torque of $Q = 1.63\,\mathrm{N\,m}$. Although the BEM predictions carried significant uncertainty, the maximum rotor loads were two orders of magnitude smaller than the thrust and torque transducer's rated capacity of $T = 1800\,\mathrm{N}$ and $Q = 100\,\mathrm{N\,m}$.

Measurement of Blade Root Bending Moments

Following a similar approach to other researchers [165, 184, 191], a bespoke transducer equipped with strain gauges was designed and manufactured for installation at the root of each blade, enabling the accurate, instantaneous measurement of both the flapwise and edgewise root bending moments. The flexure geometry was devel-

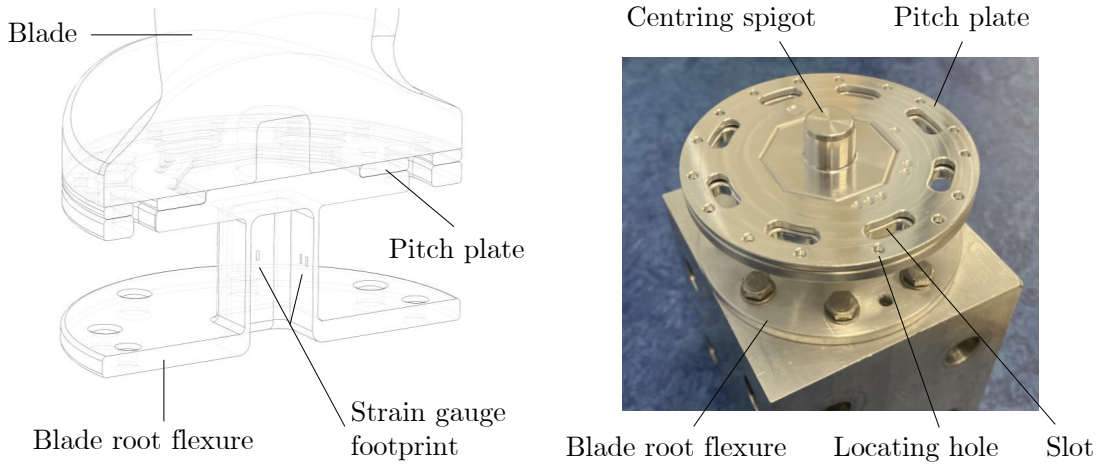


Figure 7.4: (a) Sectional drawing of the blade sub-assembly and (b) photo of a pre-anodised blade root flexure and pitch plate.

oped in SolidWorks, using BEM-derived blade loads as inputs to a finite element model of the blade sub-assembly (see Figure 7.4a) for statics analysis. A preliminary blade geometry, based on the description provided by Gaurier *et al.* [188], was used[2].

To construct a 3D model of the blade, a similar approach to Payne *et al.* [184] was employed. A generic NACA 63-418 profile shape, obtained from [192], was manipulated into a series of 100 hydrofoil sections using prescribed twist and pitch angles, with the blade axis passing through the quarter-chord point of each section. A lofting function was then used to generate smooth, interpolated curves along the outer edges of the blade, transitioning to a circular flange near the root at $0.23R$, which served as the attachment point to the flexure.

The flexure design needed to balance two key criteria: generating a measurable flexural response across a range of hydrodynamic loads while also remaining resistant to yielding. An iterative design process was followed, in which non-linear load distributions were applied along the blade in both the positive flapwise and edgewise directions as a function of tip-speed ratio, where $\lambda \in \{3, 5, 7\}$. For

[2]The flexure design was developed before the final blade geometry was available.

each load case, the geometry of the deformable section between the upper and lower flanges (see Figure 7.4) was modified to maximise the measurable vertical strain across the active areas of the strain gauges, represented by two rectangular footprints ($0.5 \times 1.5\,\text{mm}$) on each internal wall. A safety factor of at least five was maintained between the simulated von Mises stress and the material yield stress. The vertical strain distribution resulting from the flexure's simulated response was averaged across each active area and used to predict a signal output in both loading directions, based on the balancing relations of a full Wheatstone bridge configuration, as described in [193]. A signal threshold of 0.1 mV per input volt (equating to approximately $250\,\mu\epsilon$) was set to ensure the output voltage from each bridge exceeded the signal noise floor. Given the magnitude of the predicted loads, this threshold was only exceeded in the positive flapwise direction, with the edgewise signal remaining below the threshold across the tip-speed ratio range. For all load cases, the predicted tip deflection due to the flexure's deformation was $< 1\,\text{mm}$ in the positive flapwise direction.

Prior to strain gauging, the flexures—manufactured from aluminium 2014A due to its high strength and excellent machining characteristics—were hard anodised with a layer thickness of $25\,\mu\text{m}$ by MP Eastern, in accordance with ISO 10074:2017, to protect against surface corrosion.

Each flexure was then equipped with two Wheatstone bridges—one for the flapwise and one for the edgewise root bending moments—each of which produced a voltage differential that was converted to a current output (4–20 mA) by a corresponding ICA4 amplifier [194], integrated into a bespoke printed circuit board (PCB) arrangement inside the nose cone enclosure (see Figure 7.5). As noted by Payne *et al.* [184], positioning the amplifiers close to the strain gauges helps preserve signal integrity through the drivetrain, as voltage signals are typically more vulnerable to electromagnetic interference and signal degradation. Building on the lessons learned from a previous design iteration used in the study of McNaughton *et al.* [191], the new design incorporated discrete PCBs to separately

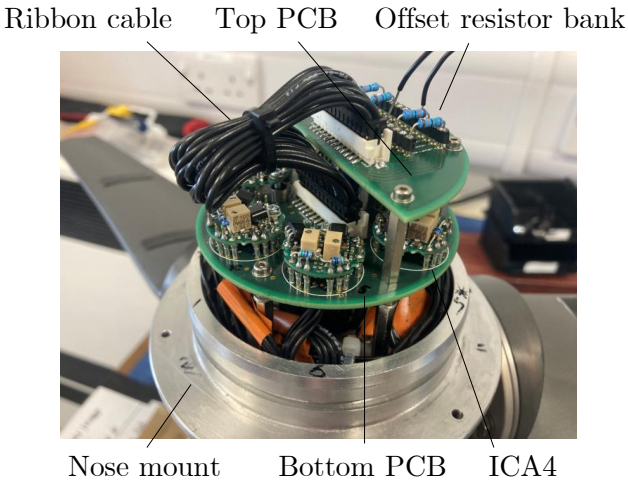


Figure 7.5: Printed circuit board (PCB) assembly inside the nose cone enclosure.

mount the amplifiers and offset resistors, allowing for efficient replacement and adjustment during the calibration process (see Section 7.2).

Blade Pitch Angle Adjustment

Accurate setting of the blade pitch angle is essential for optimal rotor performance, as any angular misalignment alters the blade's intended angle of attack, leading to a sub-optimal lift-to-drag ratio for the target hydrofoil. To set the static pitch angle of each blade, the author followed the approach of Payne *et al.* [184], who devised a mechanical arrangement consisting of an adjustable intermediate plate between the blade and the root flexure, as shown in Figure 7.4. The design allows the blade to rotate about its axis, aligned with the axis of the centring spigot of the flexure. Precise angular alignment is achieved by inserting an interference-fit dowel into the base of the blade and into one of several locating holes near the outer edge of the pitch plate. Each locating hole corresponds to a specific pitch angle, ranging from $-2°$ to $3°$.

The plate design was adapted from the version used by McNaughton *et al.* [191] for the twin turbine model rotors in previous experimental campaigns. Key modifications included tightening the tolerances at the blade root flexure interface

to minimise angular play between the components, thereby reducing error in the blade's angle of attack. Additionally, a 0.6 mm fillet radius was applied to all edges to ensure the parts could be anodised effectively (layer thickness 25 μm, in accordance with ISO 10074:2017) for protection against surface corrosion. The systematic error in the pitch angle was attributed to two sources: (i) an angular tolerance of 0.1° during machining, and (ii) a maximum angular misalignment of 0.19° at the interface between the plate and the flexure, yielding $\delta_{\text{sys}} = \pm 0.29°$.

Hydrodynamic Blade Design

The rotor blade was specifically designed for the flume's high blockage, with the hydrofoil selection and geometric definition of the three-dimensional profile led by a fellow student, Brinkmann [195]. To account for the low-Reynolds-number flow around the blades, the blade design was based on variations of the NACA 63-418 profile, chosen for its suitability at chord-based Reynolds numbers of approximately 100 000 at 70% span (see Equation 8.1). Since low-Reynolds-number turbine blade designs are often susceptible to laminar separation and increased profile drag, geometric modifications—such as camber and thickness adjustments—are commonly used to mitigate performance losses [196]. The design methodology followed a two-stage process. First, a model that couples blade element theory with a RANS solver was used to calculate the optimal blade chord and twist distributions that correspond to the maximum lift-to-drag ratio [136]. Second, the preliminary design was refined using a blade-resolved simulation with a moving reference frame method, which captured the complex flow behaviour at the root and tip, where lower-order models are less accurate [197]. The results of the CFD analysis are not included here, as they are yet to be published at the time of writing.

Upon receipt of the blade geometry, the mechanical interface to the flexure and pitch plate was prepared, based on the design of McNaughton *et al.* [191], with small refinements to account for the growth of the oxide film during the anodising process. Like the root flexures and pitch plates, the machined blades were hard

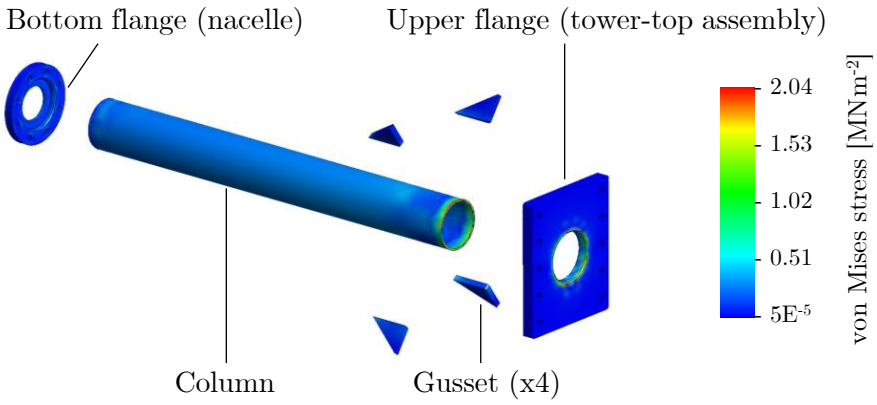


Figure 7.6: von Mises stress distribution across the tower assembly, shown in exploded form. The mating parts for both flanges are indicated in parentheses. The legend is not scaled linearly.

anodised with a layer thickness of 25 μm.

7.1.3 Tower Assembly

The design of the tower assembly (see Figure 7.2b) is similar to that used in the experimental campaigns of McNaughton *et al.* [25] and Tucker Harvey *et al.* [165], and comprises a standard stainless steel tube section (length 780 mm, outer diameter 88.9 mm, wall thickness 3.05 mm) with an adapter flange welded at either end, which offer attachment points for the nacelle and the tower-top assembly.

To minimise unnecessary weight in the assembly and account for the lower installation and operational loads in the flume, a thinner wall section was used compared to previous designs, which facilitated easier handling and positioning during the turbine installation process (see Section 7.3). To model this, a finite element analysis was conducted in SolidWorks, yielding a safety factor of seven based on the calculated von Mises stress for a fillet weld radius of 3 mm. Figure 7.6 presents the stress distribution across the assembly, with the peak stress occurring at the welded interface between the column and upper flange, based on the maximum expected loads during the turbine installation process: a weight of 267 N and a bending moment of 53 Nm.

One of the key manufacturing criteria for the assembly was to ensure both end flanges remained parallel within a 100 μm tolerance, to minimise any misalignment of the rotor axis relative to the centreline of the channel. However, due to material distortion during the welding process, the measured variation across the top flange was approximately 700 μm, exceeding the desired tolerance. When compared to the flume's build tolerances, particularly at the junctions between neighbouring sections, this variation was smaller than the geometric misalignments inherent in the flume's construction and was therefore deemed acceptable. Further discussion on the turbine's alignment and positioning within the flume is provided in Section 7.3.

7.2 Calibration of Blade Root Bending Moments

The initial phase of the blade root flexure calibration was conducted by Applied Measurements, who calibrated the sensitivity of the six amplifiers to match the target load range (FW = $\pm$40 N; EW = $\pm$10 N), applied statically at a fixed distance from the base of the flexure. The specified lever arm corresponds to an effective radius, r_{eff}, defined as the point along the blade span where the hydrodynamic loads are thought to be concentrated. For this analysis, $r_{\text{eff}}\,(\text{FW}) = 0.7R$ and $r_{\text{eff}}\,(\text{EW}) = 0.6R$. Both the design loads and effective radii were determined from blade loading distributions provided by Brinkmann [195].

The next phase of the calibration involved defining the offset resistances needed to balance each of the Wheatstone bridges. A decade box was connected to the PCB to empirically determine the required values, ensuring that the output current from each amplifier measured 12 mA at zero load.

The final stage of the calibration process involved generating linear calibration curves for both the flapwise and edgewise loads. Following BS 8422:2003 [198], known static loads were applied incrementally across the specified load ranges to each blade, and the corresponding output signals from the amplifiers were recorded. Each flexure was calibrated sequentially in its design-intent condition as

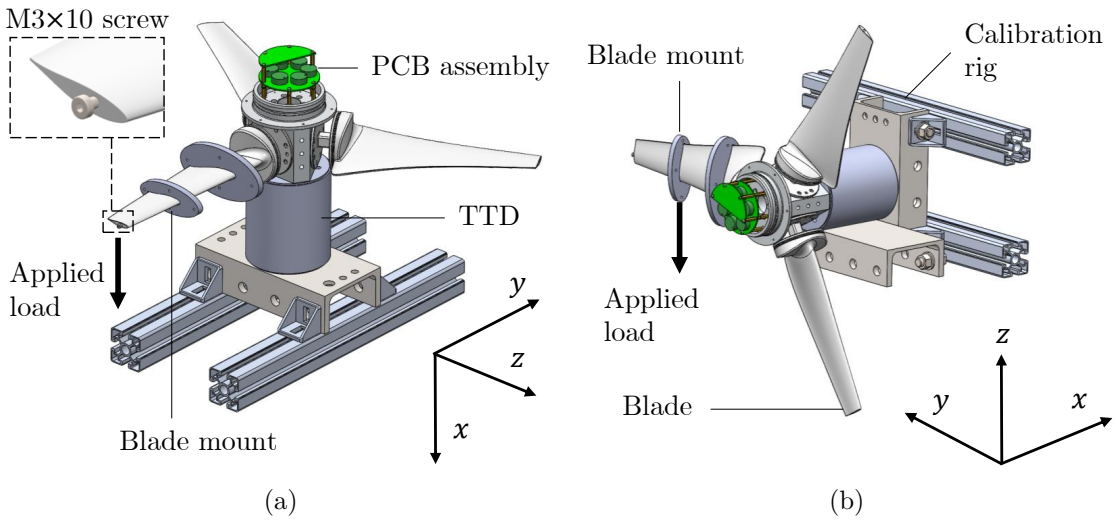


Figure 7.7: Illustrations of the blade root flexure calibration setup for (a) flapwise and (b) edgewise configurations. Calibration weights were suspended from 3D-printed blade mounts at $r/R < 1$ or from an M3×10 screw inserted into the blade tip at $r/R = 1$. The rotor remained stationary during the calibration procedure.

part of the blade sub-assembly, which was mounted directly onto the rotor hub to ensure the component interfaces remained undisturbed. A simple calibration rig, reoriented depending on the loading direction of interest, was developed for this purpose and is shown in Figure 7.7. This approach builds on the lessons learned from McNaughton *et al.* [25], who observed significant variation in the calibration curves whenever the flexure interfaces were disturbed due to the sensitivity of the transducers to mounting bolt torques.

M1 calibration weights were suspended at various radial locations along the blade using bespoke 3D-printed mounts (see Figure 7.7) to evaluate whether the flexures would yield a consistent response, irrespective of the load application point. Figure 7.8 presents the resulting calibration curves at each radial location for blade 1, revealing discrepancies in both the flapwise and edgewise directions, which grow proportionally with the applied load. At maximum load, the discrepancies equate to ranges of 0.88 N m in flapwise bending and 0.21 N m in edgewise bending, when averaged across the three blades. The results suggest that the flexures respond differently depending on where the load is applied, likely due to factors such as

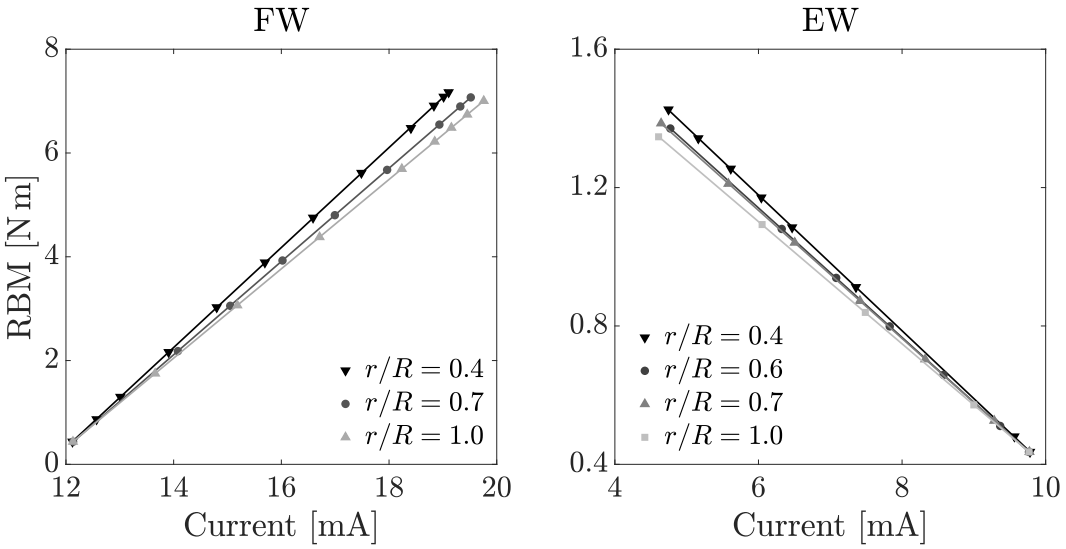


Figure 7.8: Linear calibration curves of the root bending moments from positive flapwise (left panel) and edgewise (right panel) loading applied to blade 1. The different markers represent the effective radii along the blade where the load was applied. RBM estimates are based on the mean of the loading and unloading phases.

spanwise variation in blade stiffness, structural asymmetry from the blade's taper and twist, and non-uniform load distribution between the 3D-printed mounts and the local blade surface. Hysteresis effects between the loading and unloading phases of the calibration procedure were negligible, measuring $< 0.4\%$ of the applied load.

Due to blade twist, the blade's flexural response about one principal axis inevitably results in some blade movement perpendicular to the other [26]. To investigate the crosstalk between the Wheatstone bridges in each flexure, the linear coefficients derived from the calibration curves were used to calculate the root bending moments in the axis perpendicular to the primary loading direction. Figure 7.9 presents the results of this analysis for blade 1, revealing errors proportional to the applied load. When the peak edgewise load is applied at the blade tip, the impact on the flapwise signal is minimal, resulting in a maximum error of just 0.06 N m, or 0.8% of the maximum measurable flapwise bending moment (when averaged across the three blades). In contrast, a mean error of 0.15 N m, or 9.0% of the maximum measurable edgewise bending moment, is observed under peak flapwise loading, representing a significant source of systematic error. In both loading axes,

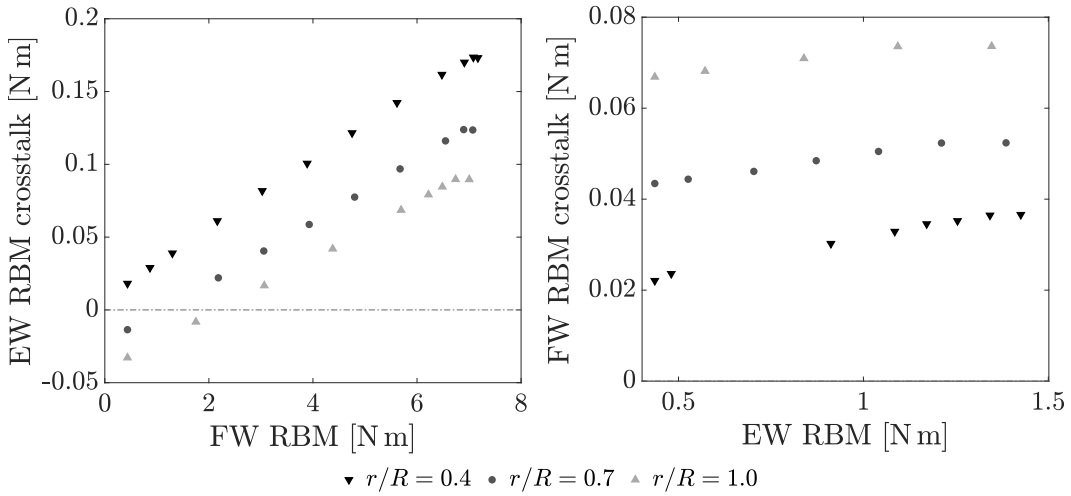


Figure 7.9: Crosstalk between the pair of Wheatstone bridges in the root flexure of blade 1. The x-axis corresponds to the primary loading axis. The different markers represent the effective radii along the blade where the load was applied: $r/R = 0.4$ (down-pointing triangles), $r/R = 0.7$ (circles), and $r/R = 1.0$ (up-pointing triangles). RBM estimates are based on the mean of the loading and unloading phases. In the left-hand panel, the dash-dotted line indicates zero crosstalk.

the crosstalk shows a dependency on the load application point, with the flapwise signal positively correlated to the effective radius, while the edgewise signal shows a negative correlation. Attributing a cause for this behaviour is challenging, but a likely contributor is the non-uniform load distribution at each effective radius, resulting from the limited precision in the fit between the 3D-printed mounts and the blade. As both the mounts and the blade sections differ along the span, the load distribution also varies.

Uncertainty Quantification

For the uncertainty analysis, the first step involved considering a range of parameters in the calculation of systematic error, including hysteresis, crosstalk, and other measurement errors throughout the experimental setup, such as analogue-to-digital conversion, lengths, and component weights. Uncertainty in the calibration curve fit was accounted for by evaluating the standard error of the estimate (SEE), as proposed by Coleman and Steele [63]. The second step was to evaluate measurement

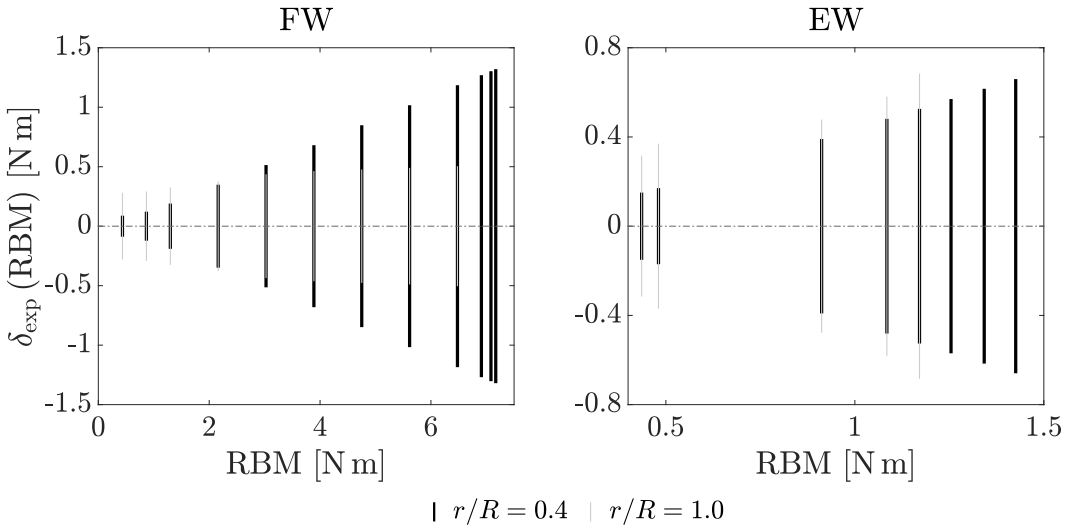


Figure 7.10: Error bars representing the expanded uncertainty, δ_{exp}, in the root bending moments from positive flapwise (left panel) and edgewise (right panel) loading applied to blade 1. The bar colours represent the effective radii along the blade where the load was applied: $r/R = 0.4$ (black) and $r/R = 1.0$ (grey), noting that fewer calibration weights were used at the tip. The uncertainties are based on the loading phase only. The dash-dotted line indicates zero uncertainty.

repeatability, which proved to be very high, demonstrated by the low standard error of the mean, $\mathcal{O}(10^{-5})$ N m, from three repeated measurements at each radial location. After combining the systematic and random errors (see Equation 2.5), a coverage factor based on two degrees of freedom was applied, yielding an expanded uncertainty (δ_{exp}) at the 95% confidence level as a function of applied load, effective radius, and blade number.

Figure 7.10 presents the results of the expanded uncertainty analysis for blade 1, with only two effective radii shown for clarity. In both loading directions, the error contribution from the calibration weights (accuracy: ± 0.0175 g per 500 g) accounts for the positive correlation between uncertainty and the applied load, reaching maxima of ± 1.32 N m for flapwise loading and ± 0.68 N m for edgewise loading at the 95% confidence level. Notably, the uncertainty correlates differently with the radial location of the applied load: a negative correlation for flapwise loading, likely due to the use of fewer and lighter weights further outboard to achieve the target loads, and a positive correlation for edgewise loading, resulting from

increased sensitivity to systematic errors at greater radial distances. When averaged across the load range, the expanded uncertainty corresponds to 17–18% of the nominal applied load in the flapwise direction and 40–63% in the edgewise direction, depending on the radial location used. At lower nominal loads ($< 2\,\mathrm{N\,m}$ (FW) and $< 1.2\,\mathrm{N\,m}$ (EW)), the error due to crosstalk causes the uncertainty associated with tip loading to exceed that at $r/R = 0.4$. Deviations in linearity contribute $< 0.01\%$ to the systematic error, while the error associated with the resolution of the data acquisition (DAQ) system was also minimal, at just 0.3%. In both loading axes, the combined uncertainty was dominated almost entirely (99.9%) by systematic errors, with measurement tolerances accounting for the largest proportion (93.9%) along the blade span.

7.3 Methodology for Turbine Test Campaign

7.3.1 Turbine Installation

Given the limited vertical clearance above the flume, a carefully planned procedure was developed to ensure the safe installation of the turbine. The procedure involved three key stages, as illustrated in Figure 7.11:

i. Initial turbine build (excluding the motor section, sealing covers, shrouds, and tower assembly) on an assembly cradle outside the flume.

ii. Transfer of the cradle onto the tower-top assembly, where the turbine build and electrical integration could be completed.

iii. Removal of supporting fixtures and the cradle from the tower-top assembly, followed by lowering the turbine into the flume.

The design philosophy behind the procedure was to ensure a controlled and sequenced turbine assembly process, while minimising weight where possible to facilitate easier adjustment and handling during installation. The assembly cradle,

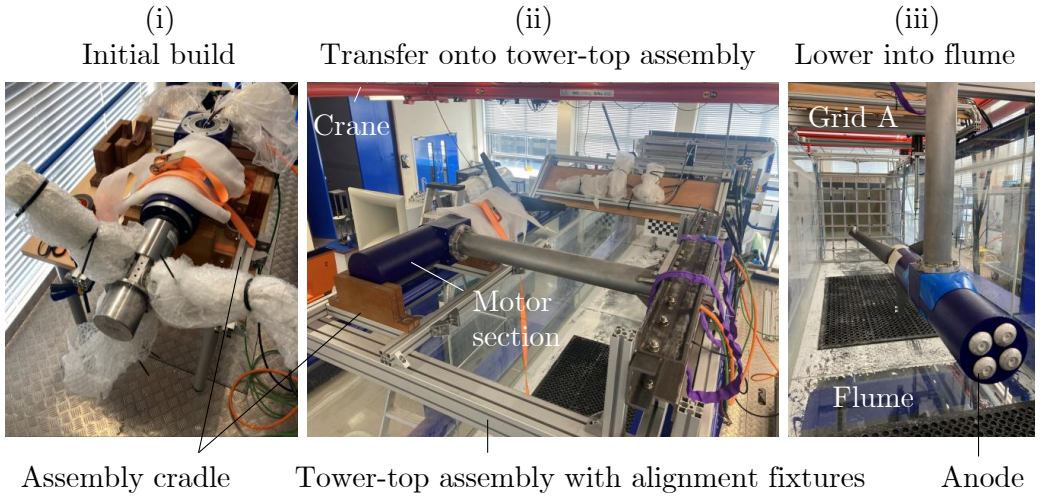


Figure 7.11: Photographs of the key stages of the turbine installation procedure: the initial build on the assembly cradle outside the flume (left panel), the transfer of the cradle onto the tower-top assembly (middle panel), and the lowering of the turbine into the flume (right panel). Four sacrificial zinc anodes were added to the motor cover to provide galvanic protection for the nacelle.

fitted with bespoke wooden mounts shaped to match the nacelle's cylindrical profile, provided a stable base for assembly and a means of safely transferring the turbine onto and off the flume.

Due to time constraints and the challenges associated with moving the turbine in such a confined space, a single rotor location was selected for the test campaign, $x = 3.9\,\mathrm{m}$, equating to $x - x_\mathrm{F} = 2.4\,\mathrm{m}$, or four rotor diameters downstream of the turbulence grid and shear profile mechanism plane. To align the rotor axis with the centre of the channel, a laser mounted on the nacelle was aligned with a target placed just upstream of the rotor, referenced to known horizontal and vertical datums in the flume. After accounting for the geometrical offset between the laser and rotor axes, the deviations in both directions were within 1 mm of the intended position.

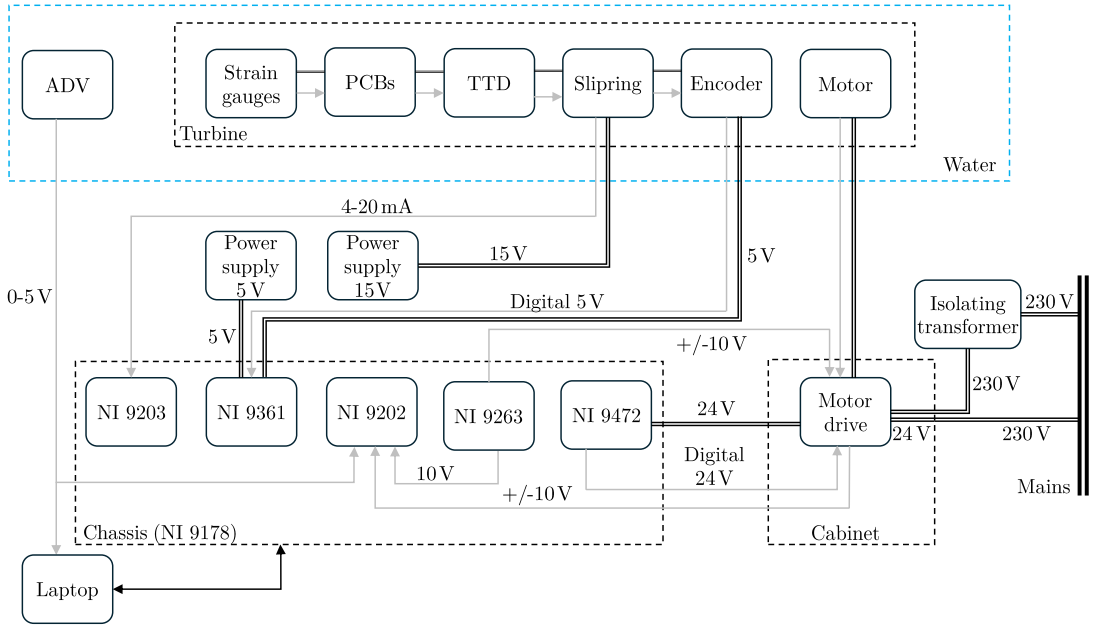


Figure 7.12: DAQ system schematic for the turbine, where grey arrows represent signal connections and paired black lines indicate power connections. A series of National Instruments (NI) modules were used to communicate with the turbine sensors, motor drive, and the ADV. The specific function of each module is detailed in Table 7.3.

7.3.2 Data Acquisition and Control Strategy

The turbine's DAQ system, adapted from the experimental campaign of Tucker Harvey *et al.* [165], is shown in Figure 7.12, with a list of the National Instruments (NI) modules used in the system provided in Table 7.3. A LabVIEW code from the campaign was used to operate and control the turbine, with small modifications to enable concurrent reference velocity measurements alongside turbine and motor signals, and to accommodate the reduced variable count. The turbine's operation was governed by set-point speed control of the motor drive. To maintain a constant rotor speed, the drive motor also acted as a generator by applying resistive torque to the rotor, with the excess energy dissipated as heat through the brake resistor (see Figure 7.1).

The angular resolution of the encoder, based on 720 pulses per revolution and with quadrature decoding, was 0.125°. All signals were acquired with a sampling

Module	Type	Function
NI 9178	CompactDAQ chassis	Hosts NI modules
NI 9472	Digital output (current)	Sourcing to motor drive
NI 9263	Analogue output (voltage)	Output for motor speed control
NI 9202	Analogue input (voltage)	Input from motor drive and ADV
NI 9361	Digital input (voltage)	Counter input from encoder
NI 9203	Analogue input (current)	Input from TTD and RBM amplifiers

Table 7.3: NI modules used for the turbine DAQ system.

frequency of 125 Hz, meaning that for a maximum rotor speed of 14.03 rad s^{-1}, the acquisition system provided an angular resolution of 6.4° per sample.

To define a sampling period for data acquisition, a similar approach to that detailed in Section 2.2.2 was followed, with the key difference being that a 30-minute steady-state time series of the turbine's rotor loads was used to evaluate signal stationarity. As a result, the variance for each sampling period of interest (1–600 s in 1-second increments) was calculated separately for only three equal and consecutive periods, rather than six, as was done for flow sampling. As before, the individual variances of each signal were ensemble-averaged to obtain $\sigma^2(i_{\text{period}})$, where i represents the signal of interest.

Figure 7.13 illustrates the convergence of $\sigma^2(i_{\text{period}})$ towards the corresponding variance over 30 minutes, $\sigma^2(i_{30})$, as the sampling period increases. The time taken for $\sigma^2(i_{\text{period}})$ to stabilise within ±3% of $\sigma^2(i_{30})$ was $t_{\text{stat}} = 149$ s, representing the minimum theoretical sampling period for each turbine test case. The data acquisition period was conservatively set to 180 s. Given the t_{stat} estimate for flow sampling (300 s) in Section 2.2.2, it is acknowledged that the turbine's approach flow was likely to be non-stationary; however, any impact on the turbine loads was expected to be minor and very unlikely to affect the conclusions of the investigation.

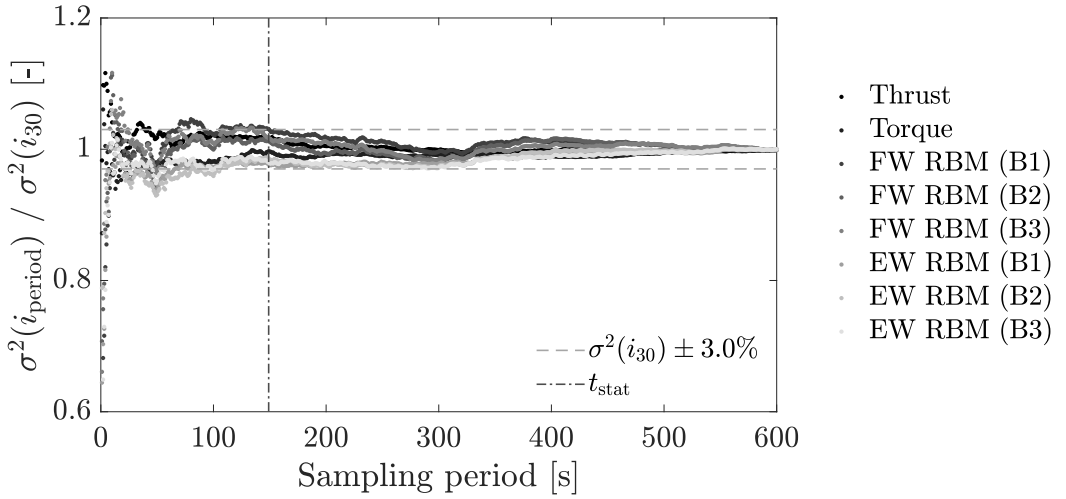


Figure 7.13: Variances of the turbine loads for each sampling period of interest (greyscale), where i represents each signal, normalised on the variance of each signal over 30 minutes, $\sigma^2(i_{30})$, under clean flow conditions. Also shown are a $\pm 3\%$ threshold about unity (light dashed) and the period of stationarity (dash-dotted), t_{stat}. In the legend, Bj represents the blade number. Test conditions: $\overline{U_{\text{T}}} = 0.57\,\text{m}\,\text{s}^{-1}$ (centreline velocity); $(x, y, z) = (2.7, 0, 0)$ (ADV co-ordinates); $\overline{\lambda} = 5.07$; $\overline{\Omega} = 9.63\,\text{rad}\,\text{s}^{-1}$.

7.3.3 Data Processing of Turbine Signals

All turbine load and angular position data were initially processed using a Hampel filter with a window size of 13 points on either side of each measurement sample to detect and remove outliers. Following this, a low-pass filter was applied to eliminate the influence of high-frequency noise. Pass and stop band frequencies of 12 and 15 times the turbine's fundamental rotational frequency (i.e. four and five times the blade-passing frequency), f_{rot}, where $f_{\text{rot}} = \Omega/2\pi$, were used, with a stop band attenuation of 40 dB.

For each root bending transducer, the combined effects of the blade's buoyancy and self-weight introduced a periodic component in the azimuthal load profiles of the edgewise signals, unrelated to the dynamic loads from turbine operation. To account for this, a two-stage process was applied: first, an azimuthal map of the edgewise loads due to buoyancy and weight was created using a sinusoidal model fitted to tare measurements taken before each test during the campaign, with each measurement depending on the angular position, ϕ, of the corresponding blade,

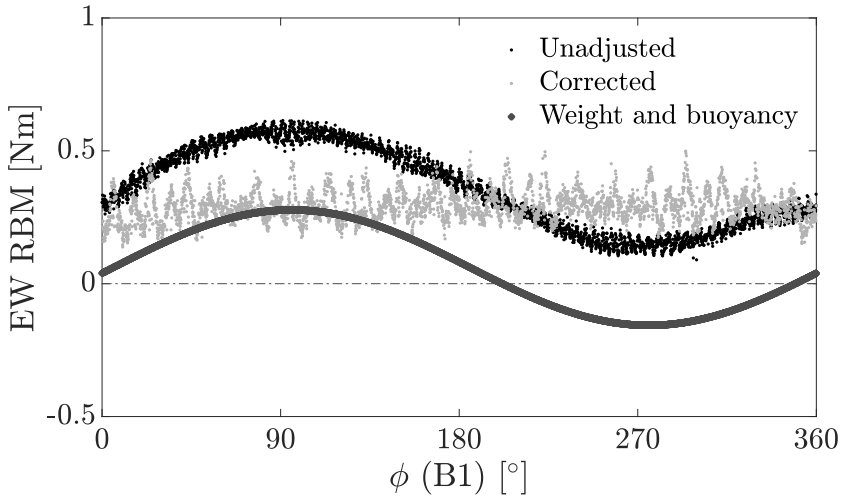


Figure 7.14: Azimuthal variation of the edgewise root bending moments across 46 rotations for blade 1 (B1) under clean flow conditions. The raw, unadjusted moments are shown in black, while the moments corrected for the blade's buoyancy and self-weight are shown in light grey, representing the steady-state hydrodynamic loads. The bending moments attributed to buoyancy and weight are shown in dark grey. Test conditions: $\overline{U_\mathrm{T}} = 0.57\,\mathrm{m\,s^{-1}}$ (centreline velocity); $(x, y, z) = (2.7, 0, 0)$ (ADV co-ordinates); $\overline{\lambda} = 5.08$; $\overline{\Omega} = 9.65\,\mathrm{rad\,s^{-1}}$.

where $\phi = 0°$ aligns with top dead centre (TDC). Second, the bending moments due to buoyancy and weight were subtracted from the unadjusted edgewise root bending moments to isolate the hydrodynamic loads. Figure 7.14 illustrates the outcome of the correction process, showing the azimuthal variation[3] of the edgewise root bending moments for blade 1 under clean flow conditions. The sinusoidal variation, attributed to the blade's buoyancy and self-weight, has a maximum amplitude of 0.28 N m, occurring when the blade is rotated to either 90° or 270° anti-clockwise from TDC. The slight offset from zero post-correction (0.04 N m) is likely due to an error in calculating the blade's volume in SolidWorks and, hence, its buoyancy.

[3]Following McNaughton *et al.* [25], blade loads are presented as phase-averaged values across all three rotor blades. The time series of each blade root bending moment signal was divided into one-degree bins based on the low-speed shaft position, with the data in each bin averaged. Unless otherwise stated, the binned loads from each blade are combined by aligning their phase and then averaged.

7.3.4 Test Strategy

A feature of the turbine controller was its ability to record a 20-second data file containing zero readings for each sensor. This enabled the use of a standardised data processing technique, whereby the sensor signals were pre-processed before being adjusted using their respective calibration factors. This method, known as zero-offset calibration, ensures that any sensor drift or baseline offsets are corrected prior to further analysis. The zero file was recorded 15 minutes after the flume's pumps were stopped, with the rotor held stationary. By this time, the variance of each turbine signal had stabilised to within $\pm 3\%$ of its respective variance over 30 minutes, effectively minimising the risk of residual turbulence contaminating the measurements.

After initially sampling the flow and turbine data with the flow at rest, both the flow and rotor speeds were gradually increased to achieve the target tip-speed ratio. Although the flume and turbine were operated independently on separate DAQ systems, efforts were made to manually synchronise the speed ramps (during both the acceleration and deceleration phases) to maintain a consistent tip-speed ratio during turbine operation and reduce the risk of unnecessary stall or overspeed events. While the turbine ramp rates were adjustable, the flow speed ramp rates were not, necessitating detailed characterisation in advance of the test campaign to fine-tune the turbine ramp rates based on the target flow speed. An example time series of the speed ramp and steady-state phases is shown in Figure 7.15, illustrating the variation in the instantaneous tip-speed ratio during turbine operation. The data window began once steady-state conditions had been reached.

7.3.5 Influence of ADV Position

The precise definition of the turbine reference velocity, U_{T}, has a significant impact on estimations of a turbine's non-dimensional performance [199]. The International Electrotechnical Commission's Technical Specification IEC TS 62600-200 [200]

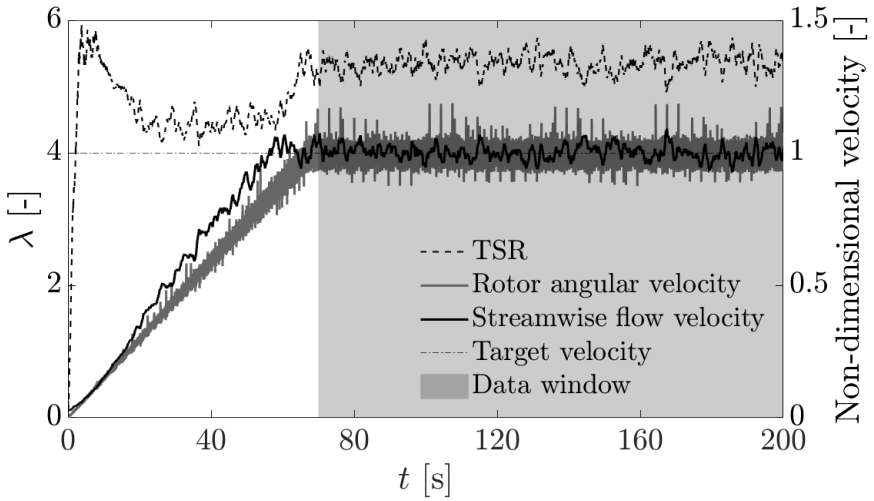


Figure 7.15: Time series of streamwise flow (black solid) and rotor angular (grey solid) velocities, normalised on their corresponding target values, with a non-dimensional target of unity shown for clarity (dash-dotted). The instantaneous tip-speed ratio, λ, is also indicated (black dashed), along with a data window (shaded), which begins once the target speeds are reached. The ramp-down phase is not included, as data recording stops at the end of the data window. Test conditions (values averaged over the data window): $\overline{U_\mathrm{T}} = 0.56\,\mathrm{m\,s^{-1}}$ (centreline velocity); $(x, y, z) = (2.7, 0, 0)$ (ADV co-ordinates); $\overline{\lambda} = 5.36$; $\overline{\Omega} = 9.84\,\mathrm{rad\,s^{-1}}$.

provides guidance for tidal developers on evaluating power performance. The specification advises that the flow measurement instrument, ideally an ADCP, be positioned far enough upstream to avoid turbine-induced flow disturbances, yet close enough to accurately capture the true flow characteristics [201]. For an in-line orientation, this typically requires placing the instrument between two and five rotor diameters upstream of the rotor plane and within half a rotor diameter laterally from the rotor centreline. The specification also recommends using a power-weighted rotor average (PWRA) velocity, which accounts for the power available in the flow through the cube-root-mean-cube of the velocity magnitude and for any vertical shear over the rotor plane through an area-weighted average of measurements taken at specified depth intervals [197]. For smaller rotor diameters in constrained flow domains, such as flumes, such an approach can present practical challenges.

Using an ADV rather than an ADCP, a single-point measurement was chosen

for the turbine reference velocity, consistent with other flume-based studies, such as Gaurier *et al.* [202] and Payne *et al.* [203]. Prior to defining the measurement location, preliminary tests were conducted to quantify the influence of the ADV position on the blade root bending moments. Three ADV positions consistent with IEC TS 62600-200 guidelines were tested and compared with load measurements taken without the ADV present:

- $(y, z) = (0, 0.3)$, aligned with TDC,
- $(y, z) = (0, 0)$, aligned with the flume's centreline and rotor axis, and
- $(y, z) = (0.3, 0)$, positioned 90° anti-clockwise from TDC.

The streamwise location of the ADV was set to two rotor diameters upstream of the rotor plane at $x = 2.7\,\mathrm{m}$.

Figure 7.16 shows the azimuthal variation in the flapwise and edgewise root bending moments across three tip-speed ratios for the clean flow case, with the loads normalised on the azimuthal average obtained without the ADV present. In cases where the ADV is not placed along the flume's centreline, the flapwise loads exhibit $< 2\%$ variation in the normalised loads and maintain a reasonably uniform profile around the rotor azimuth, with only slight asymmetry observed in the interval $0 \pm 45°$. When the ADV is placed along the centreline, the influence of the mast (see illustration in Figure 2.2) becomes very pronounced, particularly at the lowest tip-speed ratio, $\lambda = 3.09$, where its effect extends across almost half of the rotor plane ($0° \leq \phi \leq 137°$ and $329° \leq \phi < 0°$). Notably, at TDC, the local reduction in flow speed caused by the mast induces a once-per-revolution (1P) load fluctuation equivalent to approximately 10% of the azimuthal average, with this effect diminishing at higher tip-speed ratios as the loading profiles progressively converge towards the no-ADV case. A similar effect is observed for edgewise loading, although the 1P load fluctuation is more substantial, reaching almost 20% at the highest tip-speed ratio, $\lambda = 7.15$. Additionally, the profile asymmetry about the vertical centre plane is more pronounced, particularly at $\lambda = 3.09$, where the increased likelihood of stall elicits a much less uniform loading response. Another

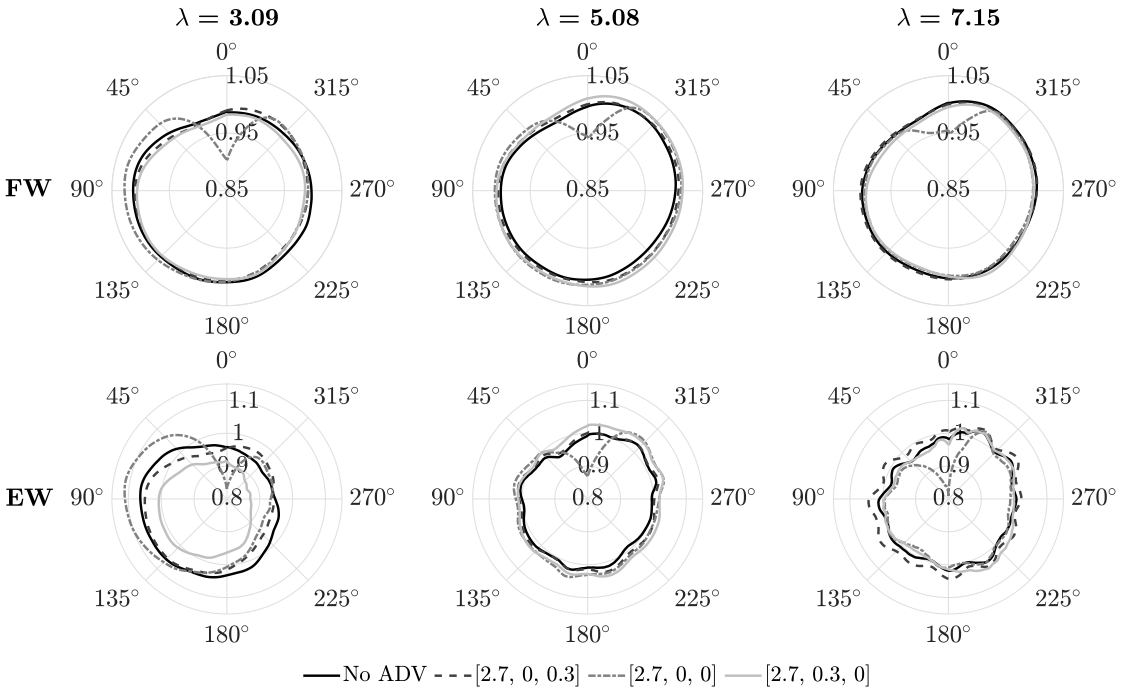


Figure 7.16: Azimuthal variation of flapwise (top row) and edgewise (bottom row) root bending moments as a function of ADV position and tip-speed ratio for the clean flow case. Measurements from three ADV positions (x, y, z), distinguished by different line styles, are compared with those obtained without the ADV present, where $x = 2.7\,\mathrm{m}$ corresponds to $x - x_\mathrm{F} = 1.2\,\mathrm{m}$ for unsteady flow cases. The loads shown are averaged across the three blades, phase-averaged in 1° bins, and normalised on the azimuthal average without the ADV present. The tip-speed ratio was varied by adjusting the rotor speed. Test conditions: $\overline{U_\mathrm{T}} = 0.57\,\mathrm{m\,s^{-1}}$ (centreline velocity).

defining feature of the edgewise loading profiles is the presence of uniformly spaced lobes at $\lambda \geq 5.08$, although it is unclear whether these arise from an increased sensitivity to load fluctuations due to inherently lower mean loads, or if they represent a mechanical artefact of the turbine's drivetrain.

To further quantify the influence of the ADV position, Figure 7.17 presents a selection of summary statistics for the blade root bending response, averaged over the rotor azimuth and plotted as a function of each flow regime. The values are expressed as percentage changes relative to baseline measurements taken without the ADV present. The mean differences between each ADV position and measurements obtained without the ADV are negligible, remaining below $0.05\,\mathrm{N\,m}$ for both flapwise and edgewise loads, regardless of the tip-speed ratio or flow regime. The

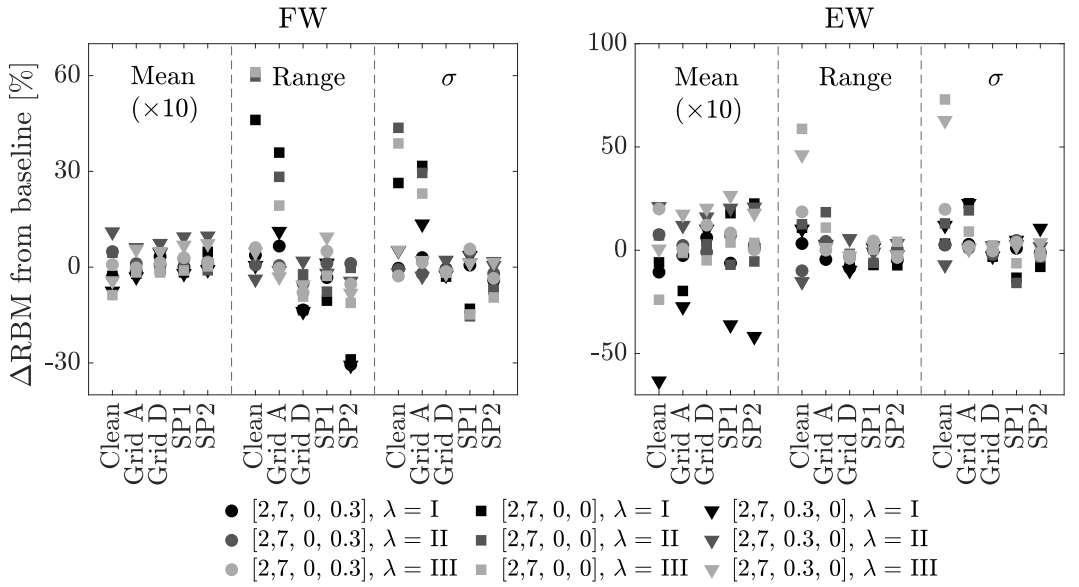


Figure 7.17: Summary statistics for flapwise (left panel) and edgewise (right panel) root bending moments as a function of ADV position, tip-speed ratio (see Table 7.4 for exact values), and flow regime. The loads, measured at three ADV co-ordinates (x, y, z), are azimuthally averaged and then averaged across the three blades, where $x = 2.7\,\mathrm{m}$ corresponds to $x - x_\mathrm{F} = 1.2\,\mathrm{m}$ for unsteady flow cases. Values are presented as the percentage change relative to baseline measurements without the ADV present, with baseline loads for the clean flow case provided in Table 7.5 for reference. The tip-speed ratio was varied by adjusting the rotor speed. Test conditions (centreline velocities): $\overline{U_\mathrm{T}} = 0.57\,\mathrm{m\,s^{-1}}$ (clean), $0.58\,\mathrm{m\,s^{-1}}$ (grid A), $0.56\,\mathrm{m\,s^{-1}}$ (grid D), $0.59\,\mathrm{m\,s^{-1}}$ (SP1), and $0.60\,\mathrm{m\,s^{-1}}$ (SP2).

most significant changes appear in the load range, where, for the clean flow case, relative increases of around 60% are observed for centreline ADV measurements. This corresponds to a range increase of 0.27 N m for flapwise loading and 0.10 N m for edgewise loading, both of which are well within the expanded uncertainty intervals established during the calibration analysis (see Figure 7.10). Smaller load increments are observed for the other four, more turbulent flow cases, which is to be expected given the increased fluctuation magnitudes in the turbine's approach flow, with the distribution of each statistic broadly centred around zero relative difference, indicating minimal change from the no-ADV case. Similar patterns are noted for the standard deviations, with no discernible trends regarding changes in the tip-speed ratio.

λ [-]	Clean	Grid A	Grid D	SP1	SP2
I	3.09	3.11	3.06	3.03	3.01
II	5.08	4.98	4.99	5.04	5.02
III	7.15	6.93	7.05	7.08	7.02

Table 7.4: Tip-speed ratios for each flow regime, based on centreline velocities measured two rotor diameters upstream of the rotor plane. Roman numerals correspond to nominal tip-speed ratios of $\lambda = 3$ (I), $\lambda = 5$ (II), and $\lambda = 7$ (III), with slight variations in the actual values across flow regimes.

λ [-]	Mean [N m]	Range [N m]	σ [N m]
I	1.86 | 0.42	0.40 | 0.30	0.06 | 0.07
II	2.99 | 0.39	0.37 | 0.19	0.05 | 0.02
III	3.67 | 0.24	0.44 | 0.16	0.06 | 0.02

Table 7.5: Summary statistics of blade root bending moments across three tip-speed ratios (see Table 7.4 for exact values) in the clean flow case. Values for flapwise loads are shown on the left of the vertical bar (|), while values for edgewise loads are shown on the right.

Following Gaurier *et al.* [202], centreline ADV measurements were preferred for model-scale testing over less invasive lateral or vertical offsets from the rotor axis. While increases in load fluctuations are undesirable, centreline measurements are crucial for obtaining a more representative turbine reference velocity, enabling a more accurate assessment of a rotor's non-dimensional performance. In such a constrained flow environment, where the approach flow is often highly non-uniform, this approach is considered prudent. However, to more accurately evaluate the rotor loading response, discrete tests without the ADV will also be conducted to eliminate interference from the ADV mast.

7.3.6 Selection of Effective Radii

Rather than considering the complete loading distribution along the blade, a single representative point—the effective radius—can be used for practical analysis. As described in Section 7.2, three radial positions were considered for calibration of the blade root flexures: $r/R = 0.4$, 0.7, and 1.0, yielding distinct calibration coefficients

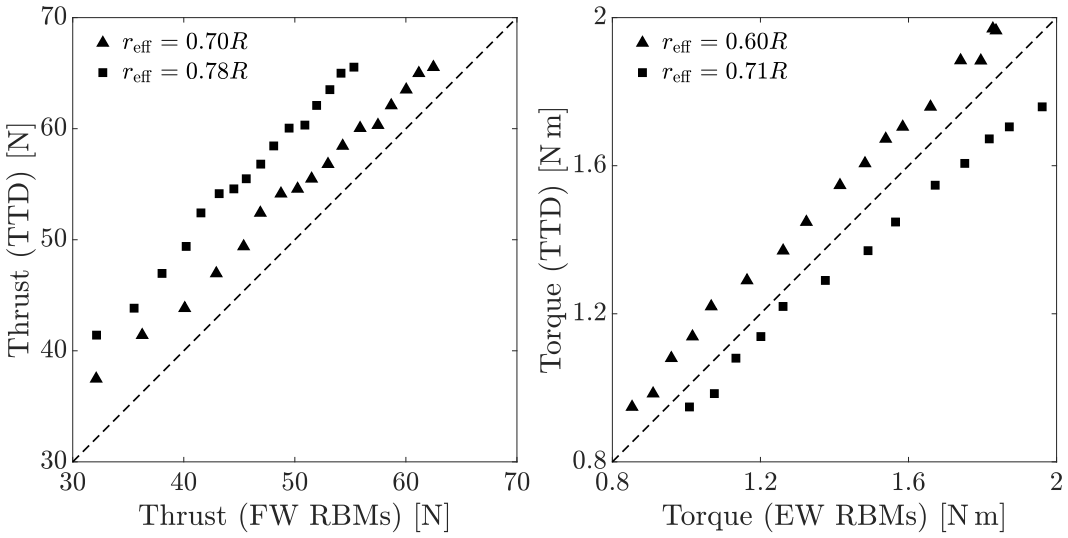


Figure 7.18: Measured thrust (left panel) and torque (right panel) from the thrust and torque transducer (TTD) are compared with the corresponding loads inferred from blade root bending moments in clean flow. The effective radii for the inferred loads were based on both a single radial location (triangles) and a weighted average across three radial locations (squares). The dashed line represents a 1:1 correlation between the measured and inferred loads. Estimates of nose-cone drag are included in the calculation of inferred thrust loads. The rotor thrust and torque were varied by adjusting the rotor speed. Test conditions: $\overline{U_{\text{T}}} = 0.57\,\text{m}\,\text{s}^{-1}$ (centreline velocity); $(x, y, z) = (2.7, 0, 0)$ (ADV co-ordinates).

for each position and loading direction to convert strain gauge signals into root bending moments. This analysis seeks to determine a single set of coefficients (one per loading direction) for post-processing, based on an estimate of the hydrodynamic centre of loading.

To select the effective radii, the thrust and torque loads measured directly from the thrust and torque transducer[4] were compared with the corresponding loads inferred from the blade root bending moments. To calculate the inferred loads, two approaches were used to determine the effective radii, based on blade loading distributions provided by Brinkmann [195]:

i. The moment contributions from each radial element (each 2 mm in length)

[4]Following the arrangement described by Payne *et al.* [184], the thrust and torque transducer sits upstream of two spherical roller bearings and radial shaft seals, enabling rotor-averaged load measurements without mechanical losses. Calibration of the transducer was performed by the supplier, Applied Measurements, as detailed by McNaughton *et al.* [25].

were summed and then divided by the corresponding integrated force component, yielding effective radii of $r_{\text{eff}}\,(\text{FW}) = 0.7R$ and $r_{\text{eff}}\,(\text{EW}) = 0.6R$. The linear coefficients corresponding to these locations were obtained directly from the calibration study.

ii. To account for all lever arms tested during the calibration process, the moment contributions from each radial segment[5] were integrated to determine each segment's contribution to the overall blade root bending moment. A weighted average was then applied to the set of linear calibration coefficients derived for both flapwise and edgewise loading, yielding slightly higher effective radii of $r_{\text{eff}}\,(\text{FW}) = 0.78R$ and $r_{\text{eff}}\,(\text{EW}) = 0.71$.

A comparison between the measured and inferred loads for the clean flow case is shown in Figure 7.18, with the estimated drag from the turbine nose (approximately 0.77 N, based on a drag coefficient of 0.3 for a rotating projectile [204]) accounted for in the calculation of inferred thrust. For both effective radii, the inferred thrust values underpredict the ground-truth TTD measurements, with larger discrepancies observed when the effective radii are calculated using a weighted average approach. The weighted average approach yields root mean square errors (RMSEs) of 9.92 N and 0.14 N m for thrust and torque, respectively, compared with 4.21 N and 0.12 N m when only a single radial location is considered in determining the linear coefficients. For model-scale testing, the latter approach was applied.

To better align the thrust and torque measurements with the inferred values, coefficients based on an effective radius of $r_{\text{eff}} = 0.65R$ would be required for both flapwise and edgewise loads. Identifying the reasons for discrepancies between the inferred loads and ground-truth thrust and torque measurements is challenging, as they may arise from unaccounted secondary flow effects, inaccuracies in estimating nose-cone drag, or other contributing factors.

[5]These segments corresponded to $0.25R$–$0.4R$, $0.4R$–$0.7R$, and $0.7R$–$1.0R$ for flapwise loading, and $0.25R$–$0.4R$, $0.4R$–$0.6R$, $0.6R$–$0.7R$, and $0.7R$–$1.0R$ for edgewise loading.

7.4 Summary

In preparation for the model-scale testing of a horizontal axis tidal stream turbine, significant planning and logistical efforts were undertaken to ensure the turbine's readiness for testing in the flume and its safe operation. This included the design, development, and procurement of new turbine hardware, which were essential not only for the integration of the turbine into the flume but also for accurately quantifying the blades' response to the onset flow conditions.

Building on the lessons learned from previous experimental campaigns, a bespoke rig was developed to calibrate the blade root flexures in their design-intent condition as part of the rotor assembly. The calibration analysis revealed slight variations in the flexures' response depending on where the load was applied, likely due to the non-uniform distribution of the calibration load between the local blade surface and the blade mount. Measurement tolerances were identified as the most significant source of uncertainty, which varied as a function of the applied load and its application point.

A carefully designed installation procedure was developed to overcome challenges posed by the confined laboratory space. This approach ensured the safe assembly of the turbine and its precise positioning within the flume, while minimising risks to both the flume and the turbine hardware.

A test strategy that accounted for the operational independence of the turbine and flume DAQ systems was described. The approach relied on a zero-offset calibration and manual synchronisation of the flow and rotor speeds to maintain a consistent tip-speed ratio during turbine operation, reducing the risk of unnecessary stall or overspeed events. Under steady-state conditions, the required turbine running time was determined to be at least 180 s for each test case, based on a stationarity analysis of the turbine's rotor loads.

The influence of ADV position on the blade root bending moments was evaluated by testing three different ADV positions, consistent with IEC TS 62600-200 guide-

lines, and comparing the results to measurements taken without the ADV. When the ADV was placed along the flume's centreline, the mast's influence extended across nearly half of the rotor plane at the lowest tip-speed ratio, inducing a 1P load fluctuation equivalent to approximately 10% of the azimuthal average. A similar effect was observed for edgewise loading, with the 1P load fluctuation reaching nearly 20% at the highest tip-speed ratio. Despite the higher load fluctuations for centreline ADV measurements, this represents a small trade-off to obtain more representative turbine reference velocities for performance and loading analysis.

A comparison of ground-truth thrust and torque measurements with the corresponding loads inferred from the blade root bending moments revealed smaller discrepancies when calibration coefficients were derived from a single radial location rather than a weighted average across multiple locations. For model-scale testing, linear coefficients corresponding to an effective radius of $r_{\text{eff}} = 0.7R$ for flapwise loading and $r_{\text{eff}} = 0.6R$ for edgewise loading were applied.

CHAPTER 8

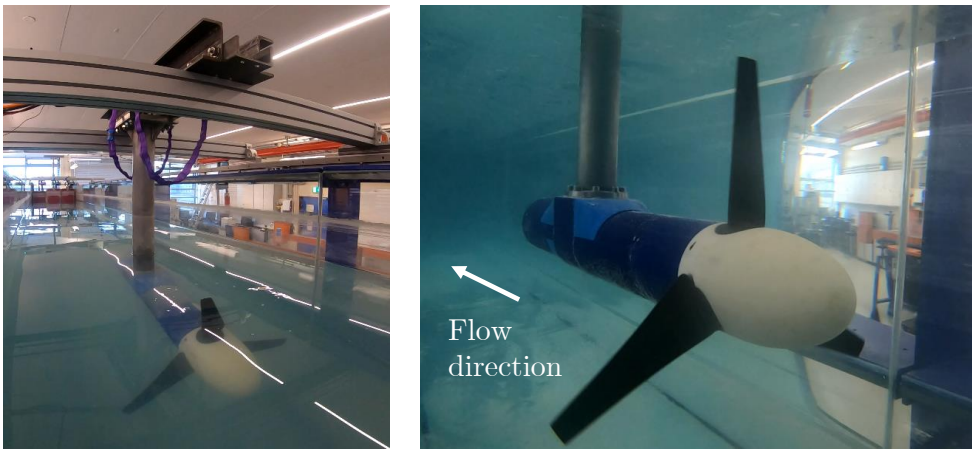
Turbine Performance and Loading Response

This chapter examines the performance and loading response of a model-scale tidal stream turbine under clean, turbulent, and sheared flow regimes, as characterised in Part I of this thesis. The work aims to expand the experimental database for the tidal energy community, offering fresh insights into unsteady rotor loading and providing validation points for engineering models. By doing so, it seeks to reduce uncertainty and conservatism in the design process.

The chapter begins by outlining the test conditions, providing context for the experimental setup. This is followed by an analysis of the turbine's approach flow and rotor performance across a range of operating conditions and different definitions of the turbine reference velocity. Steady-state rotor loads are then examined, with consideration for blockage effects and measurement uncertainty across the various flow regimes. Following an analysis of the unsteady blade loads, the chapter concludes with a discussion of the investigation's limitations.

8.1 Test Conditions

For tip-speed ratio sweeps between $\lambda = 3$–7, the ADV was positioned at $(x, y, z) = (2.7, 0, 0)$, in line with the rotor axis and located two rotor diameters upstream of the rotor plane, which was fixed at $x = 3.9\,\mathrm{m}$. For unsteady flow cases,



a) b)

Figure 8.1: Photographs of the turbine setup in the flume: (a) the view above the waterline and (b) the view below the waterline.

$x = 2.7\,\mathrm{m}$ corresponds to $x - x_\mathrm{F} = 1.2\,\mathrm{m}$. Since the exact turbine reference velocity was not known *a priori*, the rotor speed was adjusted to achieve the target tip-speed ratio based on the measured upstream flow speed. As noted in Section 7.3.5, tests without the ADV were also conducted to evaluate rotor loading response without interference from the ADV mast. The blade pitch angle was held at zero for all test runs. Additionally, the water temperature in the flume during the eight-week campaign ranged from 18.1–22.4°C, resulting in an approximate 11% variation in Reynolds number. The turbine test setup is shown in Figure 8.1.

8.2 Preliminary Flow and Performance Analysis

As a first step in the test campaign, preliminary flow and turbine measurements were conducted to develop insight into the experimental setup and to apply this learning to refine the testing and data analysis strategies.

8.2.1 Upstream Flow Characterisation

While flow characterisation in the absence of a turbine provides valuable baseline data on the hydrodynamic conditions, it is equally important to consider the physical processes governing the interaction between the channel and the turbine, which leads to differences between the characterised flow and the flow experienced by the turbine. One such process is the induction of backflow by the rotor wake, which slows the mean flow into the rotor [205]. To investigate whether the induction effect could be detected in the turbine's approach flow, vertical and cross-stream traverses of the ADV were conducted two rotor diameters upstream of the rotor plane across three nominal tip-speed ratios of $\lambda = 3$, 5, and 7 (which correspond to $\lambda =$ I, II, and III, respectively, as shown in Table 7.4), using a constant flow speed under clean flow conditions. Due to physical constraints in the experimental setup, only a single streamwise location was examined.

Figure 8.2 presents the results of the upstream flow characterisation, overlaid onto the corresponding flow profiles from three streamwise locations measured in the absence of the turbine, which were also used to interpolate a velocity profile at the streamwise location of the ADV, $x = 2.7\,\mathrm{m}$. Note that, to minimise turbine operating time during the flow characterisation experiments, ADV measurements were not repeated. The RMSEs between the interpolated profiles and those measured upstream of the turbine indicate a maximum deviation of $0.005\,\mathrm{m\,s^{-1}}$ across both axes, with no discernible trend with respect to the tip-speed ratio. By comparison, the standard error of the mean, calculated for each measurement point and then spatially averaged across each axis independently, was $0.007\,\mathrm{m\,s^{-1}}$.

Consistent with other studies, such as Deskos *et al.* [206], the results indicate that the turbine's induction effect was not detectable in the sampled flow two rotor diameters upstream, suggesting that a smaller separation distance between the rotor and the flow measurement point is necessary to observe this effect. In a corresponding analysis for turbulence intensity (not shown for brevity), no effect

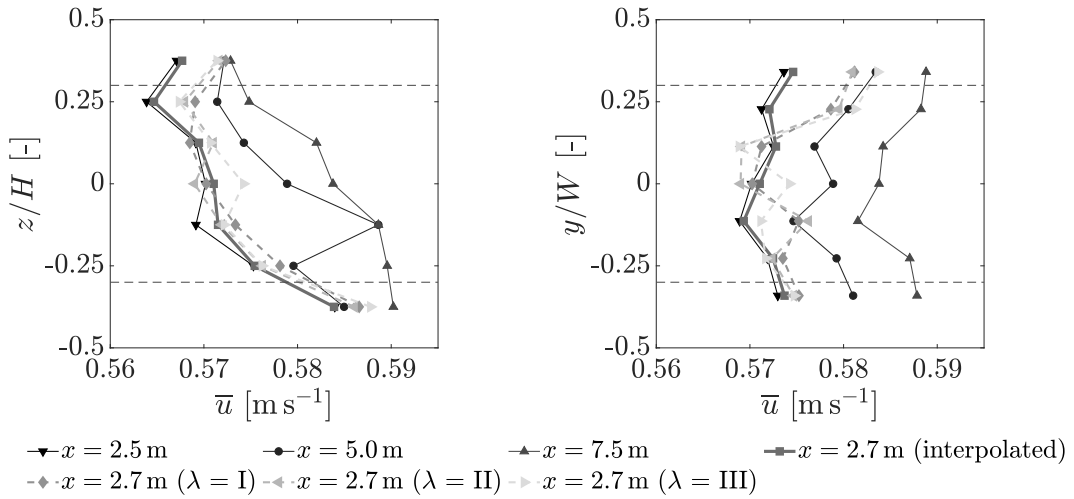


Figure 8.2: Streamwise evolution of depthwise (left panel) and cross-stream (right panel) velocity profiles in clean flow. Solid lines represent flow measurements at three streamwise locations in the absence of the turbine: $x = 2.5$ m (down-pointing triangles), 5.0 m (circles), and $x = 7.5$ m (up-pointing triangles). An interpolated velocity profile at $x = 2.7$ m is shown in each measurement axis (squares). Dashed lines represent the corresponding velocity profiles measured two rotor diameters upstream of the turbine across three tip-speed ratios, corresponding to the values in Table 7.4: $\lambda = \text{I}$ (diamonds), $\lambda = \text{II}$ (left-pointing triangles), and $\lambda = \text{III}$ (right-pointing triangles). Depthwise profiles are measured along the flume's vertical centre plane, while cross-stream profiles are taken along the horizontal centre plane, as illustrated in Figure 2.11. Linear piecewise fits have been added as a visual aid. The intended swept area of the rotor is also shown (dashed). Test conditions: $\overline{U_\text{T}} = 0.57\,\text{m s}^{-1}$ (centreline velocity).

from the rotor was observed. The turbulence intensities upstream of the turbine ranged between 0.97–1.54%, closely matching the values reported in the clean flow analysis (see Section 3.2.1). None of the other flow regimes (turbulence or shear) were evaluated in this manner, as flow measurements at $x = 2.7$ m were not conducted for these regimes prior to turbine installation. Furthermore, the transient nature of the unsteady flow regimes makes interpolation between the measurement planes unreliable.

8.2.2 Turbine Reference Velocity

Further to the discussion in Section 7.3.5, which explained the rationale for using centreline ADV measurements for the turbine reference velocity, the following analysis

examines the impact of using flow measurements taken in the absence of the turbine. Several researchers, including Blackmore *et al.* [50] and McNaughton *et al.* [197], have employed undisturbed flow measurements for turbine performance analysis, with a clear limitation of this approach being that it does not capture the instantaneous flow conditions experienced by the turbine.

Figure 8.3 illustrates how differences in the definition of the turbine reference velocity, U_{T}, can lead to substantial variation in the power and thrust coefficients (see Equations 6.1 and 6.2). For concurrent reference velocities measured two rotor diameters upstream of the rotor plane, the turbine operates most efficiently under clean flow conditions, achieving a maximum power coefficient of $C_{P,\,\mathrm{max}} = 0.57$ at an optimal tip-speed ratio of $\lambda_{\mathrm{opt}} = 4.87$. This is at least 1.8% greater than the maximum power coefficients observed in the other flow regimes, with the turbine's response to the flow downstream of grid A yielding the second-highest non-dimensional performance (see Table 8.2). Although the optimal tip-speed ratios for peak power performance vary considerably across the five flow regimes ($\lambda_{\mathrm{opt}} = 3.9$–$5.3$), the C_P-λ curves—with the exception of grid D—generally collapse within a band no wider than $0.05C_P$ across the operational range. The maximum thrust coefficient, $C_{T,\,\mathrm{max}} = 1.43$, also occurs under clean flow conditions, at the highest tip-speed ratio of $\lambda = 7.12$ (see Table 8.2), underscoring the superior performance of the turbine in this flow regime. Blockage corrections to the power and thrust coefficients are provided in Section 8.3.2.

For undisturbed flow measurements at the rotor plane, the impact on both the power and thrust coefficients becomes apparent, most notably for grid D, where a substantial flow deceleration along the centreline between $x - x_{\mathrm{F}} = 1.2$–$2.4\,\mathrm{m}$ (see Figure 4.3) significantly improves the non-dimensional power and thrust response. Using centreline and spatially averaged reference velocities, the maximum power coefficients are $C_{P,\,\mathrm{max}} = 0.61$ and 0.58, respectively, while the maximum thrust coefficients are $C_{T,\,\mathrm{max}} = 1.57$ and 1.50, representing relative increases of 26–50% compared to concurrent velocity measurements upstream of the turbine. Such

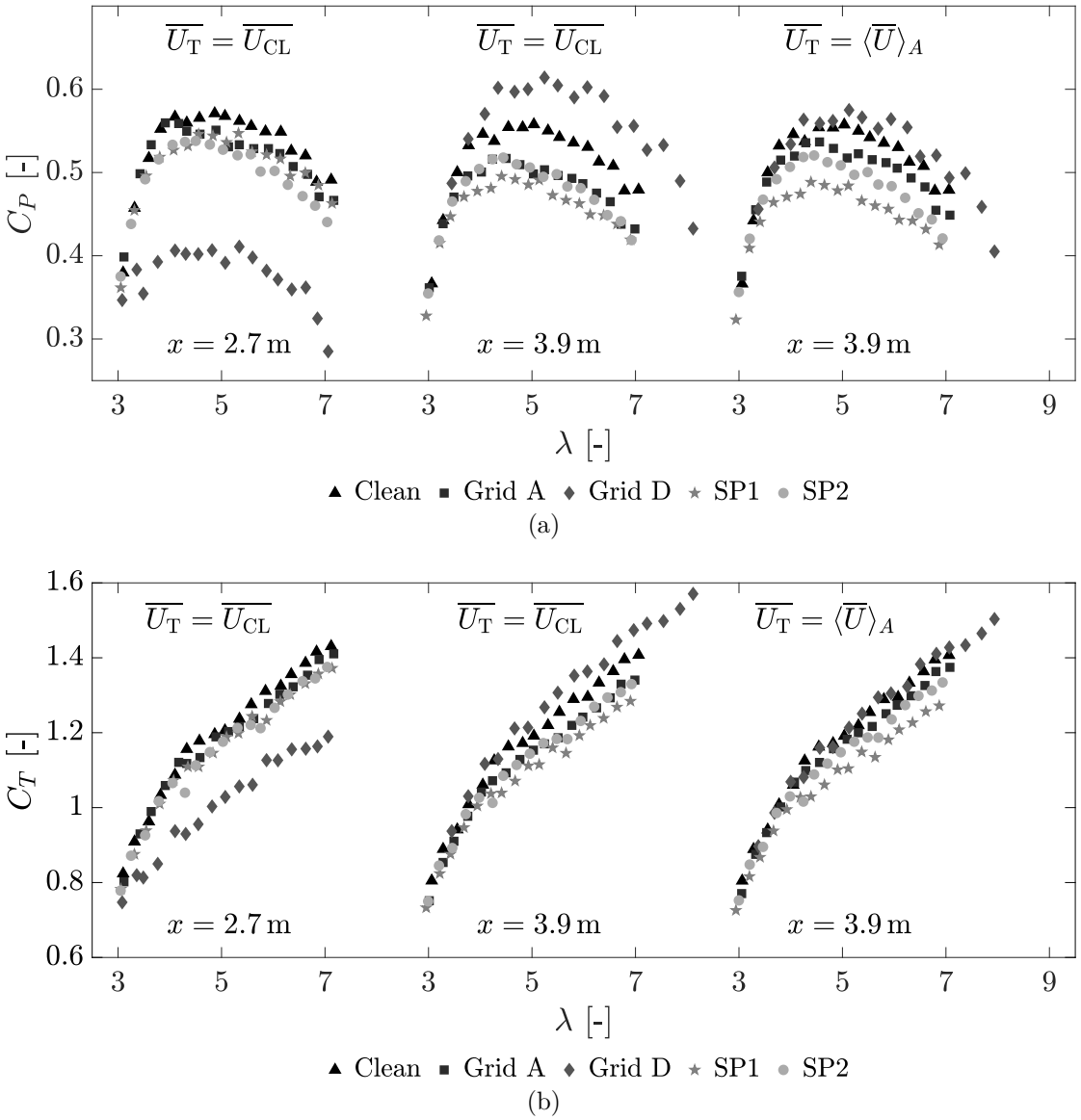


Figure 8.3: Variation in the coefficients of (a) power and (b) thrust as a function of tip-speed ratio, flow regime, and turbine reference velocity, the definition of which depends on the ADV measurement location and whether centreline or spatially averaged velocities across the swept area of the rotor are used. Note that $x = 2.7\,\mathrm{m}$ corresponds to a concurrent velocity measurement taken two rotor diameters upstream of the rotor plane, while $x = 3.9\,\mathrm{m}$ is aligned with the rotor plane and refers to measurements taken in the absence of the turbine. The tip-speed ratio was varied by adjusting the rotor speed, with the corresponding turbine reference velocities shown in Table 8.1.

discrepancies illustrate how the definition of the turbine reference velocity can significantly bias assessments of model-scale rotor performance.

The variation in performance metrics across different definitions of the turbine

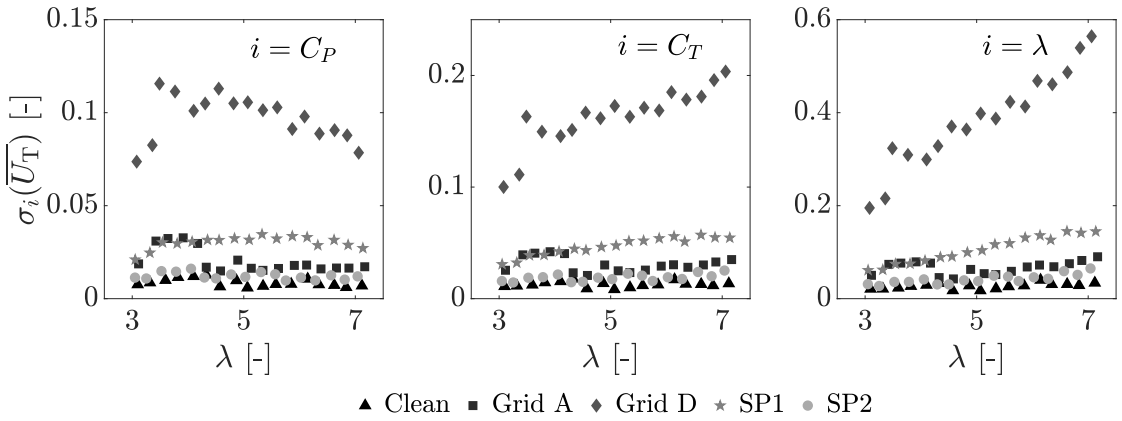


Figure 8.4: Variations in the coefficients of power (left panel) and thrust (middle panel), as well as the tip-speed ratio (right panel), resulting from three different definitions of the turbine reference velocity. The variations are represented by the standard deviation of the three results at each turbine operating point and are plotted as a function of each flow regime. The tip-speed ratio was varied by adjusting the rotor speed, with the corresponding turbine reference velocities shown in Table 8.1.

$\overline{U_T}$ [-]	x [m]	Measurement [-]	Clean	Grid A	Grid D	SP1	SP2
$\overline{U_{CL}}$	2.7	Concurrent	0.569	0.578	0.562	0.586	0.600
$\overline{U_{CL}}$	3.9	Undisturbed	0.575	0.594	0.492	0.606	0.609
$\langle\overline{U}\rangle_A$	3.9	Undisturbed	0.575	0.587	0.503	0.609	0.608

Table 8.1: Turbine reference velocity as a function of each flow regime. The definition of the reference velocity depends on the measurement location and whether centreline or spatially averaged velocities across the swept area of the rotor are used[a]. A constant volumetric flow rate, $0.61\,\mathrm{m^3\,s^{-1}}$, was maintained across all flow regimes. All velocities represent the mean of three repeated measurements and are given in $\mathrm{m\,s^{-1}}$.

[a]Spatially averaged values were calculated from interpolated velocity data across the swept area of the rotor, which were also used to generate the velocity contours in Part I of this thesis.

reference velocity is quantified in Figure 8.4, demonstrating increased sensitivity in more unsteady flows—most notably grid D—to the choice of the reference velocity. In contrast, more uniform flow conditions yield a more consistent non-dimensional response across all definitions of the reference velocity, with the clean flow case exhibiting the least variation in the power and thrust coefficients, as well as the tip-speed ratio.

To complement Figures 8.3 and 8.4, Table 8.1 highlights differences in the turbine reference velocity at the maximum allowable volumetric flow rate, which

corresponds to the design speed of the flume under clean flow conditions. Notably, for grid D, the undisturbed reference velocities are, on average, 10–12% lower than concurrent upstream measurements. In contrast, for all other flow regimes, the opposite trend is observed, with the relative differences being more modest, ranging between 1–4%.

Another notable feature of the non-dimensional power curves in Figure 8.3a is their flattening around the optimal tip-speed ratio ($\lambda_{\text{opt}} \pm 1$). Likewise, the C_T-λ curves in Figure 8.3b reveal a small inflection within a comparable range of tip-speed ratios, potentially indicating transitional effects on the blades that result in sub-optimal rotor performance. Another notable feature of the C_P-λ curves is the difference between the two sheared flow cases at higher tip-speed ratios. For $\lambda > 5$, the relative deterioration in the less sheared flow case (SP2) is attributed to increased drag forces acting on the rotor, a consequence of applying slightly higher rotor speeds ($+0.21\,\text{rad}\,\text{s}^{-1}$) for the SP2 performance curves. This adjustment was necessary to achieve equivalent operating points, owing to the slightly elevated turbine reference velocity compared to the SP1 flow regime (see Table 8.1).

8.2.3 Reynolds Number Independence

Reynolds number independence testing evaluates whether turbine performance metrics asymptote at a critical Reynolds number, determined by the turbine's geometry and operating conditions (specifically, the onset flow velocity and turbine rotor speed), to verify that model-scale test results are scalable and free from low-Reynolds-number effects. Since rotor performance is predominantly influenced by the blade section characteristics, chord-based Reynolds numbers at 70% span are a commonly used metric, estimated as:

$$\text{Re}_{0.7} = \frac{c_{0.7} U_{\text{T}} \sqrt{1 + (0.7\lambda)^2}}{\nu}, \tag{8.1}$$

where ν represents the kinematic viscosity and $c_{0.7}$ is the chord length at 70%

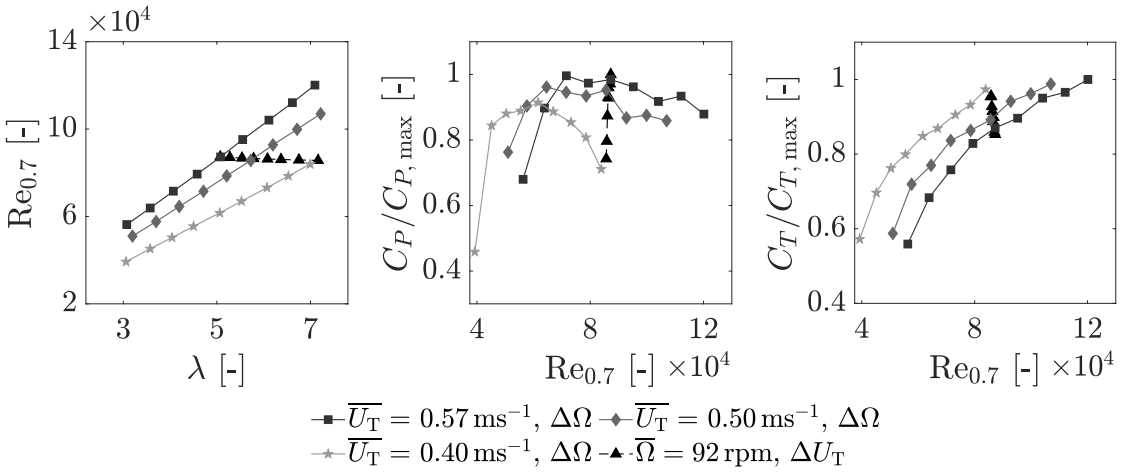


Figure 8.5: Reynolds number independence analysis for the clean flow case. For each panel, variation in the chord-based Reynolds numbers at 70% span, $\mathrm{Re}_{0.7}$, is achieved by changes to either the rotor speed, $\Delta\Omega$, or the turbine reference velocity (filled triangles), ΔU_T. For changes to the rotor speed, three different reference velocities are evaluated: $\overline{U_\mathrm{T}} = 0.57\,\mathrm{m\,s^{-1}}$ (filled squares), $0.50\,\mathrm{m\,s^{-1}}$ (filled diamonds), and $0.40\,\mathrm{m\,s^{-1}}$ (filled stars). The left-hand panel shows analytical predictions of $\mathrm{Re}_{0.7}$ as a function of tip-speed ratio. The middle panel presents the turbine power coefficient, normalised on its maximum experimental value ($C_{P,\,\mathrm{max}} = 0.57$), as a function of $\mathrm{Re}_{0.7}$. Similarly, the right-hand panel shows the variation in the turbine thrust coefficient, normalised on its maximum experimental value ($C_{T,\,\mathrm{max}} = 1.43$), as a function of $\mathrm{Re}_{0.7}$. Linear piecewise fits have been added in each panel as a visual aid. Test conditions: $(x, y, z) = (2.7, 0, 0)$ (ADV co-ordinates).

blade span, which, for the blades used in this study, was $c_{0.7} = 0.044\,\mathrm{m}$. This spanwise location is widely regarded as representative of the region of the blade that experiences the highest hydrodynamic loading, and aligns closely with experimental results presented earlier in this study (see Section 7.3.6). Note that Equation 8.1 assumes that rotor induction effects are negligible.

The geometric scale of the experiments was such that the blade profiles were likely operating around transition. To verify whether the results were independent of low-Reynolds-number effects, rotor performance across a range of chord-based Reynolds numbers was examined. The Reynolds numbers were varied by changing either the turbine reference velocity or the rotor speed within the nominal operating range, $\lambda = 3$–7.

Figure 8.5 illustrates the analysis of Reynolds number independence for the

clean flow case. The left-hand panel shows that Reynolds number variations across the tip-speed ratio range are predicted to be two orders of magnitude greater when driven by changes in rotor speed rather than by the turbine reference velocity. For investigations into rotor performance and unsteady blade loading, a chord-based Reynolds number that is less sensitive to changes in tip-speed ratio is advantageous, as it would help isolate the effects of unsteadiness across the operating range.

The middle panel, which examines the turbine's power coefficient as a function of Reynolds number, indicates that both adjustment strategies yield incremental improvements in maximum power performance. However, there is no evidence to suggest that Reynolds number independence has been reached at the optimal tip-speed ratio. Verifying this would require additional test points at flow velocities beyond the flume's design speed. Due to the sharp deterioration in the power coefficient for $\lambda > 6$ and the limited range of testable operating conditions ($\lambda = 5$–7) for Reynolds number changes driven solely by the turbine reference velocity, the tip-speed ratio was instead adjusted by varying the rotor speed (while maintaining a constant reference flow velocity) for the remainder of the test campaign.

The thrust response, in contrast, remains relatively stable across the range of turbine reference velocities (see right-hand panel). Since thrust is primarily a function of the axial force on the rotor, which is dominated by lift, C_T is much less sensitive to changes in drag—and, by extension, the Reynolds number—than C_P. To assess the similarity of the thrust curves, a two-sample Kolmogorov–Smirnov test [207] was conducted, comparing a universal fit derived from the union of all data to the individual curve fits, with the results showing no significant differences at the 5% significance level.

To examine the effects of freestream turbulence on Reynolds number independence, a similar analysis was conducted whereby the turbine power coefficient in response to grid-generated turbulence was mapped as a function of chord-based Reynolds number. The analysis, shown in Figure 8.6, includes results for grid A, which produces slightly elevated freestream turbulence levels ($I_{3D} \approx 4\%$) compared

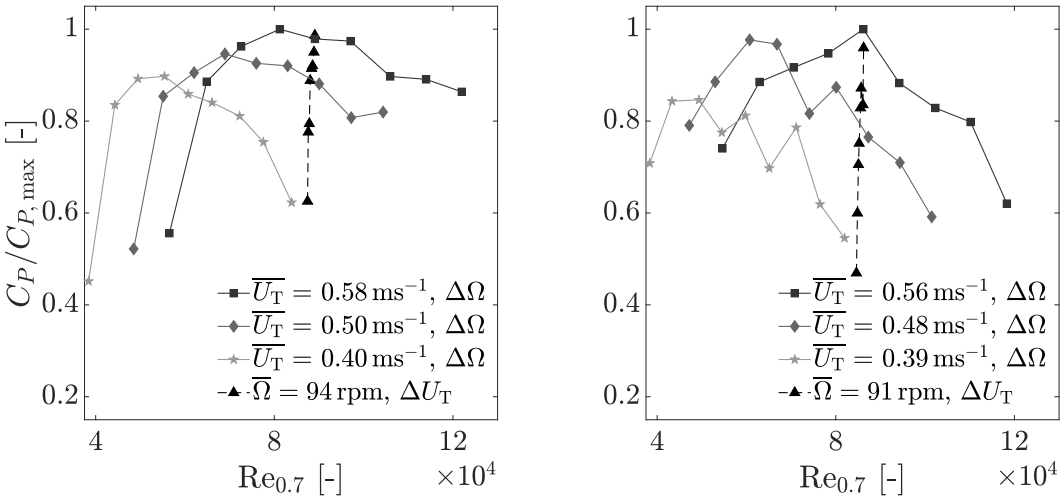


Figure 8.6: Variation of the power coefficient with chord-based Reynolds number at 70% span, $\mathrm{Re}_{0.7}$, for grids A (left panel) and D (right panel). The power coefficient is normalised on its maximum experimental value for the corresponding flow regime: $C_{P,\max} = 0.56$ for grid A and 0.44 for grid D. Variations in $\mathrm{Re}_{0.7}$ are driven by adjustments to either the rotor speed, $\Delta\Omega$, or the turbine reference velocity, ΔU_T. For changes to the rotor speed, three different reference velocities are evaluated for each turbulence grid. Linear piecewise fits have been added in each panel as a visual aid. Test conditions: $(x, y, z) = (2.7, 0, 0)$ (ADV co-ordinates).

to the clean flow case ($I_{3\mathrm{D}} \leq 2\%$), and for grid D, which generates significantly higher turbulence levels ($I_{3\mathrm{D}} \approx 12\%$). The results for grid A are similar to those for the clean flow case, where it is unlikely that Reynolds number independence has been achieved. A 5% relative difference is observed between the peak power coefficients at the two highest turbine reference velocities. At the lower end of the Reynolds number range ($\approx 5 \times 10^4$), where the blades approach stall, laminar separation bubbles are more likely to extend over a significant portion of the foil [208], resulting in degraded rotor performance.

In contrast, the turbine's response to the flow downstream of grid D reveals only a 2% discrepancy between the peak power coefficients for $\overline{U_\mathrm{T}} \geq 0.48\,\mathrm{m\,s}^{-1}$, suggesting that higher freestream turbulence likely triggers an earlier transition to turbulence in the blades' boundary layers, allowing more modest flow speeds to approach Reynolds number independence. Beyond the maximum power coefficient, however, rotor performance deteriorates more significantly than in the clean and

grid A flow regimes, suggesting that increased freestream turbulence has a more detrimental impact on rotor performance away from the design point.

8.3 Steady-State Rotor Loads

8.3.1 Integrated Quantities

Building on the turbine performance metrics discussed in Section 8.2, Figure 8.7 presents further analysis of the steady-state rotor performance and loads across the various flow regimes. These are represented by the ratio of the power and thrust coefficients, C_P/C_T, and the blade root bending moment response, which, in non-dimensional form, is defined as:

$$C_{\mathrm{RBM}} = \frac{\mathrm{RBM}}{\frac{1}{2}\rho U_{\mathrm{T}}^2 AR}. \tag{8.2}$$

Similar to the power and thrust coefficients presented in Figure 8.3, the C_P/C_T curves—which represent the hydrodynamic efficiency of the turbine—largely collapse across the various flow regimes, with the exception of grid D. The similarity of the curves underscores the turbine's robustness to moderate turbulence levels and velocity shear, suggesting minimal impact on the efficiency of energy extraction relative to the overall thrust exerted by the turbine on the flow. As before, the clean flow case defines the upper limit of the narrow band formed by the collapsed curves, while the less sheared flow regime (SP2) lies at the lower boundary. However, as with previous analyses, comparisons of the relative performance of each flow regime should be approached with caution due to the use of a single-point turbine reference velocity, particularly in highly non-uniform approach flows. The maximum power-to-thrust ratio, $C_P/C_T = 0.54$, occurs at a tip-speed ratio of $\lambda = 3.6$, highlighting the turbine's ability to extract energy efficiently at a moderate hydrodynamic loading. Sub-optimal values are observed at higher tip-speed ratios, where the thrust force increases disproportionately relative to power extraction.

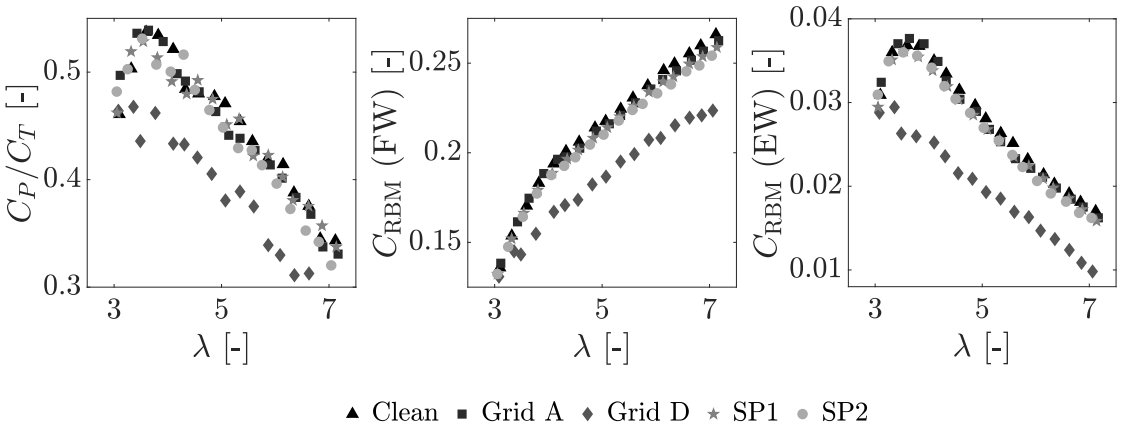


Figure 8.7: Comparison of steady-state rotor loads as a function of tip-speed ratio and flow regime. The left-hand panel presents the power-to-thrust ratio, while the middle and right-hand panels illustrate the variation in the coefficients of flapwise and edgewise root bending moments, respectively. The bending moment coefficients represent the averages from across the three blades. The tip-speed ratio was varied by adjusting the rotor speed. Test conditions: $(x, y, z) = (2.7, 0, 0)$ (ADV co-ordinates); concurrent centreline velocities are shown in Table 8.1.

Flow regime	$C_{P,\,\max}$	$C_{T,\,\max}$	$C_{\mathrm{RBM},\,\max}$ (FW)	$C_{\mathrm{RBM},\,\max}$ (EW)
Clean	0.57 (4.87)	1.43 (7.12)	0.27 (7.12)	3.68×10^{-2} (3.60)
Grid A	0.56 (3.91)	1.41 (7.17)	0.26 (7.17)	3.76×10^{-2} (3.64)
Grid D	0.41 (5.34)	1.19 (7.06)	0.22 (7.06)	2.94×10^{-2} (3.36)
SP1	0.55 (5.32)	1.37 (7.14)	0.26 (7.14)	3.61×10^{-2} (3.54)
SP2	0.54 (4.50)	1.38 (7.04)	0.25 (7.04)	3.60×10^{-2} (3.52)

Table 8.2: Maximum steady-state rotor loads, with corresponding tip-speed ratios in parentheses, for each flow regime. All quantities are non-dimensional. The turbine reference velocity was measured two rotor diameters upstream of the rotor plane.

The variation in the flapwise root bending moment coefficients closely follows the trend of the thrust coefficients with tip-speed ratio (see Figure 8.3b), while, for edgewise loading, a similar trend is observed with rotor torque (not shown), both peaking at the same tip-speed ratio as the C_P/C_T curves ($\lambda = 3.4$–3.6; see Table 8.2). In line with earlier observations, both sets of curves broadly collapse into a narrow band, with the exception of grid D, indicating minimal differences in the non-dimensional loading response of the rotor blades in clean as well as moderately turbulent and sheared flows. When expressed dimensionally, the flapwise

root bending moments are approximately 11 times larger than the corresponding edgewise loads, consistent with previous findings [172] and the expectation that thrust forces dominate over centrifugal inertial forces.

8.3.2 Blockage Correction

As discussed in Section 7.1.2, the effect of a blocked flow is to increase the flow speed through the rotor plane for a given level of thrust, resulting in elevated turbine loads and power production compared to an unblocked flow. For laboratory-scale testing, this effect can be particularly pronounced due to the higher blockage ratio compared to an open-water environment.

To account for the effects of blockage, correction methods typically seek to establish a relationship between the upstream velocity—here defined as U_{T}—and the equivalent upstream velocity in an unblocked flow [12]. In this study, the correction method developed by Barnsley and Wellicome [134], and later summarised for the marine energy research community by Bahaj *et al.* [12], was applied to the computed power and thrust coefficients. The approach, based on an actuator disc model of a turbine in a closed channel, requires only blockage and thrust information to solve for the unknown velocities, and has been widely employed to correct for blockage in a number of experimental studies, including Galloway *et al.* [157], Gaurier *et al.* [188], and Ross and Polagye [135], who applied the correction for a blockage ratio of 35%.

For model-scale testing in the Oxford flume, a high channel blockage ratio of 25.7% was maintained for all test cases. Results in Figure 8.8 indicate that the flume's high blockage significantly amplifies turbine loads across the operating range, resulting in uplifts of 18–41% in the power coefficient and 13–31% in the thrust coefficient. Peak performance in unblocked flow is estimated to be $C_P = 0.4$, well below Betz's theoretical limit of 16/27 for unbounded flow [205], and $C_T = 1.0$. A key feature of the unblocked flow results is the narrowing of the operating range, consistent with previous studies [135].

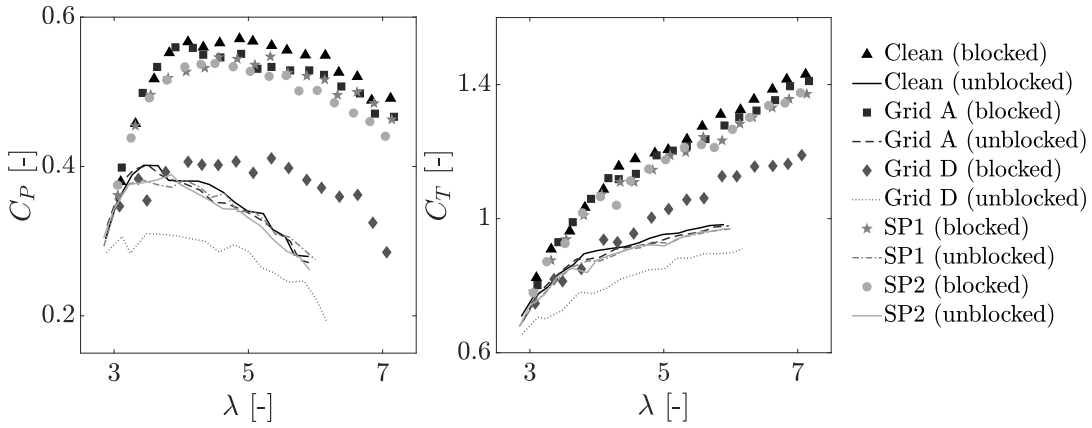


Figure 8.8: Application of Barnsley and Wellicome's [134] correction to blocked turbine performance across each flow regime. The left-hand panel shows the variation in the power coefficient, while the right-hand panel illustrates the variation in the thrust coefficient, both as functions of the tip-speed ratio. The blockage ratio was held constant for all test cases at 25.7%. The tip-speed ratio was varied by adjusting the rotor speed. Linear piecewise fits are included for the unblocked results as a visual aid. Test conditions: $(x, y, z) = (2.7, 0, 0)$ (ADV co-ordinates); concurrent centreline velocities are shown in Table 8.1.

As a first-order approximation of the unblocked flow state, the corrections appear reasonable; however, experiments in a significantly larger flow domain are needed to validate this assertion. Given the consistent blockage ratio across all test cases, the overall conclusions of this study are unlikely to be significantly impacted. Nevertheless, assessing the suitability of the correction method for such a substantial blockage ratio lies beyond the scope of this work. Both Ross and Polagye [135] and Zilic de Arcos *et al.* [133] provide comparative analyses of different blockage correction methods in their respective studies.

8.3.3 Uncertainty Quantification

Applying the methodology outlined in Sections 2.2.5 and 7.2, and following the recommended guidelines published by the International Towing Tank Conference (ITTC) [209, 210], an uncertainty analysis of selected non-dimensional parameters was undertaken, accounting for the contributions from both random and systematic sources of error. For correlated variables, the uncertainty was evaluated

using Taylor's method of propagation, as described by Coleman and Steele [63], which employs a systematic data reduction approach to account for the relationships between variables. As detailed in the remainder of this section, uncertainty was quantified for the coefficients of power and thrust, the tip-speed ratio, and both coefficients of the blade root bending moments.

Power Coefficient

Following ITTC Procedure 7.5-02-07-03.15 [210], the systematic uncertainty for the power coefficient is expressed in terms of its contributing sources of systematic error, which include rotor power, fluid density, rotor radius, and flow velocity, given by:

$$\delta^2_{\text{sys},\,C_P} = \left(\frac{\partial C_P}{\partial P}\delta_{\text{sys},\,P}\right)^2 + \left(\frac{\partial C_P}{\partial \rho}\delta_{\text{sys},\,\rho}\right)^2 + \left(\frac{\partial C_P}{\partial R}\delta_{\text{sys},\,R}\right)^2 + \left(\frac{\partial C_P}{\partial U_T}\delta_{\text{sys},\,U_T}\right)^2, \quad (8.3)$$

where each bracketed term quantifies the contribution of the corresponding source of systematic error. The partial derivatives represent the sensitivity of the power coefficient to each variable, derived using Equation 6.1. Note that the first term on the right-hand side accounts for the combined contributions of both rotor torque and speed, which are not explicitly shown for brevity.

As with the blade root flexure calibration analysis, the systematic error of the i^{th} error contribution, $\delta_{\text{sys},\,i}$, incorporates a range of measurement uncertainties throughout the experimental setup. These include instrument accuracy and resolution, the resolution of the analogue-to-digital conversion, and uncertainty in the calibration curve fits, derived either from supplier-provided data or in-house testing.

After combining the systematic and random errors using Equation 2.5, a coverage factor based on two degrees of freedom was applied, yielding an expanded uncertainty at the 95% confidence level as a function of tip-speed ratio and flow regime. As shown in the left-hand panel of Figure 8.9, the expanded uncertainty

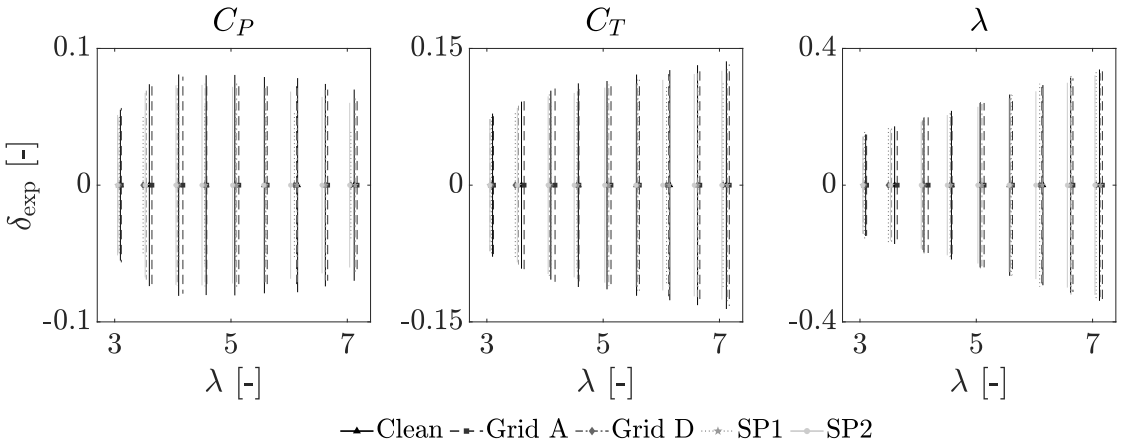


Figure 8.9: Error bars representing the expanded uncertainty, δ_{exp}, in the coefficients of power (left panel) and thrust (middle panel), and the tip-speed ratio (right panel). Different line colours, markers, and styles distinguish the flow regimes. The tip-speed ratio was varied by adjusting the rotor speed.

broadly scales with the magnitude of the power coefficient, peaking at approximately $\delta_{\text{exp},\,C_P} = \pm 0.08$ (equivalent to $\pm 0.14 C_{P,\,\text{max}}$) within a tip-speed ratio range of $\lambda = 4.1$–6.1 for the clean flow case. The largest contribution to measurement uncertainty is the systematic error associated with ADV measurements, $\mathcal{O}(10^{-2})$, which is at least one order of magnitude greater than the contributions from other error sources. Measurement errors associated with the rotor radius and rotor speed are $\mathcal{O}(10^{-3})$, while the least significant systematic error contributions, $\mathcal{O}(10^{-4})$, arise from rotor torque and the fresh water density[1]. The random error, defined here as the standard error of the mean from three repeated measurements, is $\mathcal{O}(10^{-3})$.

[1]Following ITTC Procedure 7.5-02-01-03 [211], the systematic error in the fresh water density, $\delta_{\text{sys},\,\rho}$, was evaluated with respect to the flume temperature, measured using a thermometer with an accuracy of ± 1°C.

Thrust Coefficient

Following the same methodology as for the power coefficient, the combined systematic uncertainty for the thrust coefficient (see Equation 6.2) is expressed as:

$$\delta^2_{\text{sys},\,C_T} = \left(\frac{\partial C_T}{\partial T}\delta_{\text{sys},\,T}\right)^2 + \left(\frac{\partial C_T}{\partial \rho}\delta_{\text{sys},\,\rho}\right)^2 + \left(\frac{\partial C_T}{\partial R}\delta_{\text{sys},\,R}\right)^2 + \left(\frac{\partial C_T}{\partial U_T}\delta_{\text{sys},\,U_T}\right)^2. \quad (8.4)$$

The middle panel of Figure 8.9 shows the expanded uncertainty at the 95% confidence level, demonstrating a similar relationship between the parameter of interest—C_T in this case —and the quantified error. The uncertainty peaks at approximately $\delta_{\text{exp},\,C_T} = \pm 0.14$ (equivalent to $\pm 0.10 C_{T,\,\text{max}}$) at the highest tip-speed ratio, $\lambda = 7.1$, for the clean flow case. As with the power coefficient, uncertainty is dominated primarily by the systematic error associated with ADV measurements, while contributions from the rotor radius, fresh water density, and random error remain consistent with previous observations. Owing to the high accuracy of thrust measurements (0.1%) and the low standard error of the estimate (SEE) from the calibration curve provided by the thrust and torque transducer (TTD) supplier, the corresponding systematic error is $\mathcal{O}(10^{-3})$.

Tip-speed Ratio

Building on the approach used for the performance coefficients, the combined systematic uncertainty for the tip-speed ratio (see Equation 6.3) is given by:

$$\delta^2_{\text{sys},\,\lambda} = \left(\frac{\partial \lambda}{\partial \Omega}\delta_{\text{sys},\,\Omega}\right)^2 + \left(\frac{\partial \lambda}{\partial R}\delta_{\text{sys},\,R}\right)^2 + \left(\frac{\partial \lambda}{\partial U_T}\delta_{\text{sys},\,U_T}\right)^2. \quad (8.5)$$

The influence of increasing the rotor speed is reflected in the linear growth of the expanded uncertainty with respect to the tip-speed ratio, as shown in the right-hand panel of Figure 8.9. The relative error contributions remain broadly consistent across the range of tip-speed ratios, resulting in expanded uncertainties of approximately 5% of the nominal values. As in previous cases, the systematic

error is dominated by ADV measurements, $\mathcal{O}(10^{-1})$, while the rotor speed and rotor radius contribute significantly smaller errors, $\mathcal{O}(10^{-3})$. The maximum expanded uncertainty is estimated as $\delta_{\text{exp},\,\lambda} = \pm 0.34$ at the 95% confidence level for the clean flow case, with the systematic error, on average, approximately 30 times larger than the random error.

Coefficients of Blade Root Bending Moments

Using Equation 8.2, the combined systematic uncertainty for the coefficients of the blade root bending moments can be expressed as:

$$\begin{aligned}\delta^2_{\text{sys},\,C_{\text{RBM}}} = &\left(\frac{\partial C_{\text{RBM}}}{\partial \text{RBM}}\delta_{\text{sys},\,\text{RBM}}\right)^2 + \left(\frac{\partial C_{\text{RBM}}}{\partial \rho}\delta_{\text{sys},\,\rho}\right)^2 \\ &+ \left(\frac{\partial C_{\text{RBM}}}{\partial R}\delta_{\text{sys},\,R}\right)^2 + \left(\frac{\partial C_{\text{RBM}}}{\partial U_T}\delta_{\text{sys},\,U_T}\right)^2,\end{aligned} \tag{8.6}$$

where $\delta_{\text{sys},\,\text{RBM}}$ incorporates all error sources quantified during the blade root flexure calibration process (see Section 7.2). Note that, following the selection of a single effective radius in Section 7.3.6, the quantified error was restricted to data corresponding to $r_{\text{eff}}\,(\text{FW}) = 0.7R$ and $r_{\text{eff}}\,(\text{EW}) = 0.6R$.

As with the analysis for the power and thrust coefficients, the expanded uncertainty for flapwise loading scales with the magnitude of the root bending moment coefficient, as shown in the left-hand panel of Figure 8.10. For the clean flow case, the uncertainty peaks at approximately $\delta_{\text{exp},\,C_{\text{RBM}}} = \pm 0.03$, corresponding to roughly 12% of the maximum root bending moment coefficient at the highest tip-speed ratio, $\lambda = 7.1$.

In contrast, for edgewise loading, the uncertainty scales inversely with the root bending moment coefficient, as shown in the right-hand panel of Figure 8.10. At a tip-speed ratio of $\lambda = 7.1$, the expanded uncertainty peaks at $\delta_{\text{exp},\,C_{\text{RBM}}} = \pm 0.01$ for the clean flow case, representing approximately 60% of the corresponding root bending moment coefficient. Although the systematic error contributions

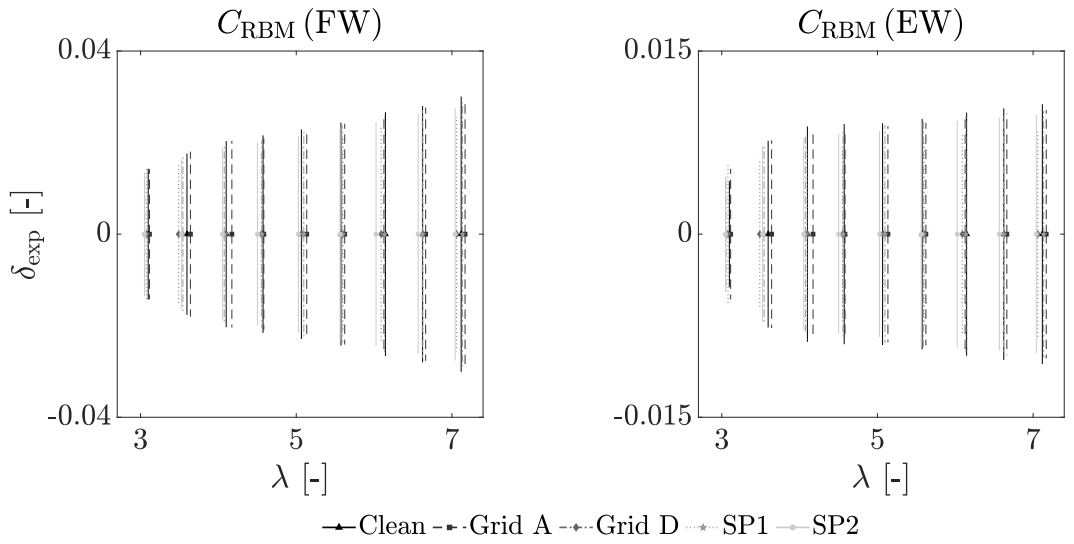


Figure 8.10: Error bars representing the expanded uncertainty, δ_{exp}, in the blade root bending moment coefficients: flapwise (left panel) and edgewise (right panel). Each error bar represents the average from across the three blades. Different line colours, markers, and styles distinguish the flow regimes. The tip-speed ratio was varied by adjusting the rotor speed.

steadily decrease with the edgewise load as tip-speed ratio increases, the random error, $\mathcal{O}(10^{-3})$, which accounts for approximately 93% of the combined uncertainty, steadily increases and ultimately drives the rise in expanded uncertainty. By comparison, the random error contributes only 23% to the combined uncertainty for flapwise loading, and thus has a much smaller influence on the trajectory of the quantified error as a function of tip-speed ratio.

Once again, the systematic uncertainty for both the flapwise and edgewise root bending moment coefficients is dominated by velocity measurement error, which exceeds the contributions of other systematic error sources by at least one order of magnitude. The next most significant contribution arises from the error associated with the measurement of the root bending moments, represented by the first bracketed term on the right-hand side of Equation 8.6, which scales with the measured load.

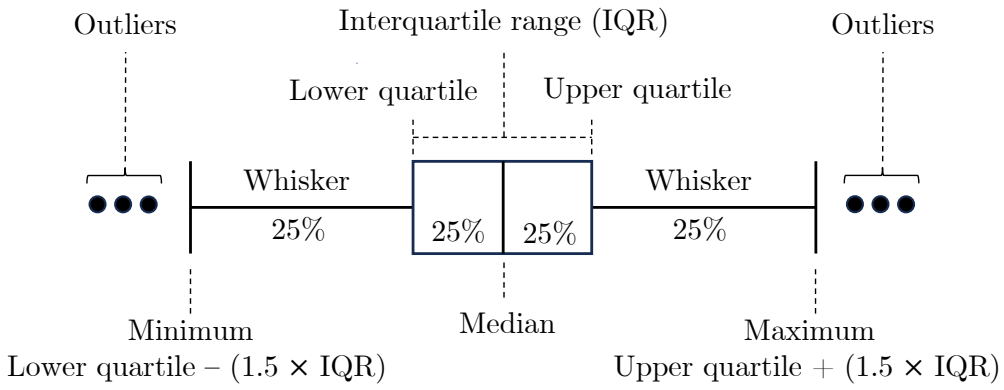


Figure 8.11: Generic boxplot descriptor illustrating the median, interquartile range (IQR), full range, and potential outliers in a dataset.

8.4 Unsteady Blade Loads

8.4.1 Loading Distributions

Boxplots are a concise visual tool for summarising key statistics from a sampling record, with a generic descriptor provided in Figure 8.11 for reference. Figure 8.12 presents loading distributions of the blade root bending moments across three nominal tip-speed ratios for the five flow regimes. By normalising the loads on their time-averaged values, the distributions effectively isolate the effects of the unsteady hydrodynamics while minimising the influence of differences in the turbine reference velocity across the flow regimes.

For the flapwise loads, the clean flow case yields the narrowest distributions, indicating lower variability and more uniform loading profiles compared to the other flow regimes. As freestream turbulence increases from the clean flow case ($I_{3D} \leq 2\%$) to grid A ($I_{3D} \approx 4\%$) and finally to grid D ($I_{3D} \approx 12\%$), the loading distributions widen, reflecting greater variability caused by larger velocity fluctuations in the turbine's approach flow. A similar trend is observed for increased vertical shear, although the effect is less visually discernible due to the comparable levels of turbulence generated by the SP1 and SP2 obstructions (see Figure 5.6). At the lowest tip-speed ratios, both the interquartile ranges (IQR) and the overall

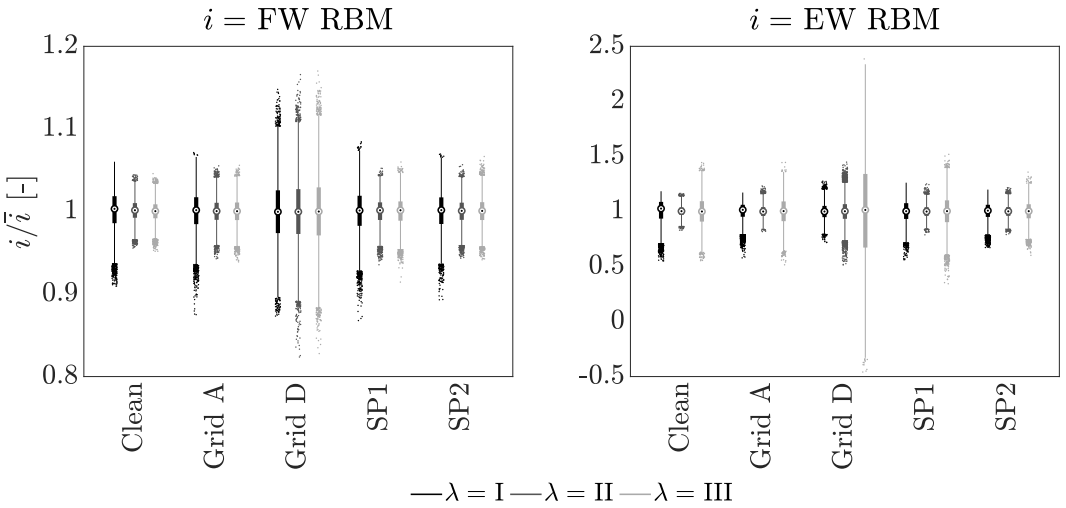


Figure 8.12: Box plots showing summary statistics for the distributions of flapwise (left panel) and edgewise (right panel) root bending moments, i, for each flow regime in the absence of the ADV. Loads are normalised on their time-averaged values, with different marker colours representing various tip-speed ratios (see Table 7.4 for exact values). Each boxplot represents the average from across the three blades. The tip-speed ratio was varied by adjusting the rotor speed.

distribution spreads increase, indicating increasingly unsteady turbulence-rotor interactions as the blades approach stall. Additionally, the negatively skewed distributions observed for the clean case, grid A, and both sheared flow regimes suggest intermittent loading events that are skewed towards lower values, possibly driven by transient flow behaviour. In contrast, the turbine's response to the flow downstream of grid D, suggests that, at the lowest tip-speed ratio, a more energised boundary layer, resulting from higher freestream turbulence, delays flow separation, resulting in more similar loading distributions across the tip-speed ratio range.

Slightly different trends emerge in the edgewise distributions, most notably the increased interquartile ranges and overall spreads at the highest nominal tip-speed ratio of $\lambda = 7$, indicating a heightened sensitivity of the edgewise response to higher rotor speeds. In dimensional terms, however, the largest load magnitudes occur at the lowest tip-speed ratios (except for grid D), reflecting the higher likelihood of sections of the blades experiencing stall and loading overshoots. Interestingly, the narrowest load distributions occur at, or near to, the optimal tip-speed ratio

($\lambda_{opt} \approx 5$). Once again, the turbine's response to the flow downstream of grid D deviates from the other flow regimes, particularly with the outsized response at $\lambda = 7$, which is likely non-physical. Even after excluding this outlier, the normalised load range remains more than twice as large as that of the flapwise loads, highlighting the greater sensitivity of the edgewise response. Another likely contributing factor to the increased loading variability is the lower signal-to-noise ratio of the edgewise signals, attributable to the much smaller edgewise loads. Negatively skewed distributions, similar to those observed in the flapwise data as the blades approach stall, are evident once again for the clean case, grid A, and both sheared flow regimes.

8.4.2 Azimuthal Load Variations

Polar Representation

Figure 8.13 illustrates the azimuthal variation in the flapwise and edgewise root bending moment coefficients across three nominal tip-speed ratios for each of the five flow regimes, providing insight into the blades' unsteady cyclic loading patterns. The coefficients are normalised on azimuthally averaged values from the clean flow case, effectively eliminating the influence of differences in the turbine reference velocity and isolating the effects of the unsteady hydrodynamics.

For grid A, the loading profiles are broadly similar, although with subtle differences across the different tip-speed ratios. As the blades approach stall, the turbine's response to grid A yields slightly higher root bending moment coefficients relative to the clean flow case, suggesting that elevated freestream turbulence delays flow separation, resulting in higher lift forces compared to clean flow conditions, where flow separation occurs more readily. At higher nominal tip-speed ratios of $\lambda \geq 5$, clean flow conditions promote more stable flow reattachment and higher time-averaged loads in the post-stall regime, whereas higher turbulence levels increase drag and likely disrupt lift recovery, resulting in reduced bending moment

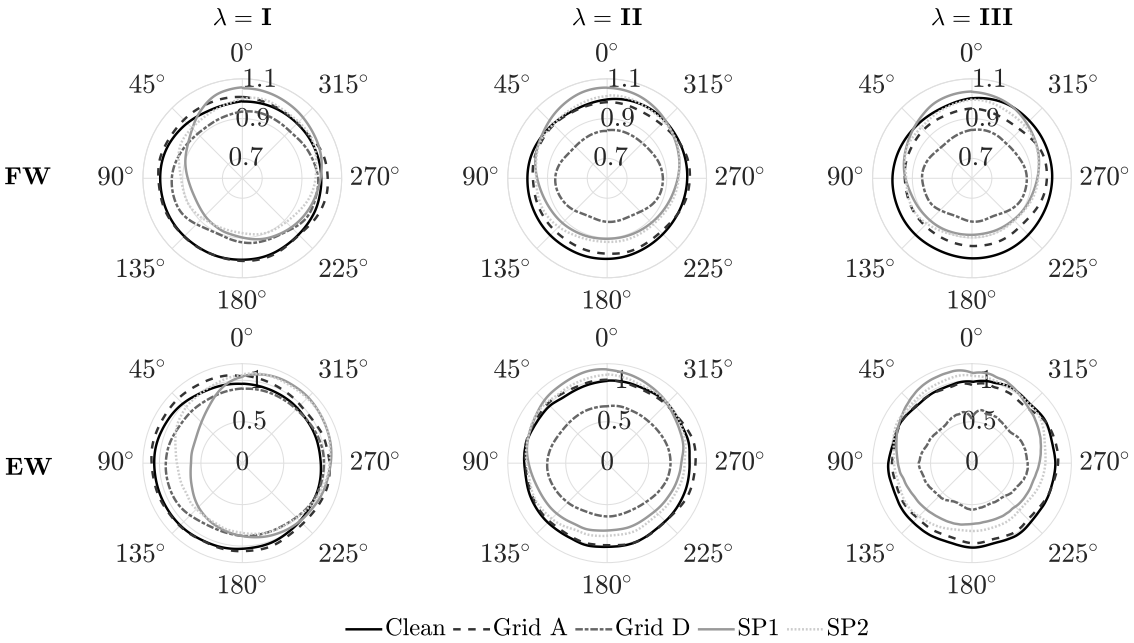


Figure 8.13: Azimuthal variation of flapwise (top row) and edgewise (bottom row) root bending moment coefficients, presented in polar form as a function of tip-speed ratio (see Table 7.4 for exact values), for each flow regime in the absence of the ADV. The coefficients are averaged across the three blades, phase-averaged into 1° bins, and normalised on azimuthally averaged values from the clean flow case. The tip-speed ratio was varied by adjusting the rotor speed, with the corresponding turbine reference velocities shown in Table 8.1.

coefficients compared to the clean flow case. A similar trend is observed for the blades' response to grid D; however, the relative coefficient magnitude is significantly lower—by approximately 14% in the flapwise direction and 31% in the edgewise direction at $\lambda = 5$—due to much smaller root bending moments compared to those at lower turbulence levels. Despite the comparable turbine reference velocities (see Table 8.1), the significant flow deceleration along the centreline observed between $x - x_F = 1.2$–$2.4\,\mathrm{m}$ (see Figure 4.3), combined with the bypass effect suggested by Figure 4.10b, likely results in a much lower flow velocity through the rotor plane compared to both the clean and grid A flow regimes. For both turbulence grids, the blade loading orbitals exhibit significantly less uniformity compared to the clean flow case, reflecting the increased spatial variation in the onset flow. In both cases, the flapwise loads reach their maximum values when the blades

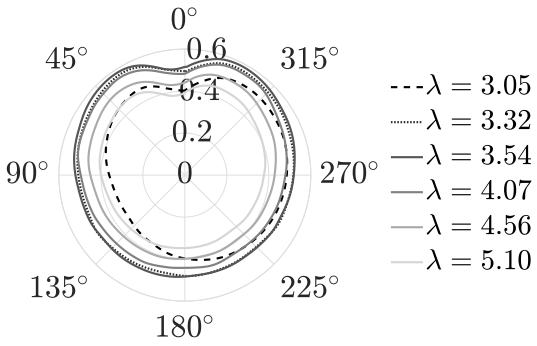


Figure 8.14: Azimuthal variation of edgewise root bending moments (in N m) presented in polar form across six tip-speed ratios in highly sheared flow (SP1). The bending moments are first averaged across the three blades and subsequently phase-averaged into 1° bins. The load reduction near top dead centre is attributed to the presence of the ADV mast during test runs. The tip-speed ratio was varied by adjusting the rotor speed. Test conditions: $\overline{U_\mathrm{T}} = 0.59\,\mathrm{m\,s^{-1}}$ (centreline velocity); $(x, y, z) = (2.7, 0, 0)$ (ADV co-ordinates).

are oriented horizontally ($\phi = 270° \pm 12°$), despite the larger tip clearance to the flume boundaries (250 mm) compared to top dead centre or bottom dead centre (200 mm). This counterintuitive result can be attributed to the flow channelling effect downstream of the turbulence grids, likely amplified by the bypass effect of the rotor. For grid D in particular, this effect is apparent in Figure 4.10b, where higher local velocities are observed closer to the sidewalls, away from the core of the channel, likely driving local increases in the blade loads.

The loading profiles for the two sheared flow cases provide further insights into the turbine's response to unsteady approach flows. Compared to the clean and turbulent flow cases, the load profiles exhibit increased horizontal asymmetry, particularly for the more sheared flow case (SP1) at the lowest tip-speed ratio. As expected, higher root bending moments are skewed towards the upper half of the rotor's swept area, where local flow speeds are greater, and are further biased high during the blade's upstroke as it approaches top dead centre. The asymmetry highlights differences in the angle of attack profiles about the vertical centre plane of the rotor and suggests a higher propensity for stall during one half of the blade's rotation. This behaviour is examined in greater detail in Figure 8.14, which

presents the edgewise root bending response at finer increments of the tip-speed ratio. As the blades approach stall, the loading profiles exhibit significantly higher loads during the upstroke, with a particularly marked reduction observed between $\phi = 55$–$210°$. At a tip-speed ratio of $\lambda = 3.54$, peak loading occurs around the rotor azimuth, followed by progressively narrower loading orbitals as the rotor speed increases, with slightly higher loads observed during the downstroke, peaking at approximately $\phi = 35°$. While the cause of these asymmetrical loading patterns remains unclear, the associated once-per-revolution (1P) load fluctuations are likely to contribute more significantly to fatigue-related failures than more uniform loading profiles.

There is no evidence to suggest that the tower-passing effect influences the azimuthal load profiles across any of the flow regimes.

Cartesian Representation

To complement the polar plots, Cartesian representations of the blade loads can reveal distinct aspects of the loading behaviour that may not be immediately apparent in polar form. Figure 8.15 presents the flapwise root bending moments and their variation in Cartesian form across three nominal tip-speed ratios and the five flow regimes.

For the clean flow case, the loading profiles at higher nominal tip-speed ratios ($\lambda \geq 5$) are closely aligned in both phase and magnitude. The loading variations, represented as $\pm 1\sigma$ about the phase-averaged load, are similarly well-aligned. Table 8.3 supplements the figure by providing a selection of summary statistics for each flow regime, showing that the normalised load range for the clean flow case is just 3% of the time-averaged loads. At the lowest nominal tip-speed ratio of $\lambda = 3$, where the blades approach stall, a phase shift exceeding 140° emerges between the azimuthal position of the maximum load and the corresponding positions at higher tip-speed ratios[2]. Additionally, the maximum load variation at this tip-speed ratio

[2]The phase shift is always reported as the smallest angular difference, independent of direction.

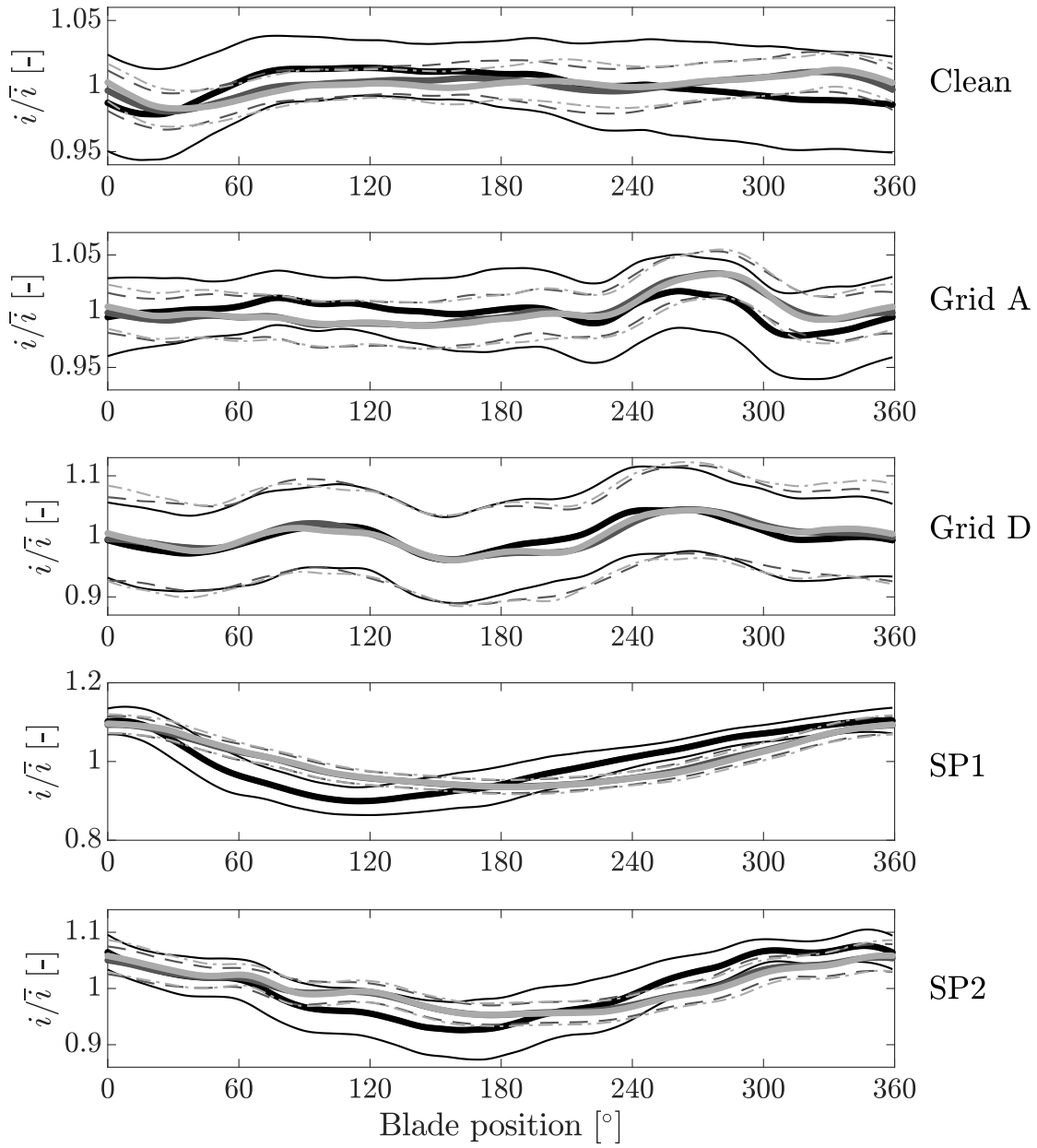


Figure 8.15: Azimuthal variation of flapwise root bending moments, i, and their variation (represented by $\pm 1\sigma$), shown in Cartesian form as a function of tip-speed ratio (see Table 7.4 for exact values) for each flow regime in the absence of the ADV. The loads are averaged across the three blades, phase-averaged into 1° bins, and normalised on their time-averaged values. The tip-speed ratio was varied by adjusting the rotor speed, with the corresponding turbine reference velocities shown in Table 8.1.

λ [-]	Maximum mean load (ϕ) [-]	Minimum mean load (ϕ) [-]	Load range [-]	Maxium load variation (ϕ) [-]
		Clean		
I	1.014 (118°)	0.979 (23°)	0.035	0.039 (311°)
II	1.011 (325°)	0.981 (29°)	0.030	0.017 (215°)
III	1.012 (334°)	0.983 (34°)	0.030	0.017 (218°)
		Grid A		
I	1.018 (263°)	0.978 (316°)	0.040	0.041 (330°)
II	1.034 (279°)	0.987 (144°)	0.046	0.022 (167°)
III	1.033 (282°)	0.987 (145°)	0.046	0.023 (198°)
		Grid D		
I	1.044 (265°)	0.961 (157°)	0.083	0.076 (177°)
II	1.044 (269°)	0.962 (159°)	0.083	0.080 (176°)
III	1.043 (270°)	0.960 (159°)	0.083	0.083 (356°)
		SP1		
I	1.104 (356°)	0.899 (116°)	0.205	0.051 (53°)
II	1.093 (4°)	0.936 (184°)	0.157	0.023 (0°)
III	1.096 (1°)	0.935 (187°)	0.161	0.025 (36°)
		SP2		
I	1.076 (347°)	0.926 (163°)	0.150	0.054 (173°)
II	1.055 (353°)	0.953 (177°)	0.102	0.025 (10°)
III	1.059 (357°)	0.953 (178°)	0.106	0.030 (10°)

Table 8.3: Summary statistics for flapwise root bending moments as a function of tip-speed ratio (see Table 7.4 for exact values) for each flow regime in the absence of the ADV. The loads are averaged across the three blades, phase-averaged into 1° bins, and normalised on their time-averaged values. The load variation is quantified as the standard deviation of the loads within each bin. The tip-speed ratio was varied by adjusting the rotor speed, with the corresponding turbine reference velocities shown in Table 8.1.

is more than double that at higher tip-speed ratios, peaking close to top dead centre on the upstroke, with its azimuthal position showing a further phase shift of approximately 100° relative to higher tip-speed ratios.

As freestream turbulence increases from the clean flow case to grid A, and finally to grid D, the blades' response exhibits notable changes, particularly in the magnitude of the loads and the phase alignment of the loading profiles across the

tip-speed ratio range. The normalised load range increases to between 4–4.6% of the time-averaged loads in response to grid A and to 8.3% for grid D, reflecting the greater variation in the turbine's approach flow and, consequently, the sectional blade forces. For grid D, the peak blade loads occur within 5°, and the minimum loads within just 3°, of each other across the tip-speed ratio range, indicating a more consistent response to the onset turbulence. These findings further support the idea that increased freestream turbulence promotes an earlier transition to a turbulent boundary layer, enabling it to stay attached to the hydrofoil for longer, resist adverse pressure gradients more effectively, and enhance foil performance at lower tip-speed ratios. For grid A, similar to the clean flow case, the maximum load variation at the lowest tip-speed ratio remains nearly double that at higher tip-speed ratios, accompanied by a substantial phase shift in the corresponding azimuthal position (at least 132°), highlighting a clear distinction in the blades' response as they approach stall. In contrast, the significantly higher freestream turbulence downstream of grid D results in loading profiles that exhibit similar overall variations across the tip-speed ratio range, peaking at approximately 8% of the time-averaged loads.

For more sheared inflows, the blade loading profiles reveal a corresponding increase in 1P load fluctuations. The flow downstream of SP2 elicits a load range of 10–15% of the time-averaged loads, while SP1 yields a range of 16–21%, reflecting the greater flow unsteadiness and imbalance in rotor loading compared to both the clean and turbulent flow cases. Variations of this magnitude align closely with the findings of Gaurier *et al.* [147], who reported a 20% variation in the flapwise loads across each blade rotation in response to bathymetry-driven sheared flow. Across the tip-speed ratio range, the maximum loads occur within 10° of each other for both SP1 and SP2 flow regimes. However, as the blades approach stall, a clear phase shift emerges in the azimuthal position of the minimum load compared to higher tip-speed ratios, which, for SP1, is approximately 70°. Consistent with the findings of other researchers, the azimuthal positions of the loading maxima and

minima are close to, but not perfectly aligned with, top and bottom dead centre, respectively [145, 148]. As with the clean and grid A flow regimes, the loading profiles at higher nominal tip-speed ratios ($\lambda \geq 5$) are distinct from those observed as the blades approach stall, although the azimuthal variations appear much more deterministic compared to the non-sheared flow cases. This is particularly evident in the turbine's response to SP1, which exhibits a single dominant sinusoidal pattern around the rotor azimuth. In contrast, SP2 induces a more complex response, with additional sinusoidal components emerging in the loading profiles.

8.4.3 Angle of Attack and Reduced Frequency Variations

To develop further insights into the blades' unsteady response, fluctuations in the angle of attack along the blade span were examined across different tip-speed ratios for the five flow regimes. First, mean streamwise velocities were extracted from the undisturbed 2D velocity fields at discrete radial distances from the centre of the rotor's swept area (see left-hand panel of Figure 8.16). Fluctuations in the flow angle, estimated using the trigonometric relation $\tan^{-1}(\overline{u}/\omega r)$ and neglecting induction effects, were taken as proxies for fluctuations in the angle of attack. As shown in the middle panel of Figure 8.16, estimates can vary considerably along the span and as a function of tip-speed ratio, with the largest fluctuations expected towards the tip and at higher rotor speeds. In clean flow, fluctuations in the angle of attack do not exceed 0.5°, whereas in sheared flow, they reach 3.7° and 2.8° for SP1 and SP2 (not shown), respectively. In contrast, downstream of the turbulence grids, fluctuations are limited to 0.6° for grid A and 2.0° for grid D (both not shown), suggesting that sheared flows induce significantly larger excursions in the angle of attack along the blade span, increasing the likelihood of stall.

To further characterise the unsteady effects, azimuthal variations in the reduced frequency (see Equation 6.4) were also examined. The right-hand panel of Figure 8.16 compares estimates of k in both clean and sheared flows at $0.7R$—approximately the hydrodynamic centre of loading—across different tip-

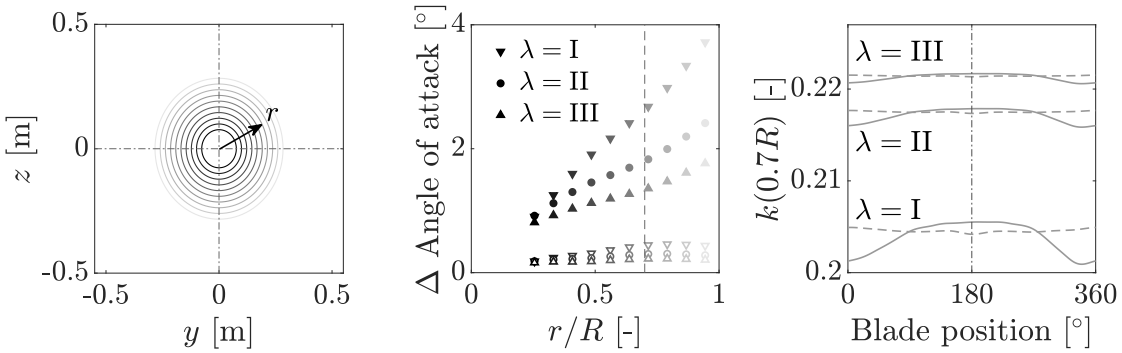


Figure 8.16: Estimates of angle of attack fluctuations and reduced frequencies (k) in both clean and vertically sheared flows (SP1 only). The left-hand panel shows ten discrete, equally spaced radial positions between 0.26–0.94R (greyscale), indicating where mean streamwise velocities were extracted from the undisturbed flow fields at the intended rotor plane (see Figure 3.5 for clean flow and Figure 5.4a for flow downstream of SP1). The middle panel presents estimates of angle of attack fluctuations along the blade span as a function of tip-speed ratio (see Table 7.4 for exact values), with unfilled markers representing the clean case and filled markers indicating sheared flow. The dashed line denotes 0.7R. The right-hand panel shows azimuthal variations of k at 0.7R as a function of tip-speed ratio, where dashed lines represent the clean case and solid lines indicate sheared flow. The dash-dotted line marks bottom dead centre.

speed ratios. Despite differences in the flow conditions, both cases yield reduced frequencies of $k \approx 0.2$ across the tip-speed ratio range. In contrast to the clean flow case, where k remains approximately constant across the azimuth at each tip-speed ratio, vertical shear elicits a pronounced 1P fluctuation in the unsteady response. At higher rotor speeds, the amplitude of the sinusoidal variation in unsteadiness decreases—despite slightly higher values of k—and may explain the rotor's reduced sensitivity to unsteady fluctuations in the onset flow (see Figure 8.13 and see also the analysis examining the influence of the ADV mast's position on blade loading in Section 7.3.5). While not shown here, expanding the analysis beyond a single radial position reveals considerable variation in the reduced frequency along the blade span. For instance, in clean flow at the optimal tip-speed ratio, values range from $k = 0.12$ near the tip ($r = 0.94R$) to $k = 0.89$ at the root ($r = 0.26R$), with estimates near the root being significantly more sensitive to changes in rotor speed than those towards the tip.

8.4.4 Loading Spectra

Comparing Rotor and Blade-Level Responses

Figure 8.17 compares the spectral responses of rotor thrust and torque with those of the blade root bending moments, showing reasonably close agreement up to the turbine's fundamental rotational frequency, f_{rot}. Beyond this point, the thrust and torque responses appear largely insensitive to the blade-related unsteadiness, highlighting the importance of blade-level instrumentation for achieving greater resolution in rotor loading analysis. The increase in spectral density observed across the rotor within the frequency range of 0.1–0.4f_{rot} closely corresponds to a similar increase in the root bending moments of all three blades. This broadband energy increase likely corresponds to streamwise integral length scales on the order of one metre, consistent with the clean flow characterisation results (see Figure 3.15). The presence of five narrow-banded peaks around f_{rot} in both the thrust and torque spectra indicate an additional forcing mechanism, leading to resonances within the turbine's drivetrain, rather than blade-specific dynamics.

The spectral responses from all three blades demonstrate excellent agreement, reinforcing confidence in the sensor calibration process. The distribution of energy across the frequency domain results in high energy concentrations at frequencies corresponding to f_{rot} and its higher harmonics. This pattern, consistent with observations from other studies such as Payne *et al.* [203], extends up to $5f_{\text{rot}}$ in the flapwise root bending moment spectra. In contrast, the edgewise response exhibits many additional peaks, including frequencies not only at multiples of f_{rot} but also at intervals of approximately $0.5f_{\text{rot}}$, suggesting the presence of superharmonics indicative of non-linear interactions or coupling effects within the system. Neither the thrust, torque, nor blade root bending moment spectra closely adhere to the $f^{-11/3}$ power-law gradient proposed by Tobin *et al.* [212].

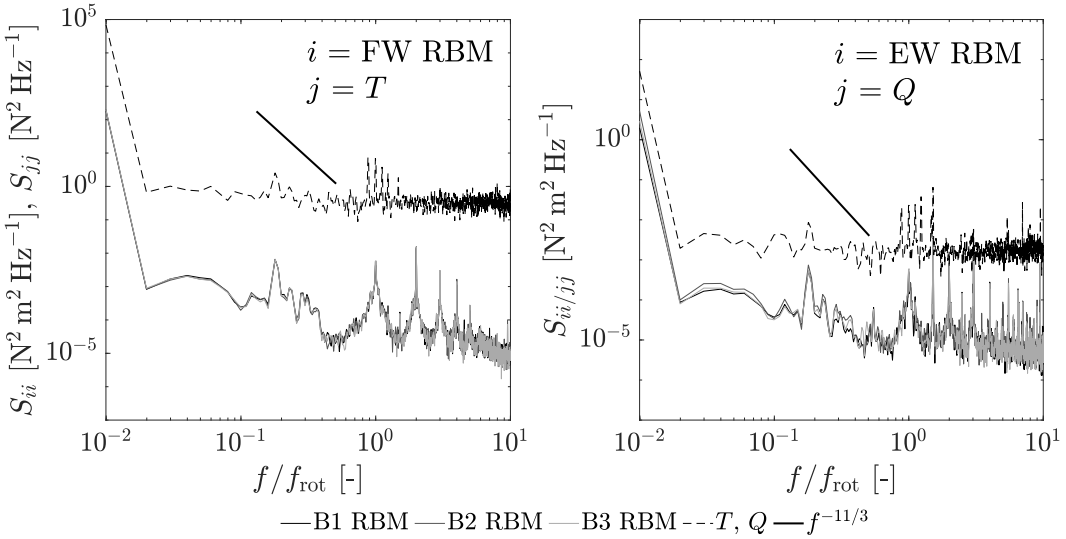


Figure 8.17: PSD estimates of thrust, T, and flapwise root bending moments (left panel), as well as torque, Q, and edgewise root bending moments (right panel), for the clean flow case in the absence of the ADV. The blade root bending moments are represented by thin greyscale lines, thrust and torque by the black dashed line, and the $f^{-11/3}$ power-law decay gradient by the thick black line. Frequencies are normalised on the turbine's fundamental rotational frequency, f_{rot}. Test conditions: $\overline{U_{\mathrm{T}}} = 0.57\,\mathrm{m\,s^{-1}}$ (centreline velocity); $\overline{\lambda} = 5.07$; $\overline{\Omega} = 9.65\,\mathrm{rad\,s^{-1}}$.

Influence of Flow Dynamics

The top panel of Figure 8.18 presents time series of the flapwise root bending moments over four blade rotations at a nominal tip-speed ratio of $\lambda = 5$ for all five flow regimes[3]. Each time series, normalised on its time-averaged value, exhibits a distinct signature depending on the flow conditions under test. The turbine's response to the clean flow case is the most uniform, characterised by a long-period load fluctuation with a period significantly greater than the turbine's period of rotation. Consistent with the polar plots in Figure 8.13, the load signature in response to grid A is broadly similar to that of the clean flow case, although the more stochastic nature of the onset flow introduces increased variability in the blade's loading response. Increasing the freestream turbulence with grid D results

[3]The corresponding edgewise signals were also analysed but are excluded here for brevity. As shown previously, edgewise loads exhibit significantly higher sensitivity to the onset flow conditions and increased superharmonic content. However, they do not dominate the unsteady rotor loads and ultimately do not alter the overall conclusions drawn from the flapwise response.

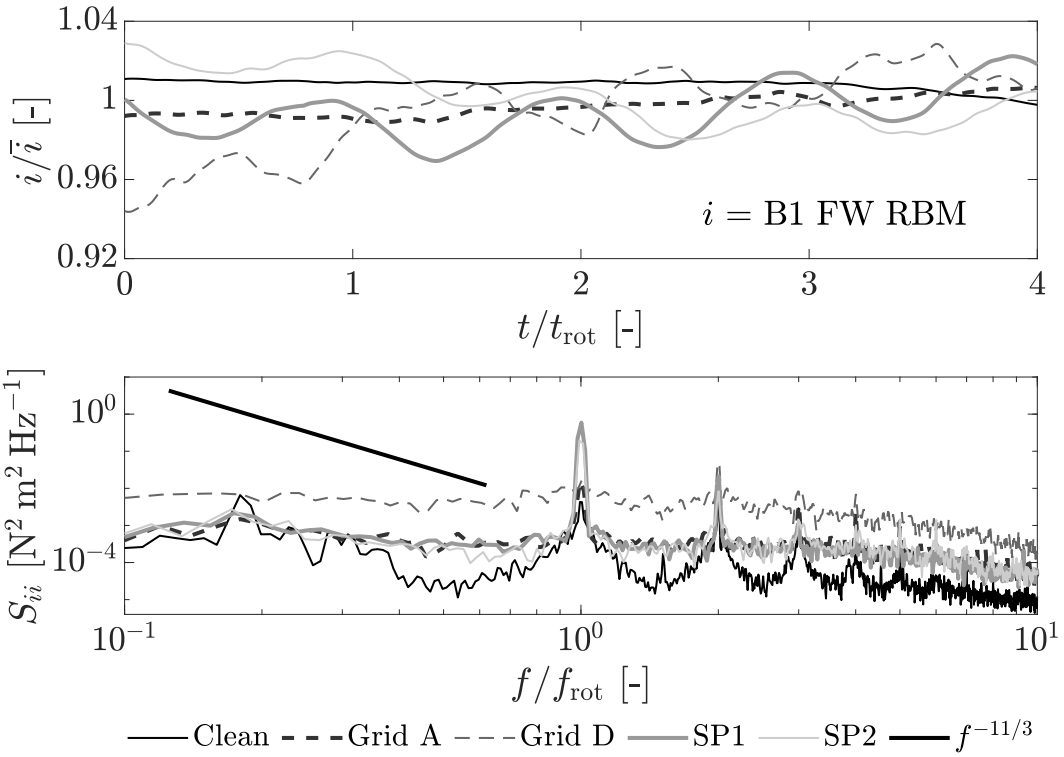


Figure 8.18: Time series (top panel) and PSD estimates (bottom panel) of blade 1 flapwise root bending moments, i, for each flow regime in the absence of the ADV. A nominal tip-speed ratio of $\lambda = 5$ (II) was set across all flow regimes (see Table 7.4 for exact values). The time series, shown as moving averages over 1 s, represent loads over four blade rotations. In the top panel, the loads are normalised on their time-averaged values over 180 s, while the time domain is normalised on the turbine's period of rotation, t_{rot}. In the bottom panel, frequencies are normalised on the turbine's fundamental rotational frequency, f_{rot}. The $f^{-11/3}$ power-law gradient is shown as a thick black line. Corresponding turbine reference velocities are provided in Table 8.1.

in a more unpredictable and complex loading response, as evidenced by a larger normalised load range of approximately 9% over the four rotations, compared to 2–3% in the clean and grid A flow regimes. In contrast, sheared flows produce a more deterministic sinusoidal response, characterised by a clear 1P load fluctuation in the time series. The more sheared flow case (SP1) induces a slightly larger normalised load range of approximately 6% compared to 5% for less sheared flow (SP2).

To complement the time series, the bottom panel of Figure 8.18 presents the corresponding PSD estimates of the flapwise root bending moments. The clean

flow case (also shown in Figure 8.17) exhibits the lowest spectral energy across the frequency range, while the turbulent and sheared flow regimes show progressively higher spectral densities. This trend culminates with grid D, which generates the highest freestream turbulence and, as a result, the greatest spectral energy. As expected, the sheared flow cases elicit the highest energy peaks for 1P load fluctuations. However, for higher harmonics of f_{rot}, between 2–5f_{rot}, grid D yields the highest energy peaks, although these are less distinct from those of the other flow regimes due to elevated background turbulence. The second and fourth harmonics are likely influenced by proximity effects resulting from blade passage close to the flow boundaries.

Figure 8.19 illustrates the effect of different tip-speed ratios on the power spectra of the flapwise root bending moments across the five flow regimes. For the clean flow case, a distinct difference in the spectral response is observed between a nominal tip-speed ratio of $\lambda = 3$, where the blades operate closer to stall, and $\lambda \geq 5$. At lower rotor speeds, the blade tip speed approaches the axial-flow velocity, increasing the angle of attack and amplifying the unsteady forcing along the blades' surfaces, resulting in higher spectral energy across the frequency range.

At slightly elevated levels of freestream turbulence downstream of grid A, the spectral responses across all three tip-speed ratios become more similar, particularly in the energy-containing range for $f \leq f_{\mathrm{rot}}$. This is primarily due to increased spectral energy at higher tip-speed ratios ($\lambda \geq 5$) compared to the clean flow case, reflecting the reduced sensitivity of the blades' response to changes in rotor speed. Notably, at the lowest tip-speed ratio, where the blades approach stall, elevated spectral energy is observed in the range 1–2f_{rot}, suggesting a stronger frequency-dependent coupling between the blades and the onset turbulence. For integral length scales of approximately 60 mm at the rotor plane, the corresponding frequencies are around 10 Hz, which fall outside this range.

For significantly higher freestream turbulence levels downstream of grid D, the spectral energy across all three tip-speed ratios is elevated by at least one order

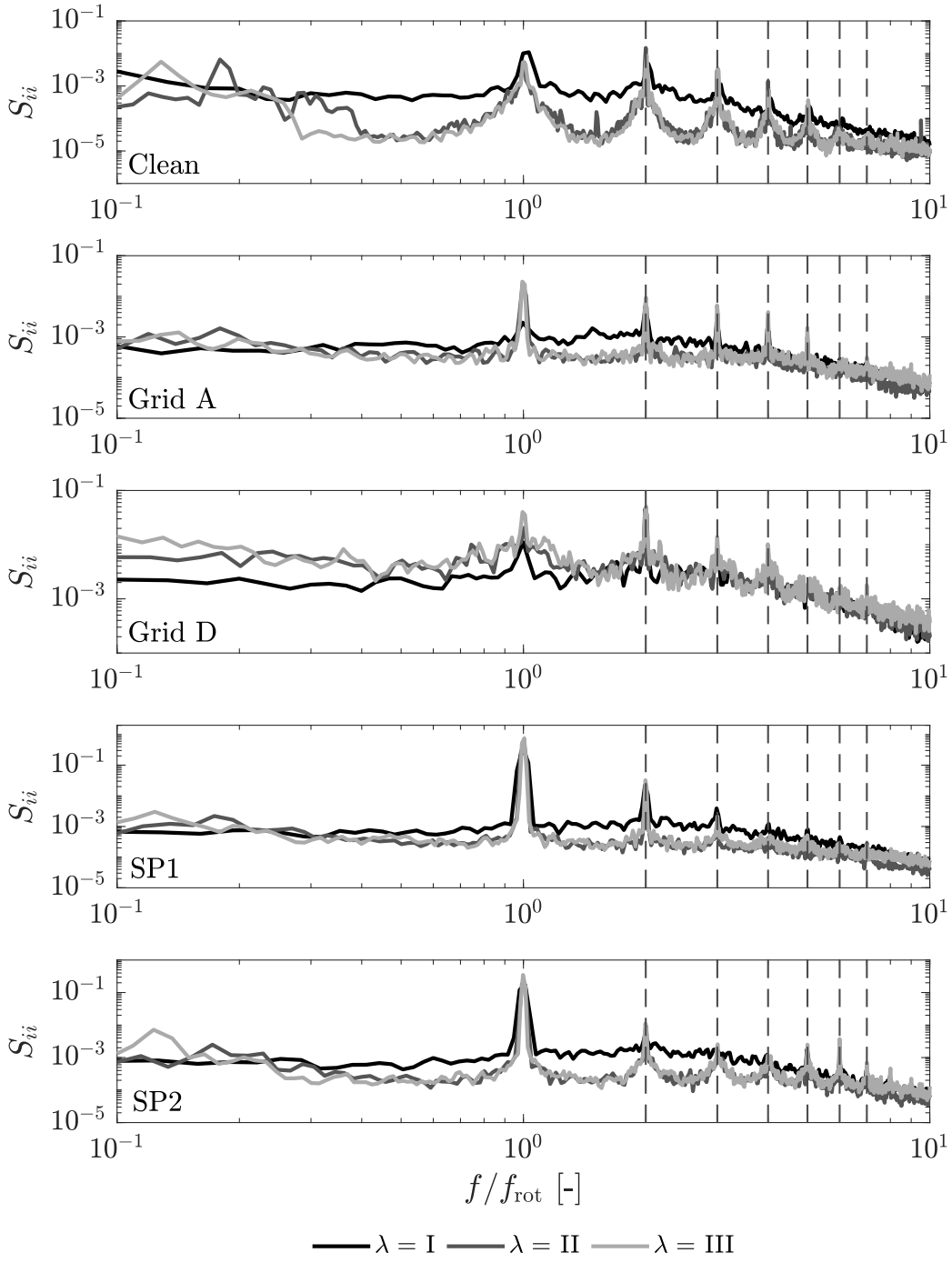


Figure 8.19: PSD estimates of flapwise root bending moments, S_{ii}, as a function of tip-speed ratio (see Table 7.4 for exact values) for each flow regime in the absence of the ADV. The PSDs are averaged across the three blades and expressed in units of $\mathrm{N^2\,m^2\,Hz^{-1}}$. Frequencies are normalised on the turbine's fundamental rotational frequency, f_{rot}. Dashed lines represent harmonics between 2–7f_{rot}. Corresponding turbine reference velocities are provided in Table 8.1.

of magnitude relative to the other flow regimes. However, a disparity emerges between the response at higher nominal tip-speed ratios ($\lambda \geq 5$) and at $\lambda = 3$ for $f \leq 1.3 f_{\text{rot}}$, suggesting that at higher relative velocities, the blades interact more strongly with the onset turbulence within the energy-containing portion of the spectrum. This contrasts with the azimuthal load response shown in Figure 8.15, which, for the flow downstream of grid D, remains largely insensitive to the tip-speed ratio. Interestingly, the spectral peaks corresponding to 1–3P forcing exhibit broader energy distributions at higher nominal tip-speed ratios ($\lambda \geq 5$) compared to when the blades operate closer to stall. This broadening reflects the reduced periodicity in the blades' response, diminishing the distinctness of the peaks at harmonics of f_{rot}. Notably, the energy peak at $5 f_{\text{rot}}$, observed in the clean and grid A flow regimes, is suppressed under these conditions.

In vertically sheared flow, the more deterministic nature of the onset unsteadiness manifests as distinct energy peaks at harmonics of f_{rot}, although the amplitude and number of harmonics vary significantly between cases. For more sheared flow (SP1), the spectral peaks corresponding to 1–3P forcing are the most energetic across all flow regimes, while peaks at higher harmonics ($f > 3 f_{\text{rot}}$) are suppressed, indicating reduced excitation at these frequencies. In contrast, for less sheared flow (SP2), harmonics are observed up to $8 f_{\text{rot}}$, although the mechanism driving this extended harmonic content is unclear. In the energy-containing region of the spectrum, the blades' response is broadly similar for both flow regimes. A small resonance, also present in the clean flow spectra, is observed at approximately 0.12 Hz for the highest nominal tip-speed ratio ($\lambda = 7$), although its origin remains unclear.

8.5 Limitations of the Investigation

Due to the scale of the experiments, the turbine was likely operating within a Reynolds number-dependent regime, suggesting that the measured performance and loading response of the rotor may not directly translate to a full-scale application.

Overcoming this limitation would require access to a larger facility with higher flow speeds, as well as the design and manufacture of a new rotor optimised for the testing conditions and constraints of the larger facility. However, since the blockage ratio was maintained across all experiments, any resulting bias was systematically carried through the campaign and is therefore unlikely to have affected the conclusions drawn.

Defining the turbine reference velocity as a single-point measurement likely introduced significant bias into assessments of the rotor's non-dimensional performance and loading response, particularly for less uniform flow conditions. While this approach ensured consistency throughout the test campaign, a spatially averaged velocity, such as a power-weighted rotor average (PWRA) velocity, would likely provide a more representative and robust reference. Implementing such an approach, however, would have posed several practical challenges, including the need to measure velocities upstream of the turbine at sufficient spatial resolution for each flow regime. This would have significantly extended the testing time beyond the eight-week campaign and rendered much of the turbine data unusable due to the variable position of the upstream ADV mast assembly. Additionally, there was caution about running the turbine for such an extended duration, as it had not been previously tested for prolonged periods. Given these constraints, the reliance on single-point velocity measurements was a necessary and pragmatic compromise. For flume-based investigations, single-point velocity measurements are likely better suited to more uniform and well-developed flow conditions, mitigating the substantial variation in performance metrics discussed in Section 8.2.2.

The investigation also highlighted the high sensitivity of the edgewise loads, primarily due to their much lower magnitude and signal-to-noise ratio compared to the flapwise loads. This sensitivity resulted in significant superharmonic signal content, making it challenging to determine whether this was noise-related, flow-induced, or a result of the turbine's mechanical response. For the loads tested, such sensitivity is almost unavoidable. While advanced filtering techniques could

help isolate the edgewise response, their application would likely require a rigorous characterisation of the dominant frequencies associated with turbine operation to distinguish flow-induced effects from noise or mechanical artefacts.

8.6 Summary

This chapter has examined the performance and loading response of a model-scale tidal stream turbine across five sub-critical flow regimes, encompassing clean, turbulent, and sheared flows, as characterised in Part I of this thesis.

The turbine operated most efficiently under clean flow conditions, achieving a maximum power coefficient of $C_{P,\max} = 0.57$ at an optimal tip-speed ratio of $\lambda_{\text{opt}} = 4.9$, exceeding the maximum power coefficients in the other flow regimes by at least 1.8%. The maximum thrust coefficient, also observed in clean flow, was $C_{T,\max} = 1.43$ at a tip-speed ratio of $\lambda = 7.1$. Around the optimal tip-speed ratio, both the power and thrust coefficients for each flow regime hinted at transitional effects on the blades, likely attributable to the geometric scale of the experiments, with chord-based Reynolds numbers $\mathcal{O}(10^4\text{–}10^5)$. This conclusion was further supported by an analysis of the turbine's power coefficient under different operating conditions, which suggested that Reynolds number independence had not been achieved at the design operating point.

The impact of using undisturbed flow measurements at the rotor plane as the basis for the turbine reference velocity was also examined, revealing increased sensitivity of the performance coefficients to the choice of reference velocity in less uniform flows. This sensitivity was most pronounced in the turbine's response to the flow downstream of grid D, where the peak power and thrust coefficients exhibited a 26–50% relative increase compared to concurrent upstream velocity measurements.

An uncertainty analysis of selected non-dimensional parameters revealed that the maximum errors were small relative to the corresponding maxima of those pa-

rameters, such as the coefficients of power ($\pm 0.14 C_{P,\,\max}$) and thrust ($\pm 0.10 C_{T,\,\max}$), as well as the tip-speed ratio ($\pm 0.02 \lambda_{\max}$). For the flapwise and edgewise blade root bending moment coefficients, the maximum errors were 12% and 60% of their respective maxima.

High-fidelity load measurements provided insights into the azimuthal variations in the blade root bending response. In clean flow, the flapwise loading profiles at higher nominal tip-speed ratios ($\lambda \geq 5$) were closely aligned in both phase and magnitude. However, as the blades approached stall, a phase shift exceeding 140° emerged between the azimuthal position of the maximum load and the corresponding positions at higher tip-speed ratios. In sheared flows, a similar trend was observed for the minimum loads, but with a smaller phase shift of approximately 70°.

With increased freestream turbulence, the azimuthal load range grew from approximately 3% of the time-averaged loads in clean flow to 8.3% in response to the flow downstream of grid D, reflecting the larger fluctuation magnitudes in the onset flow. A more consistent loading response across tip-speed ratios was also observed for grid D, likely due to an earlier transition to a turbulent boundary layer at lower tip-speed ratios. In sheared flow, the blade loading profiles exhibited a corresponding increase in 1P load fluctuations, reaching up to 16–21% of the time-averaged loads in the limiting case, suggesting that, as a first-order approximation of flow unsteadiness, vertical shear has a more pronounced effect on rotor loading. Furthermore, at the lowest tip-speed ratio, the azimuthal loading profiles exhibited increased horizontal asymmetry compared to the clean and turbulent flow regimes, suggesting a higher propensity for stall during one half of the blade's rotation.

PSD estimates of the flapwise root bending moments revealed that overall spectral energy increased with the level of freestream turbulence, with the clean flow case exhibiting the lowest energy levels. The sheared flow cases exhibited the highest energy peaks for 1P load fluctuations. In contrast, for higher harmonics of the turbine's rotational frequency (2–5f_{rot}), the flow downstream of grid D induced the largest energy peaks, although these were less distinct due to elevated

background turbulence. In clean flow, the spectral response varied significantly between $\lambda = 3$, where the blades approached stall, and higher nominal tip-speed ratios. This variation is attributed to reduced hydrodynamic efficiency at lower rotor speeds, which amplifies the unsteady turbulence-rotor interactions and increases spectral energy across the frequency range.

CHAPTER 9

Conclusions and Future Work

This thesis presents new experimental data and analyses encompassing the characterisation of unsteady onset flows for tidal rotors, as well as the performance and loading response of a model-scale tidal stream turbine. The research progresses from the detailed characterisation of a new departmental flume to the generation and control of turbulent and sheared flow regimes, culminating in an analysis of the turbine's response to these controlled flow conditions.

The remainder of this chapter is structured into three main sections: conclusions, recommendations for future work, and a summary of the scientific contributions of this research.

9.1 Conclusions

The conclusions of this thesis are presented in two parts, directly addressing the objectives outlined in Chapter 1. The first part focuses on the development and application of methodologies for characterising controlled flow conditions, as well as the generation of selected unsteady flow types, as detailed in Chapters two to five. The second part discusses the preparation, adaptation, and subsequent testing of the turbine, summarising the key findings from Chapters seven and eight.

9.1.1 Flow Characterisation and Unsteady Flow Generation

Objective 1: Development of Flow Characterisation Methodology and Clean Flow Analysis

A crucial first step in this research was the development of a robust experimental methodology and measurement system capable of achieving the required accuracy and repeatability for the hydrodynamic characterisation of a new departmental flume. A prescribed sequence of data processing steps was established, including the quantification of measurement biases and uncertainties, providing a valuable and transferable framework for researchers characterising similar facilities with an ADV. For measurements dominated by noise, such as those reported for the flume's ambient flow, corrections to account for noise in the turbulence statistics often exceeded 50%, raising questions about the suitability of established correction methods in low-turbulence conditions.

The flume exhibited high velocity uniformity, with deviations of less than 1% at the 95% confidence level, and controlled low turbulence levels ranging between 1–2% across the swept area of the rotor, providing a stable and reliable basis for evaluating model-scale turbine response. However, the high spatial variation of the integral scales underscored the sensitivity of higher-order quantities to noise contamination. The largest length scales were on the same order as the channel's cross-sectional dimensions, consistent with canonical open-channel flow experiments [76] and in-field observations [29].

Objective 2: Generation, Control, and Characterisation of Unsteady Flow Regimes

Freestream turbulence was generated by four square-mesh passive grids. Preliminary measurements along the flume's centreline provided fresh insights into flows approximating homogeneous, isotropic turbulence and were used to define a parameter space for model-scale testing, quantified in terms of the turbulence

intensity and streamwise integral length scales. The transient nature of the generated turbulence was most evident in the turbulence intensity profiles, which showed that as the grid mesh size increased for a given bar width, turbulence production weakened, and the production region shifted further downstream. At the rotor plane, turbulence along the centreline was elevated compared to the clean flow case, with turbulence intensities ranging between 4–12%, while the integral length scales remained below 20% of the 0.6 m rotor diameter. As a result, the parameter space was better suited to investigating the unsteady effects of turbulence intensity on the model-scale rotor rather than the influence of the integral length scales. Grid A represented a slightly elevated turbulence case ($I_{3D} \approx 4\%$), while grid D corresponded to a significantly higher level of turbulence ($I_{3D} \approx 12\%$) relative to clean flow measurements at the rotor plane.

Vertical velocity shear was generated by presenting a graded resistance to the flow using a non-uniformly spaced grid of parallel bars placed across the width of the working section. This approach marked the first application of Cowdrey's method [124] in an open-channel flow. The resulting flow profiles, characterised by the denominator of the power-law exponent with values of $n = 6$ and $n = 9$, established an achievable range around the widely cited value of $n = 7$, partially capturing the considerable variation observed throughout the tidal cycle. Further flow characterisation using 2D transects revealed non-uniform vertical shear across the survey area and the presence of substantial corner flows, attributed to the differential shear between the target vertical and cross-stream shear profiles. Both upstream flow obstructions produced turbulence intensities at the rotor plane comparable to those generated by grid A. However, large variations in the streamwise integral length scales were observed through the water column, ranging from $\mathcal{O}(H, W)$ towards the top, where the local flow was relatively unobstructed, to $\mathcal{O}(W_{\text{bar}})$ near the bottom. This behaviour indicates a quasi-stratification of the flow and underscores the sensitivity of the autocorrelation function to local flow

conditions.

9.1.2 Model-Scale Preparation and Testing

Objective 3: Turbine Adaptation in Readiness for Model-Scale Testing

In preparation for model-scale testing, significant planning and logistical efforts were undertaken to ensure the turbine's safe installation into the flume and readiness for testing. To accurately measure the blades' loading response to the onset flow conditions in both the flapwise and edgewise directions, a rigorous calibration procedure was developed for newly installed strain-gauged transducers at the root of each blade. The subsequent uncertainty analysis revealed relative errors at the 95% confidence level of 17–18% of the nominal applied load in the flapwise direction and 40–63% in the edgewise direction, reflecting the greater sensitivity of the edgewise loads to systematic errors, likely due to their smaller magnitudes and lower signal-to-noise ratio.

As part of the experimental methodology for the turbine test campaign, the influence of different ADV positions on the blades' root bending moments was evaluated. Centreline measurements resulted in a 1P flapwise load fluctuation equivalent to approximately 10% of the azimuthal average at the lowest tip-speed ratio, and an edgewise load fluctuation of nearly 20% under maximum thrust conditions. While centreline measurements yielded higher blade load fluctuations compared to alternative ADV positions upstream of the rotor plane, this was a minor trade-off for obtaining more representative reference velocities, which are essential for non-dimensional turbine performance and loading analysis.

Objective 4: Evaluate Turbine Performance and Loading Response Under Clean, Elevated Turbulence, and Sheared Flow Conditions

The turbine operated most efficiently under clean flow conditions, achieving a maximum power coefficient of $C_{P,\max} = 0.57$ at an optimal tip-speed ratio of

$\lambda_{\text{opt}} = 4.9$, exceeding the maximum power coefficients in the other flow regimes by at least 1.8%. The maximum thrust coefficient, also observed in clean flow, was $C_{T,\max} = 1.43$ at a tip-speed ratio of $\lambda = 7.1$. Around the optimal tip-speed ratio, both the power and thrust coefficients for each flow regime hinted at transitional effects on the blades, likely attributable to the geometric scale of the experiments, with chord-based Reynolds numbers $\mathcal{O}(10^4$–$10^5)$. There was no evidence to suggest that Reynolds number independence had been achieved at the design operating point.

Interpretation of the turbine's non-dimensional performance was shown to be highly sensitive to the choice of the reference velocity used for normalisation, a sensitivity further exacerbated by higher non-uniformity in more unsteady approach flows. The effect was most pronounced downstream of grid D, where the peak power and thrust coefficients exhibited a 26–50% relative increase compared to concurrent upstream velocity measurements.

The loading response at the blade roots was captured at high angular resolution, allowing for detailed characterisation of azimuthal variations in blade loading across different hydrodynamic conditions. The analysis provided new insights into the effects of blade stall at low tip-speed ratios, where a phase shift exceeding 140° was observed in the azimuthal position of the maximum time-averaged load in clean flow relative to higher tip-speed ratios ($\lambda \geq 5$). Furthermore, the results indicated that sheared inflows generate more pronounced fluctuations in once-per-revolution forcing (equivalent to 16–21% of the time-averaged blade loads in the limiting case) than grid-generated turbulence (maximum 8.3%), suggesting that, as a first-order approximation of flow unsteadiness, vertical shear has a more significant effect on rotor loading. However, with increased freestream turbulence, a more consistent loading response across tip-speed ratios was observed, likely due to an earlier transition to a turbulent boundary layer at lower tip-speed ratios.

9.2 Future Work

9.2.1 Unsteady Flow Generation

Part I of this thesis presented methodologies for generating two distinct types of hydrodynamic unsteadiness relevant to tidal stream turbines: freestream turbulence and vertical velocity shear. Flume-based investigations also provide opportunities to explore additional sources of unsteadiness, both deterministic and stochastic. For instance, the rotor axis of an in-field turbine is rarely aligned with the mean flow direction, making turbine yaw a logical next step for further investigation. To implement this in the Oxford flume, the tower-top assembly shown in Figure 7.2b could be readily adapted to allow nacelle rotation about the tower axis.

A more complex extension would involve simulating harmonic inputs such as surging motions, similar to the experimental work of Whelan [170], or pendulum-type motions as studied numerically by Osman and Willden [182]. Provided free-surface effects do not significantly influence the experimental results, this approach could offer valuable insights into discrete forcing mechanisms associated with platform-induced motions. However, the experimental design would be non-trivial, requiring careful consideration of the achievable parameter space, expected mechanical loads, and equipment specifications.

Free-surface waves offer further opportunities to investigate unsteady loading effects. However, implementing this at full depth in the flume would require an additional wave-generating mechanism, separate from the flume's built-in capability—such as a point-absorber-type device. The scope of such a project would also need to address wave dissipation to prevent reflections from the flume's boundaries propagating back towards the turbine.

9.2.2 Turbine Optimisation and Load Relief

The turbine used in this study was a modified version of one of two existing model-scale devices, with instrumentation originally sized for higher loads in larger test facilities. For investigations in the Oxford flume, some drivetrain components were oversized, which may have increased signal noise and reduced the accuracy of the measured rotor loads. To enhance the turbine design for future studies, incorporating a lighter, more appropriately sized servo motor and TTD, along with optimised shrouding and nacelle covers, would reduce assembly weight, making handling and installation easier, while also improving measurement resolution and hydrodynamic efficiency.

Another interesting avenue to explore is the integration of a load relief mechanism, potentially through an active pitch system in the rotor. While package constraints may limit the feasibility of such a mechanism, particularly for all three blades, a simplified collective pitch control system could offer a practical compromise for model-scale experiments. In this case, a uniform gust across the rotor plane—simulated by a surging motion—would be a likely candidate as an unsteady forcing mechanism of interest.

9.3 Contributions

Development and Application of Flow Characterisation Methodology

Chapter two presented a comprehensive methodology for the hydrodynamic characterisation of a hydraulic flume, in preparation for model-scale testing. As part of this work, a 2D linear traverse system was developed, incorporating a user interface and dedicated processing code, which has been made publicly available [213]. The methodology was applied to deliver the first characterisation of the Oxford flume (detailed in Rowe *et al.* [214]), providing a valuable resource for researchers interested in the flume's flow characteristics or in characterising similar facilities

using an ADV.

Controlled Generation of Freestream Turbulence and Vertical Shear

To enable a flexible approach for testing parameter spaces of interest in unsteady flows, a submersible outer frame was developed to accommodate various flow-resisting geometries. This provided a cost-effective and practical means of generating controlled unsteady flows in the flume and can be readily adapted by other researchers to explore additional parameter spaces of interest. For this investigation, four turbulence-generating grids and a mechanism for producing controlled vertical shear profiles were developed. The resulting flow characterisations complement the existing literature for both flow types, offering new insights into the evolution of grid-generated turbulence and vertical shear in flume-based investigations.

Turbine Adaptation for Model-Scale Testing

The turbine was adapted for use in the Oxford flume through modifications to the rotor upstream of the TTD, including the development of a new PCB assembly, blades, and root flexures. Building on the lessons learned from previous experimental campaigns, a bespoke test rig was developed to calibrate the root flexures in their design-intent condition as part of the rotor assembly. Additionally, the turbine's integration into the flume—incorporating assembly aids, a meticulous installation procedure, and an upgraded data acquisition system—ensured that the setup could be readily used by other researchers for future experiments.

Model-scale Turbine Performance and Loading Response

The turbine test campaign was the first of its kind in the Oxford flume, featuring an extended test period that enabled detailed analysis of the turbine's performance and loading response under clean, turbulent, and sheared flow conditions. The study underscored the challenges in defining the turbine reference velocity within a

highly constrained flow domain and provided new insights into the blades' loading behaviour across the turbine's operating range.

APPENDIX A

Flow Mapping Co-ordinates

This appendix presents the ADV measurement co-ordinate maps for flow profiling.

Clean Flow Cruciform Map

Cruciform flow profiles comprise a 100 mm measurement increment along the axis of interest (see Figure A.1), except for the two deepest measurement co-ordinates, which are separated by 85 mm to avoid ADV signal weak spots [45].

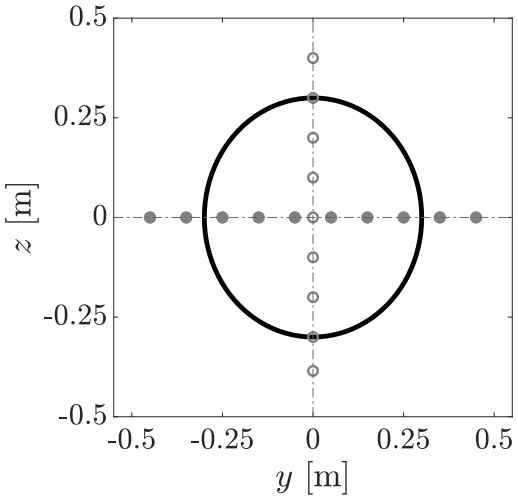
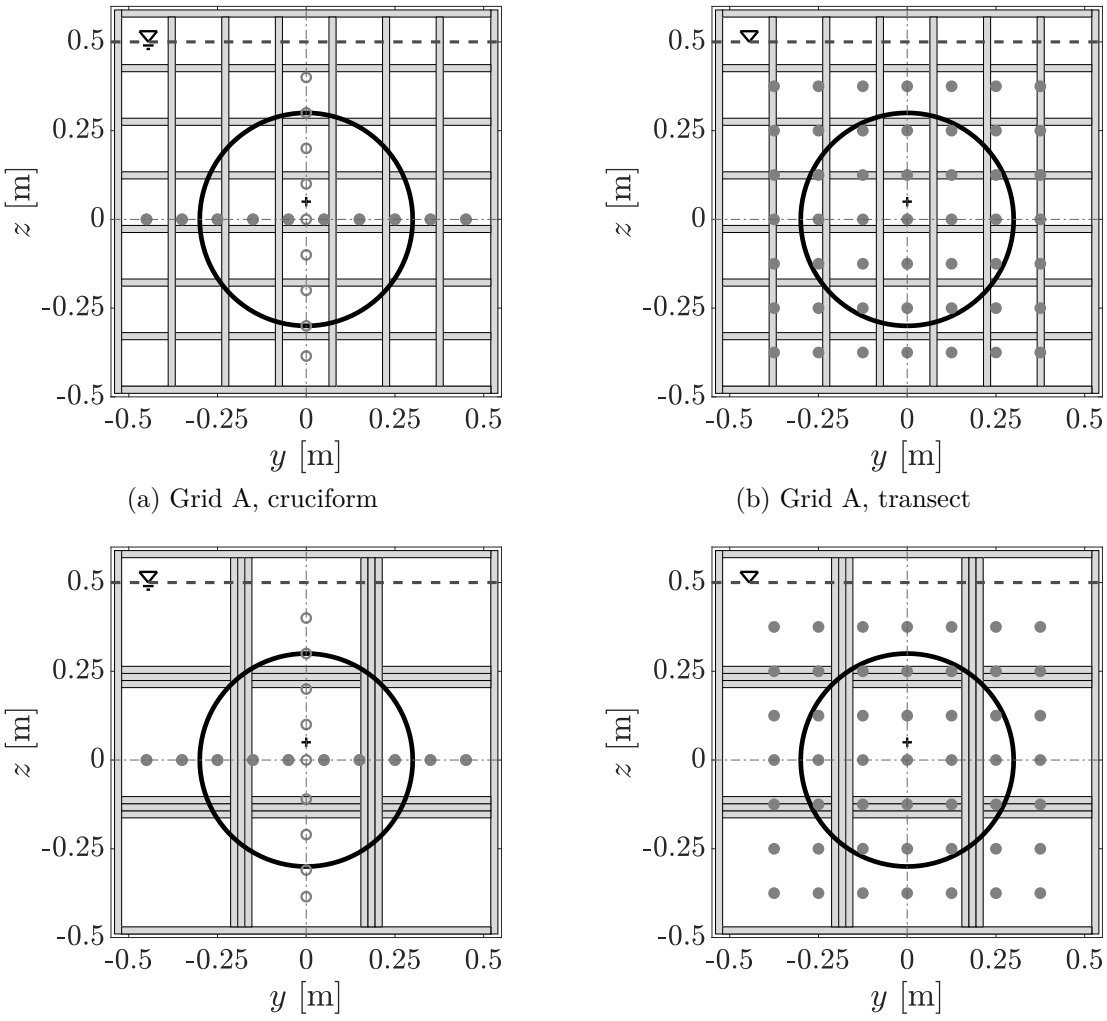


Figure A.1: ADV measurement co-ordinates for cruciform flow profiling, comprising a vertical traverse (unfilled grey circles) and a horizontal traverse (filled grey circles). The box outline delineates the channel cross section, with dash-dotted lines indicating the centre planes. Also shown is the intended swept area of the turbine rotor (black circle).

Turbulence Grid Flow Maps

Figure A.2 presents the ADV measurement co-ordinate maps for cruciform and transect flow profiling downstream of turbulence grids A and D.



(a) Grid A, cruciform

(b) Grid A, transect

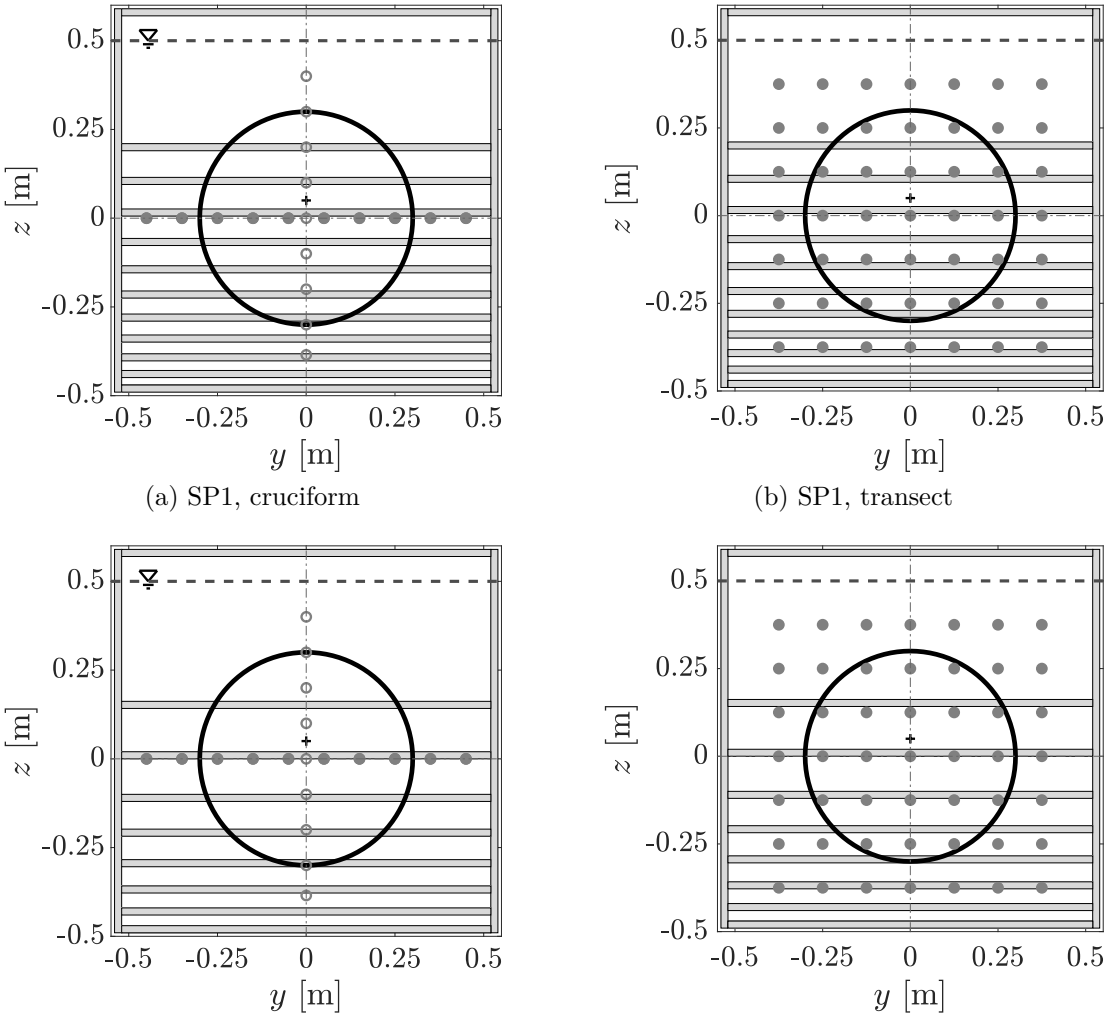
(c) Grid D, cruciform

(d) Grid D, transect

Figure A.2: ADV measurement co-ordinates for cruciform and transect flow profiling overlaid onto grids A and D. The cruciform profile comprises a vertical traverse (unfilled grey circles) and a horizontal traverse (filled grey circles). The box outline delineates the channel cross section, with dash-dotted lines indicating the centre planes. Also shown are the intended swept area of the turbine rotor (black circle), the still water level (dashed), and the geometrical centre of each grid (black cross).

Vertical Shear Profile Apparatus Flow Maps

Figure A.3 presents the ADV measurement co-ordinate maps for cruciform and transect flow profiling, overlaid onto two parallel bar arrangements designed to generate vertically sheared flow profiles in the flume.



(a) SP1, cruciform

(b) SP1, transect

(c) SP2, cruciform

(d) SP2, transect

Figure A.3: ADV measurement co-ordinates for cruciform and transect profiling overlaid onto two graded obstructions, SP1 and SP2, designed to generate vertically sheared flow profiles, corresponding to $n = 6$ and $n = 9$, respectively. The cruciform profile comprises a vertical traverse (unfilled grey circles) and a horizontal traverse (filled grey circles). The box outline delineates the channel cross section, with dash-dotted lines indicating the centre planes. Also shown are the intended swept area of the turbine rotor (black circle), the still water level (dashed), and the geometrical centre of each grid (black cross).

APPENDIX B

Definition of Resistance Grading for Vertical Shear

A method for generating vertical shear profiles approximated by a power-law model using non-uniformly spaced parallel rods was first proposed by Cockrell and Lee [34] for practical application in wind tunnels, building on the general theory presented by Elder [118]. Cowdrey [124] later refined this approach by assuming zero lateral flow downstream of the obstruction, the target profile forming just upstream, and a uniform pressure field on either side. These adjustments enabled the model to predict greater velocity shear near the channel bed, resolving discrepancies between the theoretical and measured profiles in Cockrell and Lee's work. The following section presents a derivation of Cowdrey's solution, which was used for the initial geometric definition of the graded obstructions described in Chapter 5 to achieve the target shear profiles.

By Bernoulli's theorem, a loss of static pressure, Δp, across the obstruction for a given streamline can be expressed non-dimensionally as:

$$\frac{\Delta p}{\frac{1}{2}\rho U_\infty^2} = \left(\frac{u(z)}{U_\infty}\right)^2 (1 + K_{\text{loc}}) - 1 = K_{\text{tot}} \quad \text{and} \quad \left(\frac{u(z)}{U_\infty}\right)^2 = \frac{1 + K_{\text{tot}}}{1 + K_{\text{loc}}}, \tag{B.1}$$

where ρ is the fluid density, $u(z)$ is the local streamwise velocity downstream of the obstruction as a function of elevation from the channel bed (where $z/H \in \{0, 1\}$),

U_∞ is the freestream velocity (representing a uniform velocity field), K_{loc} is the local resistance coefficient, and K_{tot} represents the overall resistance coefficient of the obstruction. For a given power-law velocity profile:

$$\frac{u(z)}{z^{1/n}} = \text{constant}, \tag{B.2}$$

where $1/n$ is the power-law exponent, the conservation of mass can be applied to define a relationship between the velocity and the height of the flow passage, H:

$$U_\infty H = \int_0^H u(z)\,\mathrm{d}z = \frac{u(z)}{z^{1/n}} \int_0^H z^{1/n}\,\mathrm{d}z, \tag{B.3}$$

$$\frac{u(z)}{U_\infty} = \frac{n}{1+n}\left(\frac{z}{H}\right). \tag{B.4}$$

Expressing the local resistance coefficient in terms of the rods' characteristic dimension (here, the diameter), d, and their centre-to-centre spacing, l, yields:

$$K_{\text{loc}} = \frac{d/l}{\left(1 - d/l\right)^2}, \tag{B.5}$$

where $\left(1 - d/l\right)^2$ represents the porosity of the obstruction (cf. Equation 4.1). This formulation allows Equation B.1 to be rewritten in terms of a power-law relationship, given by:

$$\frac{z}{H} = \left(\frac{n}{1+n}\right)^n \left(\frac{1+K_{\text{tot}}}{1+K_{\text{loc}}}\right)^{n/2}, \tag{B.6}$$

providing a tractable means of arranging the rods in the yz-plane. The overall resistance coefficient can be approximated for each target profile using the following relation [34, 117]:

$$\frac{1+n}{n} = \left(\frac{1+K_{\text{tot}}}{1+\frac{K_{\text{tot}}}{2}}\right). \tag{B.7}$$

Bibliography

[1] D. Gielen, F. Boshell, D. Saygin, M. D. Bazilian, N. Wagner, and R. Gorini, "The role of renewable energy in the global energy transformation," *Energy Strategy Reviews*, vol. 24, pp. 38–50, 2019.

[2] International Energy Agency (IEA), "Net zero roadmap: a global pathway to keep the 1.5°C goal in reach," IEA, Paris, Tech. Rep., 2023.

[3] "Chapter 3: earth tides and tidal deformations," in *Marine Gravity*, ser. Elsevier Oceanography Series, P. Dehlinger, Ed., vol. 22, Netherlands: Elsevier, 1978, pp. 51–70.

[4] National Oceanic and Atmospheric Administration (NOAA), *Tides and water levels*, Accessed: 15-Oct-2024. [Online]. Available: https://oceanservice.noaa.gov/education/tutorial_tides/tides08_othereffects.html.

[5] National Oceanic and Atmospheric Administration (NOAA), *Fundy tides: the world's largest tidal variations*, Accessed: 15-Oct-2024. [Online]. Available: https://www.noaa.gov/ocean/fundy-max.

[6] F. O'Rourke, F. Boyle, and A. Reynolds, "Tidal energy update 2009," *Applied Energy*, vol. 87, no. 2, pp. 398–409, 2010.

[7] European Marine Energy Centre (EMEC), *Tidal devices*, Accessed: 15-Oct-2024. [Online]. Available: https://www.emec.org.uk/marine-energy/tidal-devices/.

[8] Z. Zhou, M. Benbouzid, J.-F. Charpentier, F. Scuiller, and T. Tang, "Developments in large marine current turbine technologies – a review," *Renewable and Sustainable Energy Reviews*, vol. 71, pp. 852–858, 2017.

[9] A. I. Winter, "Differences in fundamental design drivers for wind and tidal turbines," in *Proceedings of 2011 OCEANS Conference*, Santander, Spain: Institute of Electrical and Electronics Engineers (IEEE), 2011, pp. 1–10.

[10] T. A. A. Adcock, S. Draper, R. H. J. Willden, and C. R. Vogel, "The fluid mechanics of tidal stream energy conversion," *Annual Review of Fluid Mechanics*, vol. 53, pp. 287–310, 2021.

[11] C. Garrett and P. Cummins, "The efficiency of a turbine in a tidal channel," *Journal of Fluid Mechanics*, vol. 588, pp. 243–251, 2007.

[12] A. S. Bahaj, A. F. Molland, J. R. Chaplin, and W. M. Batten, "Power and thrust measurements of marine current turbines under various hydrodynamic flow conditions in a cavitation tunnel and a towing tank," *Renewable Energy*, vol. 32, no. 3, pp. 407–426, 2007.

[13] M. Deb, Z. Yang, K. Haas, and T. Wang, "Hydrokinetic tidal energy resource assessment following International Electrotechnical Commission guidelines," *Renewable Energy*, vol. 229, p. 120 767, 2024.

[14] Y. Wen and P. Lin, "Exploitation potential of tidal current energy in southern China seas," *Energy Conversion and Management*, vol. 267, p. 115 901, 2022.

[15] "UK tidal current resource & economics," Black & Veatch Ltd., London, UK, Tech. Rep., 2011.

[16] Tethys, *MeyGen tidal energy project - phase i*, Accessed: 2021-12-26, 2016. [Online]. Available: https://tethys.pnnl.gov/project-sites/meygen-tidal-energy-project-phase-i.

[17] Tethys, *Nova Innovation - Shetland Tidal Array (Bluemull Sound)*, Accessed: 2021-12-26, 2016. [Online]. Available: https://tethys.pnnl.gov/project-sites/nova-innovation-shetland-tidal-array-bluemull-sound.

[18] Orbital Marine Power, *O2: the world's most powerful tidal turbine*, Accessed: 15-Oct-2024. [Online]. Available: https://www.orbitalmarine.com/o2/.

[19] Alstom, *Alstom produced electricity with its 1 MW tidal turbine for the first time in real conditions*, Accessed: 15-Oct-2024, 2013. [Online]. Available: https://www.alstom.com/press-releases-news/2013/3/alstom-produced-electricity-with-its-1-mw-tidal-turbine-for-the-first-time-in-real-conditions.

[20] E. Serin, P. Andres, R. Martin, A. Shah, and A. Valero, "Sustainable growth opportunities from tidal stream energy in the UK," London School of Economics and Political Science, Tech. Rep., 2023.

[21] Offshore Renewable Energy (ORE) Catapult, "Tidal stream and wave energy cost reduction and industrial benefit," ORE Catapult, Tech. Rep., 2018.

[22] UK Government, *Contracts for Difference (CfD) allocation round 6: results*, Accessed: 15-Oct-2024, 2024. [Online]. Available: https://www.gov.uk/government/publications/contracts-for-difference-cfd-allocation-round-6-results.

[23] P. Liu and B. Veitch, "Design and optimization for strength and integrity of tidal turbine rotor blades," *Energy*, vol. 46, no. 1, pp. 393–404, 2012.

[24] BBC, *Blade fault on giant tide turbine AK1000 in Orkney*, Accessed: 2021-12-28, 2010. [Online]. Available: https://www.bbc.co.uk/news/uk-scotland-highlands-islands-11492829.

[25] J. McNaughton, S. Ettema, F. Zilic de Arcos, C. R. Vogel, and R. H. J. Willden, "An experimental investigation of the influence of inter-turbine spacing on the loads and performance of a co-planar tidal turbine fence," *Journal of Fluids and Structures*, vol. 118, p. 103 844, 2023.

[26] T. Burton, D. Sharpe, N. Jenkins, and E. Bossanyi, *Wind Energy Handbook*. UK: John Wiley & Sons Ltd., 2001.

[27] M. Lewis, S. P. Neill, P. Robins, M. R. Hashemi, and S. Ward, "Characteristics of the velocity profile at tidal-stream energy sites," *Renewable Energy*, vol. 114, pp. 258–272, 2017.

[28] D. Ingram, G. Smith, C. Bittencourt-Ferreira, and H. Smith, "Protocols for the equitable assessment of marine energy converters," The University of Edinburgh, Tech. Rep., 2011.

[29] I. A. Milne, R. N. Sharma, R. G. J. Flay, and S. Bickerton, "Characteristics of the turbulence in the flow at a tidal stream power site," *Philosophical Transactions of the Royal Society A: Mathematical, Physical and Engineering Sciences*, vol. 371, no. 1985, p. 20 120 196, 2013.

[30] M. Thiébaut, J.-F. Filipot, C. Maisondieu, G. Damblans, C. Jochum, L. F. Kilcher, and S. Guillou, "Characterization of the vertical evolution of the three-dimensional turbulence for fatigue design of tidal turbines," *Philosophical Transactions of the Royal Society A: Mathematical, Physical and Engineering Sciences*, vol. 378, no. 2178, p. 20 190 495, 2020.

[31] J. Thomson, B. Polagye, V. Durgesh, and M. C. Richmond, "Measurements of turbulence at two tidal energy sites in Puget Sound, WA," *IEEE Journal of Oceanic Engineering*, vol. 37, no. 3, pp. 363–374, 2012.

[32] P. E. Roach, "The generation of nearly isotropic turbulence by means of grids," *International Journal of Heat and Fluid Flow*, vol. 8, no. 2, pp. 82–92, 1987.

[33] P.-Å. Krogstad and P. A. Davidson, "Freely decaying, homogeneous turbulence generated by multi-scale grids," *Journal of Fluid Mechanics*, vol. 680, pp. 417–434, 2011.

[34] D. J. Cockrell and B. E. Lee, "Production of shear profiles in a wind tunnel by cylindrical rods placed normal to the stream," *Journal of the Royal Aeronautical Society*, vol. 70, no. 667, pp. 724–725, 1966.

[35] U. Karnik and S. Tavoularis, "Generation and manipulation of uniform shear with the use of screens," *Experiments in Fluids*, vol. 5, no. 4, pp. 247–254, 1987.

[36] T. Mori, K. Naganuma, R. Kimoto, R. Yakushiji, and S. Nagaya, "Hydrodynamic and hydroacoustic characteristics of the Flow Noise Simulator (keynote)," in *Proceedings of the ASME/JSME 2007 5th Joint Fluids Engineering Conference. Volume 2: Fora, Parts A and B*, California, USA, 2007, pp. 121–127.

[37] J. T. Park, J. M. Cutbirth, and W. H. Brewer, "Hydrodynamic performance of the Large Cavitation Channel (LCC)," in *Proceedings of the ASME/JSME 2003 4th Joint Fluids Summer Engineering Conference. Volume 2: Symposia, Parts A, B, and C*, Hawaii, USA, 2003, pp. 87–100.

[38] D. R. J. Sutherland, D. R. Noble, J. Steynor, T. Davey, and T. Bruce, "Characterisation of current and turbulence in the FloWave Ocean Energy Research Facility," *Ocean Engineering*, vol. 139, pp. 103–115, 2017.

[39] J. McNaughton, F. Zilic de Arcos, C. R. Vogel, and R. H. J. Willden, "Dynamic loading of two side-by-side tidal stream turbines in regular waves," *Journal of Fluids and Structures*, vol. 133, p. 104 259, 2025.

[40] J. T. Park, J. M. Cutbirth, and W. H. Brewer, "Experimental methods for hydrodynamic characterization of a very large water tunnel," *Journal Fluids Eng.*, vol. 172, no. 6, pp. 1210–1214, 2005.

[41] FLEXIM, *Flexible Inductrial Measurement - product catalogue*, Brochure, Accessed: 2024-08-07. [Online]. Available: https://cabaleraengg.com/wp-content/uploads/2017/03/FLEXIM-Product-Catalogue.pdf.

[42] B. Gaurier, M. Ikhennicheu, G. Germain, and P. Druault, "Experimental study of bathymetry generated turbulence on tidal turbine behaviour," *Renewable Energy*, vol. 156, pp. 1158–1170, 2020.

[43] S. Tedds, "Scale model testing of tidal stream turbines: wake characterisation in realistic flow conditions," Ph.D. dissertation, University of Liverpool, 2014.

[44] A. Lohrmann, R. Cabrera, and N. C. Kraus, "Acoustic-Doppler velocimeter (ADV) for laboratory use," in *Proceedings of the Symposium on Fundamentals and Advancements in Hydraulic Measurements and Experimentation*, New York, USA, 1994, pp. 351–365.

[45] Nortek, *The comprehensive manual for velocimeters*, Manual, Accessed: 2021-07-10, Norway, 2018. [Online]. Available: https://support.nortekgroup.com/hc/en-us/article_attachments/4551609336220.

[46] igus, *Lubrication-free toothed belt axes*, Accessed: 2024-08-07, 2024. [Online]. Available: https://www.igus.in/info/linear-guides-zlw-toothed-belt-axes.

[47] Arduino, *Arduino Nano 33 IoT*, Accessed: 2022-07-15. [Online]. Available: https://store.arduino.cc/products/arduino-nano-33-iot.

[48] STMicroelectronics, *LSM6DS3 iNEMO inertial module: always-on 3D accelerometer and 3D gyroscope. Datasheet*, Accessed: 2022-10-30. [Online]. Available: https://content.arduino.cc/assets/st_imu_lsm6ds3_datasheet.pdf.

[49] Edinburgh Designs Ltd., *Wave gauges*, Accessed: 2023-06-06. [Online]. Available: http://www4.edesign.co.uk/product/wavegauges/.

[50] T. Blackmore, L. E. Myers, and A. S. Bahaj, "Effects of turbulence on tidal turbines: implications to performance, blade loads, and condition monitoring," *International Journal of Marine Energy*, vol. 14, pp. 1–26, 2016.

[51] R. A. Lizardo and A. V. Mollick, "The sustainability of the U.S. current account deficit: revisiting Mann's rule," *Global Economy Journal*, vol. 9, no. 4, p. 1 850 181, 2009.

[52] H. Canilho, C. Santos, C. Taborda, I. Falorca, and C. Fael, "Measurements of suspended ashes concentration in turbulent flow with acoustic Doppler velocimeter," *Flow Measurement and Instrumentation*, vol. 87, p. 102 207, 2022.

[53] S. Yahaya, S. S. Jikan, N. A. Badarulzaman, and A. D. Adamu, "Chemical composition and particle size analysis of kaolin," *Path of Science*, vol. 3, no. 10, pp. 1001–1004, 2017.

[54] L. Songhan Plastic Technology Co., *Potters Industries sphericel 110P8 hollow glass spheres*, Accessed: 2023-02-19. [Online]. Available: http://www.lookpolymers.com/pdf/Potters-Industries-Sphericel-110P8-Hollow-Glass-Spheres.pdf.

[55] T. L. Wahl, "Analyzing ADV data using WinADV," in *Building Partnerships*. USA, 2012, pp. 1–10.

[56] M. Parsheh, F. Sotiropoulos, and F. Porté-Agel, "Estimation of power spectra of acoustic-Doppler velocimetry data contaminated with intermittent spikes," *Journal of Hydraulic Engineering*, vol. 136, no. 6, pp. 368–378, 2010.

[57] L. Cea, J. Agudo, and L. Pena, "Velocity measurements on highly turbulent free surface flow using ADV," *Experiments in Fluids*, vol. 42, pp. 333–348, 2007.

[58] D. G. Goring and V. I. Nikora, "Despiking acoustic Doppler velocimeter data," *Journal of Hydraulic Engineering*, vol. 128, no. 1, pp. 117–126, 2002.

[59] T. L. Wahl, "Discussion of "Despiking acoustic Doppler velocimeter data" by Derek G. Goring and Vladimir I. Nikora," *Journal of Hydraulic Engineering*, vol. 129, no. 6, pp. 484–487, 2003.

[60] G. Voulgaris and J. H. Trowbridge, "Evaluation of the acoustic Doppler velocimeter (ADV) for turbulence measurements," *Journal of Atmospheric and Oceanic Technology*, vol. 15, no. 1, pp. 272–289, 1998.

[61] V. I. Nikora and D. G. Goring, "ADV measurements of turbulence: can we improve their interpretation?" *Journal of Hydraulic Engineering*, vol. 124, no. 6, pp. 630–634, 1998.

[62] B. Khorsandi, L. Mydlarski, and S. Gaskin, "Noise in turbulence measurements using acoustic Doppler velocimetry," *Journal of Hydraulic Engineering*, vol. 138, no. 10, pp. 829–838, 2012.

[63] H. W. Coleman and W. Glenn Steele Jr., *Experimentation, Validation, and Uncertainty Analysis for Engineers*. USA: John Wiley & Sons, Inc., 2009.

[64] A. N. Kolmogorov, V. Levin, J. C. R. Hunt, O. M. Phillips, and D. Williams, "The local structure of turbulence in incompressible viscous fluid for very large Reynolds numbers," *Proceedings of the Royal Society of London. Series A: Mathematical and Physical Sciences*, vol. 434, no. 1890, pp. 9–13, 1991.

[65] S. Pope, *Turbulent Flows*. UK: Cambridge University Press, 2000.

[66] P. D. Welch, "The use of fast Fourier transform for the estimation of power spectra: a method based on time averaging over short, modified periodograms," *IEEE Transactions on Audio and Electroacoustics*, vol. 15, no. 2, pp. 70–73, 1967.

[67] MathWorks, *Signal processing toolbox - Welch's power spectral density estimate*, Accessed: 2022-09-26, USA, 2022. [Online]. Available: https://uk.mathworks.com/help/signal/ref/pwelch.html#d126e153043.

[68] T. von Kármán, "Progress in the statistical theory of turbulence," *Proceedings of the National Academy of Sciences*, vol. 34, no. 11, pp. 530–539, 1948.

[69] E. Cheynet, "Wind-induced vibrations of a suspension bridge: a case study in full-scale," Ph.D. dissertation, University of Stavanger, 2016.

[70] V. Durgesh, J. Thomson, M. C. Richmond, and B. L. Polagye, "Noise correction of turbulent spectra obtained from acoustic Doppler velocimeters," *Flow Measurement and Instrumentation*, vol. 37, pp. 29–41, 2014.

[71] J. O. Hinze, *Turbulence*. USA: McGraw-Hill, 1975.

[72] P. L. O'Neill, D. Nicolaides, D. R. Honnery, and J. Soria, "Autocorrelation functions and the determination of integral length with reference to experimental and numerical data," in *Proceedings of the 15th Australasian Fluid Mechanics Conference*, Sydney, Australia, 2004, pp. 1–4.

[73] A. Fuchs, S. Kharche, A. Patil, J. Friedrich, M. Wächter, and J. Peinke, "An open source package to perform basic and advanced statistical analysis of turbulence data and other complex systems," *Physics of Fluids*, vol. 34, no. 10, p. 101 801, 2022.

[74] M. Romagnoli, C. M. García, and R. A. Lopardo, "Signal postprocessing technique and uncertainty analysis of ADV turbulence measurements on free hydraulic jumps," *Journal of Hydraulic Engineering*, vol. 138, no. 4, pp. 353–357, 2012.

[75] K. Shigehiko, T. Nakamura, F. Inada, and M. Kato, *Flow Induced Vibrations*. Netherlands: Elsevier, 2008.

[76] I. Nezu and H. Nakagawa, *Turbulence in Open-Channel Flows*. UK: Routledge, 1993.

[77] R. Soulsby, *Physical Oceanography of Coastal and Shelf Seas* (Elsevier Oceanography Series). Netherlands: Elsevier, 1983.

[78] T. von Kármán, "Mechanische Aenlichkeit und Turbulenz," *Nachrichten von der Gesellschaft der Wissenschaften zu Göttingen, Mathematisch-Physikalische Klasse*, vol. 1930, pp. 58–76, 1930.

[79] F. de Castro, *Fitmethis version 1.6.1*, Retrieved: 2023-06-06, 2021. [Online]. Available: https://uk.mathworks.com/matlabcentral/fileexchange/40167-fitmethis.

[80] R. V. Hogg, J. W. McKean, and A. T. Craig, *Introduction to Mathematical Statistics*. USA: Prentice Hall, 2005.

[81] K. Christakos, J. Reuder, and B. Furevik, "Experimental characterization of the marine atmospheric boundary layer in the Havsul area, Norway," *Energy Procedia*, vol. 35, pp. 121–127, DeepWind'2013 – Selected papers from 10th Deep Sea Offshore Wind R&D Conference, Trondheim, Norway, 2013.

[82] T. Lee, "Lognormality in turbulence energy spectra," *Entropy (Basel)*, vol. 22, no. 6, Art. no. 669, pp. 1–11, 2020.

[83] H. Mouri, A. Hori, and M. Takaoka, "Large-scale lognormal fluctuations in turbulence velocity fields," *Physics of Fluids*, vol. 21, no. 6, p. 065 107, 2009.

[84] O. Reynolds, "IV. On the dynamical theory of incompressible viscous fluids and the determination of the criterion," *Philosophical Transactions of the Royal Society of London. (A.)*, vol. 186, pp. 123–164, 1895.

[85] C. Klipp, "Turbulent friction velocity calculated from the Reynolds stress tensor," *Journal of the Atmospheric Sciences*, vol. 75, no. 4, pp. 1029–1043, 2018.

[86] J. Connell, "The spectrum of wind speed fluctuations encountered by a rotating blade of a wind energy conversion system," *Solar Energy*, vol. 29, no. 5, pp. 363–375, 1982.

[87] A. Naberezhnykh, D. Ingram, I. Ashton, and J. Culina, "How applicable are turbulence assumptions used in the tidal energy industry?" *Energies*, vol. 16, no. 4, Art. no. 1881, pp. 1–21, 2023.

[88] Y. Nakamura, Y. Ohya, and S. Ozono, "The effects of turbulence on bluff-body mean flow," *Journal of Wind Engineering and Industrial Aerodynamics*, vol. 28, no. 1, pp. 251–259, 1988.

[89] L. Bowen, A. Celik, and M. Azarpeyvand, "A thorough experimental investigation on airfoil turbulence interaction noise," *Physics of Fluids*, vol. 35, no. 3, p. 035 123, 2023.

[90] A. Al-Abadi, Y. Kim, Ö. Ertunç, and A. Delgado, "Turbulence impact on wind turbines: experimental investigations on a wind turbine model," *Journal of Physics: Conference Series*, vol. 753, no. 3, p. 032 046, 2016.

[91] L. Neuhaus, F. Berger, J. Peinke, and M. Hölling, "Exploring the capabilities of active grids," *Experiments in Fluids*, vol. 62, Art. no. 130, pp. 1–12, 2021.

[92] P. C. Valente and J. C. Vassilicos, "The decay of turbulence generated by a class of multiscale grids," *Journal of Fluid Mechanics*, vol. 687, pp. 300–340, 2011.

[93] L. F. G. Simmons, C. Salter, and G. I. Taylor, "Experimental investigation and analysis of the velocity variations in turbulent flow," *Proceedings of the Royal Society of London. Series A, Containing Papers of a Mathematical and Physical Character*, vol. 145, no. 854, pp. 212–234, 1934.

[94] D. S. K. Ting, *Basics of Engineering Turbulence*. UK: Academic Press, 2016.

[95] F. Murzyn and M. Bélorgey, "Experimental investigation of the grid-generated turbulence features in a free surface flow," *Experimental Thermal and Fluid Science*, vol. 29, no. 8, pp. 925–935, 2005.

[96] H. Yao, L. Cao, D. Wu, Y. Gao, S. Qin, and F. Yu, "PIV study on grid-generated turbulence in a free surface flow," *Water*, vol. 13, no. 7, Art. no. 909, pp. 1–23, 2021.

[97] J. P. Panda, A. Mitra, A. P. Joshi, and H. V. Warrior, "Experimental and numerical analysis of grid generated turbulence with and without mean strain," *Experimental Thermal and Fluid Science*, vol. 98, pp. 594–603, 2018.

[98] T. Ebdon, M. J. Allmark, D. M. O'Doherty, A. Mason-Jones, T. O'Doherty, G. Germain, and B. Gaurier, "The impact of turbulence and turbine operating condition on the wakes of tidal turbines," *Renewable Energy*, vol. 165, pp. 96–116, 2021.

[99] P. Bearman and T. Morel, "Effect of free stream turbulence on the flow around bluff bodies," *Progress in Aerospace Sciences*, vol. 20, no. 2, pp. 97–123, 1983.

[100] T. Kurian and J. H. M. Fransson, "Grid-generated turbulence revisited," *Fluid Dynamics Research*, vol. 41, no. 2, p. 021 403, 2009.

[101] P. G. Saffman, "The large-scale structure of homogeneous turbulence," *Journal of Fluid Mechanics*, vol. 27, no. 3, pp. 581–593, 1967.

[102] M. Kazemi, B. Khorsandi, and L. Mydlarski, "Effect of acoustic Doppler velocimeter sampling volume size on measurements of turbulence," *Journal of Atmospheric and Oceanic Technology*, vol. 38, no. 2, pp. 259–268, 2021.

[103] Ö. Ertunç, N. Özyilmaz, H. Lienhart, F. Durst, and K. Beronov, "Homogeneity of turbulence generated by static-grid structures," *Journal of Fluid Mechanics*, vol. 654, pp. 473–500, 2010.

[104] J. Groth and A. V. Johansson, "Turbulence reduction by screens," *Journal of Fluid Mechanics*, vol. 197, pp. 139–155, 1988.

[105] G. K. Batchelor, A. A. Townsend, and G. I. Taylor, "Decay of isotropic turbulence in the initial period," *Proceedings of the Royal Society of London. Series A. Mathematical and Physical Sciences*, vol. 193, no. 1035, pp. 539–558, 1948.

[106] P.-Å. Krogstad and P. A. Davidson, "Is grid turbulence Saffman turbulence?" *Journal of Fluid Mechanics*, vol. 642, pp. 373–394, 2010.

[107] G. Comte-Bellot and S. Corrsin, "The use of a contraction to improve the isotropy of grid-generated turbulence," *Journal of Fluid Mechanics*, vol. 25, no. 4, pp. 657–682, 1966.

[108] F. Murzyn and A. Mehel, "Influence of the virtual origin on the turbulent length scales in the grid-generated turbulence," *International Journal of Fluid Mechanics Research*, vol. 43, no. 1, pp. 62–78, 2016.

[109] M. S. Mohamed and J. C. Larue, "The decay power law in grid-generated turbulence," *Journal of Fluid Mechanics*, vol. 219, pp. 195–214, 1990.

[110] I. A. Milne, A. H. Day, R. N. Sharma, and R. G. J. Flay, "The characterisation of the hydrodynamic loads on tidal turbines due to turbulence," *Renewable and Sustainable Energy Reviews*, vol. 56, pp. 851–864, 2016.

[111] J. McGhee, D. Wagh, J. Farnsworth, and G. Vijayakumar, "Impact of canonical perturbations in the inflow on wind turbine loads," *Journal of Physics: Conference Series*, vol. 2265, no. 2, p. 022 017, 2022.

[112] F. Ahmed and B. E. Lee, "The production of shear flow profiles in a wind tunnel by a shaped honeycomb technique," *Journal of Fluids Engineering*, vol. 119, no. 3, pp. 713–715, 1997.

[113] R. J. Hearst and B. Ganapathisubramani, "Tailoring incoming shear and turbulence profiles for lab-scale wind turbines," *Wind Energy*, vol. 20, no. 12, pp. 2021–2035, 2017.

[114] M. J. Emes, M. Marano, and M. Arjomandi, "Heliostat wind loads in the atmospheric boundary layer (ABL): Reconciling field measurements with wind tunnel experiments," *Solar Energy*, vol. 277, p. 112 742, 2024.

[115] J. Counihan, "An improved method of simulating an atmospheric boundary layer in a wind tunnel," *Atmospheric Environment (1967)*, vol. 3, no. 2, pp. 197–214, 1969.

[116] C. Gramespacher, H. Albiez, M. Stripf, and H. J. Bauer, "The generation of grid turbulence with continuously adjustable intensity and length scales," *Experiments in Fluids*, vol. 60, Art. no. 85, pp. 1–15, 2019.

[117] P. R. Owen and H. K. Zienkiewicz, "The production of uniform shear flow in a wind tunnel," *Journal of Fluid Mechanics*, vol. 2, no. 6, pp. 521–531, 1957.

[118] J. W. Elder, "Steady flow through non-uniform gauzes of arbitrary shape," *Journal of Fluid Mechanics*, vol. 5, no. 3, pp. 355–368, 1959.

[119] A. Robert, A. G. Roy, and B De Serres, "Changes in velocity profiles at roughness transitions in coarse grained channels," *Sedimentology*, vol. 39, no. 5, pp. 725–735, 1992.

[120] M. Islam, D. Spencer, P. Herrington, D. Walker, H. Moideen, and Y. C. Park, "Sheared current generation in flume tank for experimental research," in *Proceedings of the ASME 2013 32nd International Conference on Ocean, Offshore and Arctic Engineering. Volume 1: Offshore Technology*, Nantes, France, 2013, Art. no. V001T01A008, pp. 1–12.

[121] M. Magnier, G. Germain, B. Gaurier, and P. Druault, "Velocity profile effects on a bottom-mounted square cylinder wake and load variations," in *Proceedings of the 14th European Wave and Tidal Energy Conference (EWTEC 2021)*, Plymouth, UK, 2021, Art. no. 2249, pp. 1–10.

[122] M. Magnier, N. Delette, P. Druault, B. Gaurier, and G. Germain, "Experimental study of the shear flow effect on tidal turbine blade loading variation," *Renewable Energy*, vol. 193, pp. 744–757, 2022.

[123] A. Vinod, C. Han, and A. Banerjee, "Tidal turbine performance and near-wake characteristics in a sheared turbulent inflow," *Renewable Energy*, vol. 175, pp. 840–852, 2021.

[124] C. F. Cowdrey, "A simple method for the design of wind-tunnel velocity-profile grids," National Physical Laboratory, Tech. Rep. Aero Note 1055, 1967.

[125] J. M. Wallace, H. Eckelmann, and R. S. Brodkey, "The wall region in turbulent shear flow," *Journal of Fluid Mechanics*, vol. 54, no. 1, pp. 39–48, 1972.

[126] J. M. Wallace, "Quadrant analysis in turbulence research: history and evolution," *Annual Review of Fluid Mechanics*, vol. 48, pp. 131–158, 2016.

[127] I. A. Milne, R. N. Sharma, and R. G. J. Flay, "The structure of turbulence in a rapid tidal flow," *Proceedings of the Royal Society A: Mathematical, Physical and Engineering Sciences*, vol. 473, no. 2204, p. 20 170 295, 2017.

[128] S. S. Lu and W. W. Willmarth, "Measurements of the structure of the Reynolds stress in a turbulent boundary layer," *Journal of Fluid Mechanics*, vol. 60, no. 3, pp. 481–511, 1973.

[129] C. R. Vogel, R. H. J. Willden, and G. T. Houlsby, "Blade element momentum theory for a tidal turbine," *Ocean Engineering*, vol. 169, pp. 215–226, 2018.

[130] F. Zilic de Arcos, C. R. Vogel, and R. H. J. Willden, "Extracting angles of attack from blade-resolved rotor CFD simulations," *Wind Energy*, vol. 23, no. 9, pp. 1868–1885, 2020.

[131] A. Wimshurst, C. R. Vogel, and R. H. J. Willden, "Cavitation limits on tidal turbine performance," *Ocean Engineering*, vol. 152, pp. 223–233, 2018.

[132] A. S. Bahaj, W. M. J. Batten, and G. McCann, "Experimental verifications of numerical predictions for the hydrodynamic performance of horizontal axis marine current turbines," *Renewable Energy*, vol. 32, no. 15, pp. 2479–2490, 2007.

[133] F. Zilic de Arcos, G. Tampier, and C. R. Vogel, "Numerical analysis of blockage correction methods for tidal turbines," *Journal of Ocean Engineering and Marine Energy*, vol. 6, pp. 183–197, 2020.

[134] M. J. Barnsley and J. F. Wellicome, "Final report on the 2nd phase of development and testing of a horizontal axis wind turbine test rig for the investigation of stall regulation aerodynamics," ETSU, Tech. Rep. E.5A/CON5103/1746, 1990.

[135] H. Ross and B. Polagye, "An experimental assessment of analytical blockage corrections for turbines," *Renewable Energy*, vol. 152, pp. 1328–1341, 2020.

[136] J. Schluntz and R. H. J. Willden, "The effect of blockage on tidal turbine rotor design and performance," *Renewable Energy*, vol. 81, pp. 432–441, 2015.

[137] H. Gonabadi, A. Oila, A. Yadav, and S. Bull, "Fatigue life prediction of composite tidal turbine blades," *Ocean Engineering*, vol. 260, p. 111 903, 2022.

[138] F. Zilic de Arcos, C. R. Vogel, and R. H. J. Willden, "A parametric study on the hydrodynamics of tidal turbine blade deformation," *Journal of Fluids and Structures*, vol. 113, p. 103 626, 2022.

[139] C. L. Sequeira and R. J. Miller, "Unsteady gust response of tidal stream turbines," in *Proceedings of 2014 OCEANS Conference*, St. John's, Canada: Institute of Electrical and Electronics Engineers (IEEE), 2014, pp. 1–10.

[140] J. G. Leishman, "Challenges in modelling the unsteady aerodynamics of wind turbines," *Wind Energy*, vol. 5, no. 2-3, pp. 85–132, 2002.

[141] T. Theodorsen, "General theory of aerodynamic instability and the mechanism of flutter," Tech. Rep. NACA 496, 1934.

[142] W. J. McCroskey, "The phenomenon of dynamic stall," NASA Ames Research Center, Tech. Rep. NASA-TM-81264, 1981.

[143] I. M. Viola and G. T. Scarlett, *Tidal turbine modelling code*, 2018. [Online]. Available: https://github.com/gabscarlett/Tidal-turbine-hydrodynamic-model.

[144] A. Mason-Jones, D. M. O'Doherty, C. E. Morris, and T. O'Doherty, "Influence of a velocity profile support structure on tidal stream turbine performance," *Renewable Energy*, vol. 52, pp. 23–30, 2013.

[145] U. Ahmed, D. D. Apsley, I. Afgan, T. Stallard, and P. K. Stansby, "Fluctuating loads on a tidal turbine due to velocity shear and turbulence: comparison of CFD with field data," *Renewable Energy*, vol. 112, pp. 235–246, 2017.

[146] F. O'Rourke, F. Boyle, A. Reynolds, and D. M. Kennedy, "Hydrodynamic performance prediction of a tidal current turbine operating in non-uniform inflow conditions," *Energy*, vol. 93, pp. 2483–2496, 2015.

[147] B. Gaurier, P. Druault, M. Ikhennicheu, and G. Germain, "Experimental analysis of the shear flow effect on tidal turbine blade root force from three-dimensional mean flow reconstruction," *Philosophical Transactions of the Royal Society A: Mathematical, Physical and Engineering Sciences*, vol. 378, no. 2178, p. 20 200 001, 2020.

[148] C. R. Vogel, T. Tang, S. L. Dubon, and J. Steynor, "Simulations of tidal turbine blade loading in flood and ebb tides," in *Proceedings of the 14th European Wave and Tidal Energy Conference (EWTEC 2021)*, Plymouth, UK, Sep. 2021, Art. no. 2389, pp. 1–8.

[149] S. R. J. Powles, "The effects of tower shadow on the dynamics of a horizontal-axis wind turbine," *Wind Engineering*, vol. 7, no. 1, pp. 26–42, 1983.

[150] A. Ghandour, T. De Troyer, and M. C. Runacres, "A combined potential flow–BEM model to study the tower shadow effect in wind turbines," *Journal of Wind Engineering and Industrial Aerodynamics*, vol. 229, p. 105 131, 2022.

[151] S. Muchala and R. H. J. Willden, "Influence of support structures on tidal turbine power output," *Journal of Fluids and Structures*, vol. 83, pp. 27–39, 2018.

[152] G. Shoukat, B. Gaurier, J.-V. Facq, and G. S. Payne, "Experimental investigation of the influence of mast proximity on rotor loads for horizontal axis tidal turbines," *Renewable Energy*, vol. 200, pp. 983–995, 2022.

[153] J. N. Sørensen and W. Z. Shen, "Numerical modeling of wind turbine wakes," *Journal of Fluids Engineering*, vol. 124, no. 2, pp. 393–399, 2002.

[154] C. Li, Y. Zhang, Y. Zheng, Y. Qian, E. Fernandez-Rodriguez, and E. Benini, "Research on the effect of yawing motion on tidal turbine performance based on actuator-line method," *Ocean Engineering*, vol. 279, p. 114 345, 2023.

[155] Y. Qian, Y. Zhang, Y. Sun, H. Zhang, Z. Zhang, and C. Li, "Experimental and numerical investigations on the performance and wake characteristics of a tidal turbine under yaw," *Ocean Engineering*, vol. 289, p. 116 276, 2023.

[156] G. T. Scarlett and I. M. Viola, "Unsteady hydrodynamics of tidal turbine blades," *Renewable Energy*, vol. 146, pp. 843–855, 2020.

[157] P. W. Galloway, L. E. Myers, and A. S. Bahaj, "Quantifying wave and yaw effects on a scale tidal stream turbine," *Renewable Energy*, vol. 63, pp. 297–307, 2014.

[158] P. Ouro, M. Harrold, T. Stoesser, and P. Bromley, "Hydrodynamic loadings on a horizontal axis tidal turbine prototype," *Journal of Fluids and Structures*, vol. 71, pp. 78–95, 2017.

[159] P. Ouro and T. Stoesser, "Impact of environmental turbulence on the performance and loadings of a tidal stream turbine," *Flow, Turbulence and Combustion*, vol. 102, pp. 613–639, 2019.

[160] H. Mullings and T. Stallard, "Assessment of dependency of unsteady onset flow and resultant tidal turbine fatigue loads on measurement position at a tidal site," *Energies*, vol. 14, no. 17, Art. no. 5470, pp. 1–13, 2021.

[161] P. Wang, L. Wang, Q. Zhang, F. Zhu, and B. Huang, "A model for predicting the unsteady hydrodynamic characteristics on the blades of a horizontal axis tidal turbine," *Applied Mathematical Modelling*, vol. 127, pp. 506–528, 2024.

[162] D. M. McNae, "Unsteady hydrodynamics of tidal stream turbines," Ph.D. dissertation, Imperial College London, 2013.

[163] A. Suzuki and A. Hansen, "Generalized dynamic wake model for YawDyn," in *37th Aerospace Sciences Meeting and Exhibit*, Reno, USA, Jan. 1999, pp. 186–191.

[164] F. Maganga, G. Germain, J. King, G. Pinon, and E. Rivoalen, "Experimental characterisation of flow effects on marine current turbine behaviour and on its wake properties," *IET Renewable Power Generation*, vol. 4, no. 6, pp. 498–509, 2010.

[165] S. W. Tucker Harvey, X. Chen, D. Rowe, J. McNaughton, C. R. Vogel, K. Bhavsar, T. Allsop, J. Gilbert, H. Mullings, T. Stallard, A. M. Young, I. Benson, and R. H. J. Willden, "Tidal turbine benchmarking project: stage i - steady flow experiments," in *Proceedings of the 15th European Wave and Tidal Energy Conference (EWTEC 2023)*, Sep. 2023, Art. no. 553, pp. 1–10.

[166] L. P. Chamorro, C. Hill, S. Morton, C. Ellis, R. E. A. Arndt, and F. Sotiropoulos, "On the interaction between a turbulent open channel flow and an axial-flow turbine," *Journal of Fluid Mechanics*, vol. 716, pp. 658–670, 2013.

[167] L. P. Chamorro, C. Hill, V. S. Neary, B. Gunawan, R. E. A. Arndt, and F. Sotiropoulos, "Effects of energetic coherent motions on the power and wake of an axial-flow turbine," *Physics of Fluids*, vol. 27, no. 5, Art. no. 055104, pp. 1–11, 2015.

[168] B. J. Stanislawski, R. Thedin, A. Sharma, E. Branlard, G. Vijayakumar, and M. A. Sprague, "Effect of the integral length scales of turbulent inflows on wind turbine loads," *Renewable Energy*, vol. 217, p. 119 218, 2023.

[169] I. A. Milne, R. N. Sharma, R. G. J. Flay, and S. Bickerton, "The role of onset turbulence on tidal turbine blade loads," in *Proceedings of the 17th Australasian Fluid Mechanics Conference*, Auckland, New Zealand, Dec. 2010, pp. 444–447.

[170] J. I. Whelan, "A fluid dynamic study of free-surface proximity and inertia effects on tidal turbines," Ph.D. dissertation, Imperial College London, 2010.

[171] I. A. Milne, A. H. Day, R. N. Sharma, and R. G. J. Flay, "Blade loads on tidal turbines in planar oscillatory flow," *Ocean Engineering*, vol. 60, pp. 163–174, 2013.

[172] I. A. Milne, A. H. Day, R. N. Sharma, and R. G. J. Flay, "Blade loading on tidal turbines for uniform unsteady flow," *Renewable Energy*, vol. 77, pp. 338–350, 2015.

[173] J. V. Norris and E. Droniou, "Update on EMEC activities, resource description, and characterisation of wave-induced velocities in a tidal flow," in *Proceedings of the 7th European Wave and Tidal Energy Conference (EWTEC 2007)*, Porto, Portugal, Sep. 2007, pp. 1–8.

[174] S. C. Tatum, C. H. Frost, M. Allmark, D. M. O'Doherty, A. Mason-Jones, P. W. Prickett, R. I. Grosvenor, C. B. Byrne, and T. O'Doherty, "Wave-current interaction effects on tidal stream turbine performance and loading characteristics," *International Journal of Marine Energy*, vol. 14, pp. 161–179, 2016.

[175] C. Guy, E. Hart, V. Vengatesan, and D. Forehand, "Numerical modelling of a 1.5 MW tidal turbine in realistic coupled wave–current sea states for the assessment of turbine hub-depth impacts on mechanical loads," *Ocean Engineering*, vol. 292, p. 116 577, 2024.

[176] N. Barltrop, K. S. Varyani, A. Grant, D. Clelland, and X. Pham, "Wave-current interactions in marine current turbines," *Proceedings of the Institution of Mechanical Engineers, Part M: Journal of Engineering for the Maritime Environment*, vol. 220, no. 4, pp. 195–203, 2006.

[177] B. Gaurier, P. Davies, A. Deuff, and G. Germain, "Flume tank characterization of marine current turbine blade behaviour under current and wave loading," *Renewable Energy*, vol. 59, pp. 1–12, 2013.

[178] C. Lloyd, M. Allmark, S. Ordonez-Sanchez, R. Martinez, C. Johnstone, G. Germain, B. Gaurier, A. Mason-Jones, and T. O'Doherty, "Validation of the dynamic load characteristics on a tidal stream turbine when subjected to wave and current interaction," *Ocean Engineering*, vol. 222, p. 108 360, 2021.

[179] S. Draycott, J. Steynor, A. Nambiar, B. Sellar, and V. Vengatesan, "Experimental assessment of tidal turbine loading from irregular waves over a tidal cycle," *Journal of Ocean Engineering and Marine Energy*, vol. 5, pp. 173–187, 2019.

[180] F. Zilic de Arcos, C. R. Vogel, and R. H. J. Willden, "A numerical study on the hydrodynamics of a floating tidal rotor under the combined effects of currents and waves," *Ocean Engineering*, vol. 286, p. 115 612, 2023.

[181] M. H. Bin Osman, R. H. J. Willden, and C. R. Vogel, "The effects of surge motion on floating horizontal axis tidal turbines," *International Marine Energy Journal*, vol. 3, no. 2, pp. 45–54, 2020.

[182] M. H. Bin Osman and R. H. J. Willden, "Added mass and damping forces of a floating tidal turbine undergoing pendulum motion," *Ocean Engineering*, vol. 283, p. 115 014, 2023.

[183] S. A. Brown, E. J. Ransley, N. Xie, K. Monk, G. M. De Angelis, R. Nicholls-Lee, E. Guerrini, and D. M. Greaves, "On the impact of motion-thrust coupling in floating tidal energy applications," *Applied Energy*, vol. 282, p. 116 246, 2021.

[184] G. S. Payne, T. Stallard, and R. Martinez, "Design and manufacture of a bed supported tidal turbine model for blade and shaft load measurement in turbulent flow and waves," *Renewable Energy*, vol. 107, pp. 312–326, 2017.

[185] G. T. Scarlett, B. Sellar, T. van den Bremer, and I. M. Viola, "Unsteady hydrodynamics of a full-scale tidal turbine operating in large wave conditions," *Renewable Energy*, vol. 143, pp. 199–213, 2019.

[186] S. A. Ning, "A simple solution method for the blade element momentum equations with guaranteed convergence," *Wind Energy*, vol. 17, no. 9, pp. 1327–1345, 2014.

[187] P. J. Moriarty and A. C. Hansen, "AeroDyn theory manual," National Renewable Energy Laboratory (NREL), Tech. Rep. NREL/TP-500-36881, 2005.

[188] B. Gaurier, G. Germain, J.-V. Facq, C. M. Johnstone, A. D. Grant, A. H. Day, E. Nixon, F. Di Felice, and M. Costanzo, "Tidal energy round robin tests comparisons between towing tank and circulating tank results," *International Journal of Marine Energy*, vol. 12, pp. 87–109, 2015, Special Issue on Marine Renewables Infrastructure Network.

[189] M. Drela, "XFOIL: an analysis and design system for low Reynolds number airfoils," in *Low Reynolds Number Aerodynamics. Lecture Notes in Engineering*, T. J. Mueller, Ed., vol. 54, Springer Berlin Heidelberg, pp. 1–12, Jun. 1989.

[190] G. T. Houlsby, S. Draper, and M. L. G. Oldfield, "Application of linear momentum actuator disc theory to open channel flow," University of Oxford, Tech. Rep. OUEL 2296/08, 2008.

[191] J. McNaughton, B. Cao, C. R. Vogel, and R. H. J. Willden, "Model scale testing of multi-rotor arrays designed to exploit constructive interference effects," in *Proceedings of the 13th European Wave and Tidal Energy Conference (EWTEC 2019)*, Sep. 2019, pp. 1–13.

[192] Unknown, *Airfoil tools - airfoil database and tools*, Accessed: 2023-06-30, 2024. [Online]. Available: http://www.airfoiltools.com/.

[193] Unknown, *Electrical resistance strain gage circuits*, Accessed: 2023-10-05, 2000. [Online]. Available: https://p.urbanpro.com/tv-prod/documents%2Fnull-strain-gages.pdf.

[194] Mantracourt, *ICA4 S and H versions user manual*, Brochure, Accessed: 2022-06-10, 2011. [Online]. Available: https://appmeas.co.uk/pdf/manuals/ICA4-Manual.pdf.

[195] S. Brinkmann, Personal communication, 2023.

[196] J. Winslow, H. Otsuka, B. Govindarajan, and I. Chopra, "Basic understanding of airfoil characteristics at low Reynolds numbers (104–105)," *Journal of Aircraft*, vol. 55, no. 3, pp. 1050–1061, 2018.

[197] J. McNaughton, B. Cao, A. Nambiar, T. Davey, C. R. Vogel, and R. H. J. Willden, "Constructive interference effects for tidal turbine arrays," *Journal of Fluid Mechanics*, vol. 943, A38, 2022.

[198] British Standards Institution (BSi), "Force measurement - strain gauge load cell systems - calibration method," BSi, Standard BS 8422:2003, 2003.

[199] J. McNaughton, S. Harper, R. Sinclair, and B. Sellar, "Measuring and modelling the power curve of a commercial-scale tidal turbine," in *Proceedings of 11th European Wave and Tidal Energy Conference (EWTEC 2015)*, Nantes, France, Sep. 2015, Art. no. 09A2, pp. 1–9.

[200] International Electrotechnical Commission (IEC), "Marine energy - wave, tidal and other water current converters - part 200: electricity producing tidal energy converters - power performance assessment," IEC, Standard IEC/TS 62600-200, 2013.

[201] L. Evans, I. Ashton, and B. Sellar, "Tidal turbine power performance assessments following IEC TS 62600-200 using measured and modelled power outputs," *Renewable Energy*, vol. 212, pp. 138–150, 2023.

[202] B. Gaurier, G. Germain, and G. Pinon, "How to correctly measure turbulent upstream flow for marine current turbine performances evaluation?" In *Proceedings of the 3rd International Conference on Renewable Energies Offshore (RENEW 2018)*, Lisbon, Portugal, Oct. 2018, pp. 23–30.

[203] G. S. Payne, T. Stallard, R. Martinez, and T. Bruce, "Variation of loads on a three-bladed horizontal axis tidal turbine with frequency and blade position," *Journal of Fluids and Structures*, vol. 83, pp. 156–170, 2018.

[204] S. F. Hoerner, *Fluid-Dynamic Drag: Practical Information on Aerodynamic Drag and Hydrodynamic Resistance*. USA: Hoerner Fluid Dynamics, 1965.

[205] A. Betz, "Das Maximum der theoretisch möglichen Ausnützung des Windes durch Windmotoren," *Zeitschrift für das gesamte Turbinenwesen*, vol. 26, pp. 307–309, 1920.

[206] G. Deskos, G. S. Payne, B. Gaurier, and M. Graham, "On the spectral behaviour of the turbulence-driven power fluctuations of horizontal-axis turbines," *Journal of Fluid Mechanics*, vol. 904, A13, 2020.

[207] "Kolmogorov–Smirnov test," in *The Concise Encyclopedia of Statistics*. USA: Springer New York, 2008, pp. 283–287.

[208] P. B. S. Lissaman, "Low-Reynolds-number airfoils," *Annual Review of Fluid Mechanics*, vol. 15, pp. 223–239, 1983.

[209] International Towing Tank Conference (ITTC), "Uncertainty analysis, example for open water test," ITTC, Recommended Procedures and Guidelines 7.5-02-03-02.2, 2014.

[210] International Towing Tank Conference (ITTC), "Uncertainty analysis - example for horizontal axis turbines," ITTC, Recommended Procedures and Guidelines 7.5-02-07-03.15, 2017.

[211] International Towing Tank Conference (ITTC), "Testing and extrapolation methods, general density and viscosity of water," ITTC, Recommended Procedures and Guidelines 7.5-02-01-03, 2006.

[212] N. Tobin, H. Zhu, and L. P. Chamorro, "Spectral behaviour of the turbulence-driven power fluctuations of wind turbines," *Journal of Turbulence*, vol. 16, no. 9, pp. 832–846, 2015.

[213] D. T. Rowe, *ADV data processing using MATLAB*, 2023. [Online]. Available: https://github.com/eg0u30a2/adv_data_processing.git.

[214] D. T. Rowe, C. R. Vogel, and R. H. J. Willden, "Hydrodynamic characterisation of a hydraulic flume with sheared flow," *International Journal of Mechanical and Mechatronics Engineering*, vol. 18, no. 9, pp. 247–256, 2024.